1993

A model study of hydrodynamic and water quality characteristics of the Rappahannock Estuary, Virginia

Kyeong Park
College of William and Mary - Virginia Institute of Marine Science

INFORMATION TO USERS

This manuscript has been reproduced from the microfilm master. UMI films the text directly from the original or copy submitted. Thus, some thesis and dissertation copies are in typewriter face, while others may be from any type of computer printer.

The quality of this reproduction is dependent upon the quality of the copy submitted. Broken or indistinct print, colored or poor quality illustrations and photographs, print bleedthrough, substandard margins, and improper alignment can adversely affect reproduction.

In the unlikely event that the author did not send UMI a complete manuscript and there are missing pages, these will be noted. Also, if unauthorized copyright material had to be removed, a note will indicate the deletion.

Oversize materials (e.g., maps, drawings, charts) are reproduced by sectioning the original, beginning at the upper left-hand corner and continuing from left to right in equal sections with small overlaps.

Photographs included in the original manuscript have been reproduced xerographically in this copy. Higher quality 6" x 9" black and white photographic prints are available for any photographs or illustrations appearing in this copy for an additional charge. Contact UMI directly to order.

Bell & Howell Information and Learning
300 North Zeeb Road, Ann Arbor, MI 48106-1346 USA

UMI®
800-521-0600

Order Number 9317241

A model study of hydrodynamic and water quality characteristics of the Rappahannock Estuary, Virginia

Park, Kyeong, Ph.D.

The College of William and Mary, 1993

U·M·I
300 N. Zeeb Rd.
Ann Arbor, MI 48106

A MODEL STUDY OF HYDRODYNAMIC AND WATER QUALITY CHARACTERISTICS OF THE RAPPAHANNOCK ESTUARY, VIRGINIA

A Dissertation

Presented to

The Faculty of the School of Marine Science

The College of William and Mary in Virginia

In Partial Fulfillment

Of the Requirements for the Degree of

Doctor of Philosophy

by

Kyeong Park

1993

This dissertation is submitted in partial fulfillment of

the requirements for the degree of

Doctor of Philosophy

Kyeong Park

Approved, February 1993

Albert Y. Kuo, Ph.D.
Committee Chairman / Adviser

John M. Brubaker, Ph.D.

Carl F. Cerco, Ph.D.
U.S. Army Engineer Waterways Experiment Station,
Vicksburg, MS

John M. Hamrick, Ph.D.

Roger L. Mann, Ph.D.

Bruce J. Neilson, Ph.D.

TABLE OF CONTENTS

ACKNOWLEDGEMENTS

I am indebted to my major professor, Dr. Albert Y. Kuo, for his advise, guidance, support, patience and encouragement throughout my stay at VIMS. I am grateful to Dr. Bruce J. Neilson for his support, advise and encouragement. The assistance of Dr. John M. Hamrick in numerical methods and Dr. Carl F. Cerco in water quality modeling was invaluable in the completion of this study. I am thankful to Drs. John M. Brubaker and Roger L. Mann for their review of manuscripts.

For helpful discussions, I thank Drs. Leonard W. Haas, William G. MacIntyre and Maynard M. Nichols. I thank the field crew members in the Division of Physical Oceanography who collected the field data used in this study. I also wish to thank the EPA Chesapeake Bay Program Office for the field data collected by Virginia Water Control Board as a part of the Chesapeake Bay Fall Line and Tributary Water Quality Monitoring Program.

My special thanks to my parents and my wife, Aeyoung, for their loving support in all my endeavors.

LIST OF TABLES

LIST OF FIGURES

ABSTRACT

A laterally integrated, two-dimensional, real-time model, consisting of linked hydrodynamic and water quality models, is developed and applied to the Rappahannock Estuary, Virginia. The hydrodynamic model, based on the principles of conservation of volume, momentum and mass, predicts surface elevation, current velocity and salinity. The water quality model, based on the conservation of mass alone, predicts eight parameters; dissolved oxygen (DO), chlorophyll 'a', carbonaceous biochemical oxygen demand (CBOD), organic nitrogen, ammonia nitrogen, nitrite-nitrate nitrogen, organic phosphorus and inorganic phosphorus. The model equations were solved using a two time level, finite difference scheme.

The hydrodynamic model was calibrated and verified using field data collected in 1987 and 1990, and was used to study hydrodynamic processes. A reverse longitudinal salinity gradient, that has been frequently observed in the Rappahannock, was explained in terms of bottom topography and vertical mixing. This argument was further supported by the salinity data from 1981-1990 slackwater surveys. The often confusing usage of the phrase "limit of salt intrusion" in place of "limit of gravitational circulation" was clarified.

The water quality model was calibrated and verified using the field data from 1990 surveys, and was used to study water quality conditions. Hypoxia, even anoxia, persists during summer in the bottom water of the lower portion of the Rappahannock. Sensitivity analysis showed that the bottom water ends up being hypoxic regardless of DO and CBOD in the incoming bay water, and hypoxia can be relieved more by eliminating CBOD than by increasing DO in the incoming bay water. An increase in either residual velocity or vertical mixing can relieve the hypoxic condition. Water column respiration, including CBOD decay, nitrification and algal respiration, is as important as sediment oxygen demand, and the CBOD decay is the most important in the water column.

High chlorophyll concentrations in the lower portion of tidal freshwater have been observed frequently in many estuaries. Sensitivity analysis indicated that the high chlorophyll in the Rappahannock cannot be maintained without an external input of nutrients. A hypothesis was proposed to account for the nutrient source and the downriver limit of high chlorophyll concentrations.

A MODEL STUDY OF HYDRODYNAMIC AND WATER QUALITY CHARACTERISTICS OF THE RAPPAHANNOCK ESTUARY, VIRGINIA

I. INTRODUCTION

Water quality problems in a tidal system generally result from a combination of physical and biochemical processes as human activities exert stress on the system. Therefore, water quality management in estuarine and coastal waters has received increased attention in recent years as human activities in these areas increase.

Dissolved oxygen (DO) deficiency, as an index of deteriorated water quality, has been widely observed in estuarine and coastal waters such as the New York Bight (Falkowski et al. 1980), the New Jersey coast (Swanson & Sindermann 1979) and Chesapeake Bay (Officer et al. 1984). In Chesapeake Bay, for example, anoxia (no dissolved oxygen) has been known since the 1930's (Newcombe & Horne 1938). It has been more widespread and of longer duration during recent times (Flemer et al. 1983), and appears to have had significant ecological effects (Seliger et al. 1985). All major subestuaries on the western side of Chesapeake Bay have a deep basin near their mouth. Hypoxia (deficient dissolved oxygen) has been observed frequently in the deep basin of the Patuxent River, Maryland (Laubach & Summers 1987) and the Rappahannock and York rivers in Virginia (D'Elia et al. 1981; Phoel et al. 1981; Kuo & Neilson 1987; Kuo et al. 1991a; Kuo & Park 1992; Llansó 1992).

Many processes, e.g., physical transport and biochemical transformations, may combine to cause the depletion of DO in the water column (Officer et al. 1984; Smith et al. 1992). Living organisms such as benthic organisms, bacteria and plankton in the water column consume the oxygen, while weak mixing due to the strong vertical stratification of the water column and weak wind and increased turbidity combine to

prevent the replenishment of oxygen. Then, the low DO concentration results in high benthic mortalities and in turn, to make matters worse, the decomposition of these dead organisms further consumes DO in the water column. In addition to the natural processes, the anthropogenic processes, such as excessive loadings of organic and inorganic wastes, can exacerbate the anoxic/hypoxic phenomena.

Inasmuch as these manifold processes affect the DO distribution in the water column, it is difficult to assess the relative importance of each process. To this end, a mathematical model based on physical and biogeochemical principles is useful both to aid in understanding the system and to provide consistent, rational predictions of dynamic responses of the system to changes in specified factors.

1-1. Model Selection

Most mathematical models of water quality consist of a hydrodynamic model and a water quality model, linked either externally or internally. The hydrodynamic model generates time-series records of water velocity and surface elevation that are used in the simulation of physical transport processes in the water quality model.

So far, advances in hydrodynamic modeling far exceed those in water quality modeling. This is mainly because the mathematical expressions describing biochemical processes, compared to those describing physical processes, are more coarse approximation of the properties of the system being modeled, and thus subject to less accuracy. Also the field data that can be obtained from the current sampling techniques have finer spatial and temporal resolutions, and are of higher quality for the hydrodynamic parameters than the water quality ones. This makes the calibration and verification of the hydrodynamic model easier and more reliable.

Primarily because of their simplicity, one-dimensional longitudinal models have been widely employed for water quality management in lakes, estuaries and coastal

waters (Shanahan & Harleman 1982; Thomann & Fitzpatrick 1982; Williams & Kuo 1984; Cerco et al. 1987; Ambrose et al. 1988; Kuo et al. 1991b). These models are based on the one-dimensional momentum, continuity and salt balance equations and the mass balance equations for DO and other water quality parameters, assuming no vertical and lateral parameter variations. Despite its limitation, the one-dimensional approach has helped us to understand many aspects of the natural system and is still being employed for systems in which there is virtually no sectional variation.

The flow patterns in partially mixed estuaries, however, call for an explicit description of vertical structures of velocity and density in the numerical modeling of hydrodynamic transport (Wang et al. 1990). Besides, the vertical variations in DO often are large. This leaves only two choices for the modeling of DO distribution in partially mixed estuaries: three-dimensional or laterally integrated two-dimensional models.

Estuarine flow and DO distribution are three-dimensional in nature. To simulate these completely, a three-dimensional model with time-dependent momentum and continuity equations, mass-balance equations with detailed description of the biochemical kinetics, and sources and sinks of all dissolved constituents is necessary. It seems that the state-of-the-art computer technology enables us to do three-dimensional simulations, particularly of hydrodynamics (Caponi 1977; Oey et al. 1985; Blumberg & Mellor 1987). The current sampling capacity, however, cannot provide us with the quantity and quality of field data that are indispensable for the calibration and verification of the model, particularly the water quality model. Shanahan & Harleman (1982) have pointed out the necessity to consider both hydrodynamics and biochemistry in a compatible and even-handed fashion. In practice, the application of the three-dimensional water quality model to a natural body of water is complicated in terms of tractability and economy, and sometimes not

warranted in terms of desired results.

Relatively narrow, straight estuaries are suitable for laterally integrated two-dimensional models assuming that all properties are uniformly distributed laterally across the estuary at their respective average values (Wang et al. 1990). The assumption of no lateral variation can be applied to estuaries where both tidal pumping and dispersion produced by tidal trapping are not important.

Tidal pumping refers to the situations where the flow is distributed differently in a cross-section during ebb and flood, and is principally caused by the Coriolis force and irregular bathymetry (Fischer et al. 1979). In simplifying the three-dimensional phenomena into two-dimensional frame work, some approximations are inevitable. The typical example is that a vertical two-dimensional model cannot account for the effects of the Coriolis force and irregular bathymetry.

The importance of the Coriolis force can be estimated using the nondimensional Kelvin number (K), which is $K = B/R_o$ where B is a typical width and R_o is the external Rossby radius of deformation, and $R_o = C_o/f$ where f is the Coriolis parameter and C_o is the wave celerity (Kundu 1990). The celerity (C_o) of a long surface gravity wave is equal to $(gH)^{1/2}$, where g is the gravitational acceleration and H is a typical depth. In the Rappahannock River, where $B \approx 2$ km, $f \approx 10^{-4}$ sec^{-1} and $H \approx 10$ m, the external $K \approx 0.02$ and thus the effect of the earth's rotation is not important for the barotropic mode of the circulation. The internal structure of the estuary can be more responsive to the Coriolis force because it is governed by motions with typically much smaller phase speeds (Wang et al. 1990). In this case, the internal R_o should be based on celerities of the internal waves that is, $C_n = NH/n\pi$ where n is a positive integer and N is the buoyancy frequency (Kundu 1990). In the Rappahannock River, the internal K for the first mode ($n = 1$) is approximately 0.9 meaning that Coriolis force may play an important role for the

baroclinic mode of the circulation.

Tidal trapping is a term used to describe the effects of side embayments, small branching channels and shallow regions of an estuary, and occurs in almost all estuaries and in many tidal rivers (Fischer et al. 1979). A portion of water with its contained substances is stored temporarily in side channel, while the main flow proceeds along the estuary's major axis. If the recapture of the stored volume is out of phase with the main flow, longitudinal mixing occurs when the tide reverses.

Numerous laterally integrated two-dimensional hydrodynamic models have been applied to estuaries (Bowden & Hamilton 1975; Blumberg 1975 and 1977; Hamilton 1977; Kuo et al. 1978; Wang & Kravitz 1980; Edinger & Buchak 1980 and 1981; Perrells & Karelse 1981). Among these, the one developed by Kuo et al. (1978) accounts for tidal trapping by modeling the side embayment area. This hydrodynamic model was modified and used in the present study to simulate the flow field and salinity distribution, and the corresponding water quality model was developed to simulate the distributions of DO and other related water quality parameters.

1-2. Objectives

The main objective of this study is to develop a laterally integrated two-dimensional model of hydrodynamics and water quality in estuarine systems, and to apply the model to study the DO distribution and hypoxia in the Rappahannock Estuary, Virginia. The development of the mathematical model is described in Chapter II, and the characteristics of the study area, the Rappahannock Estuary, are described in Chapter III. The calibration and verification of the hydrodynamic model using field data collected in 1987 and 1990 is discussed in Chapter IV. The water quality model was calibrated and verified using field data collected during summer of 1990 (Chapter V).

Once calibrated and verified, the model is a powerful tool and can be used to study the characteristic behavior of the prototype. Sensitivity analysis was performed to study the hydrodynamic and water quality characteristics of the Rappahannock Estuary. The hydrodynamic responses of the prototype are included in Chapter IV. The sensitivity analysis of the water quality model (Chapter VI) emphasized the lower part of the river where hypoxia, or even anoxia, has persisted during summer in the bottom water and the middle part of the river, which was characterized with high chlorophyll concentration. The summary of this study with recommendations for future study is presented in Chapter VII.

II. DESCRIPTION OF THE MODEL

2-1. Hydrodynamic Model

2-1-1. Basic equations

The laterally integrated two-dimensional hydrodynamic model developed by Kuo et al. (1978) was modified and used to calculate the flow field and salinity. With a right-handed Cartesian coordinate system with the x-axis directed seaward and the z-axis directed upward (Fig. 2-1), the governing equations are,

$$\frac{\partial(uB)}{\partial x} + \frac{\partial(wB)}{\partial z} = 0 \tag{2-1}$$

$$\frac{\partial}{\partial t}(B_\eta \eta) + \frac{\partial}{\partial x}\int_{-H}^{\eta}(uB)\,dz = 0 \tag{2-2}$$

$$\frac{\partial(uB)}{\partial t} + \frac{\partial(uBu)}{\partial x} + \frac{\partial(uBw)}{\partial z} = -\frac{B}{\rho}\frac{\partial p}{\partial x} + \frac{\partial}{\partial x}(A_x B\frac{\partial u}{\partial x}) + \frac{\partial}{\partial z}(A_z B\frac{\partial u}{\partial z}) \tag{2-3}$$

$$\frac{\partial p}{\partial z} = -\rho g \tag{2-4}$$

$$\frac{\partial(sB)}{\partial t} + \frac{\partial(sBu)}{\partial x} + \frac{\partial(sBw)}{\partial z} = \frac{\partial}{\partial x}(K_x B\frac{\partial s}{\partial x}) + \frac{\partial}{\partial z}(K_z B\frac{\partial s}{\partial z}) + S_o \tag{2-5}$$

where

t = time,

η = position of the free surface above mean sea level,

u & w = laterally averaged velocities in the x and z directions, respectively,

s = laterally averaged salinity,

B & B_η = river width and width at the free surface,

H = total depth below mean sea level,

p & ρ = pressure and water density,

g = gravitational acceleration,

A_x & A_z = turbulent viscosities in the x and z directions, respectively,

K_x & K_z = turbulent diffusivities in the x and z directions, respectively, and

S_o = source or sink of salt.

Equations 2-1 and 2-2 are the laterally and sectionally, respectively, integrated continuity equations for an incompressible flow. Equation 2-3 is the laterally integrated equation of motion for an incompressible but non-homogeneous flow, and represents the momentum balance along the longitudinal axis of an estuary. When the hydrostatic approximation, i.e., gravity is the dominant force in the vertical direction, is applied to the equation of motion in the z direction, the result is the hydrostatic equation (Eq. 2-4). Equation 2-5 is the laterally integrated mass-balance equation for salt. The density is related to the salinity by the simplified equation of state,

$$\rho = \rho_o(1 + ks) \tag{2-6}$$

where ρ_o is the density of freshwater and k is constant (7.5×10^{-4} ppt^{-1}). This is usually regarded as a satisfactory approximation because of the large horizontal gradients of salinity in estuaries (Hamilton 1977).

Equations 2-1 through 2-3 are solved by a finite difference method to obtain the time-varying solution of the free surface elevation (η) and the laterally averaged velocity fields (u and w). The pressure term (p) is evaluated using Eq. 2-4 with the water density (ρ) from Eq. 2-6, and salinity (s) using Eq. 2-5.

2-1-2. Boundary conditions

A. Free surface conditions: The wind stress term is used to account for momentum

introduced into the estuary, and there is no mass flux through the free surface. They are, respectively, at $z = \eta$,

$$\rho A_z \frac{\partial u}{\partial z} = C_D \rho_a U_w |U_w| \quad \text{and} \quad K_z \frac{\partial s}{\partial z} = 0 \tag{2-7}$$

where C_D is the dimensionless drag coefficient (1.3×10^{-3} in centimeter-gram-second [CGS] unit), ρ_a is the air density (1.2×10^{-3} g cm^{-3}) and U_w is the wind speed (in cm sec^{-1}) at the height of 10 m above surface.

B. Bottom conditions: The bottom stress accounting for resistance by frictional force due to the bottom and side wall of the estuary is calculated using a quadratic law, and there is no mass flux through the bottom. They are, respectively, at $z = -H$,

$$A_z \frac{\partial u}{\partial z} = \kappa u_1 |u_1| = \tau_b \quad \text{and} \quad K_z \frac{\partial s}{\partial z} = 0 \tag{2-8}$$

where u_1 is the velocity at a depth 1 m above bottom, τ_b is the frictional stress and κ is the boundary frictional coefficient in the order of 0.0025. The coefficient, κ, is assumed to be identical with the one used in one-dimensional flows, and is expressed as $\kappa = g\, n^2\, h^{-1/3}$ where n is the Manning's friction coefficient and h is the total depth. When estimating the total frictional force, Blumberg's approximation (1975), $\tau_b[1 + (\partial B/\partial z)^2]^{1/2} \approx \tau_b\, \partial B/\partial z$ assuming $\partial B/\partial z \gg 1$, is used.

C. Upstream boundary: The landward boundary ($x = 0$) of the model is chosen at the fall line or landward limit of tidal influence. It is assumed that the freshwater discharge and the concentrations of the constituents being modeled are known at this boundary. They are, respectively, at $x = 0$,

$$u = \frac{Q(t)}{A} \quad \text{and} \quad c = \text{known} \tag{2-9}$$

where Q(t) is the freshwater discharge through the upstream boundary, A is the cross-

sectional area there, and c is the concentration of the constituent being modeled. Since the tide propagates farther upriver than the salt does, the salinity at the upstream boundary is specified to be zero.

D. Downstream boundary: The seaward boundary (x = L) is located near the mouth of the estuary. The surface elevation is specified either with harmonic functions or with the field measurements at this boundary.

In calculating velocities at the open boundary, the horizontal velocities are linearly extrapolated to a fictitious model transect outside the mouth, and the advective and diffusive terms are calculated over this fictitious model segment. An alternative approach is to assume that the dominant momentum balance in partially mixed estuaries takes place between the effects of surface slope, density gradient, and turbulent shear stress neglecting the horizontal advection and diffusion of momentum at the mouth. The difference between the results of the two methods is negligible, and the former method is adopted for this model.

Finally, a condition for the salt balance equation (Eq. 2-5) must be given. An "oceanic" or "bay" salinity is assumed to exist off the mouth of the estuary. During flood tide, the bay water is advected into the estuary, increasing the salinity at the mouth until the bay salinity is achieved. Following the suggestion of Thatcher & Harleman (1972), a period of adjustment is allowed after the flow starts to flood and before the salinity at the mouth reaches the bay value. In the model, an input parameter is assigned for the specification of this adjustment period, and the salinity is assumed to increase linearly with time during this period, i.e., during flood tide ($u < 0$) at $x = L$,

$$\frac{\partial s}{\partial t} = -\frac{\partial s}{\partial x} u \qquad (2\text{-}10)$$

During ebb tide, the horizontal salinity profile is assumed to have advected out of the

mouth as a "frozen" pattern, i.e., neglecting the diffusion.

2-1-3. Turbulence closure model

The three-dimensional equations for volume, momentum and salt expressed in terms of the instantaneous flow field and salinity distribution, need to be averaged over a time interval longer than the turbulence time scale but much shorter than the tidal period, to derive the equations in terms of mean quantities. This time-averaging of momentum and mass balance equations gives rise to Reynolds stress and flux terms, which account for the diffusive exchange of momentum and salt, respectively, by small-scale turbulent motion. Then these time-averaged equations are laterally averaged to obtain the basic equations in Section 2-1-1. In a system with lateral inhomogeneity, the spatial-averaging in the lateral direction of the momentum and mass balance equations produces dispersion terms. These dispersion terms, owing to their similar mathematical appearance to Reynolds terms, are usually incorporated into the Reynolds terms and treated as one term to represent the mixing of momentum or salt. In Equations 2-3 and 2-5, therefore, A_x, A_z, K_x and K_z should be interpreted as lateral average values that take account of both diffusive and dispersive processes (Fischer 1967).

The system of equations would be closed only through the parameterization of Reynolds stress and flux terms. Formulation of the Reynolds stress and flux terms mathematically, i.e., the turbulence closure model, has been, and still is, one of the most problematic steps for the laterally integrated two-dimensional or three-dimensional numerical models. The current practice ranges from a simple eddy viscosity approach to more complicated second order closure schemes (Blumberg 1986). The most reasonable way, with the current understanding of the turbulent mixing processes, is to choose cautiously the best method for an application and to

calibrate it by comparison with field data (Wang et al. 1990). The oldest, yet still the most popular method of parameterizing the Reynolds terms, is the one based upon the eddy viscosity hypothesis. In Equations 2-3 and 2-5, the Reynolds terms are already expressed in terms of eddy viscosities (A_z and A_x) and diffusivities (K_z and K_x).

A. Vertical turbulent mixing coefficients: The vertical coefficients (A_z and K_z) are strongly affected by the flow velocity, the relative roughness of the flow channel and the vertical stratification. Their values can vary over several orders of magnitude at a fixed point in an estuary during a tidal cycle (Odd & Rodger 1978).

In the present study, the mixing length concept first conceived by Prandtl is used for A_z and K_z. For an estuarine flow in a wide channel of depth h, using the mixing length form for two parallel plane boundaries (Rossby & Montgomery 1935),

$$A_z = \alpha Z^2 (1 - \frac{Z}{h})^2 \left| \frac{\partial u}{\partial z} \right| \phi_M(R_i) \qquad (2\text{-}11)$$

$$K_z = \alpha Z^2 (1 - \frac{Z}{h})^2 \left| \frac{\partial u}{\partial z} \right| \phi_S(R_i) \qquad (2\text{-}12)$$

where Z is the distance from the surface, α is a constant to be determined empirically, and ϕ_M and ϕ_S are the stability functions for momentum and mass, respectively. The local Richardson number (R_i), a measure of stability, is defined by,

$$R_i = -\frac{g}{\rho}(\frac{\partial \rho}{\partial z})(\frac{\partial u}{\partial z})^{-2} \qquad (2\text{-}13)$$

The stability functions in Equations 2-11 and 2-12 account for the inhibition of the vertical exchange of momentum and mass (salt) by a stable density structure. Many studies have been performed for ϕ_M and ϕ_S, and there seem to be as many sets of formulations for them. Although the effect of the stratification on the vertical turbulent exchange is a function of R_i, the theory does not dictate what form this function should have (Perrels & Karelse 1981).

A review of the various formulations for ϕ_M and ϕ_S shows the following general forms (Bowden & Hamilton 1975; Blumberg 1986),

$$\phi_M = (1 + \beta_M R_i)^p \tag{2-14}$$

$$\phi_S = (1 + \beta_S R_i)^q \tag{2-15}$$

where β_M, β_S, p and q are constants to be determined empirically. In the numerical modeling, these constants can be determined through model calibration. For a given condition, however, different sets of these constants can exist. That is, there are too many degrees of freedom. Results from previous studies were used to determine some of these constants. For p and q, this study adopts the values of Munk & Anderson (1948), p = -1/2 and q = -3/2, which indicates that a stable density gradient reduces the vertical turbulent exchange of mass more than that of momentum. In the numerical modeling, the constants including β_M and β_S are usually evaluated through comparison of model results with field measurements of a conservative substance such as salt. This makes the evaluation of β_M, which affects the vertical exchange of momentum, somewhat ambiguous. A priori there is no particular reason to consider that $\beta_M \neq \beta_S$. Since the difference in the effect of density structure on momentum and salt is already included in choosing the constants, p and q, it is assumed that β_M is equal to β_S.

When the wind effect is included, the resulting formulations for A_z and K_z are,

$$A_z = \alpha Z^2 (1 - \frac{Z}{h})^2 \left| \frac{\partial u}{\partial z} \right| (1 + \beta R_i)^{-\frac{1}{2}} + \alpha_w \frac{H_w^2}{T} \exp(-\frac{2\pi}{L} Z) \tag{2-16}$$

$$K_z = \alpha Z^2 (1 - \frac{Z}{h})^2 \left| \frac{\partial u}{\partial z} \right| (1 + \beta R_i)^{-\frac{3}{2}} + \alpha_w \frac{H_w^2}{T} \exp(-\frac{2\pi}{L} Z) \tag{2-17}$$

where H_w, T and L are the height, period and length, respectively, of wind-induced waves, and the constants (α, β and α_w) are determined through model calibration.

The second terms in Equations 2-16 and 2-17 account for the turbulent mixing by wind-induced waves, and the first part, $\alpha_w \cdot H_w^2/T$, is the formulation proposed by Ichiye (1967). The depth dependence deduced by Pritchard (1960) using the James River data, consists of two parts; exponential decay with depth, $\exp(-2\pi Z/L)$, and shape function with depth, $Z(1-Z/h)$. In the study of the wind effects on turbulent mixing in lakes, Ford (1976) used the exponential decay but not the shape function. The shape function having a parabolic shape with depth renders the wind effect zero at the surface ($Z = 0$). The present study includes only the exponential decay term, which does not reduce the wind mixing just below the surface. The winds blowing over an estuary influence the velocity structure, as well as the salinity structure. The response of velocity near the surface to the external forcing such as winds is quicker than that of mass (salt), making the velocity near the surface very homogeneous. In the events of wind, thus, the validity of using $\Delta u/\Delta z$ as an estimate of the velocity shear near the surface may be doubtful, and so is that of using R_i calculated from $\Delta u/\Delta z$ as a measure of stability. Besides, the vertical density gradient may be negligible in the surface mixing layer that is mostly affected by wind, and thus the stability function is not applied to the wind mixing term.

For stable conditions ($R_i > 0$), Equations 2-16 and 2-17 are used to calculate A_z and K_z. When $R_i < 0$, A_z and K_z are calculated with Equations 2-16 and 2-17 without including the effect of the stability functions, that is, assuming $R_i = 0$. This treatment, although it would allow the vertical instability to exist longer than it should, does allow the existence of the unstable conditions, which have been frequently observed in Virginia estuaries including James, York and Rappahannock estuaries (Brooks 1983)

The present model has the Mellor and Yamada Level 2 turbulence model (Mellor & Yamada 1974 and 1982) as a second choice to estimate the vertical

turbulent mixing coefficients. When the hydrodynamic model was applied to the Rappahannock River, it was not used because of the undesirable behavior, which is discussed in Appendix A.

B. Horizontal turbulent mixing coefficients: The horizontal mixing coefficients (A_x and K_x) are of the order of 10^5 of the vertical mixing coefficients (Dyer 1973). Results of diffusion measurements in English estuarine waters showed that K_x ranged from 10^4 to 10^6 cm^2 sec^{-1} (Talbot & Talbot 1974). Festa & Hansen (1976) studied the importance of exact values of A_x and K_x. Varying the momentum exchange coefficient from $A_x = A_z$ to $A_x = 10^6 A_z$ caused negligible effects on the results of their tidal average model. The change, however, in the mass exchange coefficient from $K_x = K_z$ to $K_x = 10^7 K_z$ did produce significant changes in their results.

The horizontal mixing terms, despite their relative insignificance in the momentum balance, are retained in the model for the stability consideration. The present study uses constant values for A_x and K_x and they are adjusted, within the range of 10^4 to 10^6 cm^2 sec^{-1}, through model calibration.

2-1-4. Method of solution

A. Grid system and geometry: The system of equations is solved using finite difference method with a uniform grid of spatially staggered variables. The geometry of the grid system used in the model and the location of variables within the grid are shown in Fig. 2-1. The grid system has η defined at the middle of each segment, while s, B, ρ and p at the center of the grid cell. The variables, w, A_z and K_z, are defined at the bottom faces of the grid cell, while the grid containing u, A_x and K_x is staggered by half the segment length as these are defined at the grid cell walls. This staggered grid structure, also used by many other investigators, permits easy application of the boundary conditions and evaluation of the dominant pressure

gradient force without interpolation or averaging (Blumberg 1977).

The geometry in the laterally integrated two-dimensional model is represented by the width at each depth at the center of each grid cell. A typical cross-section is illustrated in Fig. 2-2, which shows how the model accounts for the variation of width with depth.

B. Vertical integration: Large vertical gradients of variables (u and s) require a grid size that is much smaller in the vertical direction than in the horizontal direction. To accomplish this, the fluid motion is considered in horizontal slices with an exchange of momentum and mass between these slices. Integration over the height of the k^{th} layer can be performed by assuming that all variables are practically constant through the depth of any layer. Employing Leibnitz's rule and the boundary condition of no mass flux normal to the boundaries, the following equations can be obtained:

$$\frac{\partial \eta}{\partial t} = \frac{1}{B_1}[w_b B_b - \frac{\partial}{\partial x}(u_1 B_1 h_1)] \tag{2-18}$$

$$w_T = \frac{1}{B_T}[w_b B_b - \frac{\partial}{\partial x}(u_k B_k h_k)] \tag{2-19}$$

$$\frac{\partial}{\partial t}(u_k B_k h_k) + \frac{\partial}{\partial x}(u_k B_k u_k h_k) + w_T u_T B_T - w_b u_b B_b = -\frac{B_k h_k}{\rho_k}(\frac{\partial p}{\partial x})_k + \frac{\partial}{\partial x}[(A_x)_k B_k h_k (\frac{\partial u}{\partial x})_k] + (A_z B \frac{\partial u}{\partial z})_T - (A_z B \frac{\partial u}{\partial z})_b \tag{2-20}$$

$$\frac{\partial}{\partial t}(s_k B_k h_k) + \frac{\partial}{\partial x}(u_k B_k s_k h_k) + w_T s_T B_T - w_b s_b B_b = \frac{\partial}{\partial x}[(K_x)_k B_k h_k (\frac{\partial s}{\partial x})_k] + (K_z B \frac{\partial s}{\partial z})_T - (K_z B \frac{\partial s}{\partial z})_b + S_{o,1} \tag{2-21}$$

where

u_k, B_k & h_k = longitudinal velocity, width and height for the k^{th} layer, respectively,

u_b, w_b & B_b = longitudinal velocity, vertical velocity and width at the bottom of a layer, respectively, and

u_T, w_T & B_T = longitudinal velocity, vertical velocity and width at the top of a layer, respectively.

The term $S_{o,1}$ in Eq. 2-21 may represent the effect of the change in storage volume on the flanks (Fig. 2-2) with the change in tidal elevation. The subscript 1 means the interaction occurs only at the top layer. The storage in each segment will act as a source for the main channel on the falling tide and act as a sink on the rising tide. The salinity in the storage area remains the same on the falling tide, but changes on the rising tide because of the mixing between the incoming water from the main channel and the water in the storage area.

C. Finite difference treatment: A two-time level finite difference scheme is used to solve Equations 2-18 through 2-21. Three-time level (leapfrog) schemes are advantageous in dealing with the Coriolis term. They, however, tend to have problems of time-step splitting wherein the physical and computational modes alternate at each time step, even with viscous terms present (Roache 1972). The computational mode arises from using a second-order difference equation to approximate a first-order differential equation, and is a source of error (Haltiner & Williams 1980). The application of either Euler-backward scheme (Blumberg 1977; Wang & Kravitz 1980) or weak time filter (Asselin 1972; Blumberg & Mellor 1987) has been used to eliminate the time-step splitting. In the present study, the vertical two-dimensional hydrodynamic model does not include the Coriolis term and thus a two-time level scheme is used to approximate the time derivative terms in Equations 2-18, 2-20 and 2-21.

Equation 2-18 is solved explicitly to obtain the free surface elevation (η), and Equations 2-20 and 2-21 are solved to get the longitudinal velocity (u) and salinity (s),

respectively. Then, Eq. 2-19 is solved for the vertical velocity (w). To ensure stability,

1) the pressure gradient term in Eq. 2-20 is evaluated using η at a new time step,

2) the vertical mixing terms in Equations 2-20 and 2-21 are treated implicitly, and

3) the horizontal mixing terms in Equations 2-20 and 2-21 are retained.

The implicit treatment of the vertical mixing terms results in the tri-diagonal matrix in the vertical direction, which is solved using a LINPACK subroutine (SGTSL.FOR) developed at the Argonne National Laboratory. Further development of the pressure term is given in the later section. The complete finite difference forms of Equations 2-18 through 2-21 are presented in Appendix B.

In numerical modeling of the advection term, central and upwind (or upwind weighted) difference schemes are two routinely used ones. The upwind (or upwind weighted) difference scheme introduces the artificial numerical diffusion and thus suffers from severe inaccuracies, although the numerical diffusion makes the scheme stable and guarantees non-negative mass concentrations (Roache 1972). The use of fine grid spacing can alleviate this problem, but the consideration of computational aspects (speed and storage), particularly in the longitudinal direction, makes it impractical for the modeling of two or three-dimensional turbulent flows. On the other hand, the central difference scheme, which is second-order in accuracy and free of numerical diffusion, is non-convergent particularly in regions where advection dominates diffusion (Roache 1972).

The unstable feature of a central difference scheme becomes more problematic in the mass balance equation (Eq. 2-21) than in the momentum equation (Eq. 2-20) in which the sink term (friction) tends to dissipate this oscillatory behavior. Primary dynamic balance in partially mixed estuaries is between the surface slope, density gradient and vertical gradient of turbulent shear stresses. Since the horizontal and

vertical advection terms are not important in the momentum equation, they are approximated with the central difference scheme in Eq. 2-20.

The dominant salt balance, however, takes place between horizontal advection and vertical turbulent diffusion, making the accurate numerical treatment of horizontal advection essential to the faithful model behavior. While the relatively small vertical advection term can be treated with the central difference scheme in Eq. 2-21, the horizontal advective transport should be modeled with minimal introduction of artificial numerical oscillation or diffusion. The QUICKEST (Quadratic Upstream Interpolation for Convective Kinematics with Estimated Streaming Terms) scheme, that has been successfully applied to the modeling of the advection term (Leonard et al. 1978; Hall & Chapman 1985; Johnson et al. 1991), is used for the horizontal advection term in Eq. 2-21.

D. QUICKEST scheme: The scheme, derived by Leonard (1979), addresses the problems associated with both central and upwind difference schemes coming from the method of estimating the concentrations at the cell walls. The QUICKEST scheme is based on a conservative control volume formulation and estimates cell wall concentrations with a quadratic interpolation using concentrations in two adjacent cells and that at the next upstream cell. This method has the properties of high accuracy (third-order accurate in space) and significantly reduced numerical diffusion. Considering only advective transport, the estimated concentration at the right wall face of cell i (s_r^*) is,

$$s_r^* = \frac{1}{2}(s_i + s_{i+1}) - \frac{C_r}{2}(s_{i+1} - s_i) + \frac{1}{6}(C_r^2 - 1)CURV_r \qquad (2\text{-}22)$$

where

$$C_r = \text{Courant number} = \frac{\Delta t}{\Delta x} u_{i+1} \qquad (2\text{-}23)$$

$$CURV_r = CURV_i \quad \text{for } u_{i+1} \geq 0 \quad \text{where} \quad CURV_i = s_{i+1} - 2s_i + s_{i-1}$$

$$CURV_{i+1} \quad \text{for } u_{i+1} < 0$$

Equation 2-22 shows that the Courant number determines the contribution of each cell concentration to the cell wall concentration; the larger C_r (i.e., the faster the flow), the more contribution from the upstream cell.

E. Pressure gradient term: From the hydrostatic equation (Eq. 2-4), $\Delta p = - \rho g \Delta z$. Using this equation with the grid system,

$$p_{k-1} - p_k = -g(\rho_{k-1}\frac{h_{k-1}}{2} + \rho_k\frac{h_k}{2}) \tag{2-24}$$

This gives the pressure gradient averaged over the k^{th} layer,

$$(\frac{\partial p}{\partial x})_k = (\frac{\partial p}{\partial x})_{k-1} + \frac{g}{2}(h_{k-1}\frac{\partial \rho_{k-1}}{\partial x} + h_k\frac{\partial \rho_k}{\partial x}) \tag{2-25}$$

and this is the one appeared in Eq. 2-20. Therefore, with $(\partial p/\partial x)_1$ known, all other $(\partial p/\partial x)_k$'s can be calculated.

The pressure gradient can be decomposed into the barotropic and baroclinic terms,

$$\frac{\partial p}{\partial x} = \rho g\frac{\partial \eta}{\partial x} + g\int_z^{\eta}\frac{\partial \rho}{\partial x}dz \tag{2-26}$$

and the average pressure gradient for the top layer is,

$$(\frac{\partial p}{\partial x})_1 = g\rho_1\frac{\partial \eta}{\partial x} + \frac{g}{2}(\eta + h_1)\frac{\partial \rho_1}{\partial x} \tag{2-27}$$

in which η^{n+1} is used for the stability consideration.

F. Stability: The following stability criteria should be met to have a stable, convergent set of solutions,

$$\Delta t \leq \frac{\Delta x}{\sqrt{g\bar{h}}} \tag{2-28}$$

$$\Delta t \leq \frac{\Delta x}{u} \tag{2-29}$$

$$\Delta t \leq \frac{1}{2}\frac{(\Delta x)^2}{A_x} \tag{2-30}$$

where Δt is the time step and Δx is the segment length in the x direction. The Courant-Fredrick-Levy (CFL) condition (Eq. 2-28) arises from the use of η^{n+1} in evaluating the surface slope (in Eq. 2-27) in the momentum equation (Eq. 2-20). The use of η^n instead would make the numerical scheme used in this model unconditionally unstable. Equation 2-29 is the condition that the QUICKEST scheme for the horizontal advection term in the salt balance equation (Eq. 2-21) is stable up to C_r equal to one. The last diffusion condition (Eq. 2-30) is due to the explicit treatment of the horizontal mixing term in Eq. 2-20. The analogous condition for Eq. 2-21 is not necessary since A_x is always greater than, or equal to, K_x. The implicit treatment of the vertical mixing terms in Equations 2-20 and 2-21 removes the diffusion condition in the z direction.

Of the three conditions, the CFL condition is the most limiting stability requirement. For $\Delta x = 2500$ m and $H = 10$ m, $\Delta t \leq 250$ sec. The computation time turned out to be of less concern; with $\Delta t = 108$ sec, it takes approximately 2 hours to run both hydrodynamic and water quality models compiled with F77L-EM/32 compiler for 60 days using an IBM 486 PC.

2-2. Water Quality Model

2-2-1. Basic equations

The water quality model is based on the equation describing the mass-balance of DO in the water column. The equation that is solved by the finite difference method to calculate the dissolved oxygen (DO) concentration is,

$$\frac{\partial(cB)}{\partial t} + \frac{\partial(cBu)}{\partial x} + \frac{\partial(cBw)}{\partial z} = \frac{\partial}{\partial x}(K_x B\frac{\partial c}{\partial x}) + \frac{\partial}{\partial z}(K_z B\frac{\partial c}{\partial z}) + BS_e + BS_i \qquad (2\text{-}31)$$

where

c = laterally averaged DO concentration,

S_e = time rate of external addition (or withdrawal) of DO across the boundaries, and,

S_i = time rate of internal increase (or decrease) of DO by biochemical reaction processes.

Equation 2-31 gives the DO distribution using the physical parameters (u, w, η, K_x, and K_z) determined from the hydrodynamic model. The physical transport terms, both advective and diffusive, are treated in the same manner as those in the mass balance equation for salt (Eq. 2-5).

The last two terms of Eq. 2-31 represent the external sources (or sinks) and internal sources (or sinks) due to the biochemical reactions. To simulate these terms, it may be necessary to model, two dimensionally, other constituents that exert a significant effect on DO. In this study, the water quality model consists of eight interlinked components including phytoplankton population (Chl), organic nitrogen (N1), ammonia nitrogen (N2), nitrite-nitrate nitrogen (N3), organic phosphorus (P1), inorganic (ortho) phosphorus (P2), carbonaceous biochemical oxygen demand (CBOD) and DO (Fig. 2-3). Another nutrient not included in this model is silica. Silica is a limiting nutrient only for diatoms and thus it is generally modeled only when diatoms are simulated as a separate phytoplankton group (Bowie et al. 1985). The present model uses the chlorophyll 'a' concentration to quantify the whole phytoplankton population. Besides, diatoms are not predominant in summer in the western shore tributaries and lower Chesapeake Bay (Morse 1947; Pattern 1963; Marshall 1967 and 1980; Marshall & Lacouture 1986). Since the goal of the present model is to

simulate the summer conditions and to study hypoxia, the silica cycle is not included in this model.

Each rectangular box in Fig. 2-3 represents one component being simulated by the model. Each of these water quality parameters can be represented by the same equation as Eq. 2-31, but with its own representations of external (S_e) and internal (S_i) source and sink terms. The arrows between components in Fig. 2-3 represent the biochemical transformation of one substance to the other. An arrow with one end unattached to a component (rectangular box) represents an internal source (or sink) due to the biochemical reaction or an external source (or sink). The mathematical expressions used in this study for the terms, S_e and S_i, for each of the eight components are the extension of the one-dimensional water quality model described in Kuo et al. (1991b). They are presented in the following sections with emphases given to the modifications made.

A. Phytoplankton population: The phytoplankton population occupies a central role in the schematic system of Fig. 2-3. It influences, to a greater or lesser extent, all of the remaining non-conservative constituents. No simple aggregate measurement is entirely satisfactory to quantify the phytoplankton population (Ambrose et al. 1988). Because of the wealth of chlorophyll data available and the lack of alternative data sets, the concentration of chlorophyll 'a' is used as a measure of the phytoplankton population in this study.

The present model of chlorophyll (Chl) includes growth and nonpoint source inputs as sources, and respiration and mortality as sinks. For the settling of Chl, those settling down from the overlying layer act as a source, while those settling down to the bottom or to an underlying layer act as a sink for a layer. The mathematical representation is,

$$S_i = (G - R - P)Chl \tag{2-32a}$$

$$S_e = \frac{K_{Chl}}{\Delta z}(\lambda_1 Chl_{k-1} - Chl_k) + \frac{WChl}{V} \tag{2-32b}$$

where

λ_1 = 0 for k = 1 (at top layer), and

1 for $2 \leq k \leq N$, and N is the number of layers at each segment,

Chl = concentration of chlorophyll 'a' ($\mu g\ l^{-1}$),

G = growth rate of phytoplankton (day^{-1}),

R = respiration rate of phytoplankton (day^{-1}),

P = mortality rate due to predation and other factors (day^{-1}),

K_{Chl} = settling rate of phytoplankton (cm day^{-1}),

Δz = layer thickness (cm),

WChl = external loading of Chl ($\mu g\ day^{-1}$) including nonpoint source, and

V = layer volume (liter).

For the top layer, Δz is adjusted to account for the surface fluctuation.

1) Growth: Phytoplankton growth depends on nutrient availability, ambient light and temperature. A multiplicative relationship between temperature, light and nutrient limitations is assumed. The functional forms used in the model can be found in Bowie et al. (1985) and are as follow,

$$G = k_{gr}\theta_1^{T-20} L(I_a, I_s, k_e, Chl, h) \cdot N(N2, N3, P2) \tag{2-32c}$$

where

k_{gr} = optimum growth rate at 20°C (day^{-1}),

θ_1 = constant for temperature adjustment of growth rate,

T = temperature (°C),

L = attenuation of growth due to suboptimal lighting, and

N = attenuation of growth due to nutrient limitations.

The exponential function of temperature adjustment with a reference temperature of 20°C is used for the growth. This function, based on the Arrhenius relationship, is used whenever temperature adjustment is needed in the model.

The light effect (L) is based on the available solar energy and the attenuation of light through the water column. From the Beer-Lambert law and the Steele (1965) formulation, the light effect integrated over the layer depth may be expressed as,

$$L = \frac{e}{K_e \Delta z}\left[\exp\left\{-\frac{I_t}{I_s}\exp(-K_e[H_s+\Delta z])\right\} - \exp\left\{-\frac{I_t}{I_s}\exp(-K_e H_s)\right\}\right] \quad \text{(2-32d)}$$

$$K_e = k_e + K_{e,Chl}\,Chl \quad \text{(2-32e)}$$

$$I_t = I_a\left(\frac{24}{t_d - t_u}\right)\frac{\pi}{2}\sin\left(\pi\frac{t-t_u}{t_d-t_u}\right) \qquad if \quad t_u < t < t_d$$

$$= 0 \qquad if \quad t < t_u \ \ or \ \ t > t_d \quad \text{(2-32f)}$$

where

e = constant = 2.7183,

H_s = depth from the free surface to the top of the layer (cm),

K_e = light extinction coefficient (cm^{-1}) corrected for self-shading of plankton,

k_e = light extinction coefficient (cm^{-1}) at zero chlorophyll concentration,

$K_{e,Chl}$ = light extinction due to self-shading of plankton (L μg^{-1} cm^{-1}),

I_s = optimum solar radiation rate (langleys day^{-1}),

I_t = solar radiation at time t (langleys day^{-1}),

I_a = total daily solar radiation (langleys day^{-1}),

t = time of day (in hours), and

t_u & t_d = time (in hours) of sunrise and sunset, respectively.

The nutrient effect (N) is based on the minimum limiting nutrient concept assuming nitrogen and phosphorus the major growth limiting nutrients. Using the fixed stoichiometry model based on conventional Monod or Michaelis-Menten kinetics, the nutrient effect may be expressed as,

$$N = \min\left\{\frac{N2+N3}{K_{mn}+N2+N3}, \frac{P2}{K_{mp}+P2}\right\} \quad (2\text{-}32g)$$

where

N2, N3 & P2 = concentrations (mg l^{-1}) of ammonia nitrogen, nitrite-nitrate nitrogen and inorganic phosphorus, respectively, and

K_{mn} & K_{mp} = half-saturation concentrations (mg l^{-1}) for uptake of inorganic nitrogen and inorganic phosphorus, respectively.

B. Respiration: Respiration is the reverse of the photosynthesis process and thus contributes to the reduction of algal biomass. The respiration rate (R) at which algae oxidize organic carbon to CO_2 is expressed as a function of temperature (Bowie et al. 1985).

$$R = R(20)\cdot\theta_2^{T-20} \quad (2\text{-}32h)$$

where

R(20) = respiration rate at 20°C (day^{-1}), and

θ_2 = constant for temperature adjustment of respiration rate.

C. Mortality: The predatory mortality rate should be dependent on the time-variable herbivore population, which is in turn dependent upon the phytoplankton population. To avoid adding an additional trophic level to the model, however, both the predatory and non-predatory mortality rate (P) are combined into a single loss term, which is assumed to be a function of temperature.

$$P = P(20)\cdot\theta_3^{T-20} \quad (2\text{-}32i)$$

where

P(20) = mortality rate at 20°C (day^{-1}), and

θ_3 = constant for temperature adjustment of mortality rate.

B. Organic nitrogen: For the nitrogen cycle, three variables are modeled: organic nitrogen (N1), ammonia nitrogen (N2) and nitrite-nitrate nitrogen (N3). In the modeling of N1, the following processes are included; ammonification to N2, input due to algal respiration and death, settling, benthic release, and external loading. The mathematical representation is,

$$S_i = -\frac{K_{n12} N1}{K_{h12} + N1} + a_n (R + a_r P) F_n Chl \qquad (2\text{-}33a)$$

$$S_e = \frac{K_{n11}}{\Delta z} (\lambda_1 N1_{k-1} - N1_k) + \frac{BenN1}{\Delta z} \frac{B_k - \lambda_2 B_{k+1}}{B_k} + \frac{WN1}{V} \qquad (2\text{-}33b)$$

where

λ_2 = 1 for $1 \leq k \leq N\text{-}1$, and

0 for k = N (at bottom layer),

N1 = concentration of organic nitrogen ($mg\ l^{-1}$),

K_{n12} = ammonification rate of N1 to N2 ($mg\ l^{-1}\ day^{-1}$) = $K_{n12}(20) \cdot \theta_4^{T-20}$,

$K_{n12}(20)$ = ammonification rate at 20°C,

θ_4 = constant for temperature adjustment of ammonification rate,

K_{h12} = half-saturation concentration for ammonification ($mg\ l^{-1}$),

a_n = ratio of nitrogen to chlorophyll in phytoplankton (mg N per μg Chl),

a_r = fraction of consumed phytoplankton recycled by zooplankton,

K_{n11} = settling rate of N1 ($cm\ day^{-1}$),

F_n = fraction of metabolically produced nitrogen recycled to the organic pool,

BenN1 = benthic flux of N1 ($g\ m^{-2}\ day^{-1}$), and

WN1 = external loading of N1 ($mg\ day^{-1}$) including point and nonpoint sources.

The model reads in the benthic fluxes of N1, N2, N3, P1, P2 and CBOD, and sediment oxygen demand (SOD) in g m^{-2} day^{-1} and multiplies them by 100 to correct for the dimensional consistency (note Δz is in cm).

C. Ammonia nitrogen: The present model of N2 includes the following processes; ammonification from N1, input from algal respiration and death, benthic release and external loading as sources, while nitrification to N3 and uptake by algae as sinks. The model has,

$$S_i = -\frac{K_{n23}N2}{K_{h23}+N2}\frac{DO}{K_{nit}+DO} + \frac{K_{n12}N1}{K_{h12}+N1} + a_n(R+a_rP)(1-F_n)Chl - a_nG\cdot PR\cdot Chl \quad (2\text{-}34a)$$

$$S_e = \frac{BenN2}{\Delta z}\frac{B_k-\lambda_2 B_{k+1}}{B_k} + \frac{WN2}{V} \quad (2\text{-}34b)$$

where

K_{n23} = nitrification rate of N2 to N3 (mg l^{-1} day^{-1}) = $K_{n23}(20)\cdot\theta_5^{T-20}$,

$K_{n23}(20)$ = nitrification rate at 20°C,

θ_5 = constant for temperature adjustment of nitrification rate,

K_{h23} = half-saturation concentration for nitrification (mg l^{-1}),

K_{nit} = half-saturation concentration for oxygen limitation of nitrification (mg l^{-1}),

PR = preference of phytoplankton for N2 uptake, which is given by

$$= \frac{N2\ N3}{(K_{mn}+N2)(K_{mn}+N3)} + \frac{N2\ K_{mn}}{(N2+N3)(K_{mn}+N3)} \quad (2\text{-}34c)$$

BenN2 = benthic flux of N2 (g m^{-2} day^{-1}), and

WN2 = external loading of N2 (mg day^{-1}) including point and nonpoint sources.

Nitrification by aerobic autotrophs (Nitrosomonas and Nitrobacter) requires oxic conditions, and thus the inhibition of nitrification by low DO is included (Ambrose et al. 1988). Nitrification may be formulated using first-order rate equation, which increases nitrification as ammonia concentration increases. At the high level of

ammonia, however, nitrification being an enzymatic reaction by bacteria can proceed at its maximum rate and thus is zero order, i.e., independent of substrate concentration (Wild et al. 1971; Huang & Hopson 1974). Nitrification, therefore, is formulated using Monod kinetics so as to have first-order kinetics at lower ammonia concentrations (limited by substrate availability) and to have zero-order kinetics at higher concentration (limited by bacteria availability). In the present model, this Monod or saturation-type formulation is used for all processes that transform one parameter to another including ammonification and mineralization of organic phosphorus. The fact that ammonia is preferably, to nitrate, taken up by phytoplankton for growth is incorporated into the model by using the ammonia preference term.

D. Nitrite-nitrate nitrogen: Included in the modeling of N3 are sources from nitrification, benthic release and external loading, and sinks due to algal uptake and denitrification. The mathematical representation is,

$$S_i = \frac{K_{n23} N2}{K_{h23} + N2} \frac{DO}{K_{nit} + DO} - a_n G(1 - PR) Chl \qquad (2\text{-}35a)$$

$$S_e = -K_{n33} \frac{K_{h33}}{K_{h33} + DO} N3 + \frac{BenN3}{\Delta z} \frac{B_k - \lambda_2 B_{k+1}}{B_k} + \frac{WN3}{V} \qquad (2\text{-}35b)$$

where

K_{n33} = denitrification rate (day^{-1}) = $K_{n33}(20) \cdot \theta_6^{T-20}$,

$K_{n33}(20)$ = denitrification rate at 20°C,

θ_6 = constant for temperature adjustment of denitrification rate,

K_{h33} = half-saturation concentration for denitrification (mg l^{-1}),

BenN3 = benthic flux of N3 (g m^{-2} day^{-1}), and

WN3 = external loading of N3 (mg day^{-1}) including point and nonpoint sources.

Denitrification, which occurs only under extremely low DO conditions, is limited by

DO availability. This limitation is incorporated into the model using Monod type expression (Ambrose et al. 1988).

E. Organic phosphorus: For the phosphorus cycle, two variables are modeled: organic phosphorus (P1) and inorganic phosphorus (P2). The present model of P1 includes the following processes; mineralization to P2, input due to algal respiration and death, settling, benthic release, and external loading. The model has,

$$S_i = -\frac{K_{p12}P1}{K_{hp12}+P1} + a_p(R+a_rP)F_pChl \qquad (2\text{-}36a)$$

$$S_e = \frac{K_{p11}}{\Delta z}(\lambda_1 P1_{k-1} - P1_k) + \frac{BenP1}{\Delta z}\frac{B_k - \lambda_2 B_{k+1}}{B_k} + \frac{WP1}{V} \qquad (2\text{-}36b)$$

where

P1 = concentration of organic phosphorus (mg l^{-1}),

K_{p12} = mineralization rate of P1 to P2 (mg l^{-1} day^{-1}) = $K_{p12}(20)\cdot\theta_7^{T-20}$,

$K_{p12}(20)$ = mineralization rate at 20°C,

θ_7 = constant for temperature adjustment of mineralization rate,

K_{hp12} = half-saturation concentration for mineralization (mg l^{-1}),

a_p = ratio of phosphorus to chlorophyll in phytoplankton (mg P per μg Chl),

K_{p11} = settling rate of P1 (cm day^{-1}),

F_p = fraction of metabolically produced phosphorus recycled to the organic pool,

BenP1 = benthic flux of P1 (g m^{-2} day^{-1}), and

WP1 = external loading of P1 (mg day^{-1}) including point and nonpoint sources.

F. Inorganic (or ortho) phosphorus: The following processes are included to model P2; mineralization from P1, input from algal respiration and death, uptake by algae for growth, settling, benthic release, and external loading. The mathematical representation is,

$$S_i = \frac{K_{pl2}Pl}{K_{hpl2}+Pl} + a_p(R+a_rP)(1-F_p)Chl - a_pG \cdot Chl \quad (2\text{-}37a)$$

$$S_e = \frac{K_{p22}}{\Delta z}(\lambda_1 P2_{k-1} - P2_k) + \frac{BenP2}{\Delta z}\frac{B_k - \lambda_2 B_{k+1}}{B_k} + \frac{WP2}{V} \quad (2\text{-}37b)$$

where

K_{p22} = settling rate of P2 (cm day^{-1}),

BenP2 = benthic flux of P2 (g m^{-2} day^{-1}), and

WP2 = external loading of P2 (mg day^{-1}) including point and nonpoint sources.

G. Carbonaceous biochemical oxygen demand (CBOD): In the modeling of CBOD, the followings are included; CBOD decay, input from algal death, settling, benthic release, and external loading. The mathematical representation is,

$$S_i = -K_c CBOD + a_c a_{co}(a_r P) Chl \quad (2\text{-}38a)$$

$$S_e = \frac{K_{BOD}}{\Delta z}(\lambda_1 CBOD_{k-1} - CBOD_k) + \frac{SOD}{\Delta z}\frac{K_{DO}}{K_{DO}+DO}\frac{B_k - \lambda_2 B_{k+1}}{B_k} + \frac{WBOD}{V} \quad (2\text{-}38b)$$

where

CBOD = concentration of carbonaceous biochemical oxygen demand (mg l^{-1}),

K_c = first-order decay rate of CBOD (day^{-1}) = $K_c(20) \cdot \theta_8^{T-20}$,

$K_c(20)$ = CBOD decay rate at 20°C,

θ_8 = constant for temperature adjustment of CBOD decay rate,

a_c = ratio of carbon to chlorophyll in phytoplankton (mg C per μg Chl),

a_{co} = ratio of oxygen demand to organic carbon recycled = 2.67,

K_{BOD} = settling rate of CBOD (cm day^{-1}),

SOD = sediment oxygen demand (g m^{-2} day^{-1}),

K_{DO} = half-saturation concentration for benthic flux of CBOD, and

WBOD = external loading of CBOD (mg day^{-1}) including point and nonpoint sources.

Under anoxic conditions, SOD increases CBOD flux into the water column, which is incorporated into the model using Monod type expression.

H. Dissolved oxygen: The present model of DO includes the following processes; sources from photosynthesis, reaeration through surface and external loading, and sinks due to decay of CBOD, nitrification, algal respiration and sediment oxygen demand (SOD). The mathematical representation is,

$$S_i = -K_c CBOD - a_{no} \frac{K_{n23} N2}{K_{h23} + N2} \frac{DO}{K_{nit} + DO} + a_c a_{co} (PQ \cdot G - \frac{R}{RQ}) Chl \qquad (2\text{-}39a)$$

$$S_e = (1 - \lambda_1) K_r (DO_s - DO) - \frac{SOD}{\Delta z} \frac{DO}{K_{DO} + DO} \frac{B_k - \lambda_2 B_{k+1}}{B_k} + \frac{WDO}{V} \qquad (2\text{-}39b)$$

where

DO = concentration of dissolved oxygen (mg l^{-1}),

a_{no} = ratio of oxygen consumed per unit of ammonia nitrogen nitrified = 4.57,

PQ = photosynthesis quotient (moles O_2 per mole C),

RQ = respiration quotient (moles CO_2 per mole O_2),

K_r = reaeration rate (day^{-1}),

$K_r(20)$ = reaeration rate at 20°C (day^{-1}),

DO_s = saturation concentration of DO (mg l^{-1}), and

WDO = external loading of DO (mg day^{-1}) including point and nonpoint sources.

As a counterpart to CBOD flux term in Eq. 2-38b, SOD is inhibited by low DO conditions.

The reaeration coefficient (K_r) includes reaeration by turbulence generated by bottom friction (O'Connor & Dobbins 1958) and that by surface wind stress (Banks & Herrera 1977), that is,

$$K_r(20) = \left[K_{ro} \sqrt{\frac{u_{eq}}{h_{eq}}} + W_{rea} \right] \frac{1}{\Delta z} \tag{2-39c}$$

where

K_{ro} = proportionality constant = 393.3 in CGS unit,

u_{eq} = weighted velocity over cross-section = $\Sigma(u_k B_k h_k)/\Sigma(B_k h_k)$,

h_{eq} = weighted depth over cross-section = $\Sigma(B_k h_k)/B_\eta$,

B_η = width at the free surface, and

W_{rea} = wind-induced reaeration (cm day^{-1}),

$$= 72.8 U_w^{1/2} - 31.7 U_w + 3.72 U_w^2 \tag{2-39d}$$

where U_w is the wind speed (in m sec^{-1}) at the height of 10 m above surface. The reaeration rate is assumed to be temperature-dependent (Thomann & Mueller 1987),

$$K_r = K_r(20) \cdot \theta_9^{T-20} \tag{2-39e}$$

where θ_9 = constant for temperature adjustment of DO reaeration rate.

Saturated dissolved oxygen concentration (DO_s) is calculated as a function of water temperature and salinity (s in ppt) from a polynomial fitted to the tables of Green & Carritt (1967).

$$DO_s = 0.146244 \cdot 10^2 - 0.367134 T + 0.4497 \cdot 10^{-2} T^2 - (0.966 \cdot 10^{-1} - 0.205 \cdot 10^{-2} T - 0.2739 \cdot 10^{-3} S) S \tag{2-39f}$$

2-2-2. Method of solution

Equation 2-31 for each of eight water quality parameters is approximated with a finite difference scheme and solved for the time varying concentration field in the same way as the mast balance equation for salt (Eq. 2-5) in the hydrodynamic model. Wherever the equation of one water quality parameter involves other water quality

parameters, the concentrations of the other parameters are expressed in terms of known values at the beginning of the time step. Therefore, the biochemical interaction terms in the coupled equations do not introduce additional unknowns for the finite difference equation of each individual water quality parameter over that of salt.

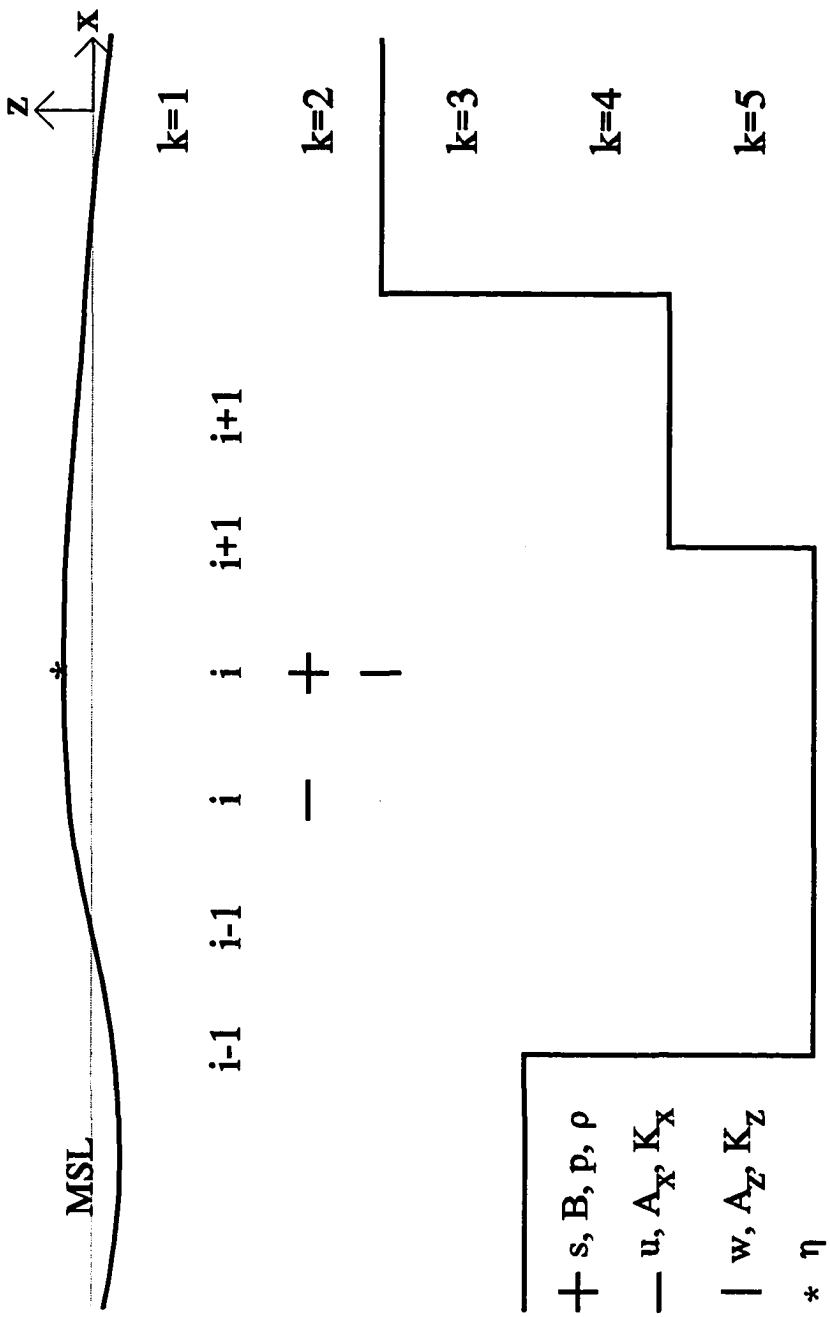

Figure 2-1. Grid pattern, location and indexing of variables.

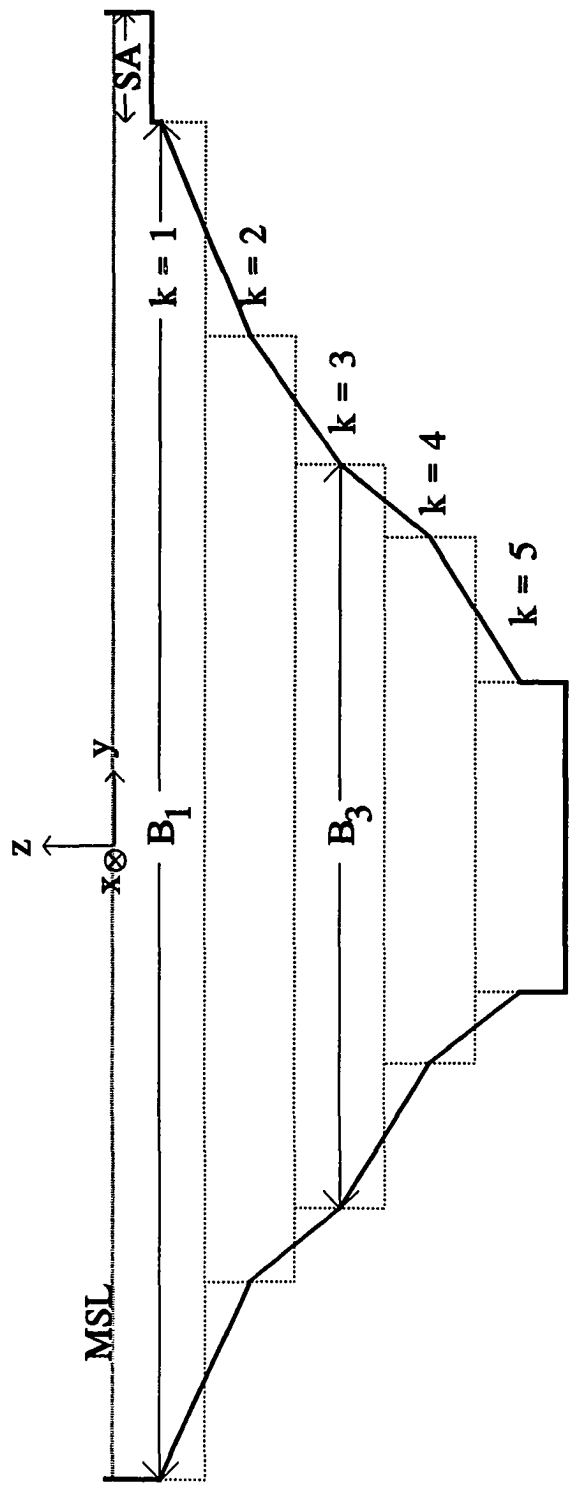

Figure 2-2. Cross-section looking downriver.

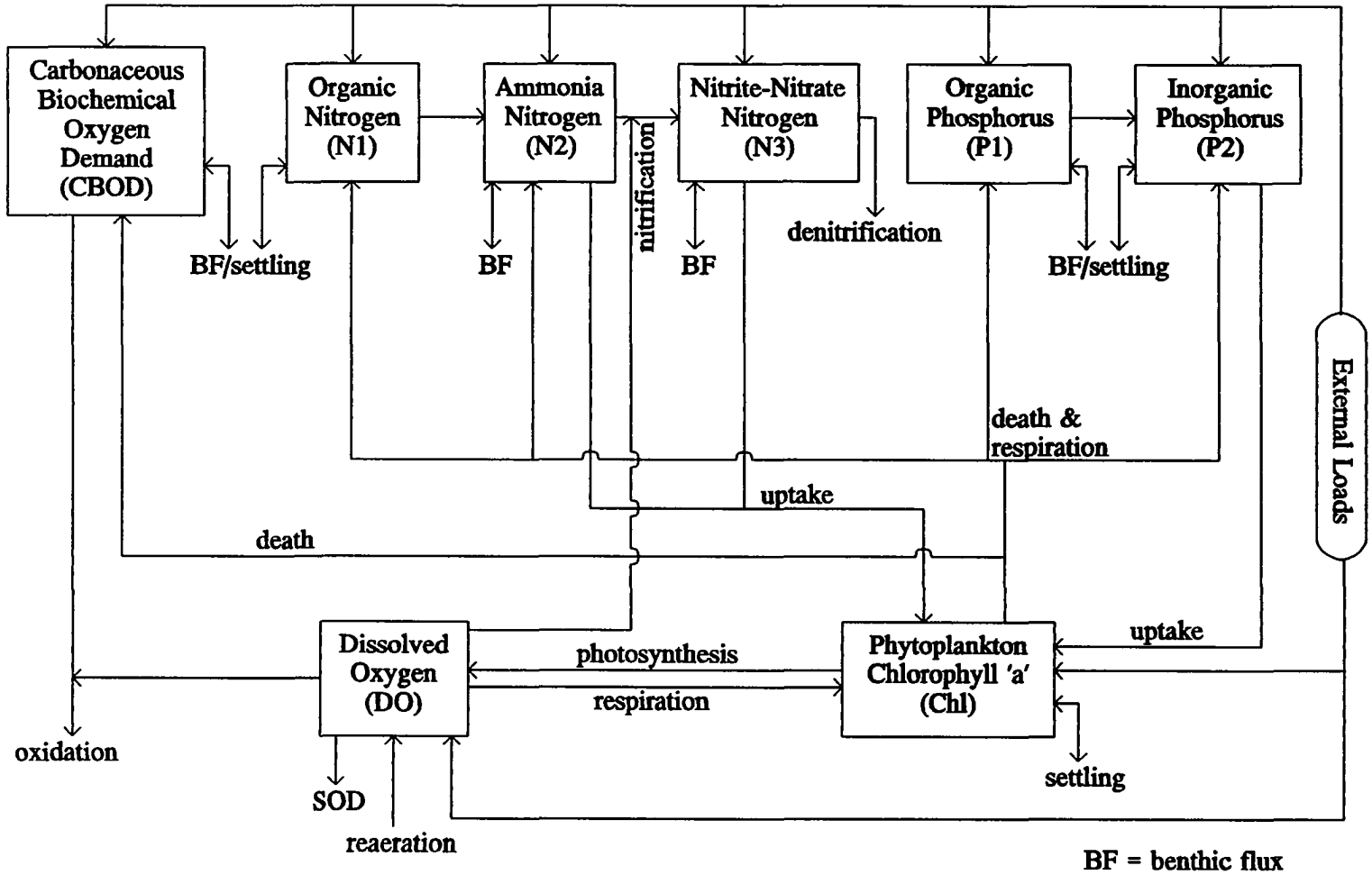

Figure 2-3. Schematic diagram of interacting water quality parameters.

III. DESCRIPTION OF STUDY AREA, RAPPAHANNOCK RIVER IN VIRGINIA

The hydrodynamic and water quality models were applied to the tidal portion of the Rappahannock River, Virginia to simulate the conditions in the summers of 1987 and 1990. This chapter describes the characteristics, both hydrodynamic and water quality, of the study area.

3-1. Hydrodynamic Characteristics

The Rappahannock River, one of the western shore tributaries of Chesapeake Bay, is located between the Potomac and York rivers. Figure 3-1 shows the map of the tidal Rappahannock River with sampling locations and geographic features mentioned in the text, and Fig. 3-2 shows the longitudinal bathymetry, both field survey data and model input. From the mouth at Windmill Point (km 0) to the fall line at Fredericksburg (km 172), the tidal river extends in a generally northwest direction (Division of Water Resources 1970). Being relatively narrow and straight, the river is suitable for the laterally integrated two-dimensional model.

The drainage area above the fall line gauging station is 4,132 km^2 (USGS 1992). Over 85 years between 1907 and 1991, the discharge ranged from 0.14 to 3,964 m^3 sec^{-1} (cms) with a mean of 46.8 cms. The annual mean discharges were 39.8 and 46.2 cms for the water years 1987 and 1990 respectively (USGS 1988 and 1991).

The tidal wave takes about 9 hours to propagate from the river mouth to the fall line, the principal tidal component being the lunar semi-diurnal tide with a period of 12.42 hours. The mean tidal range increases from 37 cm near the mouth to 55 cm

between Bowlers Wharf (km 52) and Wares Wharf (km 58), then decreases slightly to 46 cm at Leedstown (km 95), and increases again to 85 cm at Fredericksburg (National Ocean Survey 1989).

The lower portion of the tidal Rappahannock River, like other western shore tributaries of Chesapeake Bay, is a partially mixed estuary. Water movement follows a two-layered gravitational circulation, in which the longitudinal density (salinity) gradient pushes the saline bay water upriver along the bottom and gravity moves the fresh surface water downriver.

The mixing of fresh and salt water, primarily caused by the action of tides and winds, occurs over a broad transition zone. The upper extent of salt water intrusion varies in response to the freshwater flow. Since 1971, the Virginia Institute of Marine Science (VIMS) has been conducting slackwater surveys in three major estuaries in Virginia (James, York and Rappahannock estuaries). The salinity data in the Rappahannock River show that the salt water generally intrudes to around km 120 (near Nanzatico Bay) during low flow and around km 70 (near Tappahannock) during high flow. The salinity, temperature and DO data for the Rappahannock River between 1970 and 1980 can be found in Brooks (1983). Conditions range from well mixed to strongly stratified, depending upon the tide and wind energy available for mixing, in the region from the mouth to km 42 (near Tarpley Point) where the water depth ranges from 15 to 20 m. The water in the shallow reach between km 48 (near Sharps) and km 80 (near Blandfield Point) is usually well mixed, which suggests that the shallow depth (6 to 8 m) makes the region more susceptible to tidal as well as wind mixing. The sloping bottom between km 42-48 connects the deeper, lower part to the shallower, upper part of the river (Fig. 3-2).

Since the estuary empties into Chesapeake Bay, salinity in the estuary is moderated by distance from the ocean and the effect of freshwater flow from other

tributaries to the bay, especially the Susquehanna River. A large portion of the estuary and its tidal tributaries is favorable for growing oysters since salinity is high enough to allow oysters to grow, but low enough to discourage the most serious predators and diseases such as oyster drills and MSX (Kuo et al. 1975).

3-2. Water Quality Characteristics

The tidal portion of the Rappahannock River has three distinct sections, each of which exhibits characteristic water quality conditions (Figures 3-1 and 3-2); the lower (between mouth and km 50), the middle (between km 80 and km 145) and the upper (between km 155 and fall line) reaches. The 20 km reach immediately downriver of the fall line and the deep water in the lower part of the river have been identified as critical regions for DO (Kuo et al. 1975).

The upper tidal portion of the river, being very narrow, shallow and straight, is suitable for sectionally integrated one-dimensional model. A prior modeling study has shown that both point and nonpoint source loadings have significant impacts on water quality there, and the relative importance of the two sources depends on the magnitude of the river discharge (Kuo et al. 1991b).

The lower portion of the Rappahannock River between the river mouth and km 50 is characterized by persistent hypoxic conditions in the bottom water during the summer. Kuo & Neilson (1987) made a qualitative investigation of the bottom DO in the three Virginia estuaries. They reported that hypoxia has been observed most frequently in the deep water of the Rappahannock River, but it occurs rarely in the James River though it receives the heaviest wastewater loadings among three estuaries. This difference has been attributed in part to the relatively strong gravitational circulation in the James River. Due to these circulation differences, the impact of increased urbanization may be more severe in the Rappahannock River than

it has been in the James River. Development of the Rappahannock River, therefore, should be preceded by a better understanding of the water quality there.

The temporal and spatial variability of hypoxia in the lower portion of the Rappahannock River was studied by Kuo et al. (1991a). They observed a periodic reoxygenation of bottom water that was closely related to spring tide mixing. The destratification-stratification cycles caused by spring-neap tidal cycles has been documented in the Rappahannock River as well as other Virginia estuaries (Haas 1977; D'Elia et al. 1981; Ruzecki & Evans 1986). A characteristic longitudinal pattern of bottom water DO also was observed. The bottom DO concentration decreased upriver from river mouth, reaching a minimum at approximately km 42, upriver of the deepest point of the river, and then increasing as the water became shallower further upriver. A model for the bottom water DO concentration was formulated based on a simple DO budget consisting of only one source term (vertical mixing) and one sink term (including both benthic and water column oxygen demand), using a Lagrangian concept (Kuo et al. 1991a). Although this diagnostic study enabled them to investigate cause-effect relationships, the predictive application of the model was not always satisfactory due to the lack of complete information for input parameters, vertical mixing and oxygen demand. Spatially and temporally varying values for input parameters were required to improve the predictive capability of the model, which served as one impetus of the present study.

Another common feature shared by western shore tributaries of Chesapeake Bay is the presence of a sill at the river mouth, which restricts water exchange with the bay. The sill at the mouth of the Rappahannock River plays an important role in an estuary-subestuary exchange. Kuo & Park (1992) calculated, using the field data near the river mouth, that the mass exchange due to the tidal component was at least an order of magnitude smaller than that resulting from the subtidal component. The

presence of the sill, the shoreline configuration and the pycnocline oscillation due to the winds combined to affect the quality of incoming bay water along the bottom at the mouth.

The mid-reach of the river between km 80 and km 145 is bounded by shallow regions at the up and downstream boundaries (Fig. 3-2). The upper limit of salt intrusion, which moves up and down the river in response to the freshwater discharge, is located approximately at km 80. The tidal freshwater portion, just upriver of the limit of salt intrusion, in the Rappahannock River is characterized by a chlorophyll maximum (Anderson 1986). He suggested the hydrodynamic trapping of phytoplankton biomass in the region of the turbidity maximum, rapid internal cycling of essential nutrients such as silica, demise of freshwater phytoplankton during transport to the saline part of the river, and light limitation in the oligohaline reach of the river as controlling factors. This high phytoplankton concentrations in the tidal freshwater reach and low salinity mixing region of estuaries have been observed frequently in many other estuarine environments (Haertel et al. 1969; Lippson et al. 1979; Cloern et al. 1983; Pennock 1985; Relexans et al. 1988; Schuchardt & Schirmer 1991). Key mechanisms suggested by these investigators are river discharge, water residence time, solar radiation, nutrients, etc. A part of the present study is to investigate the controlling mechanism(s) for the high chlorophyll concentration in the mid-part of the Rappahannock River, which is described in Section 6-2.

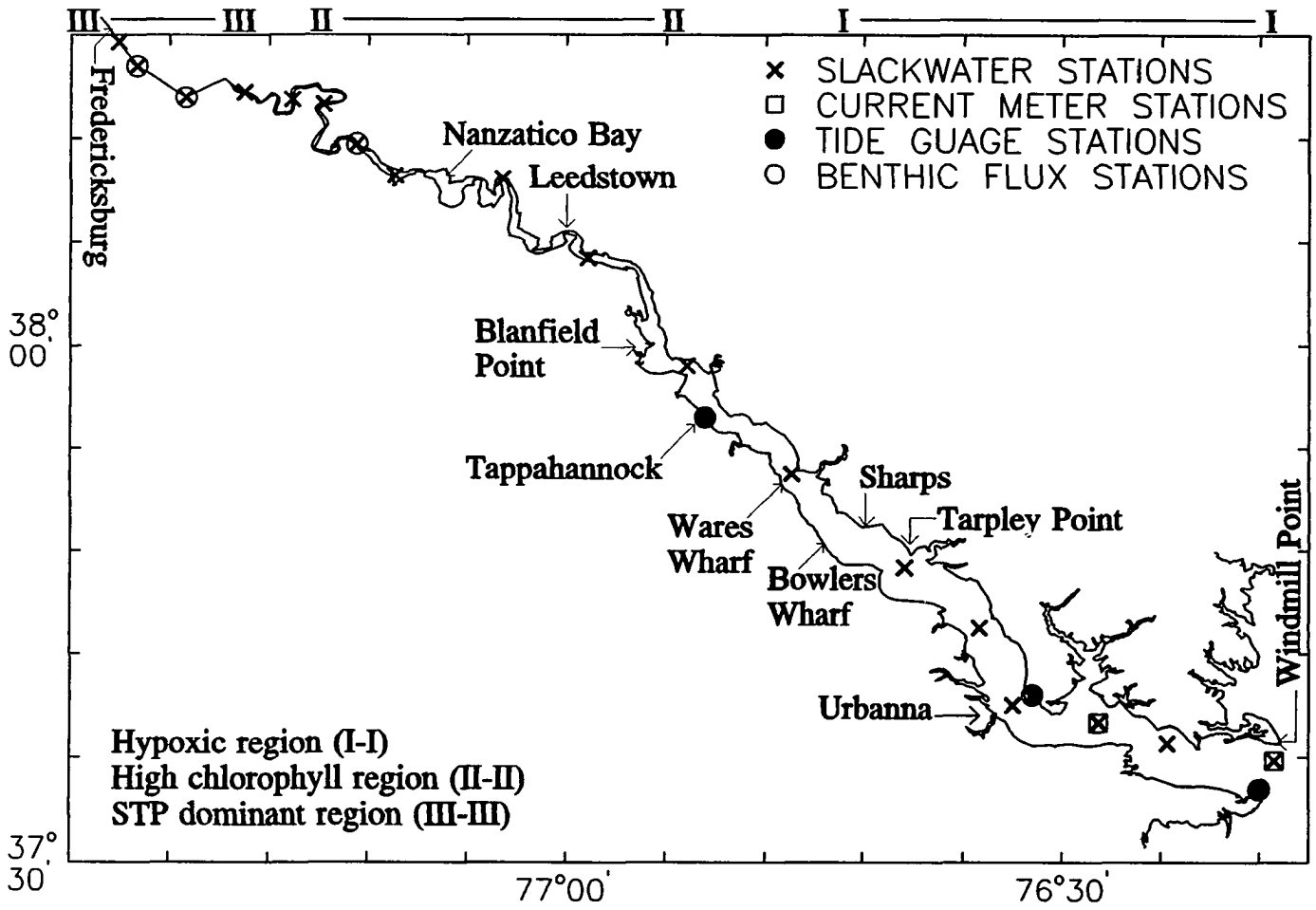

Figure 3-1. The tidal Rappahannock River in Virginia with sampling locations and geographic features mentioned in the text.

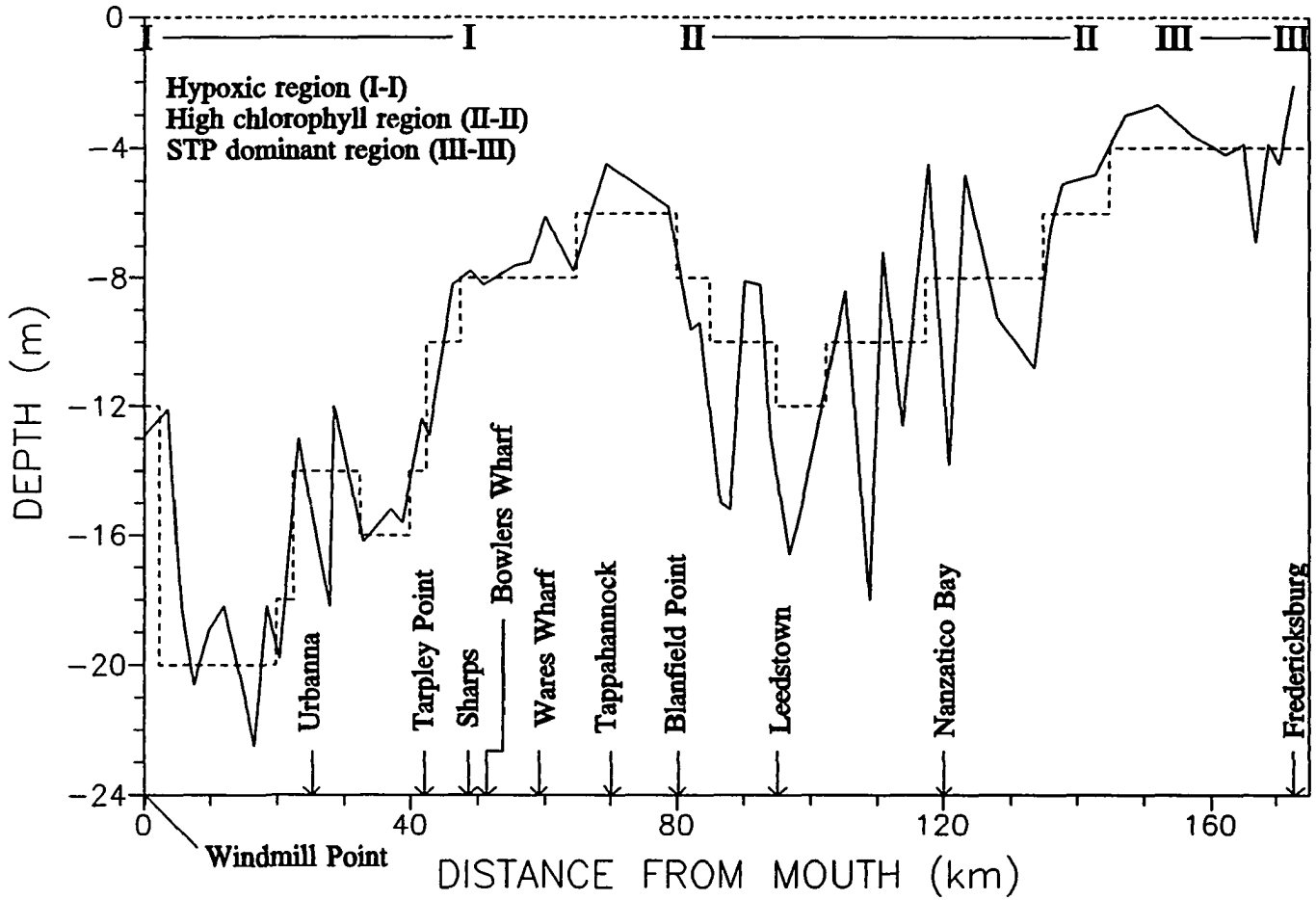

Figure 3-2. Longitudinal bathymetry of the tidal Rappahannock River: solid line is the field survey data and dashed line is the model input.

IV. APPLICATION OF THE HYDRODYNAMIC MODEL

Application of the hydrodynamic model to the Rappahannock River is discussed in this chapter. First, the geometry was specified, and the data files prepared (Section 4-1). Second, the model was calibrated such that it reproduced the tidal characteristics of the prototype. This calibration of the barotropic mode of the flow is discussed in Section 4-2. The turbulent mixing terms, both viscous and diffusive, contain constants that need to be adjusted. Third, the model was calibrated such that it reproduced the salinity structure (Section 4-3). Finally, the model's ability to predict the surface elevation, current velocity and salinity distribution was verified through comparison of model predictions and field measurements of these parameters (Section 4-4).

The field data used for the above procedures were collected in 1987 and 1990 by VIMS. The full description of field measurements can be found in Kuo & Moustafa (1989) and Kuo et al. (1991b), respectively, for the 1987 and 1990 surveys; the station locations are shown in Fig. 3-1.

4-1. Geometry

The hydrodynamic model was supplied with data describing the geometry of the Rappahannock Estuary. The geometry in the vertical two-dimensional model is represented by the width at each depth at the center of each grid cell (Fig. 2-2). A bathymetric survey in 1973 made by U.S. Corps of Engineers collected 102 bottom profiles along the tidal portion of the river (Kuo et al. 1975). These profiles were

used to schematize the river with $\Delta x = 2.5$ km and $\Delta z = 2$ m. The river was divided into 71 segments with up to 10 layers vertically (Figures 3-2 and 4-1). The geometric data used in the model are listed in Table 4-1. The side storage area was defined to include side shallow (< 2 m) regions and tributaries (Figures 2-2 and 4-1). The surface area of the side storage area was taken from nautical charts (National Ocean Survey). The center of the most downriver segment is located 1.1 km upriver from the river mouth. A time step increment (Δt) of 108 seconds, which guaranteed stability, was used for all the model runs.

4-2. Mean Tide Calibration

Manning's friction coefficient, which is virtually the only calibration parameter affecting the calculation of surface elevation and current velocity in partially mixed estuaries such as the Rappahannock Estuary, was adjusted by simulating the equilibrium-state conditions. Freshwater inflow equal to the long-term mean at the fall line (46.8 cms), and a simple sinusoidal (M2) tide with an amplitude equal to the mean at the river mouth (18.3 cm) were used to force the hydrodynamic model. The initial condition was a level surface at mean-sea level. The longitudinal velocity was initially set to be vertically uniform and equal to the mean velocity, i.e., the freshwater discharge divided by cross-sectional area. The vertical velocity was initially zero. The effect of salt on the mean tidal range was negligible. Constant density (zero salinity everywhere) and variable density model simulations produced no practical difference in the mean tidal range. Mean conditions that were obtained by running the model for a long time with constant boundary conditions were used for the boundary and initial conditions for salinity. The model required 12 tidal cycles to reach an equilibrium state, i.e., the surface elevation and velocity throughout the estuary repeated from tidal cycle to tidal cycle.

The model results during the last tidal cycle were compared with predicted mean tide characteristics in Tide Tables (National Ocean Survey 1989). Manning's coefficient was adjusted, within the commonly accepted range, until the model calculation of tidal range agreed with that from the Tide Tables. The times of high and low tides were then used to fine tune the coefficient (Fig. 4-2). The calibrated model has a Manning's friction coefficient of 0.018 between km 0-126, and 0.021 upriver of km 126.

Figure 4-2 shows the standing wave characteristics, which result from superposition of two progressive waves traveling in opposite directions. Phase difference between the outgoing reflected wave and the incident wave at a distance of one quarter wave length from the head of the tidal river, creates a nodal point of minimum tidal range near Leedstown. The model could reproduce this feature very well. As the tidal wave propagates upriver from the river mouth, the tidal range increases reaching a local maximum at km 58 (Wares Wharf), and then decreases reaching a local minimum around km 90 (near Leedstown). The maximum tidal range occurs near the head of the tidal river (Fredericksburg).

4-3. Calibration of Turbulent Mixing Terms

The constants (α, β and α_w) in the expressions for the turbulent mixing coefficients (Equations 2-16 and 2-17) were calibrated with a simulation of salinity distributions from August 4 to 24, 1987. Three time-varying boundary conditions, freshwater inflow through the upstream boundary and tide and salinity at the mouth, could be specified for the model. The upstream boundary condition was specified with daily freshwater discharge measured at the Fredericksburg gauging station (USGS 1988). The model updated the freshwater discharge by linear interpolation over a 2 hour period from 0000 to 0200 hours, and then held it constant for the

remaining 22 hours. Hourly tidal elevation measured at the mouth was used for the downstream boundary condition. The model linearly interpolated the hourly data to obtain the boundary conditions every time step. Four slackwater surveys at slack before ebb flow (SBE) were conducted on July 28 and August 4, 10 and 24. The salinity measurements at the mouth were linearly interpolated in time and used for the boundary condition.

To allow a "warming-up" time for the surface elevation and velocity, the model simulation started from July 23. The measured salinity distribution on July 28 was then inserted into the model to specify the initial condition. The constants in the turbulent mixing coefficients were evaluated by comparison of subsequent survey data and model results. The calibrated constants are $\alpha = 1.15 \times 10^{-2}$, $\beta = 0.25$ and $A_x = K_x = 5 \times 10^5$ cm^2 sec^{-1}. The resulting salinity distributions are presented as plots of isohalines in a vertical plane containing the river axis in Figures 4-3 through 4-5. Only the salinity distributions between the river mouth and km 60 are presented in the figures because the most upriver station in the 1987 surveys was located at km 57.79. The tidally averaged values of A_z on August 10 ranged from 0.46 to 26 cm^2 sec^{-1} with the spatial mean of 6.5 cm^2 sec^{-1}. Those of K_z ranged from 0.12 to 23 cm^2 sec^{-1} with the spatial mean of 5.0 cm^2 sec^{-1}.

Two physical processes are involved in the mass transport, advection and turbulent diffusion. The advective mass transport is affected by the current velocity, which is determined by two modes of the flow, barotropic and baroclinic. The barotropic flow that is forced by the surface slope has been calibrated in the previous section (mean-tide calibration). The baroclinic flow that is driven by the density (salinity) structure is calibrated in this section through the adjustment of the momentum exchange coefficients (A_x and A_z). They, in principle, should be calibrated by comparing the model results with the field measurements of current

velocity. They, in practice, are usually calibrated with measurements of the salinity distribution because of the non-availability of velocity data and the insensitivity of the velocity predictions to A_x and A_z. Calibration of the turbulent mixing coefficients, therefore, accounts for that of the baroclinic mode of the flow and the turbulent diffusive mass transport.

The agreement in the location of the isohalines between the model results and field measurements reflects that the model accurately simulated advective processes. The agreement is more than satisfactory for August 10 (Fig. 4-4) and 24 (Fig. 4-5), whereas the model prediction of the salinity is about 1 ppt higher, over the region of salt intrusion, than the field measurement on August 4 (Fig. 4-3).

The diffusive mass transport is a measure of the turbulent exchange of mass. In partially mixed estuaries, the horizontal advective transport of salt is balanced by the vertical diffusive transport, which determines the stratification in the water column. For discussion of the salinity structure in the Rappahannock River, the saline part of the river is divided into three parts; the lower between km 0-42, the upper between km 48-80, and the transitional between km 42-48.

In the lower part of the river (between km 0-42), the water depth ranges from 15 to 20 m (Fig. 3-2). Here, a well mixed condition was observed on August 10 (Fig. 4-4) and 24 (Fig. 4-5), and a moderately stratified condition was observed on August 4 (Fig. 4-3). During this period, the successive spring tides alternated in strength between strong and weak spring tides (Kuo et al. 1991a). Tidal mixing during the strong spring tide, which occurs at roughly monthly intervals, caused the well mixed situation on August 10 (Fig. 4-4). Neap tide on August 4 (Fig. 4-3) resulted in more stratified situation than August 10. The measurements taken at weak spring tide on August 24 (Fig. 4-5) show a more mixed situation than August 4 between km 0-42. These features were very well reproduced by the model (Figures

4-3 through 4-5).

Slackwater surveys in 1987, as well as those from other years (Brooks 1983), have shown that the water over the shallow part between km 48-80 (Fig. 3-2) is usually well mixed. This feature was not well reproduced by the model especially for August 4 and 10. This discrepancy may be attributable to the shallow depth (6 to 8 m), making this region more susceptible to wind mixing. Wind data from the Norfolk airport, located 65 km to the south of the Rappahannock River mouth, were examined. Strong winds with peak gust speeds of 36 mph blew from the south-west on August 3; 26 mph winds blew from the south on August 9.

The effect of wind mixing was included in the simulation through the second term in Equations 2-16 and 2-17. The height, period and length of the wind-induced waves were evaluated using the Sverdrup-Munk-Bretschneider (SMB) forecasting curves for deep water waves (U.S. Army Coastal Engineering Research Center 1973) and updated everyday. The estimated wave lengths for the wind speeds of 26 and 36 mph indicate that the wind-induced waves are deep water waves since the water depth is greater than 5 to 7 m. The salinity predictions with the inclusion of wind mixing are shown in Figures 4-3 through 4-5 as dashed contours where the constant for wind mixing (α_w) was calibrated to be 5×10^{-3}. The inclusion of wind mixing improves the agreement between the model predictions and field measurements, particularly over the top 6 to 7 meters of the water column. The inclusion of wind mixing in the model caused a more conspicuous change in salinity distribution on August 4 than on August 10. This is because the weaker tidal mixing due to neap tide on August 4 left more room for the wind mixing, and also because of the stronger wind on August 3 than on August 9. With no wind included in the model for August 24, the change in the salinity distribution by including wind mixing was least.

A. Characteristic salinity distribution: Field measurements on August 4 (Fig. 4-3)

and 24 (Fig. 4-5) showed a negative salinity gradient in the horizontal direction with salinity increasing in the upriver direction for some reaches of the river. The negative salinity gradient, which was quite distinct between km 40-50 on August 24, might be attributable to the bottom topography of the river (Fig. 3-2). The saline bay water, that enters the river through the mouth and moves upriver along the bottom, might be deflected upward in the presence of obstacles such as the sloping bottom, thereby creating the reverse horizontal gradient.

A model run with an ideal geometry (constant depth, and width varying in the vertical but not in the longitudinal direction) while keeping all other conditions the same, showed the absence of horizontal reversal in salinity gradient. Another model run with increased K_z and real geometry showed that the increased vertical mixing could erase the reverse salinity gradient. These sensitivity model runs imply that the reverse salinity gradient can be expected to occur frequently in the Rappahannock River, which has upriver-sloping bottom geometry, but that it may be erased by strong mixing during spring tides and/or by strong winds.

This hypothesis is supported by the salinity data from 55 slackwater surveys for the Rappahannock River conducted by VIMS between 1981 and 1990. No reverse gradient was observed for 18 surveys characterized by strong spring tides with or without strong winds. The data from the other 37 surveys showed the presence of the reverse salinity gradient. For 33 surveys, the measurements were taken either at neap or at weak spring tides without strong winds, and the remaining 4 surveys were conducted at strong spring tides with or without strong winds. The presence of the reversed gradient in the latter 4 surveys might be due either to the insufficient mixing and/or to the salinity of the incoming water from the bay.

4-4. Model Verification

4-4-1. Surface elevation and longitudinal velocity in 1987

For the verification of the model with respect to surface elevation and horizontal velocity, a model simulation was conducted covering the period during which field measurements were taken in the summer of 1987. The same conditions described in Section 4-3 were used. Model predictions are compared with surface elevation measurements at Urbanna (Fig. 4-6) and Tappahannock (Fig. 4-7). To show the subtidal variations in surface elevation, the time series data of predictions and measurements were subjected to a low-pass filter with a cut-off frequency of $(48\ hr)^{-1}$. The filter was a modification of the low-pass filter designed by Groves (Thompson 1983). The filtered series that are considered as subtidal components are presented in Fig. 4-8. Excellent agreement exists between the model and the data demonstrating the model's ability to reproduce the surface elevation in the prototype including both the semi-diurnal tidal fluctuations (Figures 4-6 and 4-7) and the subtidal (longer-term) variations (Fig. 4-8).

Figures 4-9 through 4-13 illustrate the comparisons of model predictions of horizontal velocity with current meter data taken at the river mouth and km 16.6. The model can reproduce the velocity measurements at the mouth very accurately, at depths of 1.2 m (Fig. 4-9) and 9.7 m (Fig. 4-10). Considering that the model calculates the lateral average velocity while the current meter data are point measurements, the model predictions of velocity here are more than satisfactory. The field measurements at depths of 1.2 m (Fig. 4-11) and 10.0 m (Fig. 4-12) at km 16.6 are again well reproduced by the model. Near the bottom (18.7 m deep) at km 16.6, the model prediction is generally less than field data (Fig. 4-13). The current meter there (S4#747) showed some technical problems while deployed. The clock in the meter, that was set to record variables every 30 minutes, shifted slightly giving

irregularly recorded signals. Examination of the data from S4#747 and S4#749 (10.0 m deep at the same location) indicates that there is no appreciable decrease in velocity with increasing depth from mid-depth toward the bottom. Considering this and the excellent model-field agreements elsewhere, the quality of the field data from S4#747 might be the cause of the discrepancy.

A. Residual velocity: The current velocity in estuaries may be decomposed into two components, tidal and residual. The dominant residual velocity is characterized by the upriver movement of more saline water in the lower layer and the downriver movement of fresher water in the upper layer. Since the mass flux due to the residual component can be very important in the Rappahannock River (Kuo & Park 1992), the model's ability to reproduce the average residual current correctly is essential.

To eliminate the diurnal and semi-diurnal tidal constituents and fluctuations of higher frequencies, the velocity time series data were subjected to a low-pass filter with a cut-off frequency of $(48\ hr)^{-1}$. The filtered series of predictions and measurements are presented in Figures 4-14b through 4-14f. The predicted residual currents (long dashed lines in Fig. 4-14) show the gravitational circulation with the downriver movement in the surface layer and the upriver movement in the bottom layer. Although the measured residual currents generally follow this pattern, they do show some variations with a dominant time scale of 4-to-6 days. This variability was attributed to local meteorological forcing and its effect on the salinity structure in the bay near the river mouth (Kuo & Park 1992). The wind affects the velocity field in the lower portion of the river both by transferring momentum through the surface and by changing the conditions in the bay. The momentum input from wind stress can be included in model calculations using Eq. 2-7. The model results (solid lines in Figures 4-8 and 4-14) using daily average wind speed and resultant wind direction from the Norfolk airport in Virginia show that inclusion of wind stress considerably

improves the model-field agreement. The predicted residual currents with wind stress have the 4-to-6 day variations but not as large as those in field measurements. This difference seems to be due to the bay conditions that are changed by wind events but have not been properly incorporated into model calculation.

Analyzing the 1987 field data used in this study, Kuo & Park (1992) showed that the density-driven current near the bottom was enhanced by the wind-driven circulation in the bay during periods of strong wind from the southwest quadrant. The time series plot of surface elevation at the river mouth (Fig. 4-14a) shows that the wind drove surface water out of the river, and thus lowered the surface elevation and caused a set-up in the bay that drove the bay water into the river along the bottom. This surface set-up in the bay favored the transport of the high salinity water from the deep portion of the bay as a result of tilting of the pycnocline in the bay, and shoreline and bathymetric configurations around the bay-subestuary junction (Kuo & Park 1992). The present model simulates the processes occurring in the subestuary (Rappahannock Estuary) but not those occurring in the bay such as surface set-up and tilting of the pycnocline. The model incorporates the effects of the bay conditions only through the downstream boundary conditions and thus needs detailed boundary conditions for surface elevation, current velocity and salinity to reproduce the effects of the processes occurring in the bay. Hourly measurements (Fig. 4-14a), which show the surface set-up at the mouth, were used for boundary conditions for surface elevation. In the present model, however, the downstream boundary conditions for velocity were estimated using the extrapolated values (Section 2-1-2). This treatment is a reasonable method due to the lack of detailed current measurements in most of modeling efforts, but it cannot adequately reflect the processes such as the enhanced circulation due to the wind-driven surface set-up outside of the mouth. Furthermore, the model recognizes the effect of the transport of the high salinity water from the

deep portion of the bay (as a result of pycnocline tilting in the bay and geometric configurations around the bay-subestuary junction) only through the downstream boundary conditions for salinity. In the 1987 model simulation, the time-varying boundary conditions were constructed using the slackwater surveys conducted on July 28 and August 4, 10 and 24 (Section 4-3). This weekly-to-biweekly sampling cannot adequately reflect the conditions in the bay that vary in the time scale of 4-to-6 days. Therefore, the difference between the predicted residual currents with wind stress and field data may be attributable to the downstream boundary conditions. Accurate and detailed downstream boundary conditions for velocity and salinity are necessary to resolve the 4-to-6 day variations in the predicted residual currents. At the bottom of km 16.6, as mentioned earlier, the quality of the field data from S4#747 might be responsible, at least in part, for the variations in Fig. 4-14e.

The predicted residual velocities averaged over 58 tidal cycles (i.e., 2 spring-neap cycles) are presented as a vector plot in Fig. 4-15, in which every other point is omitted to enhance readability. The arrow length represents the magnitude and the arrow head indicates the direction of residual velocity no matter how small the magnitude is. The limit of salt intrusion, represented by the 1 ppt isohaline, also is included. In Fig. 4-15, the null point where the level of no-net-motion (LNNM) meets the estuary bottom, is located at the limit of salt intrusion (around km 95). Near the surface above LNNM, the seaward flowing velocity increases in a downriver direction despite the enlargement of the river cross-section in that direction. This augmentation of residual current is derived from the landward intrusion of the bay water near the bottom below LNNM, which increases the flushing capacity of an estuary by an order of magnitude (Kuo et al. 1978). In the estuarine portion of the river, the maximum upriver velocity is -5.0 cm sec^{-1} in the lower layer, and the maximum downriver velocity is 3.9 cm sec^{-1} in the upper layer. Negative velocity

indicates that the water flows in the upriver direction. This residual current is far smaller than the tidal current. The residual current can be decomposed into two parts; baroclinic part due to the longitudinal density gradient and barotropic part due to the freshwater discharge. In the Rappahannock River, the baroclinic flow is small compared to the barotropic flow that includes both the tidal current and the freshwater-induced residual current.

A model simulation using constant boundary conditions was performed to examine the response of residual velocity to the spring-neap cycle. A freshwater discharge of 10.0 cms and harmonic tide with M2 (17.2 cm) and S2 (2.53 cm) components at the mouth were used to force the model. A constant salinity profile at the mouth (18 and 20 ppt at the surface and bottom, respectively, with linear variation in the vertical) was used for the boundary condition. The average residual velocities over 2 spring-neap cycles are presented in Fig. 4-16. In the saline part of the river, the maximum residual velocities are -3.9 and 2.4 cm sec^{-1} in the lower and upper layers, respectively. The null point is again located at the limit of salt intrusion. Figures 4-17 and 4-18 present the average residual velocities during spring and neap tides, respectively. The spring tide (Fig. 4-17) provides more mixing energy, and thus has weaker residual circulation than the neap tide (Fig. 4-18). In the saline part of the river, the maximum velocities in the lower and upper layers are -3.8 and 2.3 cm sec^{-1}, respectively, during spring tide and -4.2 and 2.8 cm sec^{-1}, respectively, during neap tide.

To study the alteration in residual velocity in response to the freshwater discharge, another model simulation was conducted using the annual mean freshwater discharge in 1987, 39.8 cms (Fig. 4-19). All other conditions were kept the same as above. Figure 4-19, compared to Fig. 4-16, shows that when the increased freshwater discharge pushes the limit of salt intrusion farther downriver, the increased

horizontal salinity gradient enhances the residual circulation. In the saline part of the river, the maximum bottom residual current is -4.6 cm sec^{-1} and the maximum surface residual current is 3.3 cm sec^{-1} . The null point also is pushed downriver, but farther down than the limit of salt intrusion represented as 1 ppt isohaline (Fig. 4-19).

The level of no-net-motion (LNNM) occurs where the longitudinal density gradient integrated over the water column above that depth (baroclinic) balances the mean surface slope due to the freshwater discharge (barotropic). The location of the null point, where LNNM meets the estuary bottom, depends upon the location of the limit of salt intrusion, the salinity gradient, geometry (total depth) and surface slope. Then, the location of null point relative to the limit of salt intrusion is a function of salinity gradient, geometry and surface slope. When the freshwater discharge increases from 10 cms (Fig. 4-16) to 39.8 cms (Fig. 4-19), the 1 ppt isohaline used as an indicator of the limit of salt intrusion is pushed downriver to the top of the shallow region around km 80. Despite the augmented longitudinal salinity gradient, the reduced total depth makes the increase in baroclinic forcing not as large as that in barotropic forcing (surface slope). Then, the balance between baroclinic and barotropic forcing (i.e., null point) occurs downriver of the limit of salt intrusion. If the freshwater discharge is large enough to push the limit of salt intrusion downriver of the shallow region into the deep part, the null point will occur closer to the limit of salt intrusion. This is confirmed by the results from a model simulation with the freshwater discharge of 130 cms (Fig. 4-20). Therefore, the limit of salt intrusion should not be used to express, or to judge, the limit of gravitational circulation. For example, the expressions in the preceding paragraphs, "in the saline part of the river," need to be rephrased as "in the lower part of the river where the gravitational circulation exists."

4-4-2. Salinity distributions in 1990

The model's ability to predict mass transport was verified with a simulation of salinity distributions from July 5 to August 7, 1990. Daily discharge from the fall line gauging station (USGS 1991) and the hourly measurements of the surface elevation at the mouth were used for the upstream and downstream boundary conditions respectively. The same treatments, explained in Section 4-3, were applied to freshwater discharges and to tide measurements.

Three slackwater surveys were conducted at slack before flood flow (SBF) on June 6, July 5 and August 7. As in the calibration in Section 4-3, the salinity data at the mouth were linearly interpolated in time and used for the boundary condition. The model input of the salinity boundary condition, however, requires the vertical salinity profile at the mouth at SBE. This was obtained by increasing the salt measurements at the mouth on three surveys until the model predictions at the mouth matched the field measurements. The model simulation started from June 4, and the measured salinity distribution on June 6 was used to specify the initial condition.

Using the same constants in the turbulent mixing coefficients used in Section 4-3 ($\alpha = 1.15 \times 10^{-2}$ and $\beta = 0.25$), the model predictions are compared with the field measurements on July 5 and August 7 in Figures 4-21 and 4-22, respectively. The boundary conditions at SBE were selected such that the model predictions at SBF matched the field observations at the mouth. Thus, the model-field agreement at the downstream boundary was forced by this method. Except at the mouth, the model predictions were generally lower by 2 to 3 ppt than the field measurements on both dates. The river contained less salt in the model predictions than in the field measurements. There are two possible explanations, the first of which is that advective mass transport in the model is too small and not able to transport enough salt upriver. The agreement, however, between the model and the field data in the

model verification of current velocity was excellent in Section 4-4-1. This proved the adequacy of model simulation of advective transport.

An alternate explanation is that the amount of salt coming into the river through the mouth may be responsible for the model-field discrepancy. That is, the lack of salt within the river in the model might be due to the insufficient salt in the incoming water. The boundary condition, which specifies the salinity at the mouth, was evaluated by linear interpolation using the data from three slackwater surveys (June 6, July 5 and August 7) in 1990. This boundary condition might be too low for the model predictions to have as much salt as observed in the field data. This situation could happen if three surveys conducted at approximately monthly intervals would have missed event(s) of high salinity water intruding into the river. Data from three surveys showed a monotonic increase in salinity at the mouth over the two month period. Since the intrusion of the high salinity water into the Rappahannock River has a time scale of 2 to 3 days (Kuo & Park 1992), it is highly probable that monthly sampling would miss such event(s). Thus, it was hypothesized that saltier water entered the river several days before each measurement on July 5 and August 7. Another boundary condition for salt at the mouth was constructed by assuming that the salinity at the bottom half of the water column was higher by 3 ppt on June 25 than the measurement on July 5, and by 3.5 ppt on August 2 than that on August 7. The model predictions with new boundary conditions in Fig. 4-23 show that the model-field agreement is much better than that in Figures 4-21 and 4-22.

Both July 5 and August 7 were near neap tides, and stratified conditions were observed from surface to bottom in the lower, deeper part of the river between km 0-42 (Fig. 3-2). In the shallower part of the river upriver of km 48 to the limit of salt intrusion (around km 80), well-mixed conditions existed throughout the water column on both dates. As in the calibration, wind mixing was thought to be at least

partly responsible for the observed salinity distributions. Wind data from the Norfolk airport in Virginia showed that wind with the peak gust speed of 26 mph blew from the south-west on July 4, and that with 25 mph blew from the south on August 6. The model predictions with the inclusion of the wind mixing ($\alpha_w = 5 \times 10^{-3}$) are also presented in Fig. 4-23 as dashed contours. The inclusion of wind mixing improved the model-field agreement, particularly over the shallow region. The final calibrated model, therefore, includes the wind mixing.

The salinity measurements on both July 5 and August 7, 1990 show highly stratified conditions in the deeper, lower part of the river between km 0-42 and homogeneous conditions in the shallower part of the river between km 48-80 (Figures 4-21 and 4-22). The observed Δs (vertical salinity difference between surface and bottom) around km 10 is approximately 4 and 6 ppt, respectively, on July 5 and on August 7. The observed Δs around km 55 is approximately 1 ppt on both dates. Well-mixed conditions in the shallower part of the river between km 48-80, regardless of the conditions in the deeper, lower part of the Rappahannock River, have been frequently observed (Brooks 1983). This may indicate more vigorous vertical mixing in the shallower region than in the deeper region especially during sporadic wind events. Although this mechanism sounds physically reasonable in the prototype, the turbulence closure model based upon mixing length concept behaves in the different direction. In the mixing length theory, the turbulent mixing coefficients are affected by the mixing length and the velocity shear. The shape function, Z(1-Z/h), in the mixing length part of Equations 2-16 and 2-17 will not allow more mixing in the shallower region. The shape function was not included in the formulation of the wind-induced mixing terms in Equations 2-16 and 2-17 to minimize this behavior. Although the model successfully described the general salinity distributions in the prototype, it could not always reproduce all the details observed. In Fig. 4-23, the

verification results (dashed contours) are not as stratified as the observations between km 0-42 and at the same time not as homogeneous as the observations between km 48-80. The predicted Δs around km 10 is approximately 3 and 4 ppt, respectively, on July 5 and August 7. Around km 55, the predicted Δs is approximately 2 and 2.5 ppt, respectively, on July 5 and August 7. The model predictive capability and thus applicability to other systems could be significantly improved with more understanding of the turbulent mixing processes.

Table 4-1. Geometric data for the model grid cells[a].

Segment (i)			Layer (k)									
			1	2	3	4	5	6	7	8	9	10
	DIST[b]	SST[c]	B[d]									
2	176.1	0.0	72.4	54.1								
3	173.6	0.0	76.2	54.1								
4	171.1	0.0	79.8	56.7								
5	168.6	0.0	92.7	69.6								
6	166.1	0.0	102.1	73.2								
7	163.6	0.0	103.6	78.5								
8	161.1	0.0	108.1	75.9								
9	158.6	0.0	98.1	70.6								
10	156.1	0.0	105.9	84.3								
11	153.6	0.0	123.7	82.8								
12	151.1	0.0	84.0	69.7								
13	148.6	0.0	137.0	94.7								
14	146.1	0.062	113.7	99.1								
15	143.6	0.067	130.4	100.9	67.8							
16	141.1	0.176	174.9	138.9	69.3							
17	138.6	0.103	147.6	120.2	72.4							
18	136.1	0.201	178.4	151.4	59.5							
19	133.6	0.183	142.3	124.4	87.7	71.7						
20	131.1	0.122	167.2	140.8	97.1	80.8						
21	128.6	0.246	246.3	170.6	118.1	70.0						
22	126.1	0.643	309.3	217.2	128.0	80.7						
23	123.6	0.980	212.1	143.7	104.5	78.7						
24	121.1	0.680	397.4	223.0	137.2	70.0						
25	118.6	5.170	347.1	277.8	137.9	120.4						
26	116.1	0.591	240.7	221.6	137.9	120.4	98.3					
27	113.6	2.179	290.0	248.1	167.6	129.5	99.1					
28	111.1	0.504	264.1	242.7	180.0	147.8	125.7					
29	108.6	0.0	356.6	278.9	190.3	114.3	70.0					
30	106.1	0.568	405.6	380.6	205.5	100.0	70.0					
31	103.6	1.026	409.4	347.5	182.9	91.4	70.0					
32	101.1	0.977	276.2	257.9	166.1	153.9	140.2	121.9				
33	98.6	0.645	376.1	278.1	227.1	157.7	141.8	105.9				

[a] In the model, $\Delta x = 2.5$ km and $\Delta z = 2$ m (For the top layer, Δz is adjusted to account for the surface fluctuation).
[b] DIST = Distance (km) from the river mouth to the center of each segment.
[c] SST = Surface area of the side storage area (km^2) at mean tide.
[d] B = estuarine width (m); at the surface layer, it is width at mean tide.

Table 4-1. (continued).

Segment (i)			Layer (k)									
			1	2	3	4	5	6	7	8	9	10
	DIST	SST	B									
34	96.1	0.021	365.6	283.7	220.4	171.4	130.5	75.6				
35	93.6	0.504	447.5	374.3	228.6	196.6	169.2					
36	91.1	0.757	652.3	475.5	274.3	174.3	74.3					
37	88.6	0.310	404.7	304.7	266.1	212.5	143.2					
38	86.1	0.193	605.0	441.4	307.6	211.7	138.6					
39	83.6	0.548	666.4	422.5	262.1	158.5						
40	81.1	4.020	780.0	419.9	248.4	77.0						
41	78.6	3.081	989.7	596.5	229.1							
42	76.1	2.023	1048.5	567.5	243.8							
43	73.6	4.058	1227.0	650.9	221.2							
44	71.1	3.467	1529.5	696.6	118.1							
45	68.6	0.403	1650.9	900.4	204.3							
46	66.1	1.105	1682.5	949.8	356.6							
47	63.6	3.324	2055.2	866.8	335.9	184.9						
48	61.1	0.0	2614.6	1001.5	374.6	176.0						
49	58.6	0.572	3265.8	1241.7	442.0	179.4						
50	56.1	0.605	2514.6	1333.5	457.2	197.2						
51	53.6	0.0	3129.6	1741.0	472.3	166.1						
52	51.1	0.163	3883.2	2240.3	490.7	128.0						
53	48.6	3.939	3582.3	2091.4	688.7	370.5						
54	46.1	2.559	3372.7	2019.4	912.2	599.2	271.1					
55	43.6	4.197	3937.7	2505.3	1095.8	532.0	250.6					
56	41.1	0.324	4366.8	2949.1	1298.3	535.1	307.9	207.9	107.9			
57	38.6	0.149	4335.5	3250.3	1564.9	776.2	628.8	481.5	334.2	186.8		
58	36.1	0.0	4329.0	3490.1	1867.0	1036.9	840.1	627.4	372.3	138.7		
59	33.6	0.0	4363.5	3628.1	2228.0	1330.2	869.2	480.2	324.6	138.7		
60	31.1	0.0	4395.2	3755.1	2560.3	1600.2	896.1	344.7	280.7			
61	28.6	0.589	4059.3	3519.2	2460.4	1687.6	1237.5	633.3	269.5			
62	26.1	4.495	3748.2	3300.6	2367.8	1768.6	1553.8	900.6	259.0			
63	23.6	1.157	3365.0	2957.2	2230.9	1746.0	1503.1	998.5	497.3			
64	21.1	4.035	2923.9	2535.3	2065.0	1676.4	1287.8	1028.7	861.1	655.3	464.8	266.7
65	18.6	24.015	3365.1	3036.9	2582.2	2078.0	1393.7	892.8	694.7	548.8	416.3	270.9
66	16.1	6.216	3838.9	3575.7	3137.7	2509.4	1507.5	746.9	516.0	434.4	364.3	275.4
67	13.6	0.0	4016.4	3608.2	3087.2	2557.7	1702.8	957.2	663.4	533.4	418.1	297.6
68	11.1	1.820	3965.8	3272.4	2603.0	2325.6	1941.6	1408.2	1034.8	778.8	544.1	330.7
69	8.6	2.804	5165.6	4678.0	3706.4	2584.7	1804.4	1402.1	853.4	682.8	524.3	353.6
70	6.1	4.208	3109.0	2926.1	2706.6	2286.0	1682.5	1298.5	1097.3	923.5	676.7	429.9
71	3.6	5.345	4334.4	3234.9	1767.8	1463.0	1328.9	1268.0	1194.8	877.8	512.1	268.2
72	1.1	0.0	5486.4	4663.5	4053.8	4114.8	1310.6	440.8				

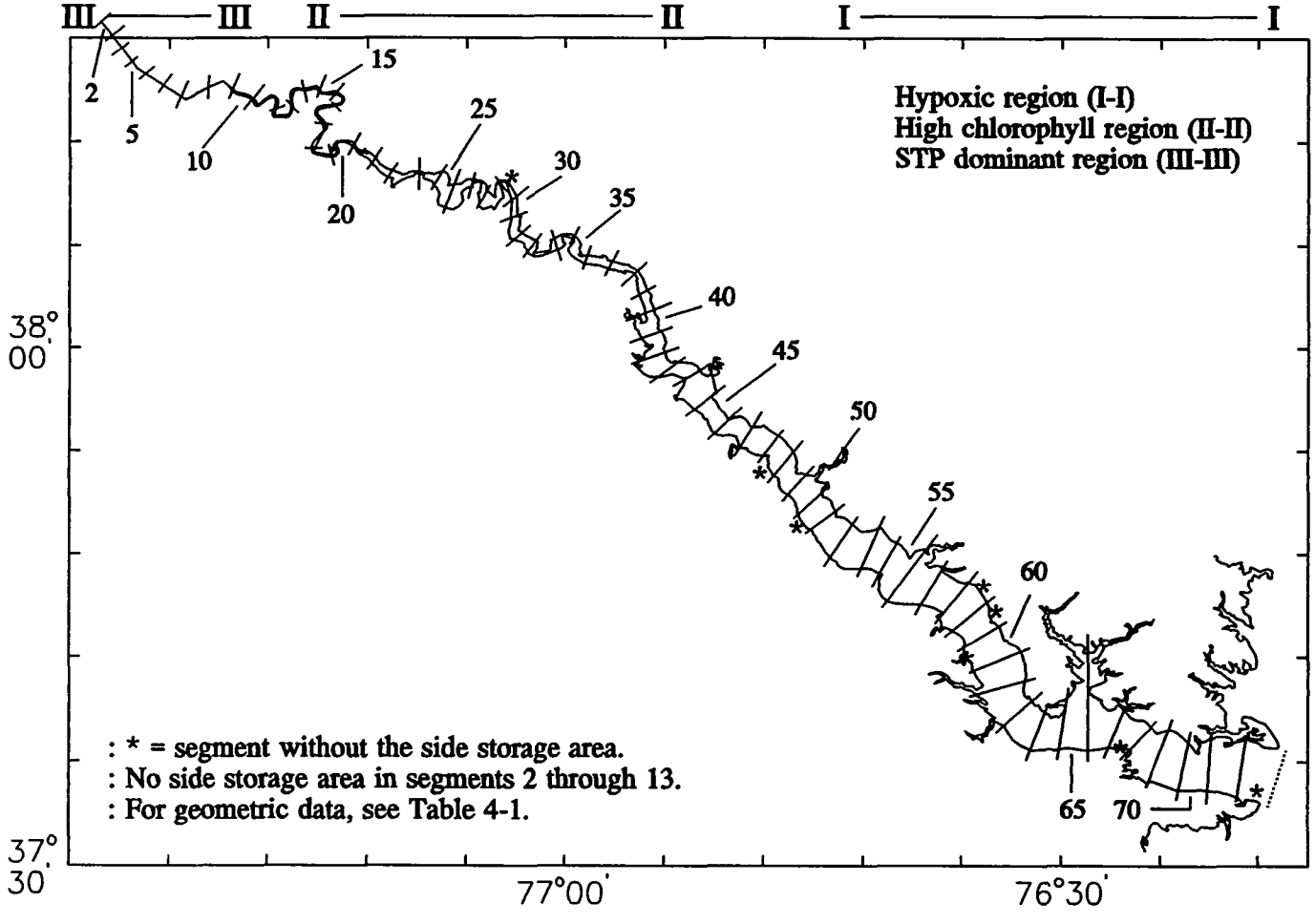

Figure 4-1. The model transects and side storage areas in the tidal Rappahannock River.

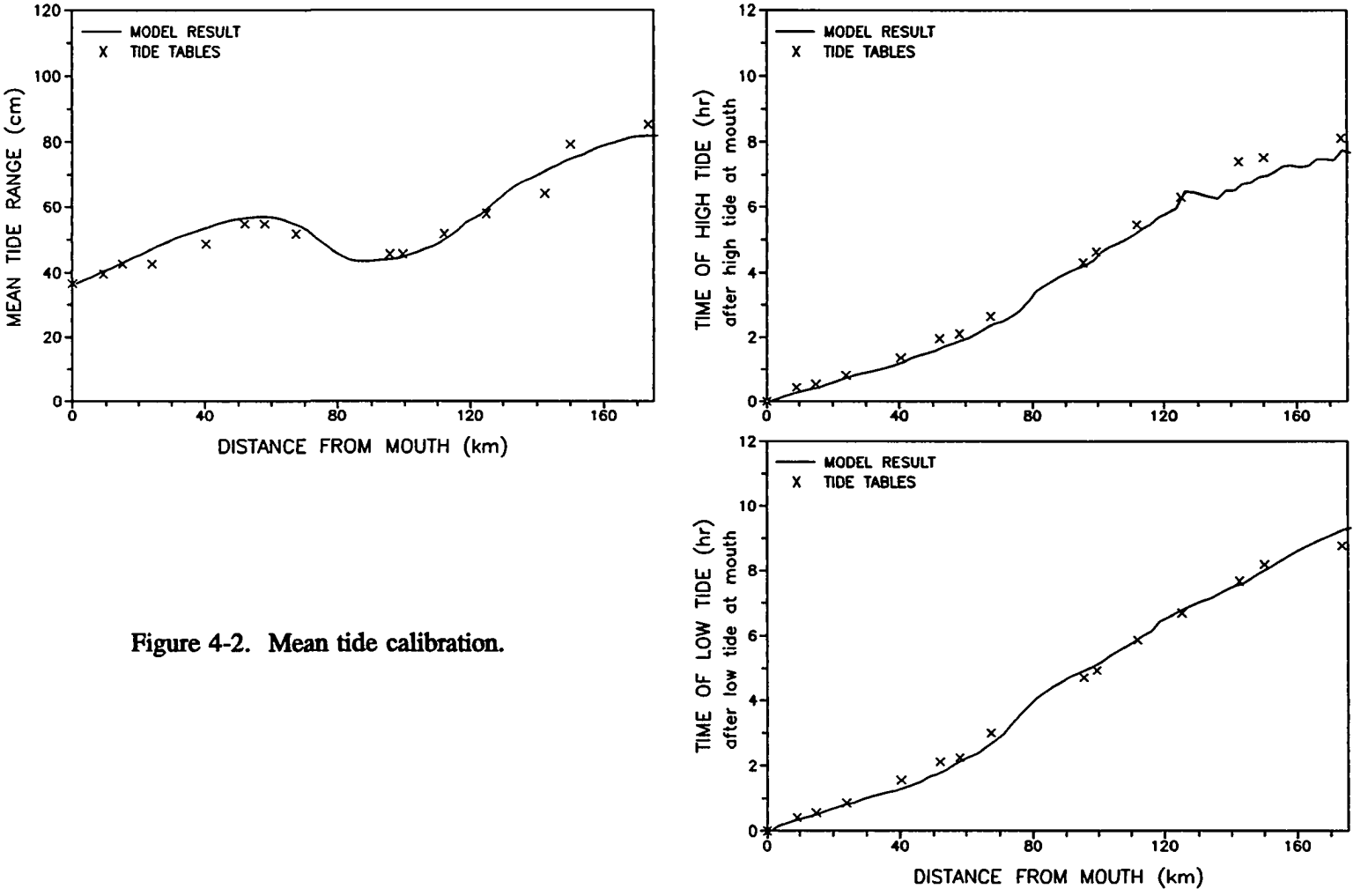

Figure 4-2. Mean tide calibration.

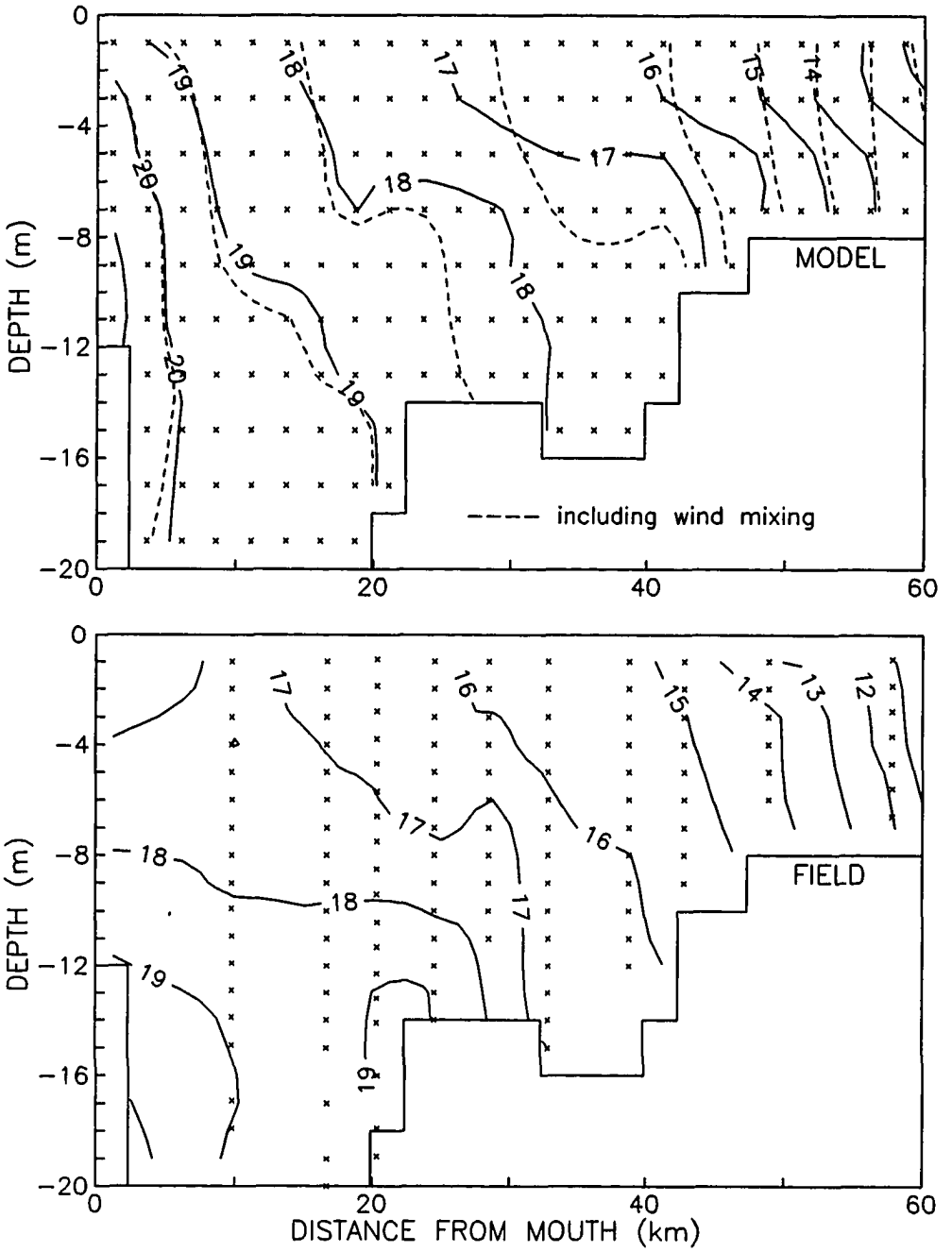

Figure 4-3. Model prediction and field measurement of salinity on 8/04/87 : the most upriver station was at km 57.79 in 1987 surveys.

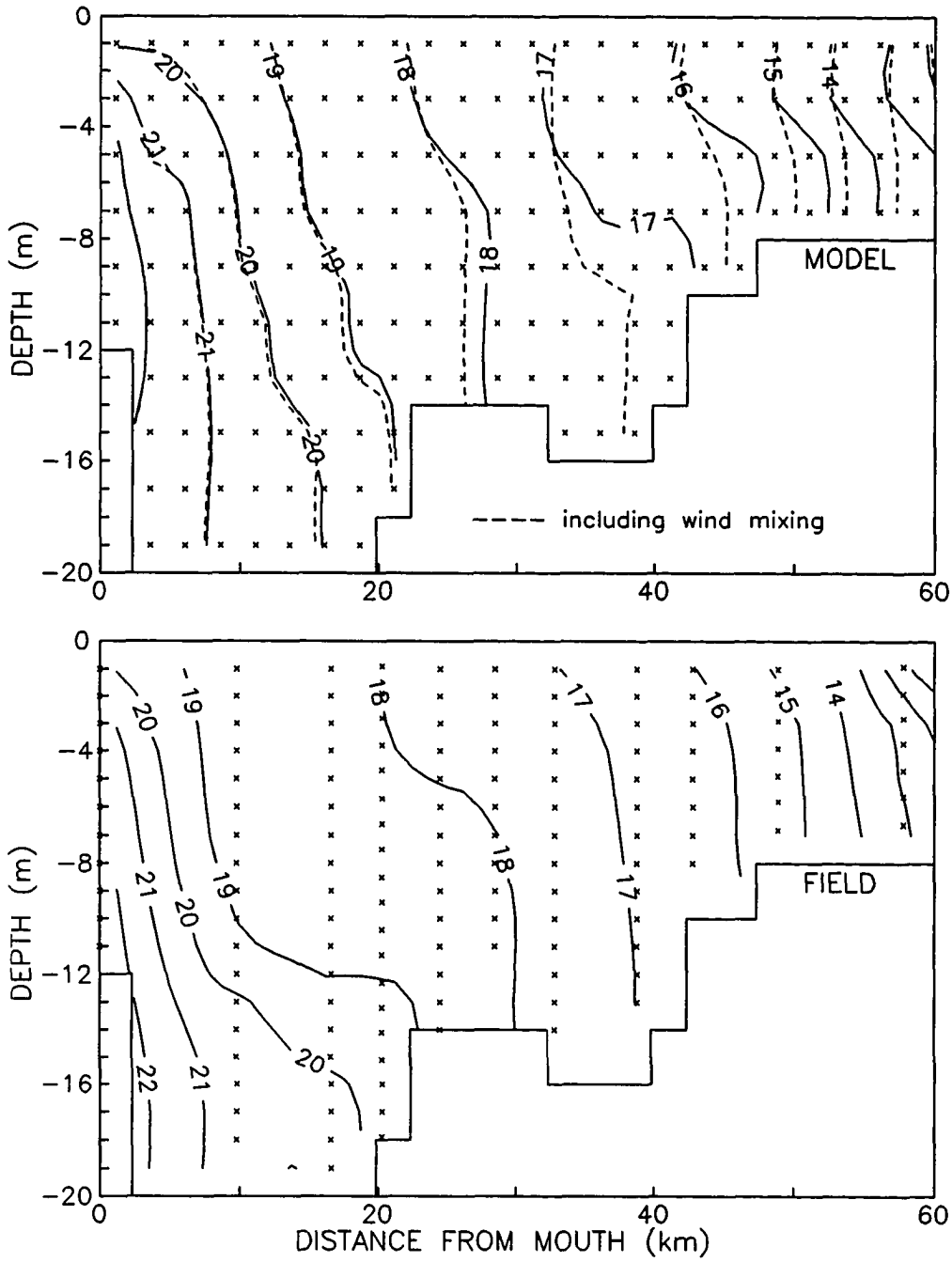

Figure 4-4. Model prediction and field measurement of salinity on 8/10/87.

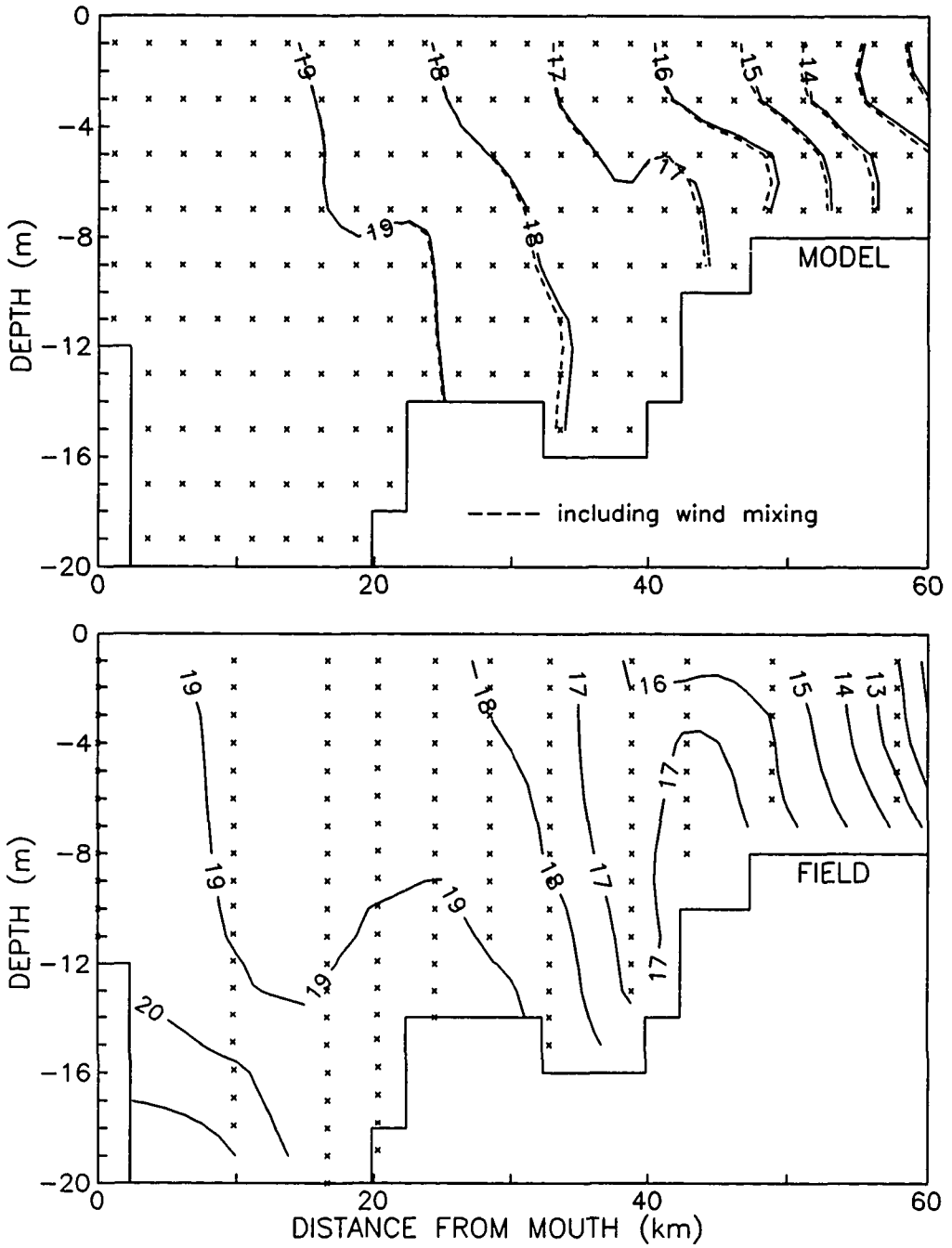

Figure 4-5. Model prediction and field measurement of salinity on 8/24/87.

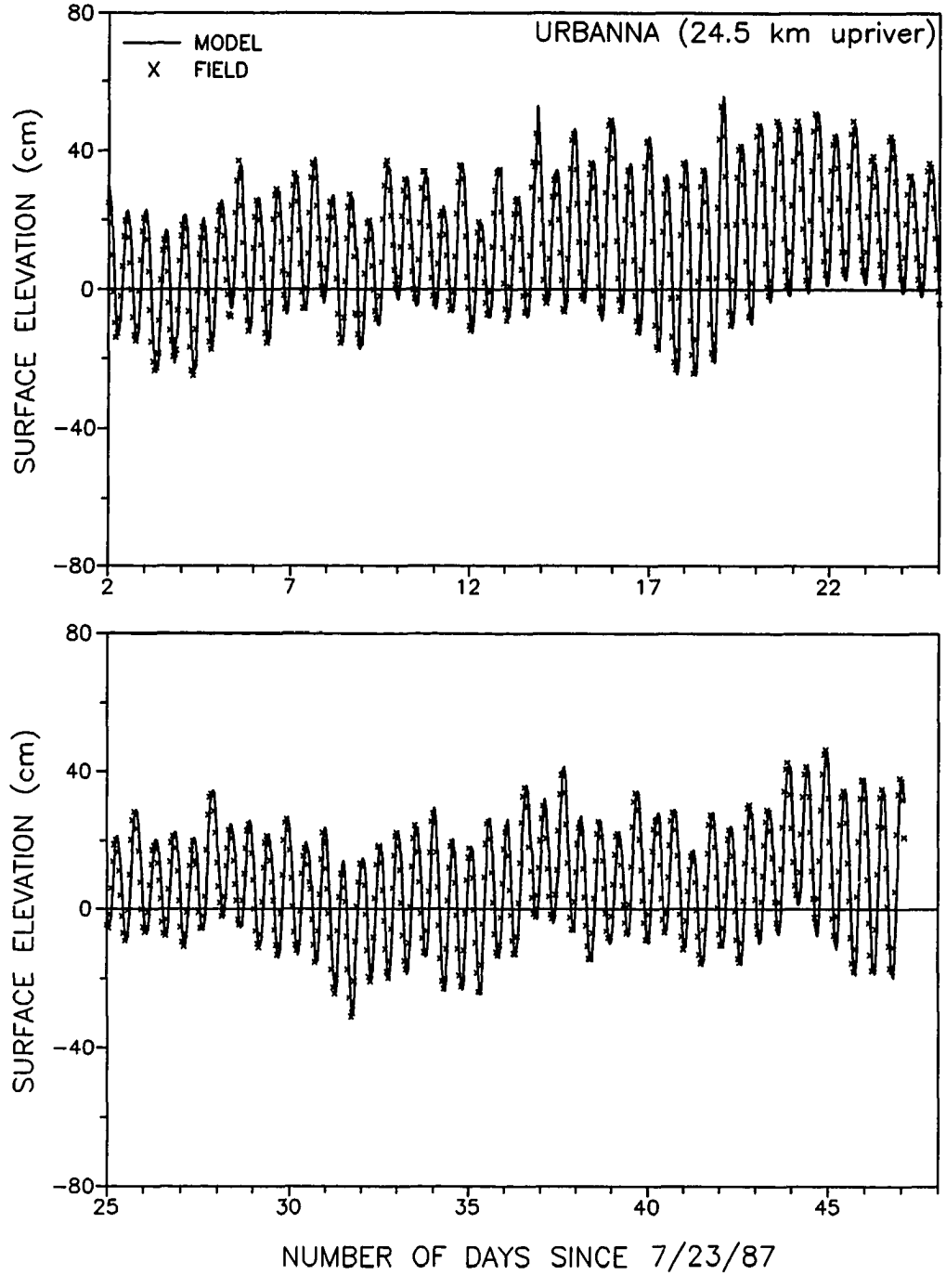

Figure 4-6. Tide simulation at 24.5 km upriver from mout

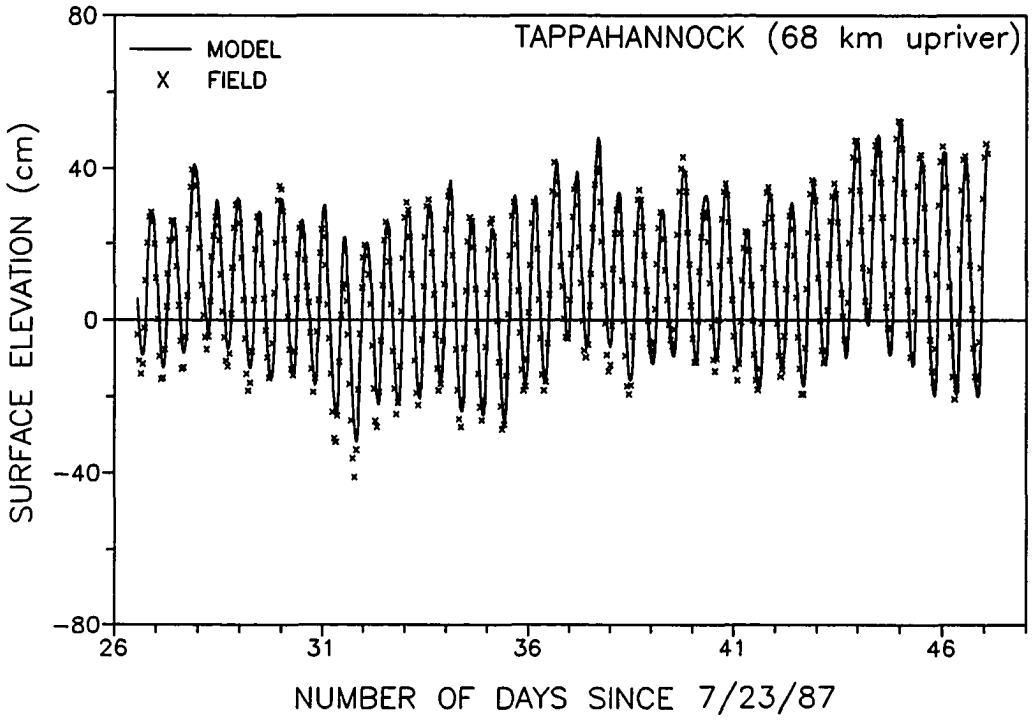

Figure 4-7. Tide simulation at 68 km upriver from mout

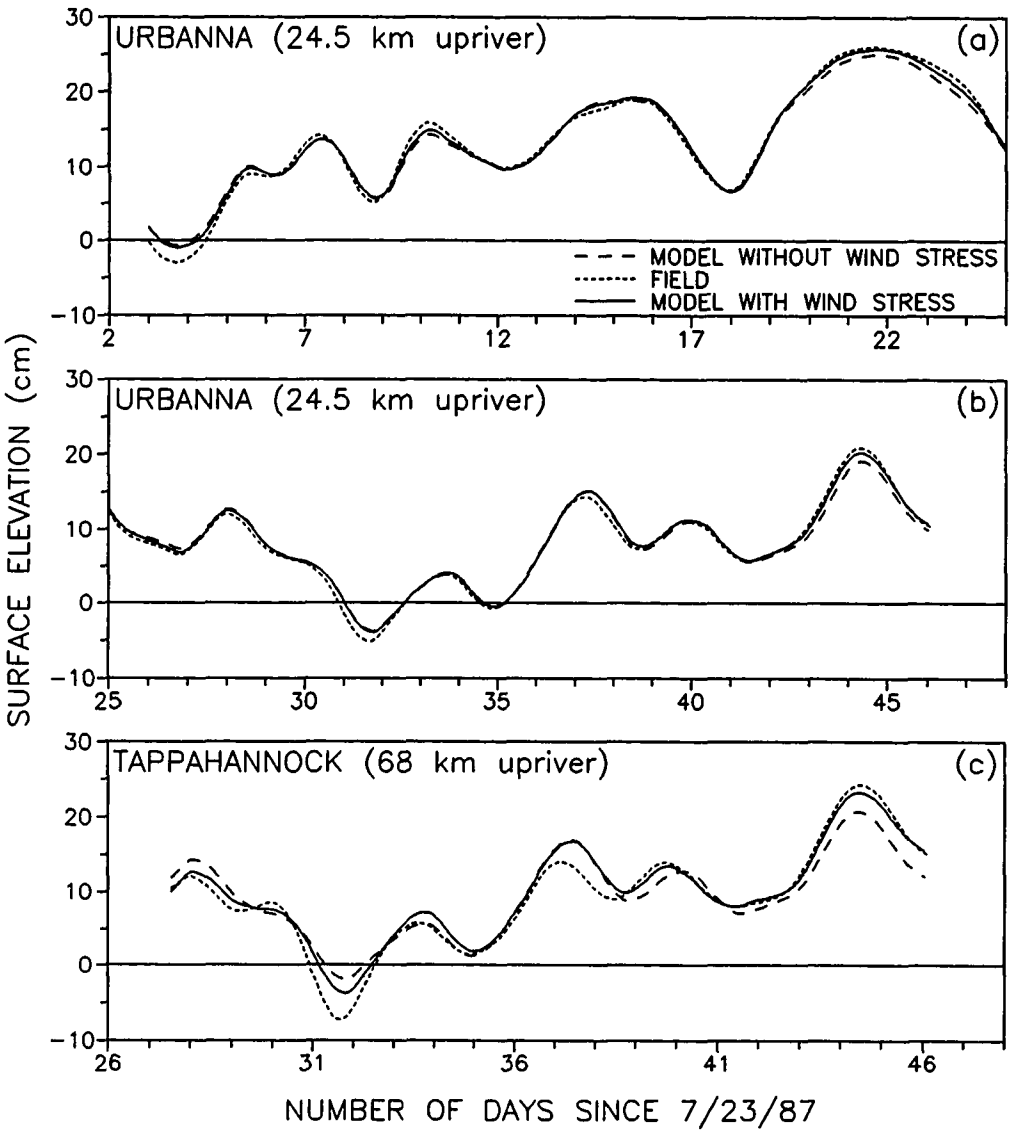

Figure 4-8. Subtidal variations in surface elevation at Urbanna (a-b) and at Tappahannock (c).

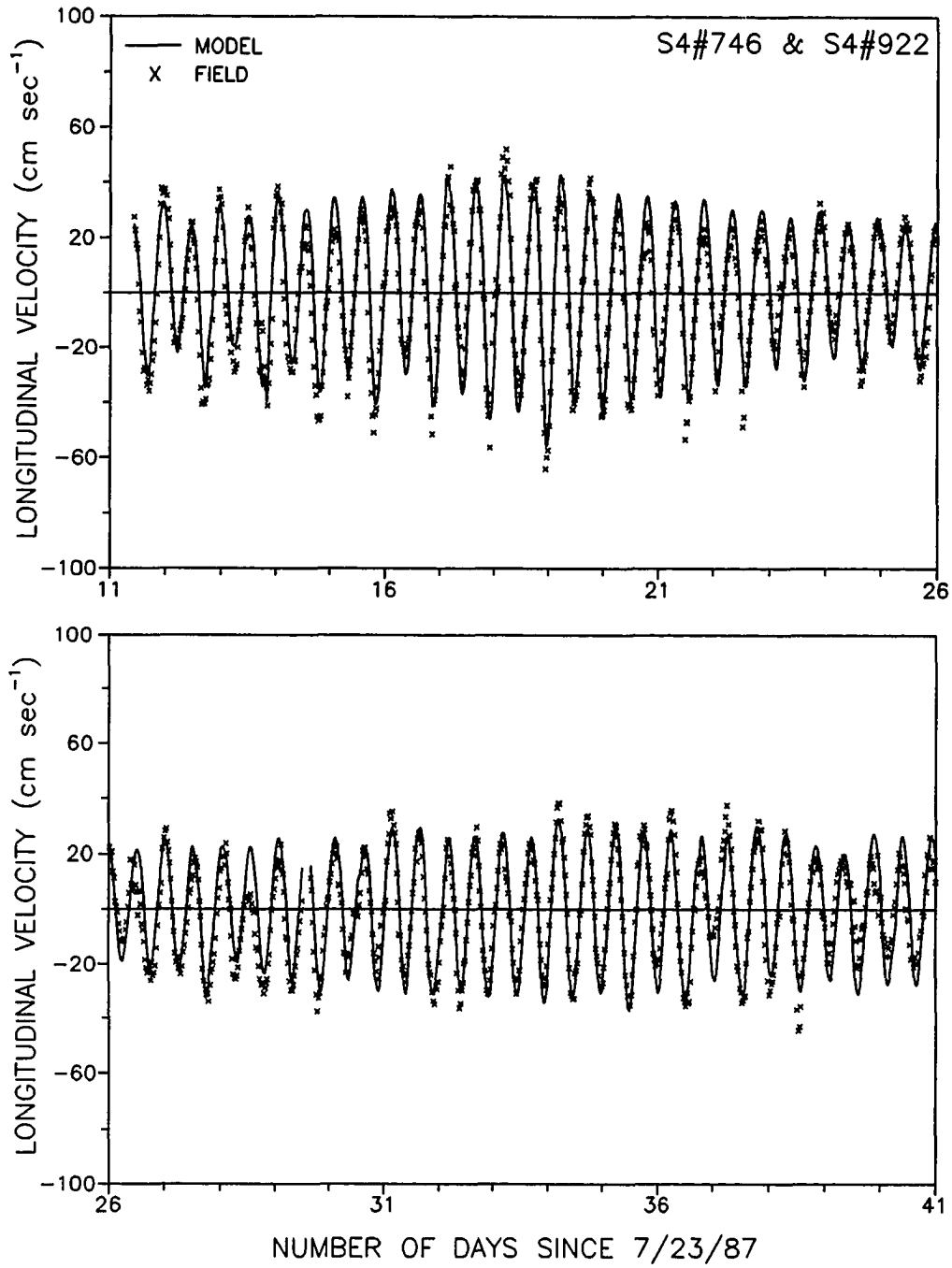

Figure 4-9. Current simulation at the mouth, depth 1.2 m.

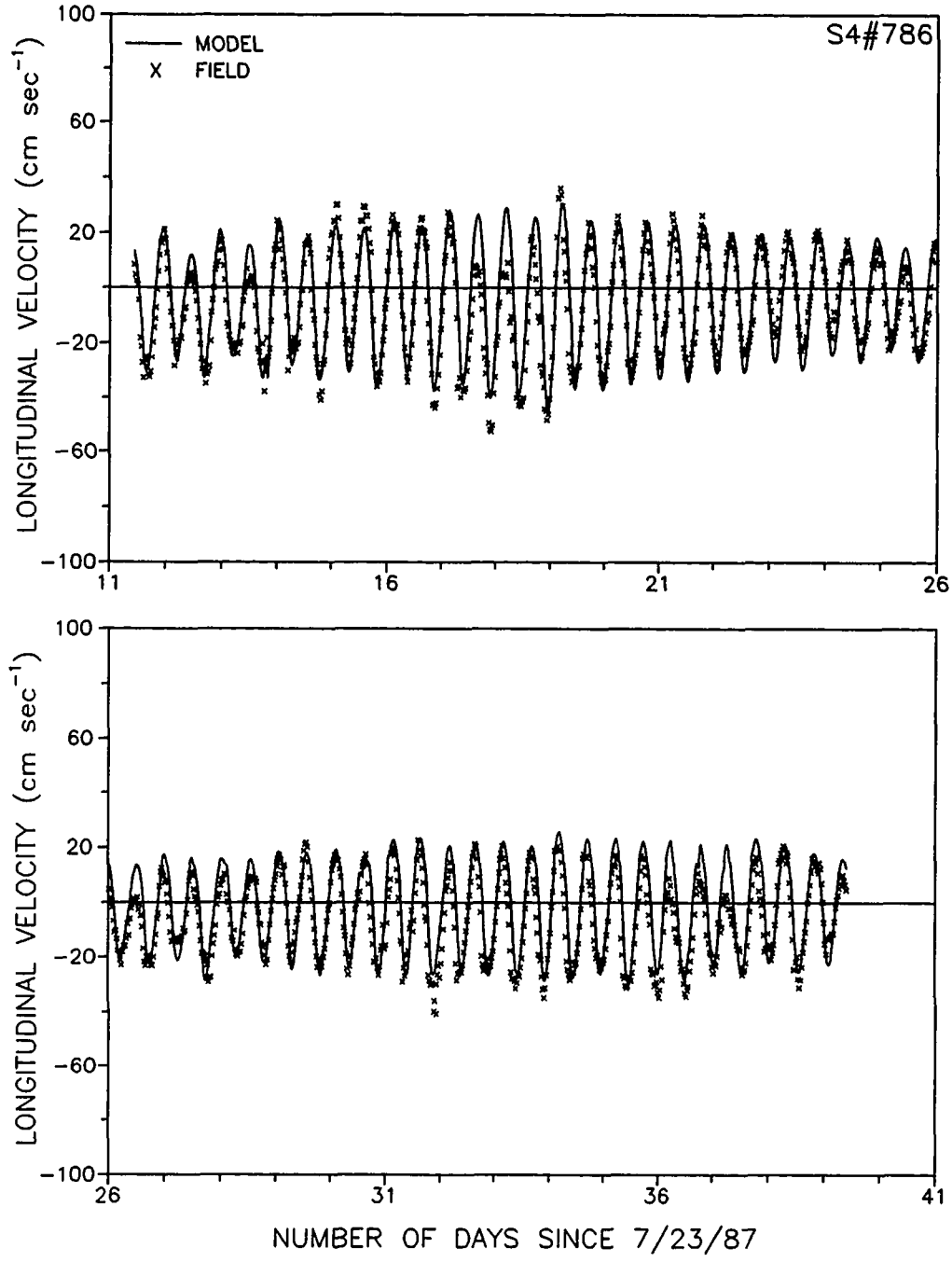

Figure 4-10. Current simulation at the mouth, depth 9.7 m.

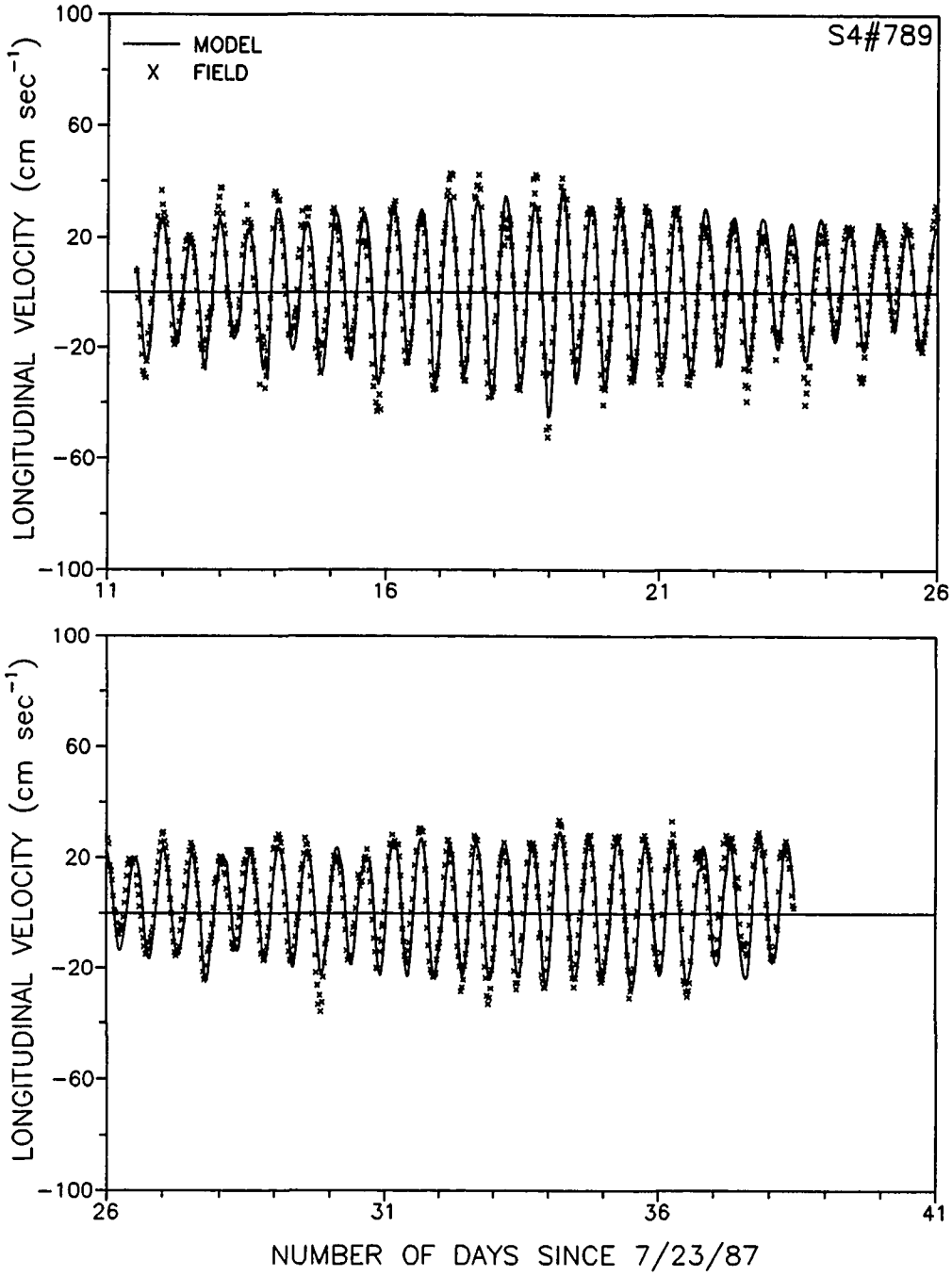

Figure 4-11. Current simulation at 16.6 km upriver from mouth, depth 1.2 m.

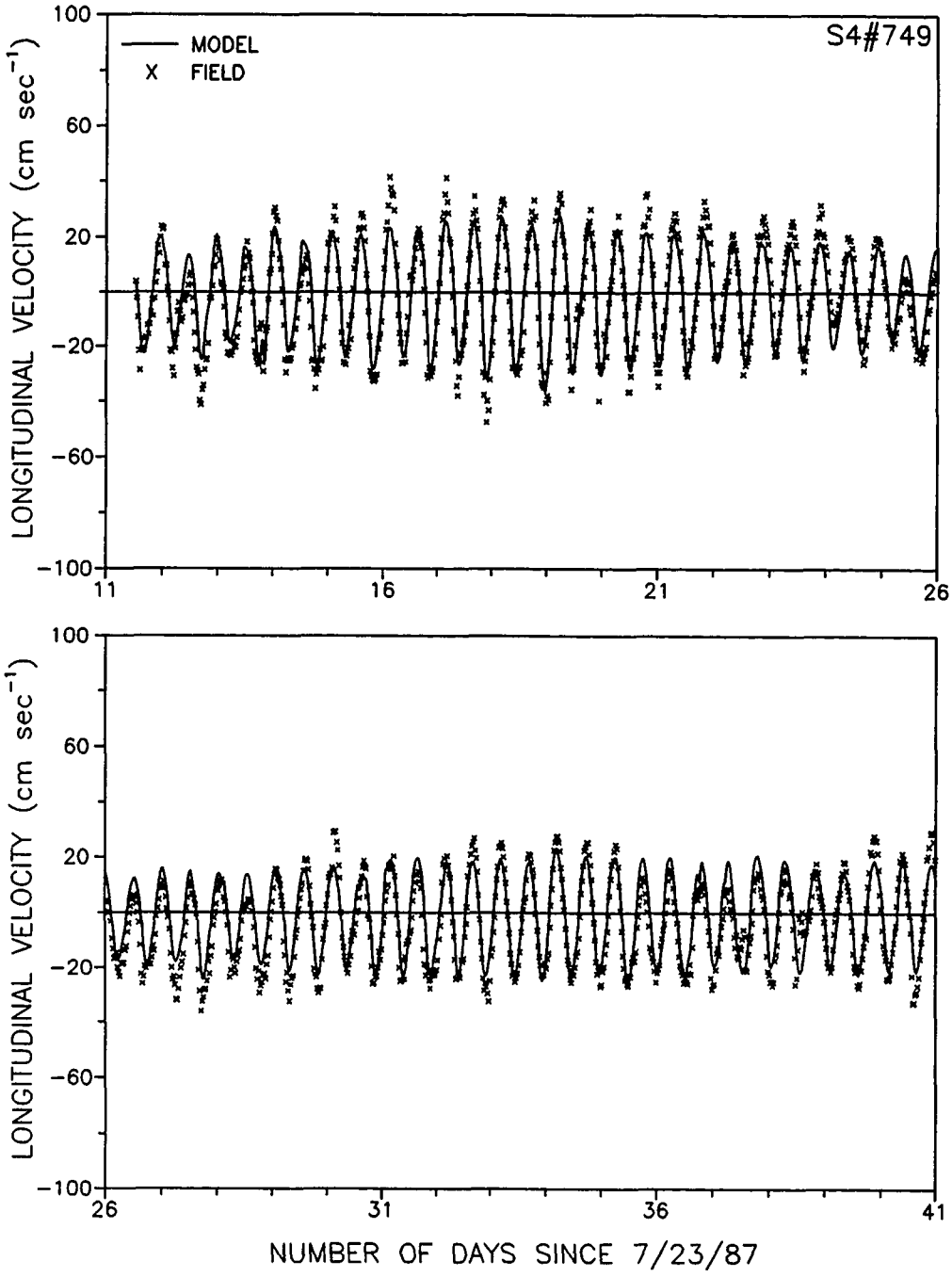

Figure 4-12. Current simulation at 16.6 km upriver from mouth, depth 10.0 m.

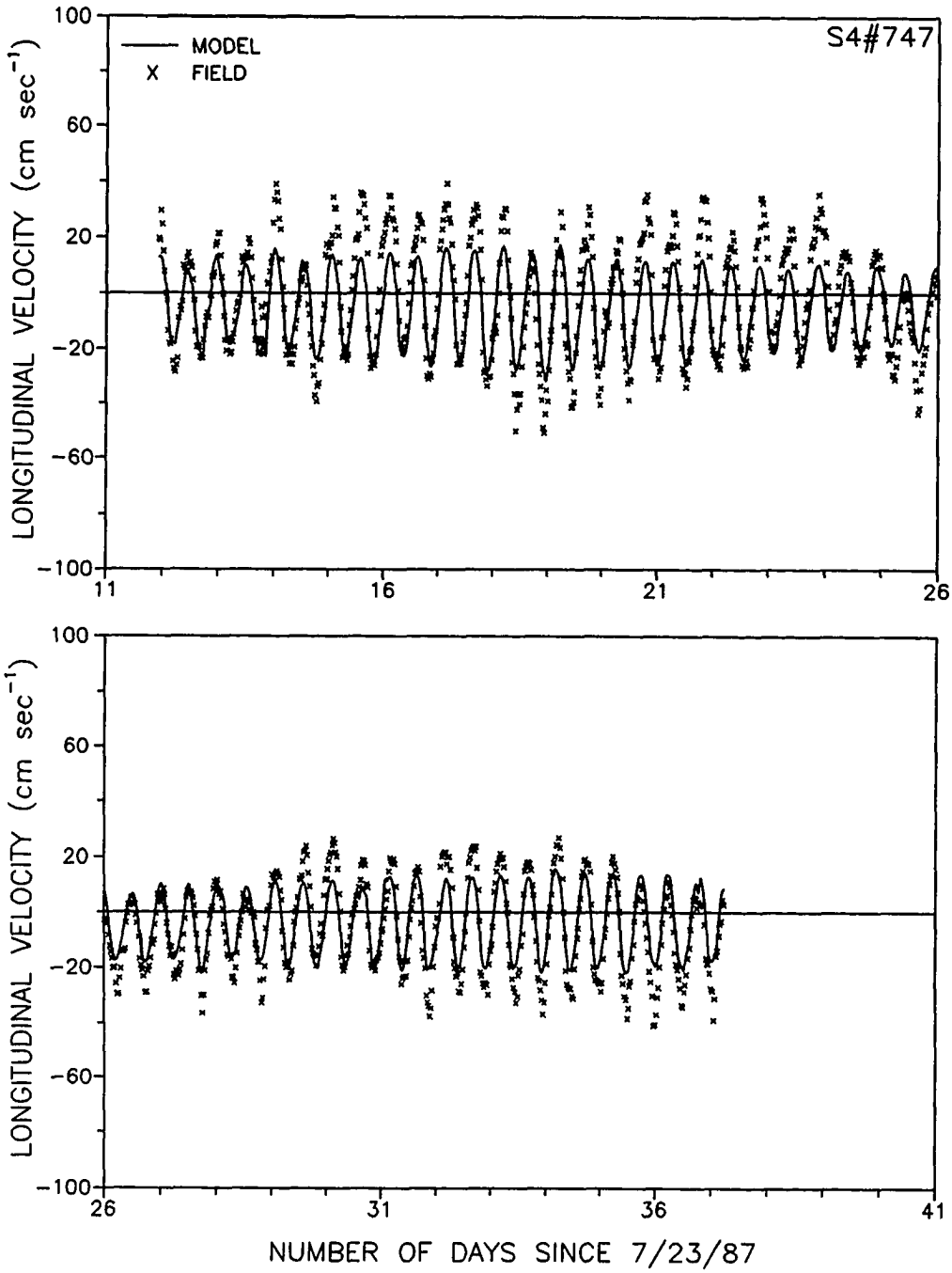

Figure 4-13. Current simulation at 16.6 km upriver from mouth, depth 18.7 m.

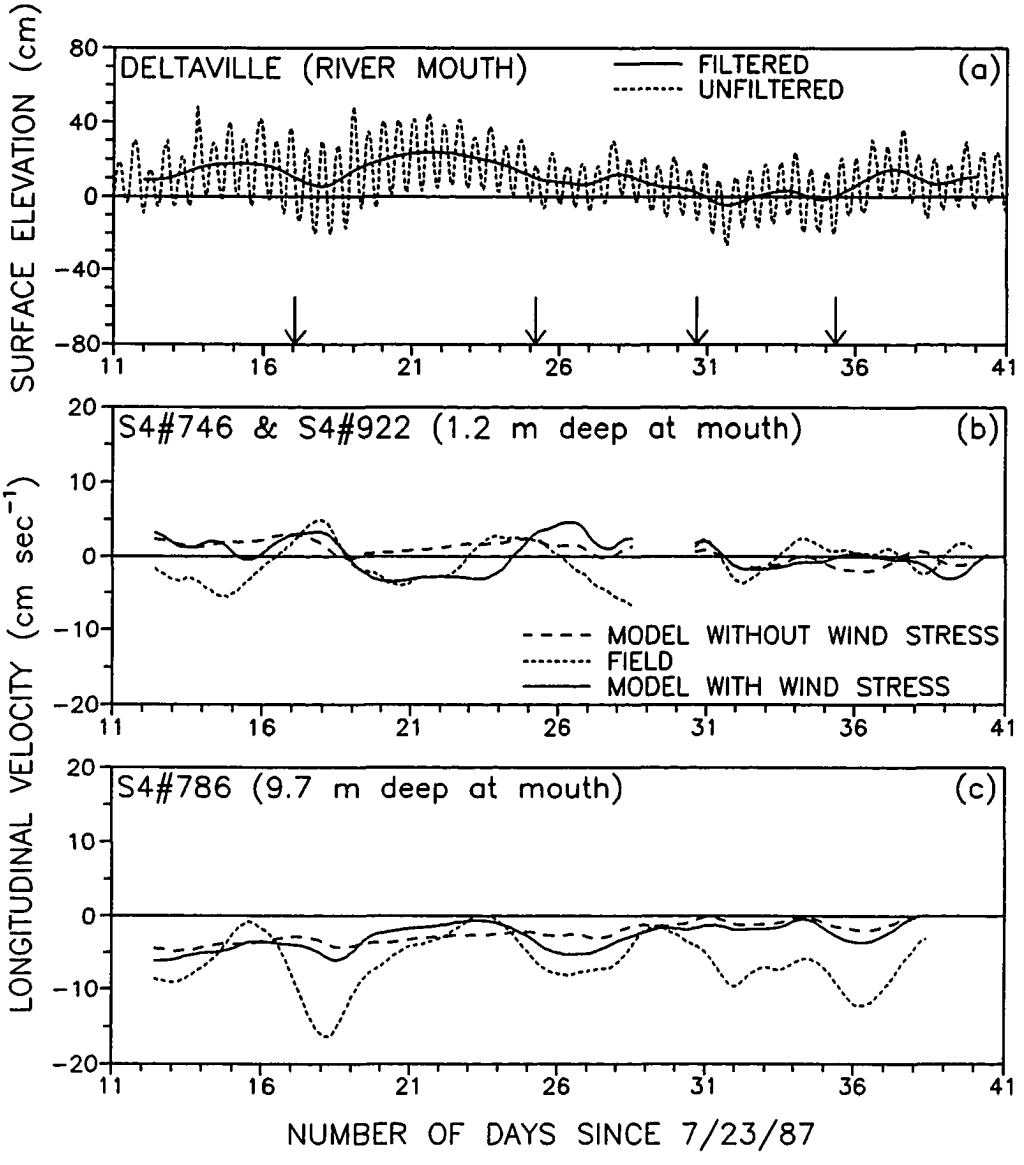

Figure 4-14. Surface elevation, both filtered and unfiltered, at river mouth (a), and subtidal variations in current velocity at river mouth (b-c) and at km 16.6 (d-f): arrows in (a) represent the events of strong southwest wind.

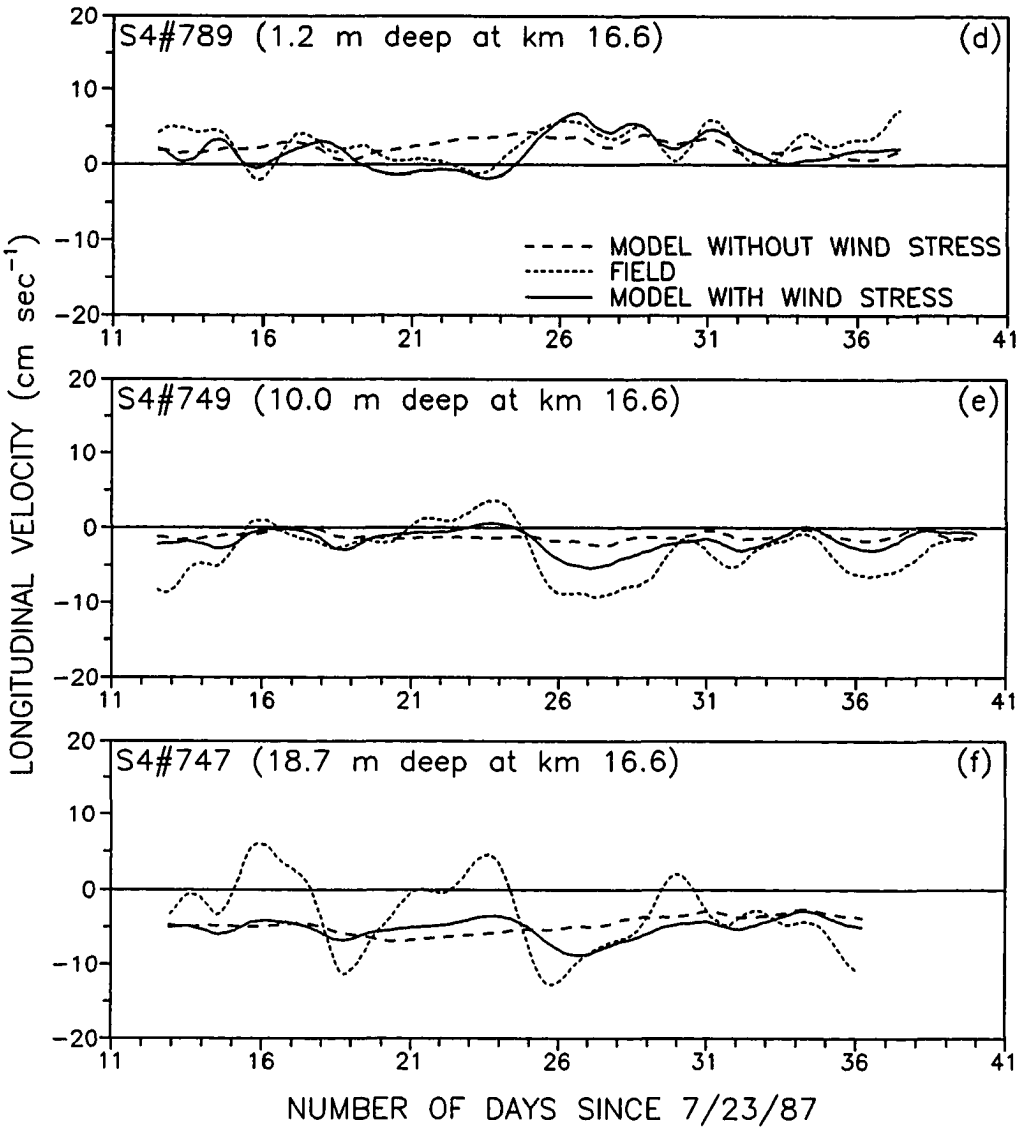

Figure 4-14. (continued).

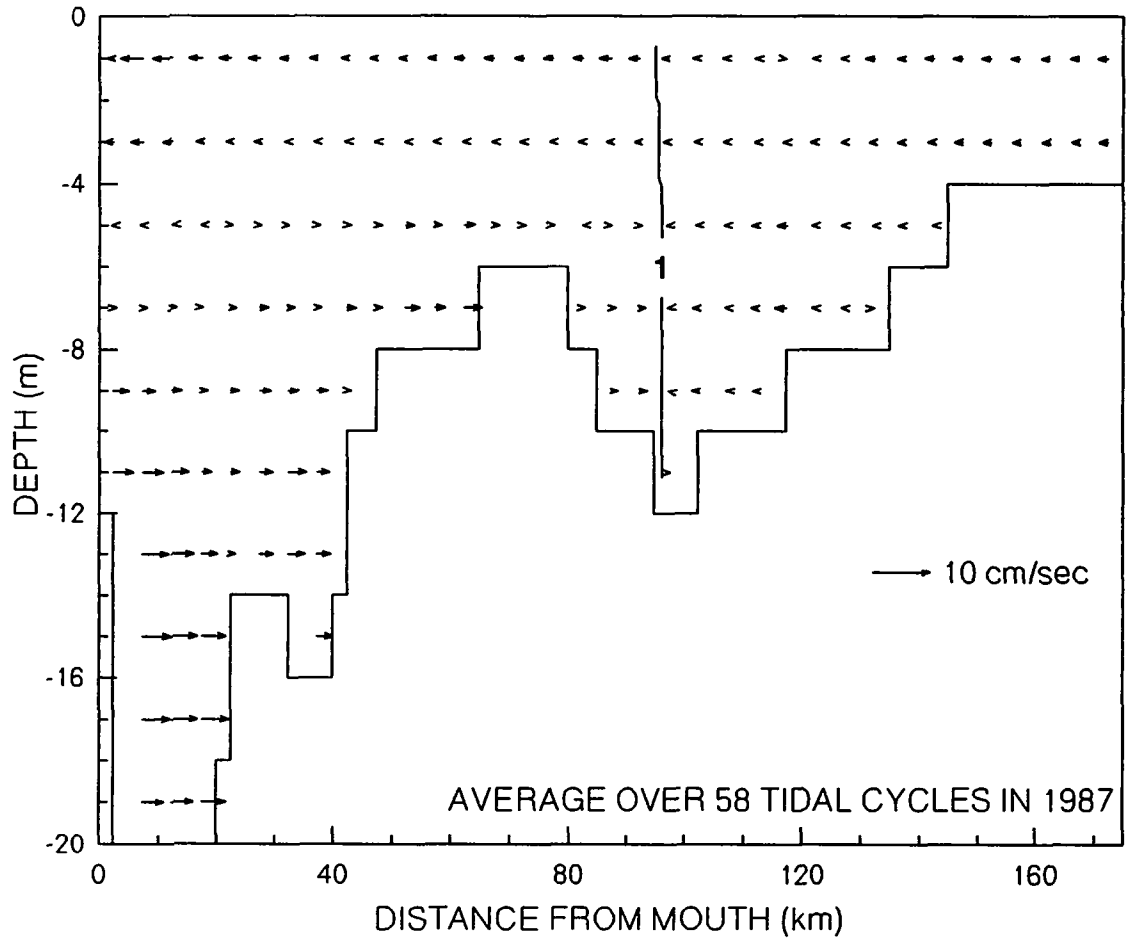

Figure 4-15. Model prediction of residual velocity over 2 spring-neap cycles from 7/29/87 to 8/25/87.

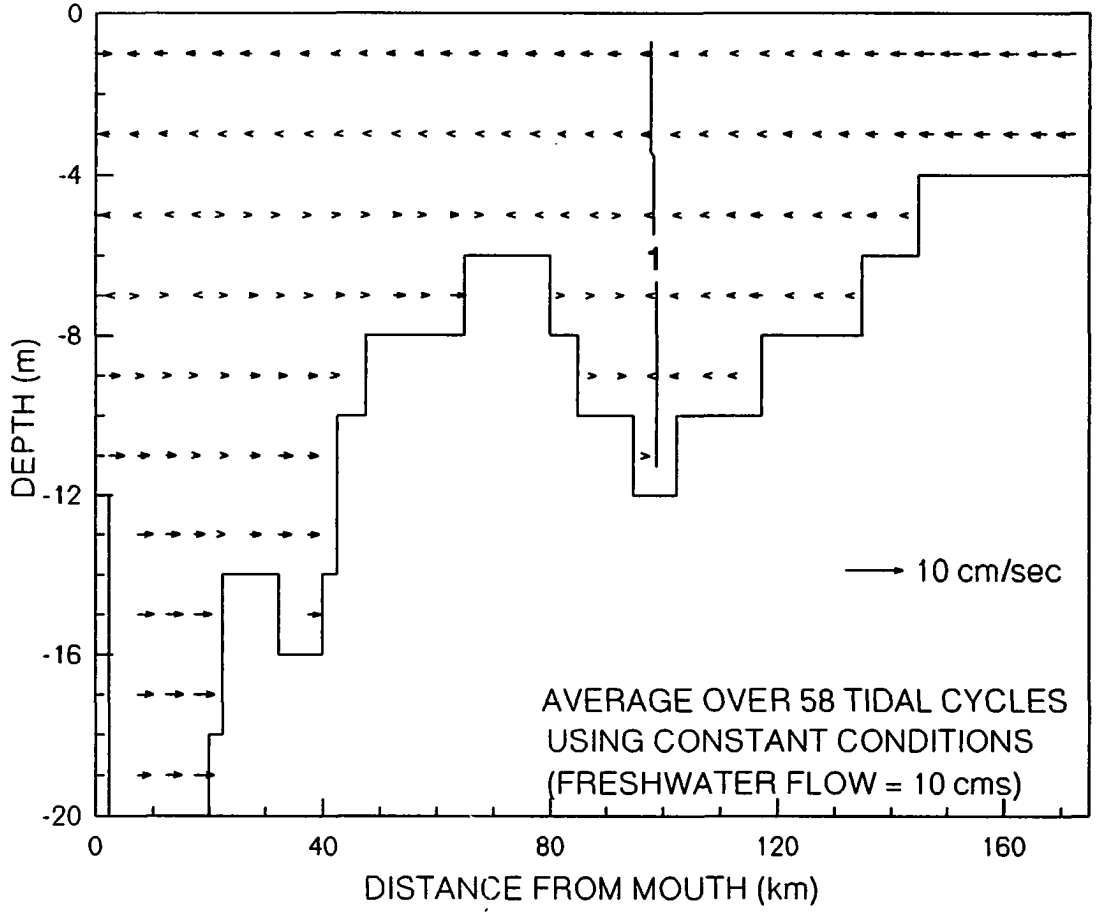

Figure 4-16. Model prediction of residual velocity over 2 spring-neap cycles with constant freshwater flow of 10 cms.

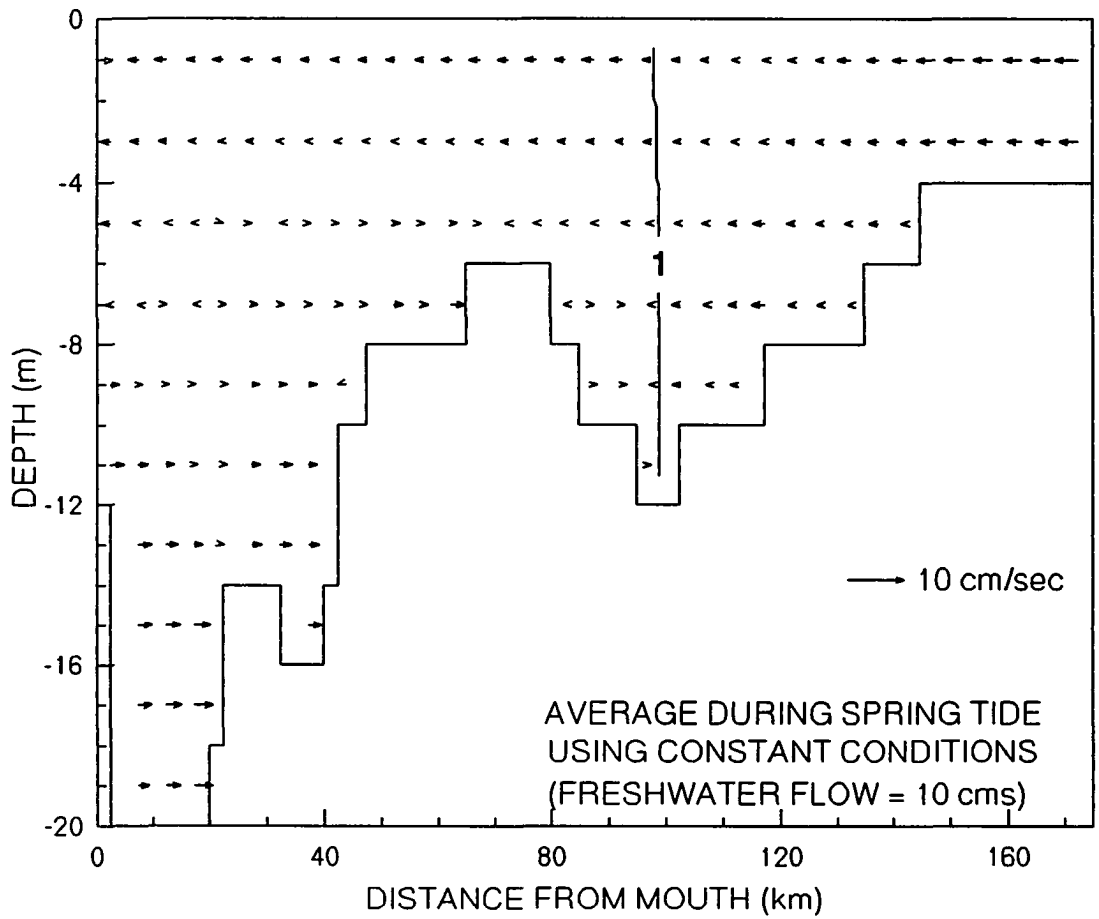

Figure 4-17. Model prediction of residual velocity during spring tide with constant freshwater flow of 10 cms.

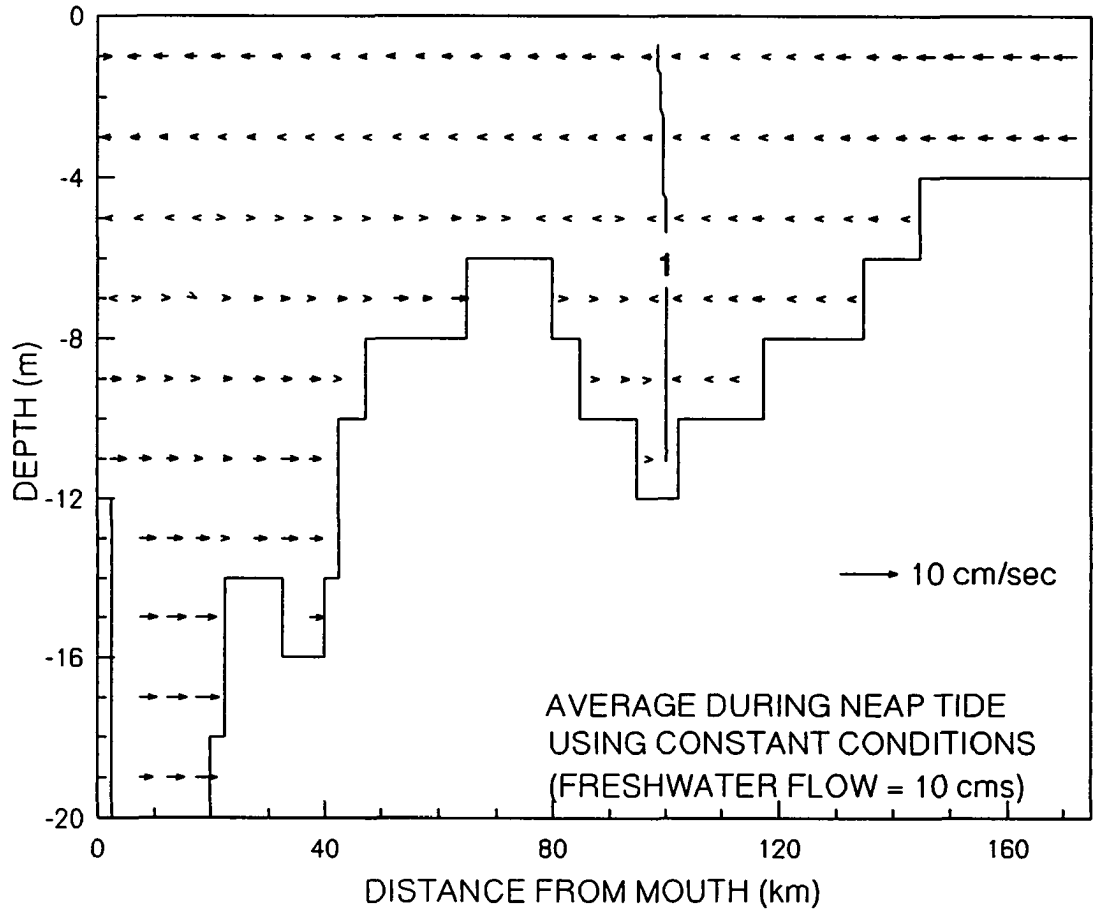

Figure 4-18. Model prediction of residual velocity during neap tide with constant freshwater flow of 10 cms.

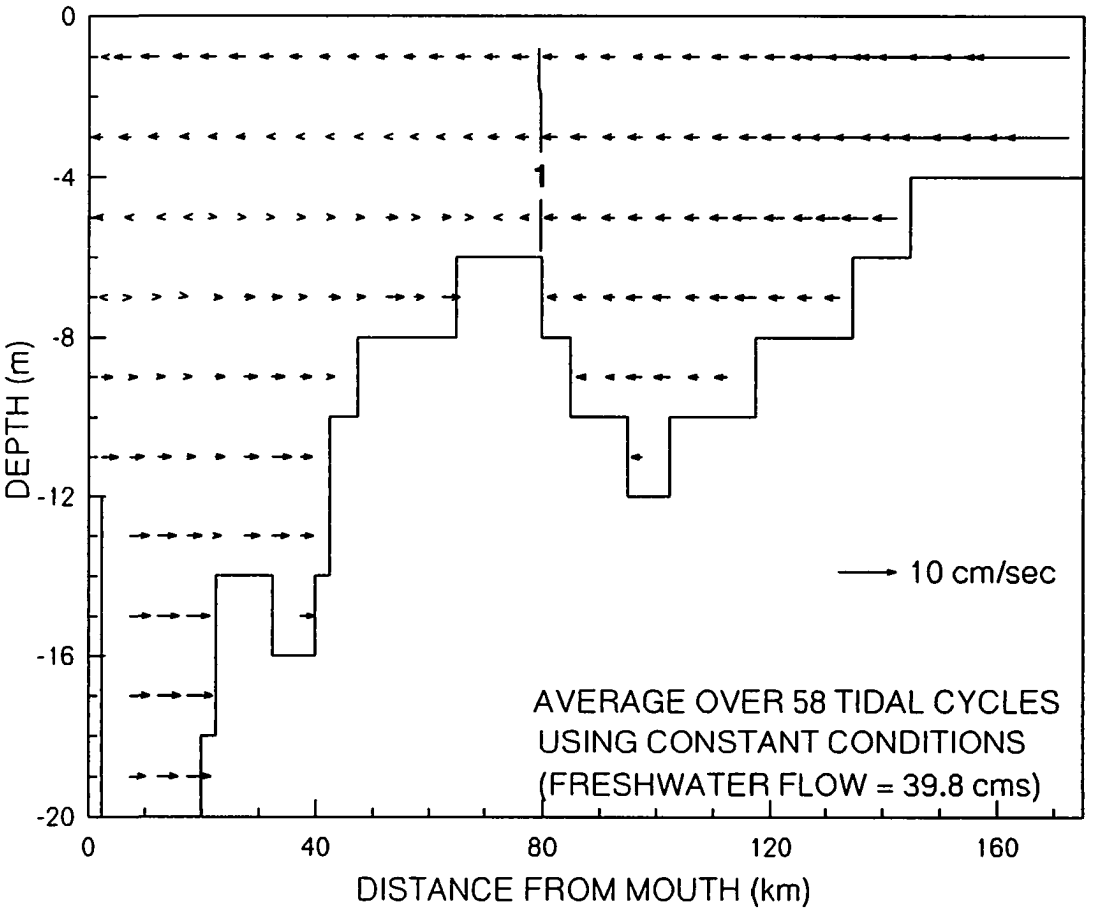

Figure 4-19. Model prediction of residual velocity over 2 spring-neap cycles with constant freshwater flow of 39.8 cms.

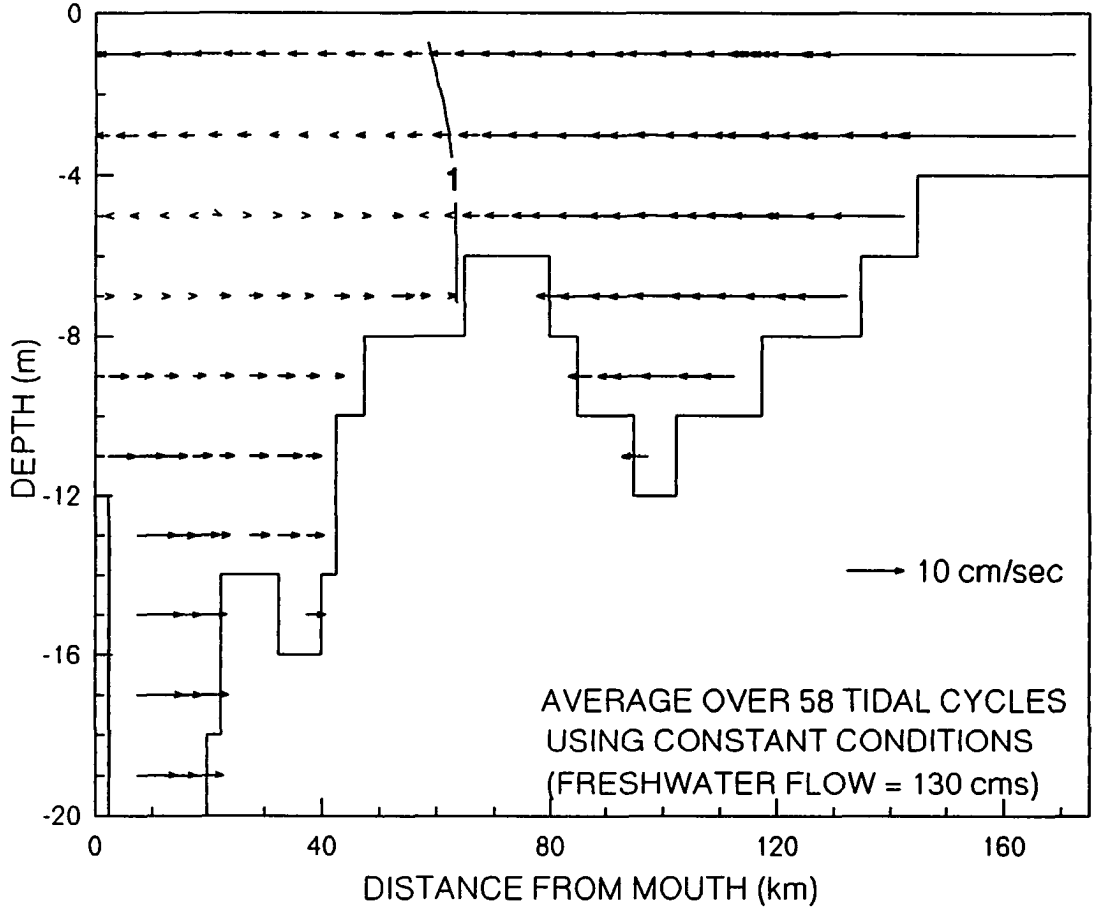

Figure 4-20. Model prediction of residual velocity over 2 spring-neap cycles with constant freshwater flow of 130 cms.

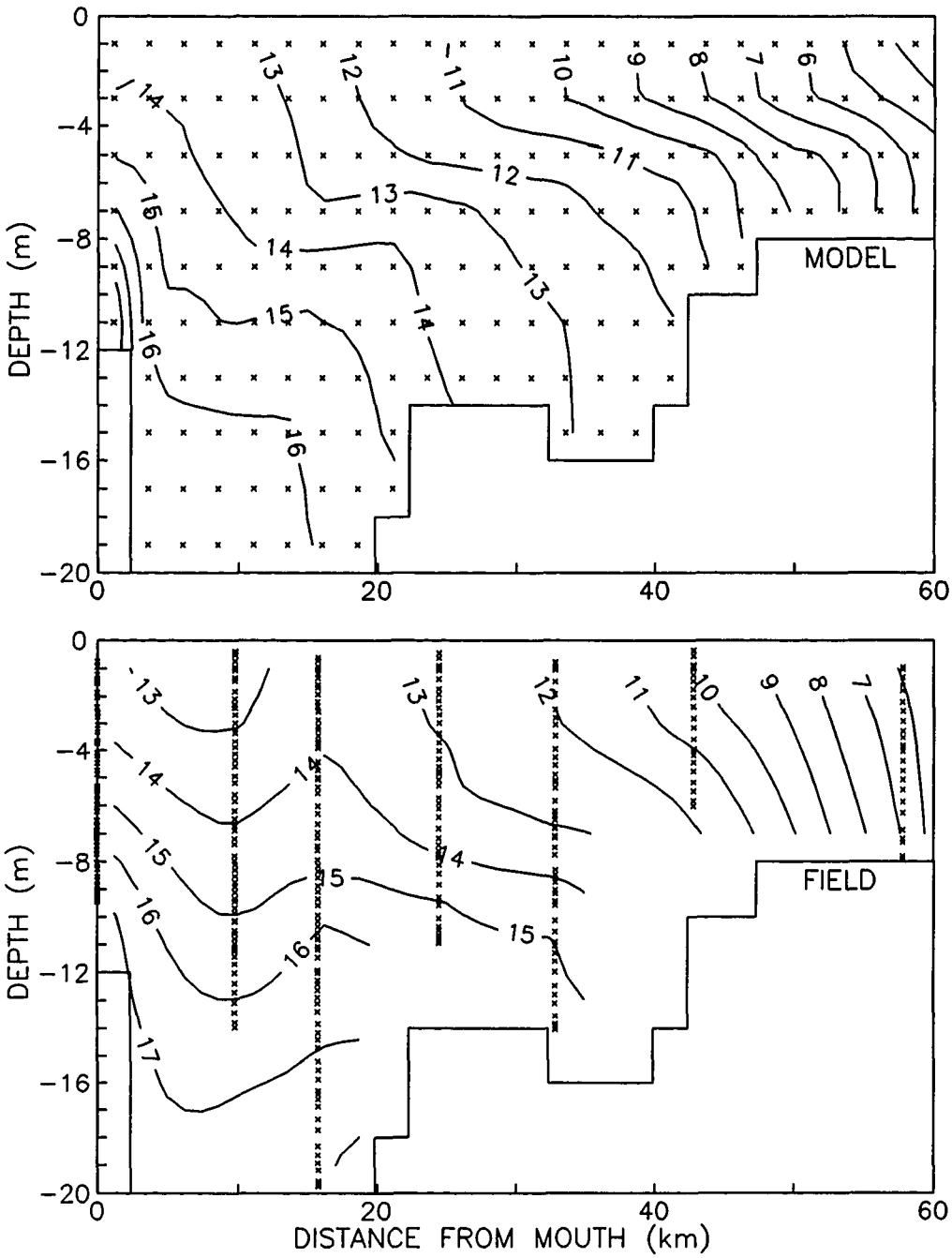

Figure 4-21. Model prediction and field measurement of salinity on 7/05/90: see text for the boundary condition used.

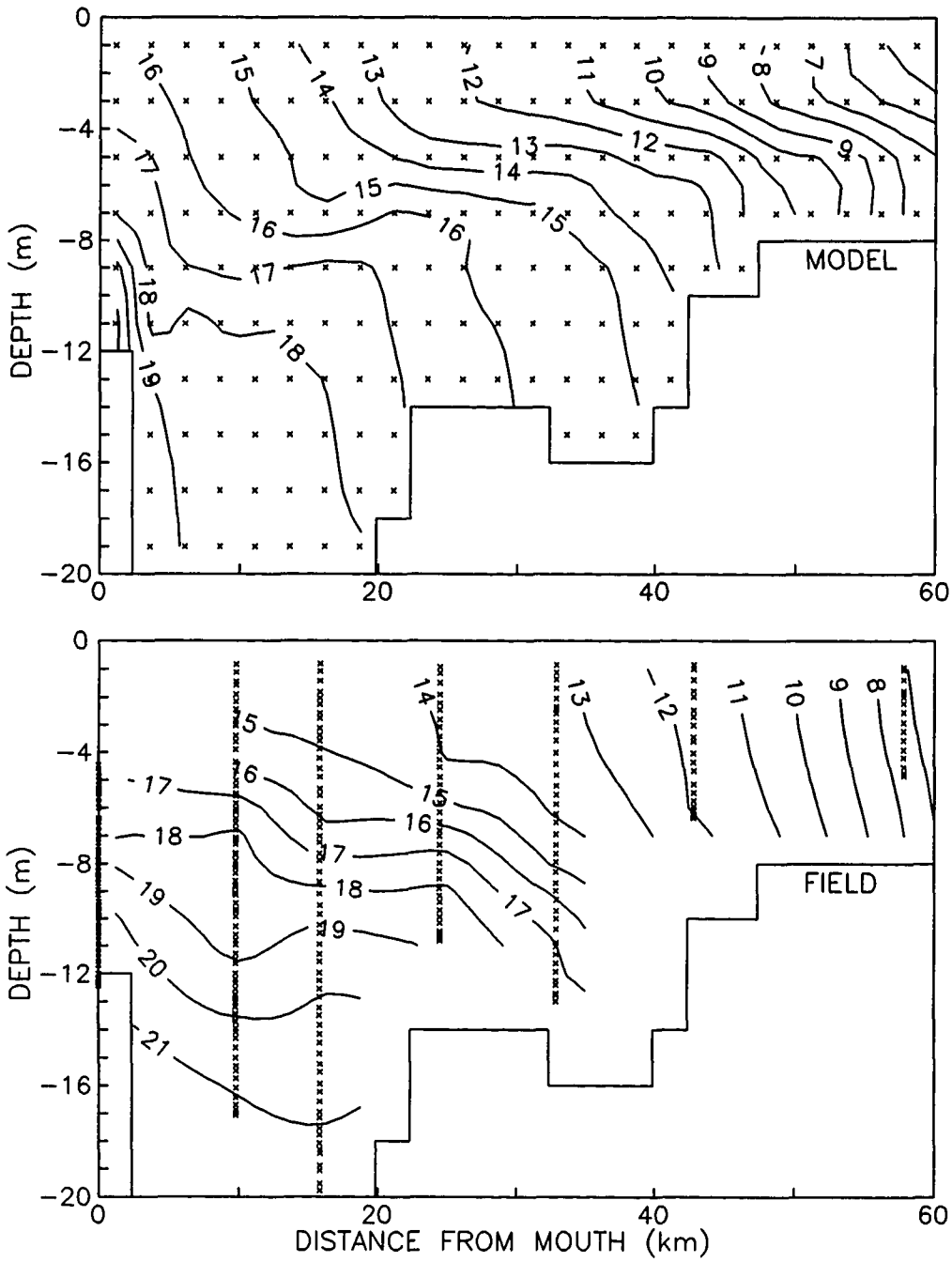

Figure 4-22. Model prediction and field measurement of salinity on 8/07/90: see text for the boundary condition used.

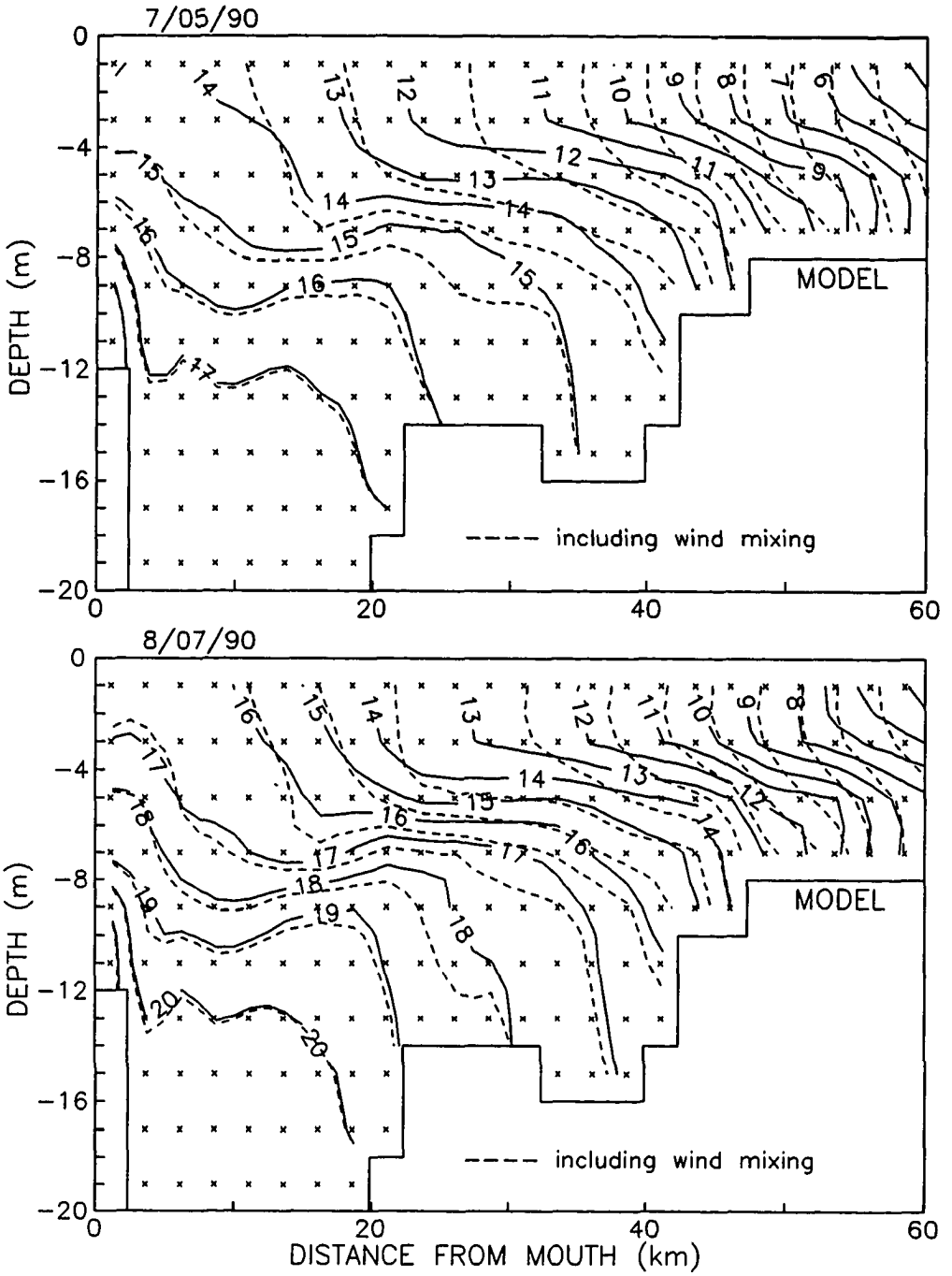

Figure 4-23. Model prediction of salinity using new boundary condition: see text for the condition used.

V. APPLICATION OF THE WATER QUALITY MODEL

The water quality model was applied to the tidal portion of the Rappahannock River. Emphasis was given to (1) the lower part of the river where hypoxia, or even anoxia, has persisted during summer in the bottom water and (2) the middle part of the river where characteristic chlorophyll maximum has been frequently observed. For each particular simulation run, appropriate input data must be determined. The water quality model is supplied with the information of the physical transport processes from the hydrodynamic model. The preparation of other input data related to the biochemical processes is discussed in Section 5-1. The water quality model was calibrated such that it reproduced the observed distributions of the water quality parameters on July 5, 1990 (Section 5-2). The model was then verified through comparisons of model predictions with two independently collected sets of field data in 1990 (Section 5-3). One is the data set from the August 7 slackwater survey by VIMS and the other is the data set on June 24, July 8 and August 5. The latter, hereafter referred to as the 'CBP data', was collected by the Virginia State Water Control Board (VSWCB) as a part of the Chesapeake Bay Fall Line and Tributary Water Quality Monitoring Program. Finally, quantitative assessments including scatterplot, the RMS error and the mean error are presented as a summary of model calibration and verification in Section 5-4.

5-1. Preparation of Input Data Set

Calibration and verification is far more difficult for the water quality model than

for the hydrodynamic model, due to the large number of predicted water quality parameters to be calibrated and verified: DO, chlorophyll 'a' (Chl), CBOD, organic nitrogen (N1), ammonia nitrogen (N2), nitrite-nitrate nitrogen (N3), organic phosphorus (P1) and inorganic phosphorus (P2). It also is due to the large number of biochemical coefficients to be determined in the calibration. For a given condition, more than one set of calibration coefficients may provide roughly equivalent results, which means too many degrees of freedom in determining the coefficients. One way of avoiding this situation is to minimize the number of coefficients to be determined through comparison of model results and field conditions. This can be achieved by providing as many coefficients as possible either with the direct field measurements or with the literature values.

The input data are grouped into three categories depending upon the sources: field measurements, literature values and calibration coefficients. The number of calibration coefficients that are evaluated in the calibration process was minimized through adherence to the following principles (Kuo et al. 1991b); 1) utilize field measurements whenever available, 2) utilize literature values when measurements are not available, and 3) utilize calibration values only when no other sources are available or when other sources are proven to be unsuitable.

Since the model predictions will change depending upon the selection of biochemical coefficients, the water quality model should employ consistent coefficient values for different simulation runs. That is, the coefficient values should be transferable for the model predictions to compare with independent sets of field observations. This must be so in the model, even though the biochemical coefficients need not be constant all the time in the prototype. Exceptions are field measurements such as light conditions, point source loadings, temperature, etc. This principle of consistency was observed wherever possible in the calibration and verification

processes. The trade-off was that the model predictions did not always agree with the field observations as closely as they might if the model was adjusted to each survey individually. Therefore, discrepancies of model predictions from field observations must be understood as illustrative of the variability of natural processes rather than indicative solely of shortcomings in the model.

5-1-1. Literature values

Literature values are those that have been evaluated in published studies of similar systems. For the present study, the primary sources for literature values are;

1) the studies in the Potomac Estuary (Thomann & Fitzpatrick 1982), after this referred to as the 'PEM Report',
2) the studies in the Virginia Potomac Embayments (e.g., Cerco & Kuo 1983), referred to as the 'VPE Reports',
3) the EPA report on model rates, constants and formulation (Bowie et al. 1985), referred to as the 'EPA Report',
4) the book on surface water quality modeling by Thomann & Mueller (1987), referred to as the 'T&M Book', and
5) the studies in the upper tidal Rappahannock River (Kuo et al. 1991b), referred to as the 'UTR Report'.

5-1-2. Field measurements

The field data collected by VIMS during summer of 1990 were used for the calibration and a part of verification of the water quality model. They include the environmental conditions such as water temperature, downstream boundary conditions, sediment oxygen demand (SOD), benthic fluxes and light intensity related parameters, and loadings including nonpoint and point source loads. The full

description of the field surveys and data are presented in Kuo et al. (1991b); the sampling locations are shown in Fig. 3-1.

A. Temperature: Slackwater survey data showed that daily average temperature was 21.1°C on June 6 and 26.9°C on July 5 and August 7. A constant water temperature of 26.5°C was used for the calibration and verification run, which covered the period from June 6 to August 7.

B. Downstream boundary conditions: Like salinity in Section 4-4-2, the water quality conditions at the mouth between the three slackwater surveys (June 6, July 5 and August 7) were linearly interpolated in time and used for the daily downstream boundary conditions for eight water quality parameters for both calibration and verification.

C. Nonpoint source loads: The nonpoint contribution from the watershed above the fall line was evaluated from freshwater discharge rates and concentrations of water quality parameters at the fall line. Daily discharge rates, those used for the hydrodynamic model, were obtained from USGS (1991). Results from a regression analysis were used for the concentrations of all nutrient forms (N1, N2, N3, P1 and P2). Daily input for the concentrations of Chl, CBOD and DO was obtained from the linear interpolation of monitoring data. The distributed nonpoint source loading below the fall line was estimated by assuming constant nonpoint source load per unit drainage area. The load per unit area was calculated using the load at the fall line.

D. Point source loads: During the sampling period, four sewage treatment plants (Claiborne Run, FMC, Fredericksburg and Massaponax STP's) discharged wastewater into the uppermost 10 km reach of the tidal river. The monitoring data from the STP's were linearly interpolated in time and used for the daily input of the point source loadings.

E. Benthic fluxes: Field measurements of SOD and benthic nutrient fluxes were

conducted for the upper portion of the river between km 130-170 (see Fig. 3-1). The SOD ranged from 0.78 to 2.14 g m^{-2} day^{-1}, and the N2 flux from 0.03 to 0.12 g m^{-2} day^{-1}. The benthic flux of N3 and P2 was nearly zero. No measurements were made for organic matter. Since the field measurements covered only the upper 40 km of the river, SOD and benthic fluxes were considered to be calibration parameters for the remaining part of the river. They were adjusted in the calibration, within the measured ranges for SOD and N2 benthic flux, especially over the region not surveyed. The estimated values were kept constant with respect to time for both calibration and verification.

F. Solar radiation and light extinction coefficient: Modeling of the growth of phytoplankton involves parameters related to the light intensity in Equations 2-32d through 2-32f; daily solar radiation (I_a), times of sunrise (t_u) and sunset (t_d), and light extinction coefficient (K_e). Daily inputs of I_a, t_u and t_d were obtained from the measurements at VIMS (Gloucester Point, VA). The light extinction coefficient as a measure of light attenuation in water is usually estimated using the secchi-depth (SD) measurement. The SD measurements in 1990 showed a good deal of scatter. The light extinction coefficients, which are derived using the assumed constancy of the product of SD and K_e, i.e., $SD \cdot K_e = 1.2$ and then corrected for self-shading of phytoplankton using Eq. 2-32e, are presented in Fig. 5-1.

Light in water is attenuated by two processes, absorption and scattering. Absorption refers to the attenuation due to the transformation of light into different forms of energy such as heat, and scattering refers to that due to the redirection of some of the light flux out of the main direction of travel (Tyler & Preisendorfer 1962). Effler (1985) recognized the variability in the product of SD and K_e for any system, and showed that the constancy of $SD \cdot K_e$ should be expected only when the relative contributions of absorption and scattering to K_e remain uniform. For

example, since scattering affects SD more than K_e, the transparency (SD) in the scattering-dominant system is low but the light attenuation (K_e) may not be as high as that estimated from a constant $SD \cdot K_e$. Besides, there are measurement errors, mostly associated with the measurement of SD, which is highly sensitive to the ambient conditions such as light and water surface roughness, and is somewhat observer dependent. Therefore, field studies concerned with phytoplankton productivity should include routine measurement of K_e (Effler 1985).

In the present study, the extinction coefficient was considered to be a calibration parameter. The coefficient was adjusted in the calibration, within the ranges estimated from SD measurements using the constancy of $SD \cdot K_e = 1.2$. Included in Fig. 5-1 are the values used for the model application, which were kept constant with respect to time in both calibration and verification.

5-2. Calibration

The water quality model was calibrated with a simulation of distributions of water quality parameters from June 6 to July 5, 1990. To allow a "warming-up" time for the physical parameters such as surface elevation and velocity, the model simulation started from June 4. The field data collected in the June 6 slackwater survey were then inserted into the model to specify the initial conditions, and the data from the July 5 slackwater survey were used for the calibration of the model. The range and mean over a day predicted by the model were compared with the observations collected on the same date.

The calibration was performed by adjusting the calibration parameters, most notably the biochemical rate constants described in Section 2-2 until agreement was achieved between the model results and the field data. Kuo et al. (1991b) studied water quality conditions using one-dimensional water quality model in the upper 60

km reach of the tidal Rappahannock River. The calibration values from this study in the 'UTR Report' generally served as starting point in model calibration. Since the way that these coefficients are obtained is as significant as the achievement of calibration itself, all model coefficients and their origins are presented before the calibration results.

5-2-1. Phytoplankton-related coefficients

The phytoplankton-related coefficients employed in the model calibration are listed in Table 5-1. The values in the 'VPE Reports' were adopted in this model application if all studies in the Virginia Potomac Embayments used the same values for those coefficients. For the temperature dependency of phytoplankton growth (θ_1), respiration (θ_2) and mortality (θ_3) rates, the 'T&M Book' provided definite values instead of ranges, and these values were used. The photosynthetic quotient (PQ) and respiration quotient (RQ) calculated from the data in the 'EPA Report' fall within very narrow ranges, and the mean values of these ranges were used. To conserve nitrogen and phosphorus within the system, 100% of phytoplankton consumed by zooplankton is assumed to be recycled within the system, i.e., $a_r = 1$. The other coefficients were either adopted from the 'PEM Report' or determined through calibration within the range of literature values.

5-2-2. Nitrogen-related coefficients

The nitrogen-related coefficients employed in the calibration are listed in Table 5-2. When coefficients had the same values in all the 'VPE Reports', those values were used. The values of other coefficients were determined either from the 'PEM Report' or through calibration within the range of literature values. Benthic flux measurements of N2 ranged from 0.03 to 0.12 g m^{-2} day^{-1} over the upper 40 km reach

of the river into which STP's discharge point source loads, mostly inorganic nutrients. In model calibration, a N2 benthic flux of 0.05 g m^{-2} day^{-1} between km 80-175 was needed to maintain the model predictions of Chl, N2 and total nitrogen as high as field measurements on July 5 (Figures 5-3 and 6-16).

5-2-3. Phosphorus-related coefficients

The phosphorus-related coefficients employed in the calibration are listed in Table 5-3. Two parameters, settling rate (K_{p22}) and benthic flux (BenP2) of inorganic phosphorus (P2), are of particular interest.

A settling rate of P2 higher than that of other parameters was required over the region upriver of km 147 to match the model results with field observations. The model simulation without settling resulted in P2 concentrations much higher than field observations in all survey data used. Since the STP discharges are the primary source of phosphate in the river, this implies that some of phosphate from STP discharges was lost (settled) before being transported out of this reach of the river. Several studies demonstrated a loss by adsorption of phosphate to sediment particles (Parfitt et al. 1975; Lake & MacIntyre 1977; Veith & Sposito 1977; Mayer & Gloss 1980). Experiments by Lake & MacIntyre (1977) showed that phosphate and tripolyphosphate were readily adsorbed to clay minerals and estuarine sediments.

In the tidal freshwater portion of the James and Potomac rivers, experiments using sediment cores indicated the existence of an equilibrium concentration of phosphate, which increases as DO decreases (Cerco 1985 and 1989). When the phosphate concentration in the water column is above the equilibrium concentration, the sediment takes up phosphate. When the phosphate concentration is below the equilibrium concentration, the sediment releases phosphate. When DO and P2 are higher than, respectively, 5.0 and 0.02 mg l^{-1}, almost all measurements in Cerco

(1989) showed sediment uptake of phosphate. In 1990, the P2 concentration was higher than 0.02 mg l^{-1} only near STP discharges (Figures 5-2 and 5-3). This loss mechanism was incorporated into the model by introducing high settling rate near the STP discharges. A similar treatment was needed in the studies of the Potomac Estuary (Thomann & Fitzpatrick 1982), the Virginia Potomac Embayments (Kuo 1985) and the upper tidal Rappahannock River (Kuo et al. 1991b).

Over the mid-reach of the river, the Chl concentrations frequently have been observed to be high. In model calibration, a P2 benthic flux of 0.005 g m^{-2} day^{-1} between km 80-147 was needed to maintain the model predictions of Chl, P2 and total phosphorus as high as field measurements on July 5 (Figures 5-3 and 6-15). This is further discussed in Section 6-2-2.

5-2-4. CBOD- and DO-related coefficients

The coefficients related to CBOD and DO employed in the model calibration are listed in Table 5-4. The SOD of 2.0 g m^{-2} day^{-1}, which is near the upper limit of the field measurements in the upper 40 km reach of the river (0.78 to 2.14 g m^{-2} day^{-1}), was used in model calibration. The coefficient K_{ro} = 12.9 for the English system of units in O'Connor & Dobbins (1958) was converted to K_{ro} = 393 for the CGS units. The definite values in the 'T&M Book' were used for the temperature dependency of CBOD decay rate (θ_8) and DO reaeration (θ_9).

5-2-5. Calibration results

The calibrated model results and field observations are shown in Figures 5-2 and 5-3, in which eight model parameters (DO, Chl, CBOD, N1, N2, N3, P1 and P2), total nitrogen and total phosphorus are presented. The daily averages of the model results presented as plots of isopleths in a vertical-longitudinal plane along the

river axis are compared with the values from field observations in Fig. 5-2. Another view of the calibration results presented in Fig. 5-3 compares the ranges and averages over a day from the model at the surface and bottom layers with the field data along the distance from the river mouth. The field data were measured at the surface, mid-depth and bottom, the depths of which are shown in Fig. 5-2. This study presents the total nitrogen and phosphorus, and their organic forms (N1 and P1) that include the portion in Chl, i.e., $a_n \cdot$Chl and $a_p \cdot$Chl, respectively, for nitrogen and phosphorus. To show the limit of salt intrusion as a reference, the tidal mean salinity distribution also is included in Figures 5-2 and 5-3.

Both figures show that generally good agreement was obtained between model results and field measurements. Discrepancies were often attributable to observance of the consistency principle between calibration and verification rather than to failure to curve-fit the model results to the field data. Some differences, however, did exist between the model results and the field measurements. The ranges of variations in the model results were generally smaller than those in the field data. This was because the model calculated the lateral average concentrations while the field data were point measurements, and also because of the random variability inherent to natural systems.

The model calibration run for Figures 5-2 and 5-3 included wind-driven reaeration using the expression (Eq. 2-39d) derived by Banks & Herrera (1977). The DO concentration when wind-driven reaeration was not included is presented in Fig. 5-4. To compare the model-field agreement with or without wind reaeration, two quantitative measures are used; the root-mean-square (RMS) error and the average. The RMS error, which is a measure of the absolute difference between predictions and observations, is defined as,

$$RMS = \sqrt{\frac{1}{n}\sum_{i=1}^{n}(P_i - O_i)^2} \quad (5\text{-}1)$$

where P_i is the i^{th} prediction (daily average), O_i is the i^{th} observation and n is the number of observations. The RMS error estimated using all data points is 0.90 and 1.01, respectively, with and without wind reaeration. Since the primary objective of this model is to study hypoxia, which occurs in the lower part of the river, the model-field agreement for DO in this part of the river is important. The RMS error at the surface between km 0-50, i.e., using 6 data points, is 0.84 and 1.42, respectively, with and without wind reaeration. At the surface between km 0-50, the average DO from the field data is 6.44 mg l^{-1}, and that from the model is 6.32 and 5.31 mg l^{-1}, respectively, with and without wind reaeration. Thus, the inclusion of wind-driven reaeration can improve the agreement between the model and the data by increasing the DO near the surface, most notably in the lower part of the river between km 0-50.

In the upper, freshwater portion of the river between km 90-175, which is mostly affected by the STP discharges, the total nitrogen from the model predictions was generally comparable to that from the field measurements except in the region between km 140-160 (Fig. 5-3). In this region (km 140-160), the model predictions of total nitrogen and N2 was lower than the field data although the model results for other forms of nitrogen (N1 and N3) agreed well with the field data. The same discrepancy was encountered in the one-dimensional modeling study of the upper tidal Rappahannock River (Kuo et al. 1991b). The STP discharges are the primary source of inorganic nutrients including ammonia, and four STP's discharged wastewater into the upper 10 km reach of the river. The monitoring data in 1990 showed that the N2 loading into the river from 4 STP's during one week before July 5 was approximately 80% of that during one week before August 7 (Kuo et al. 1991b). The Chl

concentration between km 140-160 was higher on July 5 (Fig. 5-3) than that on August 7 (Fig. 5-6), which suggests that algae should uptake more nutrients, including N2, for growth on July 5 than on August 7. Compared to the conditions on August 7, reduced input from STP's and greater uptake by algae on July 5 should lead to lower N2 concentration in this part of the river, which was shown in the model results but not in the field data. Therefore, it was suspected that there might be some errors in the measurements of either N2 concentration between km 140-160 or point source loadings of N2. With the higher point source loads of N2, the model predictions of N2 would increase and thus those of DO would decrease over this region improving the model-field agreement for DO as well as N2 (see Figures 5-2 and 5-3). No attempt, however, was made to modify the point source loadings for N2 for July 5 because the model capability of reproducing N2 and DO distributions in this region was proved in the model verification for August 7 (Figures 5-5 and 5-6).

Another thing to be noted in Figures 5-2 and 5-3 is the P2 between km 80-140, where the P2 predictions are slightly lower than the field data. A P2 benthic release of 0.005 g m^{-2} day^{-1} was used in model calibration (Table 5-3), and an increase in the P2 release could take care of the model-field discrepancy. Increasing the P2 release, however, made the P2 predictions in the verification for August 7 too high compared to the field data (see Figures 5-5 and 5-6). To observe the principle of consistency (Section 5-1), the P2 release of 0.005 g m^{-2} day^{-1} was used in the calibration and verification, leaving the P2 predictions in the calibration slightly lower than the field data. This is further discussed in Section 5-3-1.

5-3. Verification

The model was calibrated with one set of field data collected on July 5, 1990. This, however, does not guarantee that the validity of the model can be extended

beyond the data set used in the calibration process. Verification is to test the validity of the model against an independent set of field data. That is, verification tests the adequacy and consistency of the previously evaluated coefficients using a different set of field data collected independently of the calibration survey and under different ambient conditions.

In the present study, the model run for calibration was extended through August 7, 1990 without changing the coefficient values determined in calibration. The predictive capability of the model was tested through comparisons of model predictions with two independently collected data sets. One is the data from the August 7 slackwater survey by VIMS, and the other is the CBP data on June 24, July 8 and August 5. The range and mean over a day from the model were compared with the observations collected on the same date.

5-3-1. August 7 slackwater survey data by VIMS

The verification results for the August 7 data are presented in Figures 5-5 and 5-6 for eight model parameters, total nitrogen and total phosphorus. The daily averages of the model predictions presented as plots of isopleths in a vertical-longitudinal plane along the river axis are compared with the values from field observations in Fig. 5-5. Figure 5-6 has plots of the ranges and averages over a day from the model at the surface and bottom layers, along with the field data, against distance from the river mouth. To show the limit of salt intrusion, the tidal mean salinity distribution is included in Figures 5-5 and 5-6.

The model predictions of DO in Figures 5-5 and 5-6 include wind-driven reaeration, and DO distributions without including wind-driven reaeration are presented in Fig. 5-7. Again, the RMS error and average are used as quantitative measures for the difference in model-field agreement with or without wind reaeration.

The RMS error using all data points is 1.07 and 1.19, respectively, with and without wind reaeration. The RMS error at the surface between km 0-50, is 0.60 and 0.80, respectively, with and without wind reaeration. At the surface between km 0-50, the average DO from the field data is 5.71 mg l^{-1}, and that from the model is 6.04 and 4.97 mg l^{-1}, respectively, with and without wind reaeration. As in the calibration, the inclusion of wind-driven reaeration improves the model-field agreement for DO, most notably near the surface between km 0-50. The final calibrated model, therefore, includes the wind-driven reaeration of DO.

In Figures 5-5 and 5-6, the P2 predictions between km 70-95 on August 7 are higher than the field data, while the Chl predictions are lower than the data. The P2 predictions in this region on July 5 in model calibration are lower than the field data (Figures 5-2 and 5-3). Comparison of the conditions on July 5 (Fig. 5-3) with those on August 10 (Fig. 5-6) shows that the measured P2 concentrations at the surface were approximately the same (0.01 mg l^{-1}) in this region, as was the water residence time; three day average freshwater discharge was 15.0 cms from July 2 to 4 and 9.7 cms from August 4 to 6. However, total daily solar radiation (I_a) on July 5 was approximately twice that on August 7; three day average I_a was 671 langleys day^{-1} from July 3 to 5 and 373 langleys day^{-1} from August 5 to 7. The secchi-depth (SD) measurements in Fig. 5-1 show that the light extinction coefficient (K_e) used in this region between km 70-95 is larger than those estimated from the SD measurements on August 7, especially that at km 90. Thus, it seems to be the light availability (too high K_e or too low I_a) that makes the predictions of P2 higher than the data and those of Chl lower than the data on August 7. With more light available, the Chl may take up more P2 leading to higher Chl and lower P2 predictions. This is confirmed by the results in Fig. 5-8 from a model simulation in which K_e in the mid-part was lowered from 0.019 to 0.014 (average of two K_e values at km 74 and 90 in Fig. 5-1) cm^{-1}

from August 3 to 7.

Most of the CBP data for N2, N3 and P2 are below detection limits (see the following section). Therefore, the current calibration and verification of the water quality model for nutrients were conducted using two sets of slackwater survey data for July 5 and August 7 by VIMS. These data along with other conditions used in calibration and verification such as light availability (K_e and I_a) do not result in the consistent model predictions of P2 in the mid-reach of the river. This will restrict the scope of model application in performing the sensitivity analysis regarding nutrient limitation of the primary production. The present water quality model needs to be further calibrated with more thorough field data in order to conduct detailed study of nutrient limitation.

5-3-2. CBP data from VSWCB

The verification results for the CBP data are presented in Figures 5-9, 5-10 and 5-11, respectively, for June 24, July 8 and August 5. Since the CBP data were collected only at two depths for DO, Chl, P2, N2, N3 and total nitrogen, Figures 5-9 through 5-11 compare the ranges and averages over a day from the model at the surface and bottom layers with field data for these 6 parameters. It should be noted in Figures 5-9 through 5-11 that many measurements of N2 (63%), N3 (60%) and P2 (92%) are below the detection limits, which are 0.04 mg l^{-1} for N2 and N3, and 0.01 mg l^{-1} for P2 (Chesapeake Bay Program 1992). For comparison, the slackwater survey data collected by VIMS have the detection limit of 0.005 mg l^{-1} for N2 and N3, and 0.003 mg l^{-1} for P2.

5-4. Calibration and Verification Summary

The figures in the preceding sections provide a qualitative comparison of model

predictions and field observations. This traditional assessment of model accuracy, the perceived agreement between predictions and observations, depends upon the viewpoint and experience of the assessors. In order to render the evaluation of models less subjective, quantitative assessments of model accuracy are desirable. No single measure or set of measures is universally applicable for this purpose. The selection of appropriate measures is dependent upon the quantity and quality of the field data used and upon the nature of the model predictions. In the present study, scatterplot, the RMS error and the mean error are reported.

Scatterplots for point-by-point comparison of predictions and observations are presented in Fig. 5-12 for eight model parameters, total nitrogen and total phosphorus. A solid, diagonal line indicates the one-to-one correspondence. Magnitude of water quality parameters can range from zero (lower limit) to an unbounded value at the higher end. Because the scatterplot on a linear scale can be skewed by the presence of an unusually large value, all parameters except DO are plotted on a logarithmic scale.

Other measures included in Fig. 5-12 are the RMS and mean errors with n being the number of observations used to estimate them. The RMS error defined in Eq. 5-1 is a measure of the absolute difference between predictions and observations, and the RMS error of zero is ideal. Since the RMS error cannot discern the overprediction or underprediction, a second measure, the mean error, is desirable. The mean error (E) is defined as,

$$E = \frac{1}{n}\sum_{i=1}^{n}(P_i - O_i) \tag{5-2}$$

Positive E indicates that the model overpredicts the observations on the average and negative E indicates that the model underpredicts the observations on the average with zero E being ideal. Although the CBP data of N2, N3 and P2 from the VSWCB are

included in the scatterplots (Fig. 5-12), these were not used in estimating the RMS and mean errors because most of them are below the detection limits and model predictions are generally lower than the detection limits except near the STP discharges.

Table 5-1. Phytoplankton-related coefficients.

Coefficient	Equation	Value	Source[a]
a_c	2-38a	0.05 mg C per μg Chl	V
a_n	2-33a	0.007 mg N per μg Chl	II, V
a_p	2-36a	0.001 mg P per μg Chl	II, V
a_r	2-33a	1.0	Calibration
PQ	2-39a	1.0 moles O_2 per mole C	III, V
RQ	2-39a	1.33 moles CO_2 per mole O_2	III, V
K_{mn}	2-32g	0.025 mg l^{-1}	I, II, III, V
K_{mp}	2-32g	0.001 mg l^{-1}	I, II, III, V
k_{gr}	2-32c	2.0 day^{-1}	I, V
θ_1	2-32c	1.066	IV, V
I_s	2-32d	250 langleys day^{-1}	II, V
$K_{e,Chl}$	2-32e	0.00018 l μg^{-1} cm^{-1}	II, V
K_{Chl}	2-32b	10.0 cm day^{-1}	I, V
R(20)	2-32h	0.17 day^{-1}	V
θ_2	2-32h	1.08	IV, V
P(20)	2-32i	0.02 day^{-1}	I, V
θ_3	2-32i	1.0	IV, V

[a] I = PEM Report (Thomann & Fitzpatrick 1982)
II = VPE Reports (e.g., Cerco & Kuo 1983)
III = EPA Report (Bowie et al. 1985)
IV = T&M Book (Thomann & Mueller 1987)
V = UTR Report (Kuo et al. 1991b).

Table 5-2. Nitrogen-related coefficients.

Coefficient	Equation	Value	Source[a]
$K_{n12}(20)$	2-33a	0.04 mg l^{-1} day^{-1}	I/Calibration
θ_4	2-33a	1.04	II, V
K_{h12}	2-33a	1.0 mg l^{-1}	II, V
K_{n11}	2-33b	8.0 cm day^{-1}	Calibration
$K_{n23}(20)$	2-34a	0.3 mg l^{-1} day^{-1}	Calibration
θ_5	2-34a	1.04	II, V
K_{h23}	2-34a	1.0 mg l^{-1}	II, V
K_{nit}	2-34a	2.0 mg l^{-1}	I
$K_{n33}(20)$	2-35b	0.35 day^{-1}	Calibration
θ_6	2-35b	1.045	I
K_{h33}	2-35b	0.5 mg l^{-1}	Calibration
F_n	2-33a	0.75	II, V
BenN1	2-33b	0.0 g m^{-2} day^{-1}	V
BenN2[b]	2-34b	0.0 - 0.05 g m^{-2} day^{-1}	Field Data/Calibration
BenN3	2-35b	0.0 g m^{-2} day^{-1}	V

[a] see Table 5-1.

[b] 0.05 g m^{-2} day^{-1} upriver of km 80, and 0.0 elsewhere.

Table 5-3. Phosphorus-related coefficients.

Coefficient	Equation	Value	Source[a]
$K_{p12}(20)$	2-36a	0.06 mg l^{-1} day^{-1}	V
θ_7	2-36a	1.04	II, V
K_{hp12}	2-36a	1.0 mg l^{-1}	II, V
K_{p11}	2-36b	10.0 cm day^{-1}	V
F_p	2-36a	0.55	Calibration
K_{p22}[b]	2-37b	0.0 - 20.0 cm day^{-1}	Calibration
BenP1	2-36b	0.0 g m^{-2} day^{-1}	V
BenP2[c]	2-37b	0.0 - 0.005 g m^{-2} day^{-1}	Calibration

[a] see Table 5-1.

[b] 20.0 cm day^{-1} upriver of km 147, and 0.0 elsewhere.

[c] 0.005 g m^{-2} day^{-1} between km 80-147, and 0.0 elsewhere

Table 5-4. CBOD- and DO-related coefficients.

Coefficient	Equation	Value	Source[a]
$K_c(20)$	2-38a	0.1 day^{-1}	III, IV
θ_8	2-38a	1.047	I, IV
K_{DO}	2-38b	0.5 mg l^{-1}	Calibration
SOD	2-39b	2.0 g m^{-2} day^{-1}	Field Data/Calibration
K_{ro}	2-39c	393	see text
θ_9	2-39e	1.024	IV

[a] see Table 5-1.

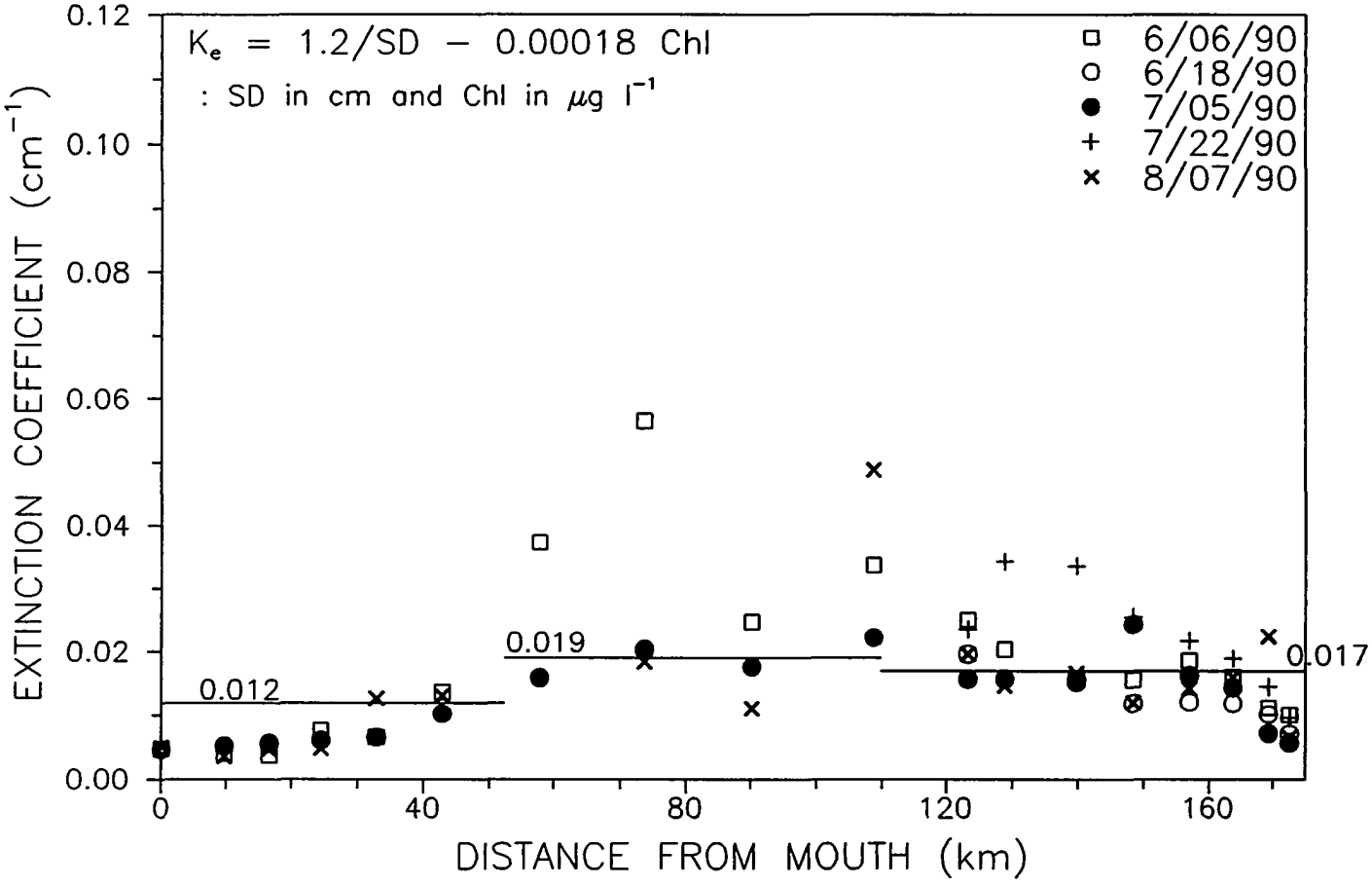

Figure 5-1. Light extinction coefficients: the horizontal lines represent the values used in model calibration and verification.

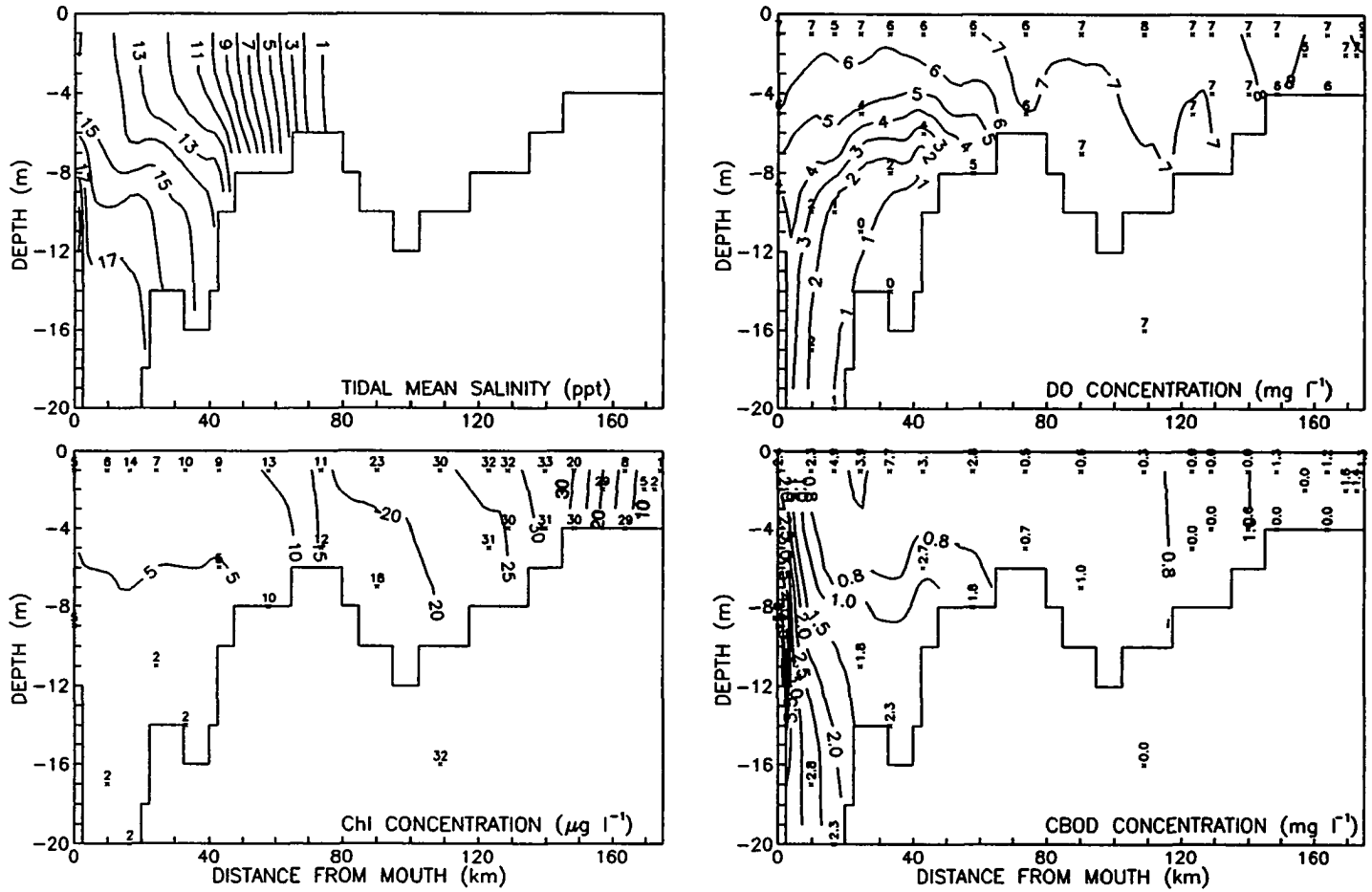

Figure 5-2. Model calibration results and tidal mean salinity on 7/05/90: the isoconcentration contours are model results and the point values are field data.

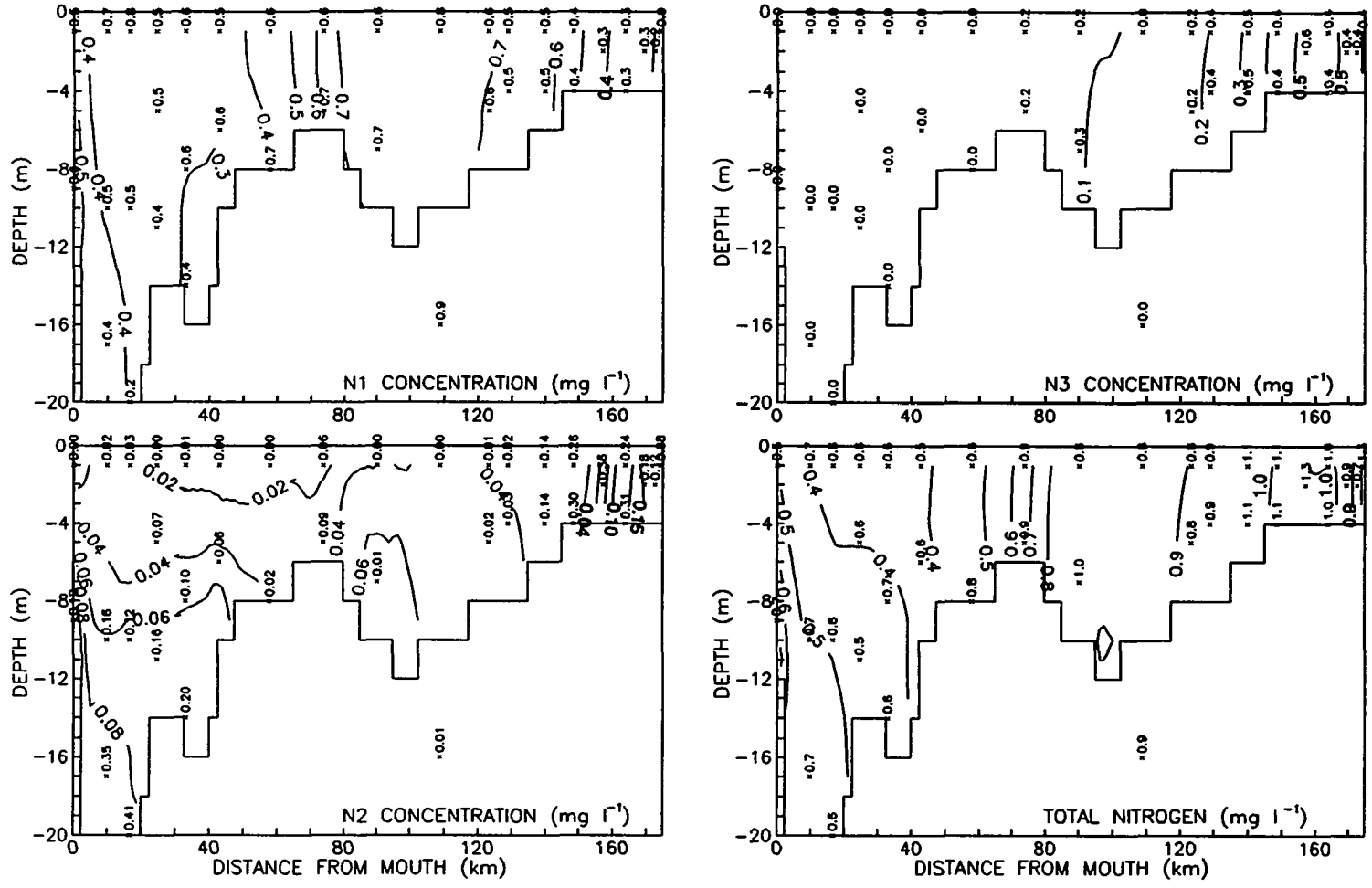

Figure 5-2. (continued).

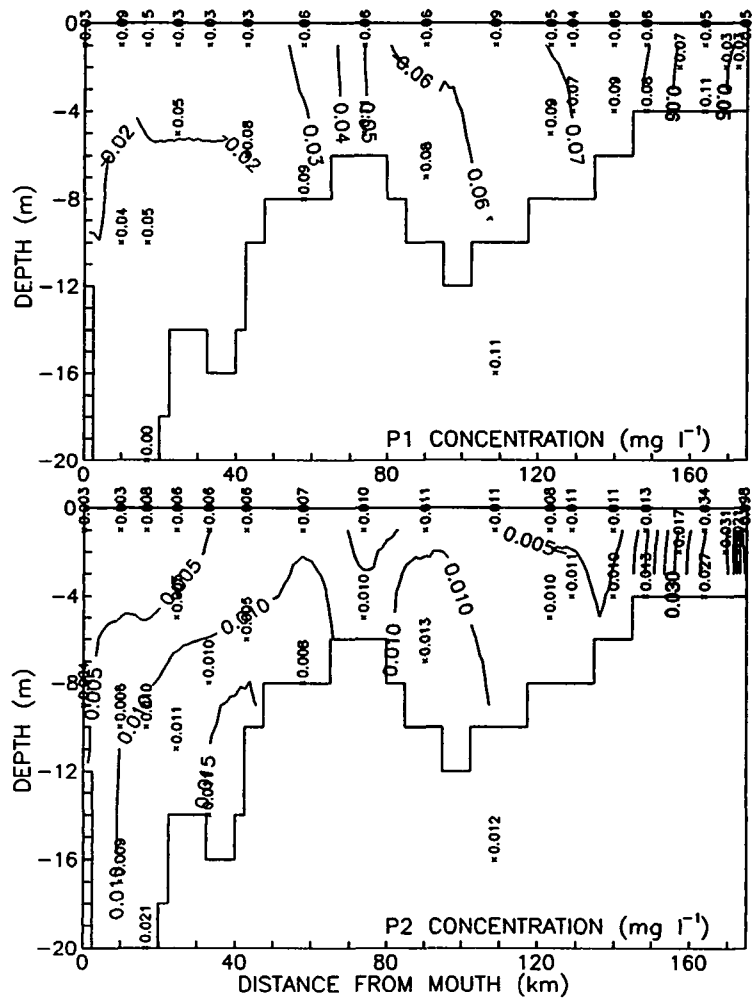

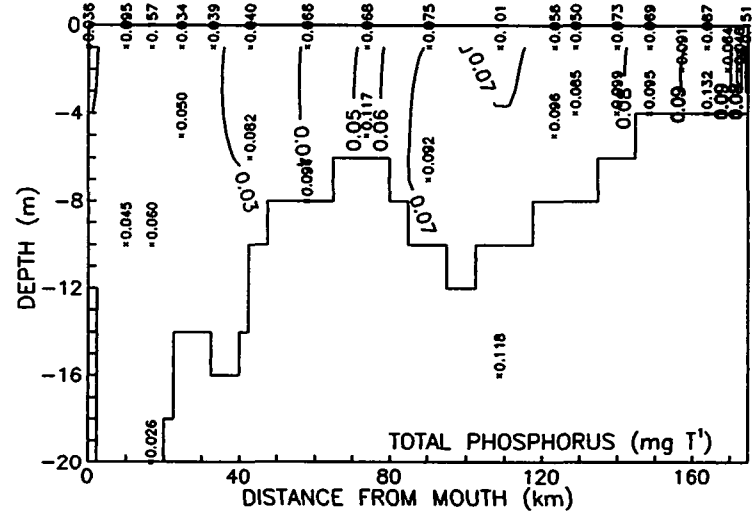

Figure 5-2. (continued).

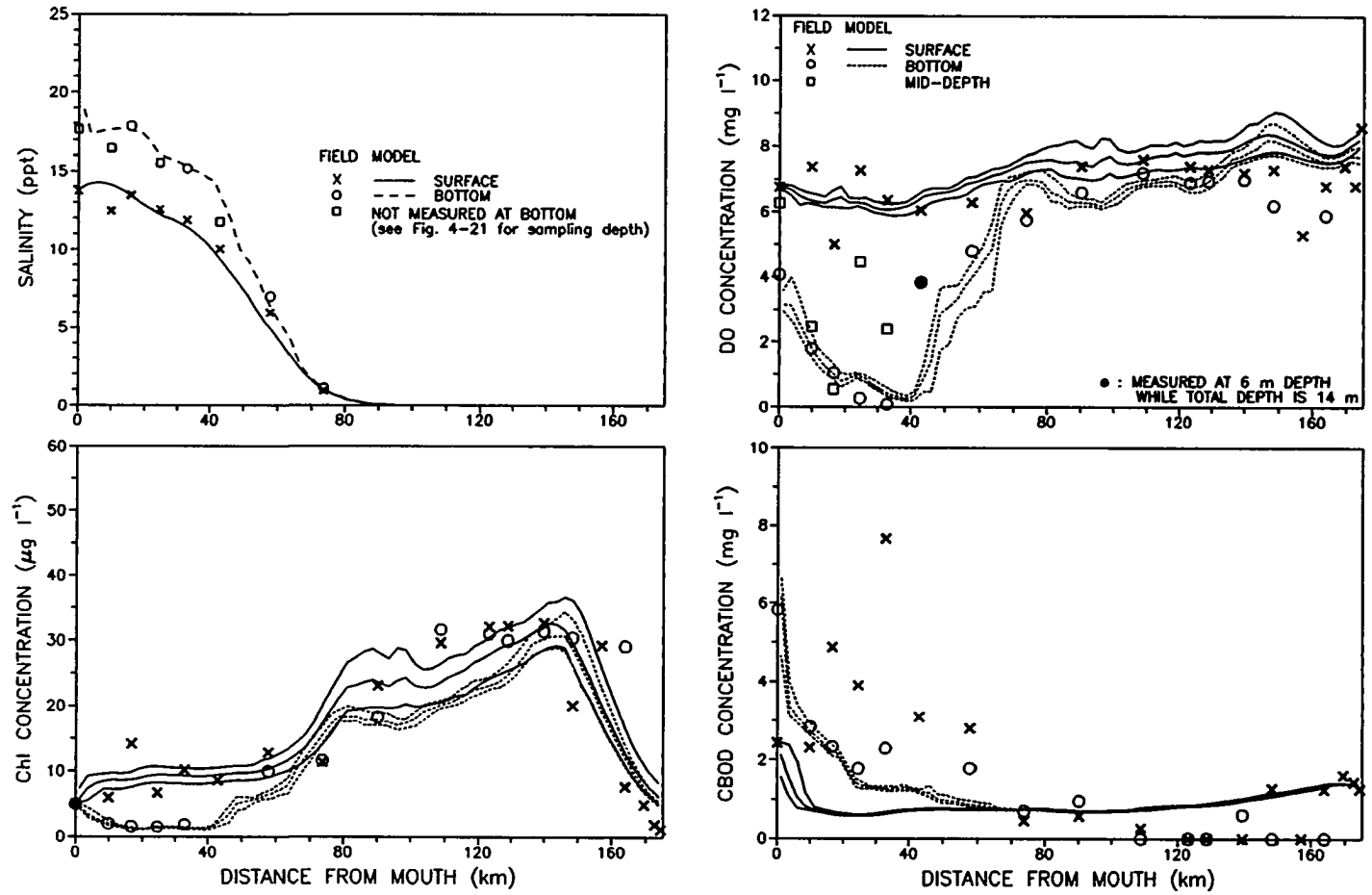

Figure 5-3. Model calibration results (daily mean, maximum and minimum) and tidal mean salinity at surface and bottom on 7/5/90.

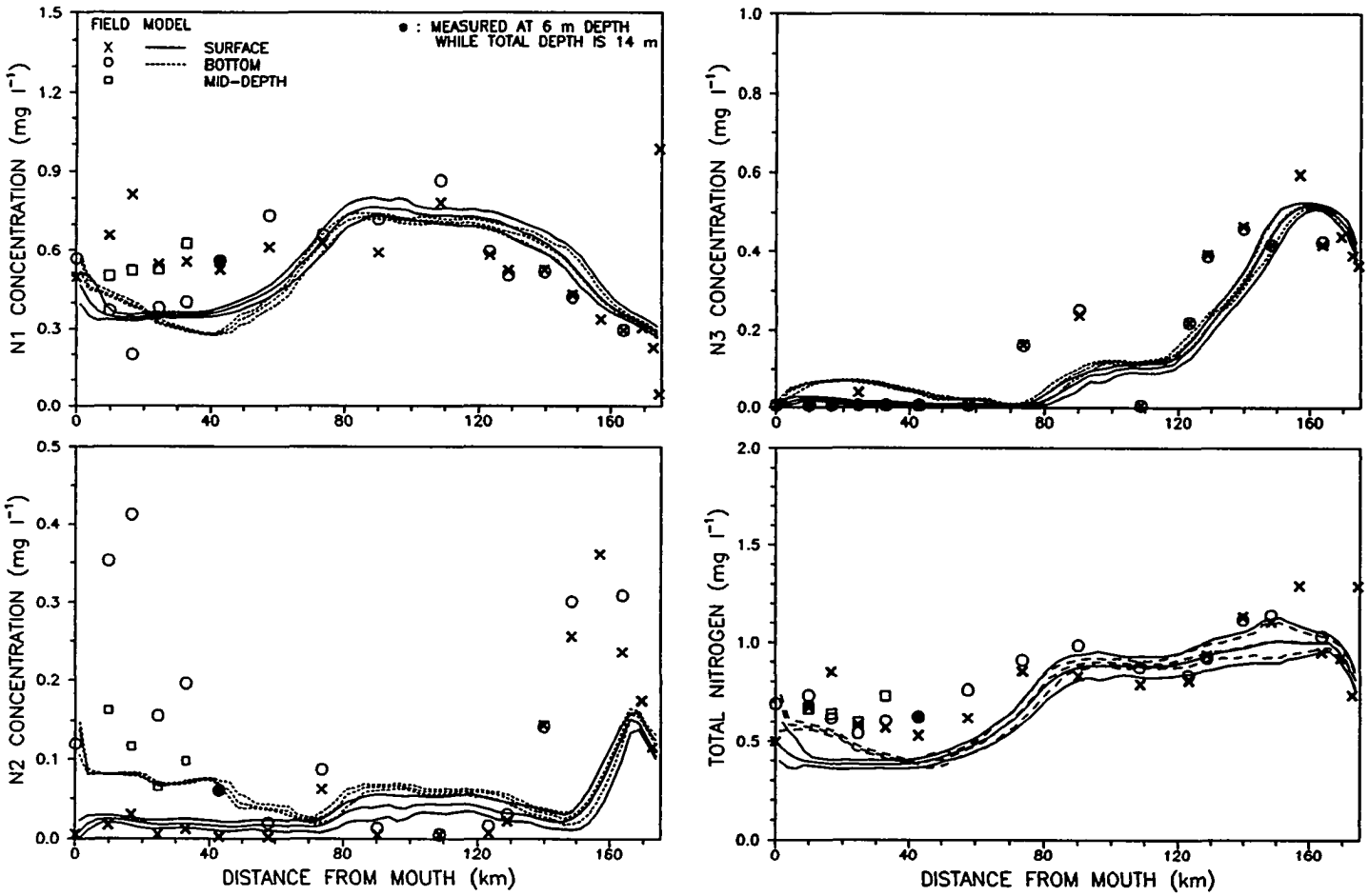

Figure 5-3. (continued).

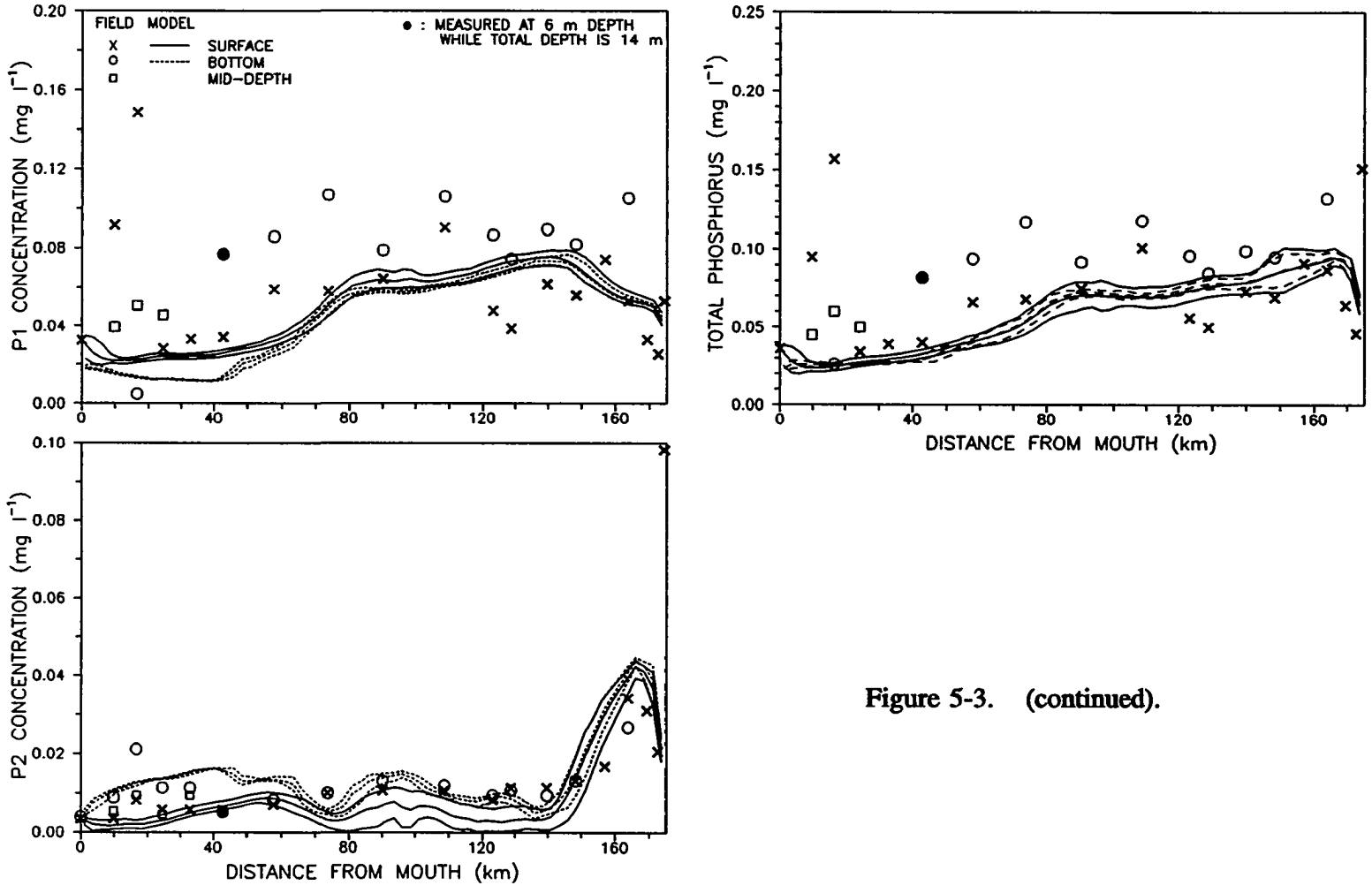

Figure 5-3. (continued).

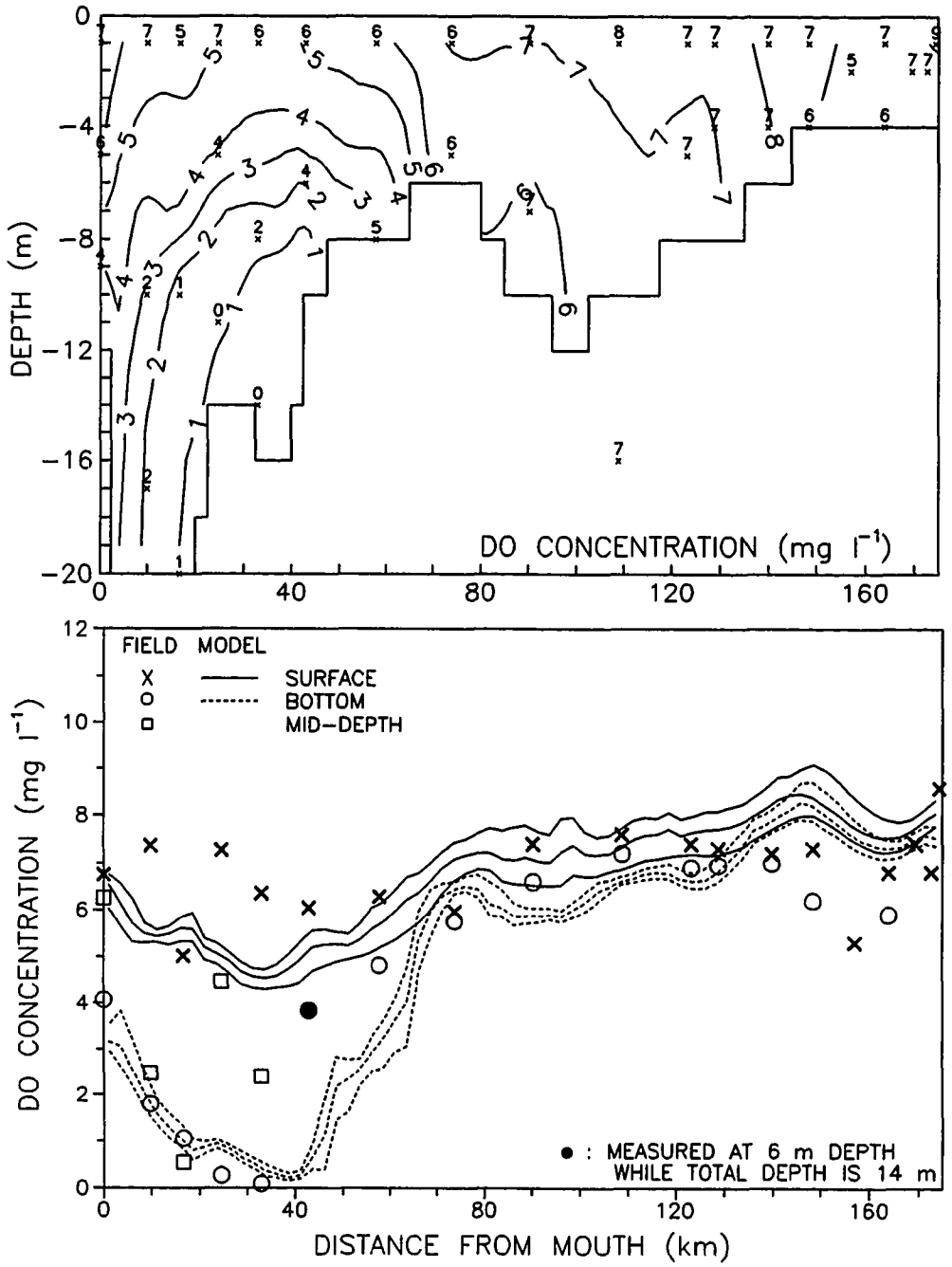

Figure 5-4. Model prediction of DO on 7/05/90 without wind reaeration.

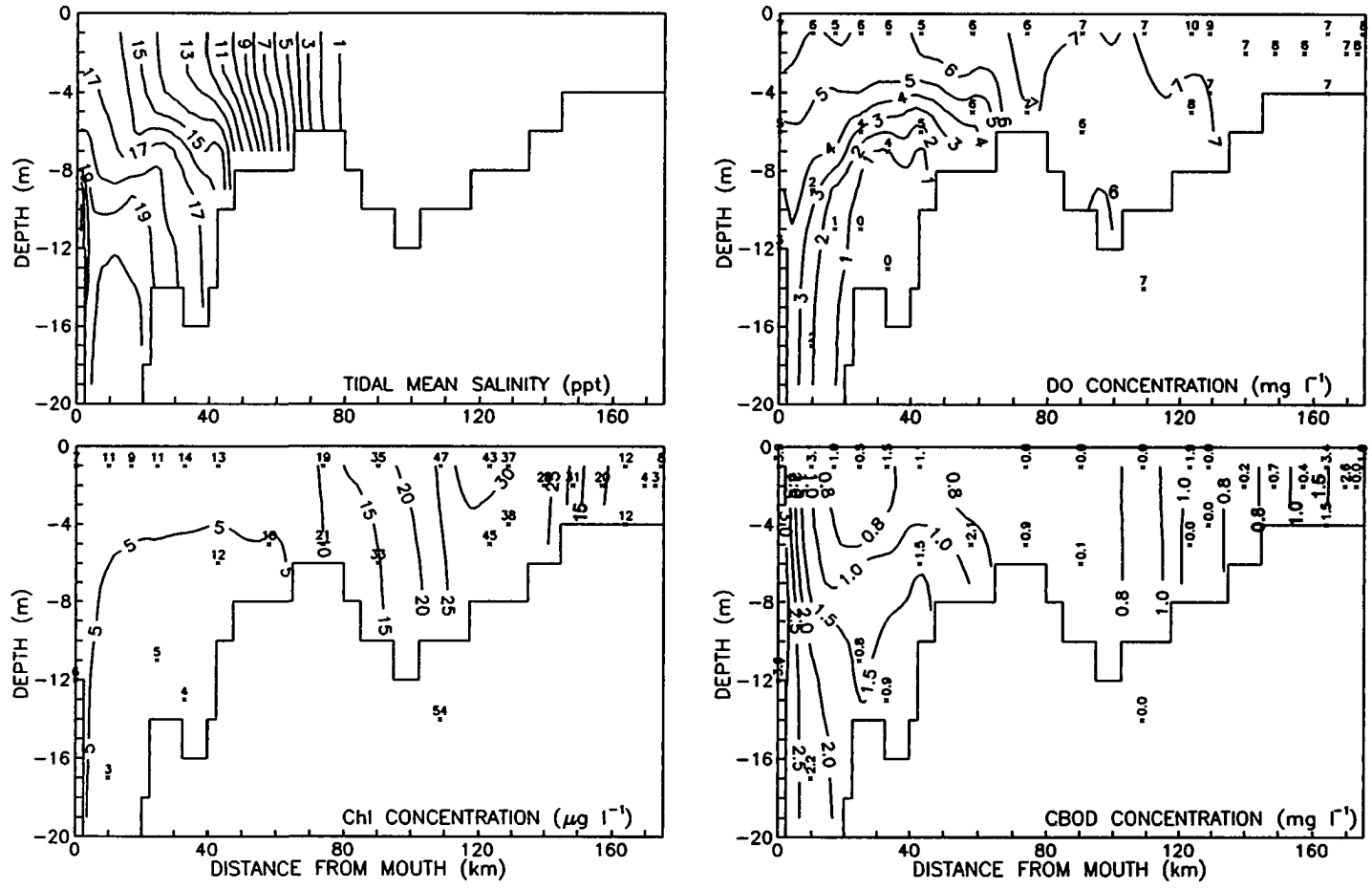

Figure 5-5. **Model verification results and tidal mean salinity on 8/07/90: the isoconcentration contours are model results and the point values are field data.**

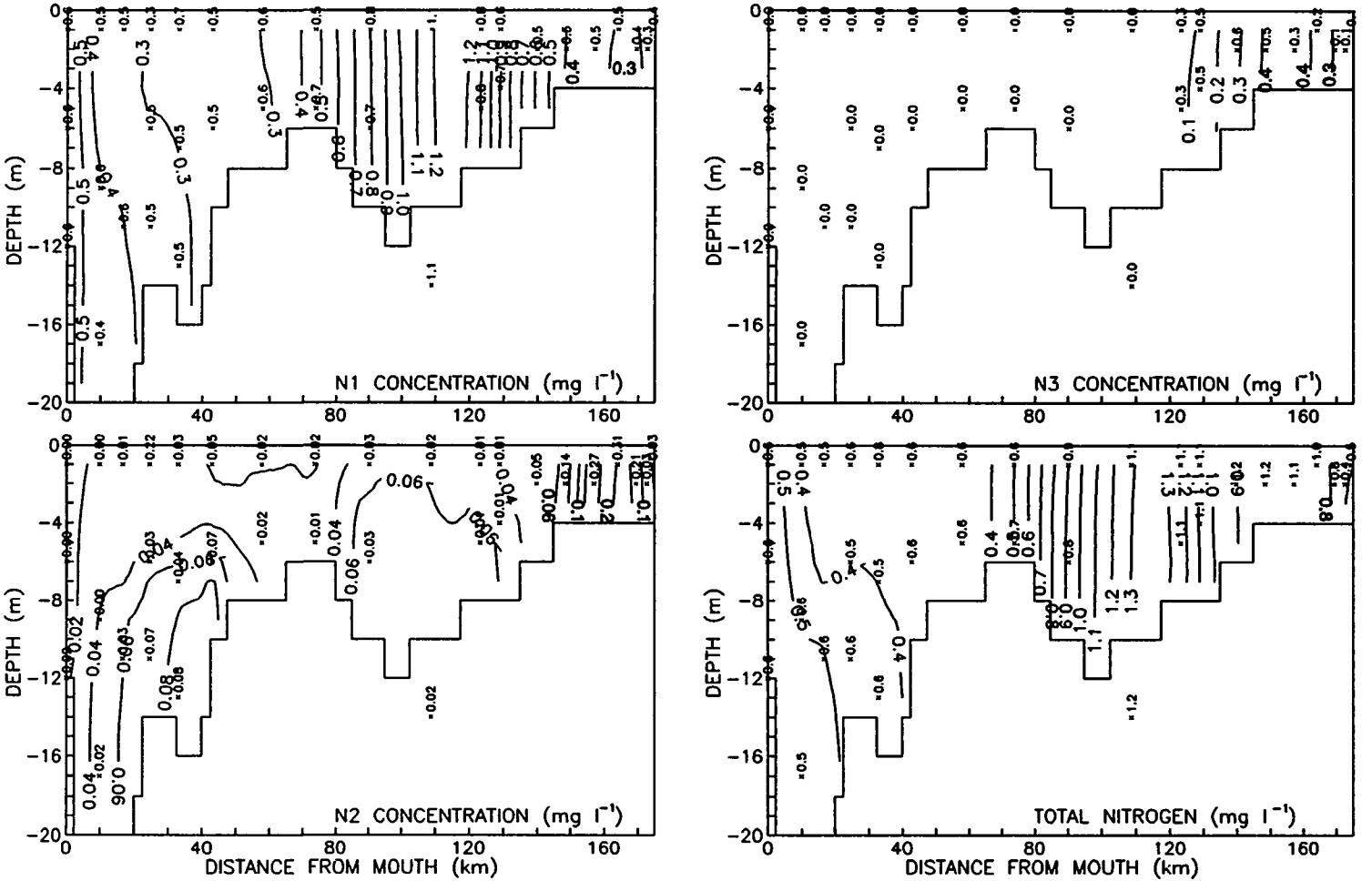

Figure 5-5. (continued).

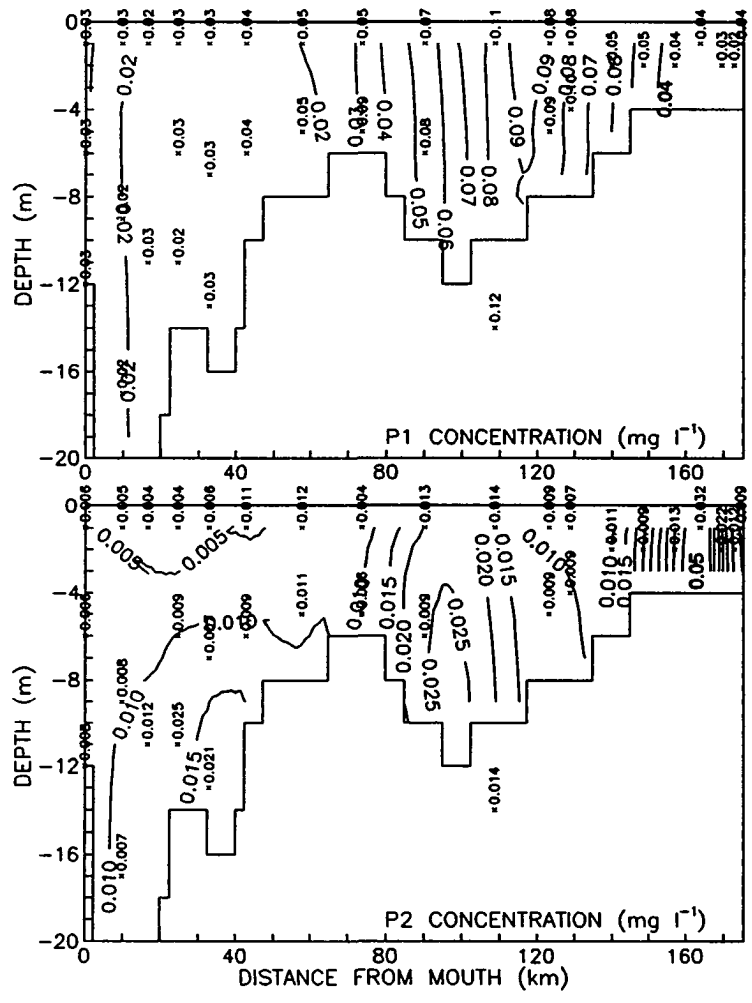

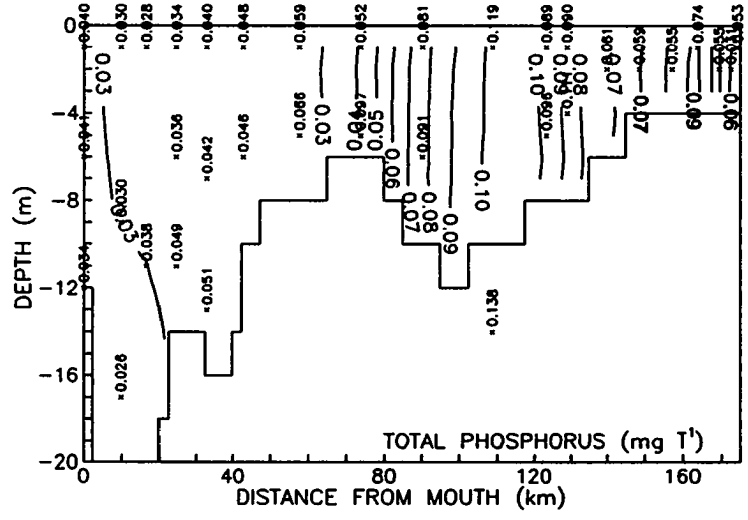

Figure 5-5. (continued).

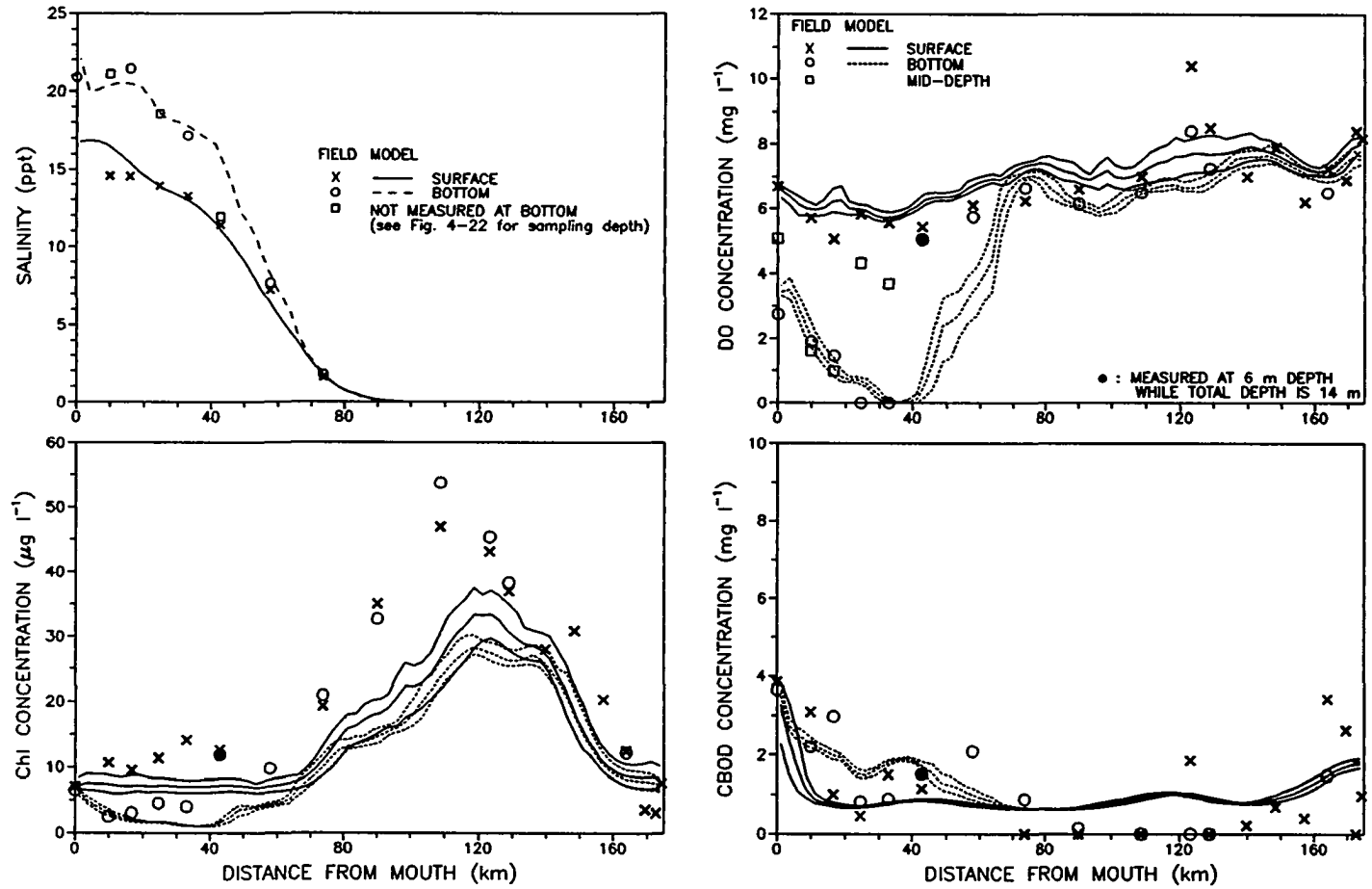

Figure 5-6. Model verification results (daily mean, maximum and minimum) and tidal mean salinity at surface and bottom on 8/07/90.

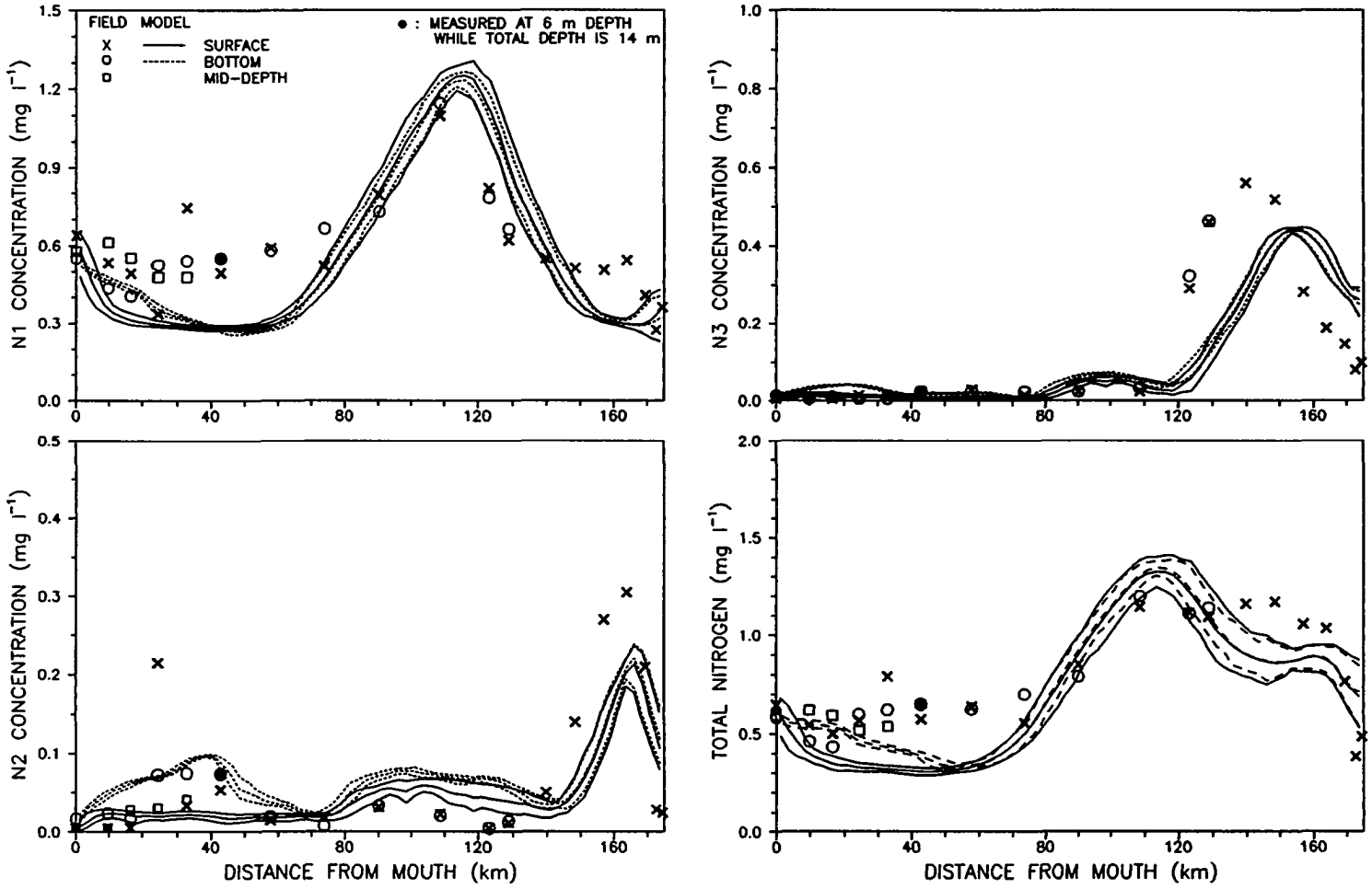

Figure 5-6. (continued).

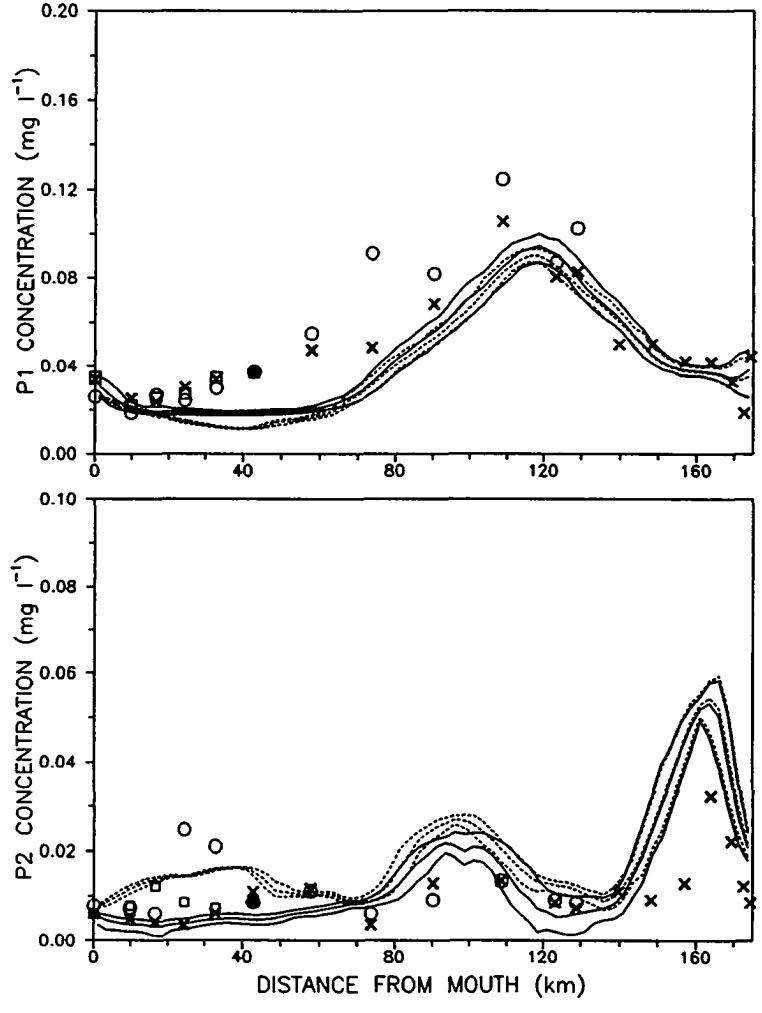

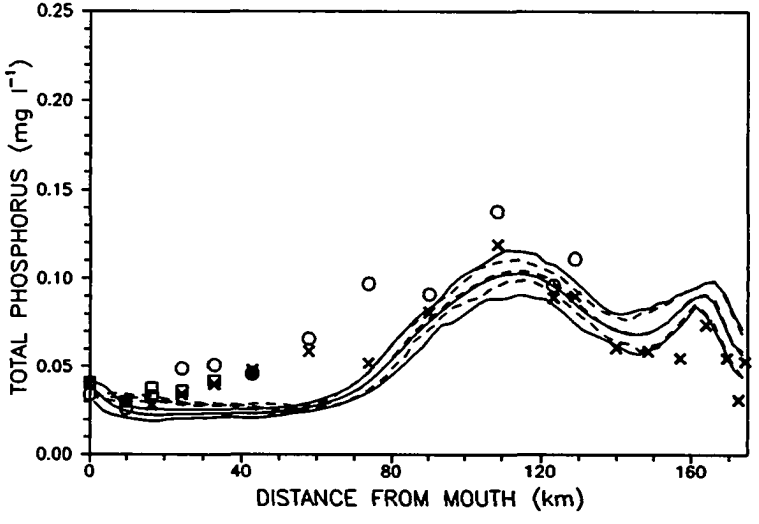

Figure 5-6. (continued).

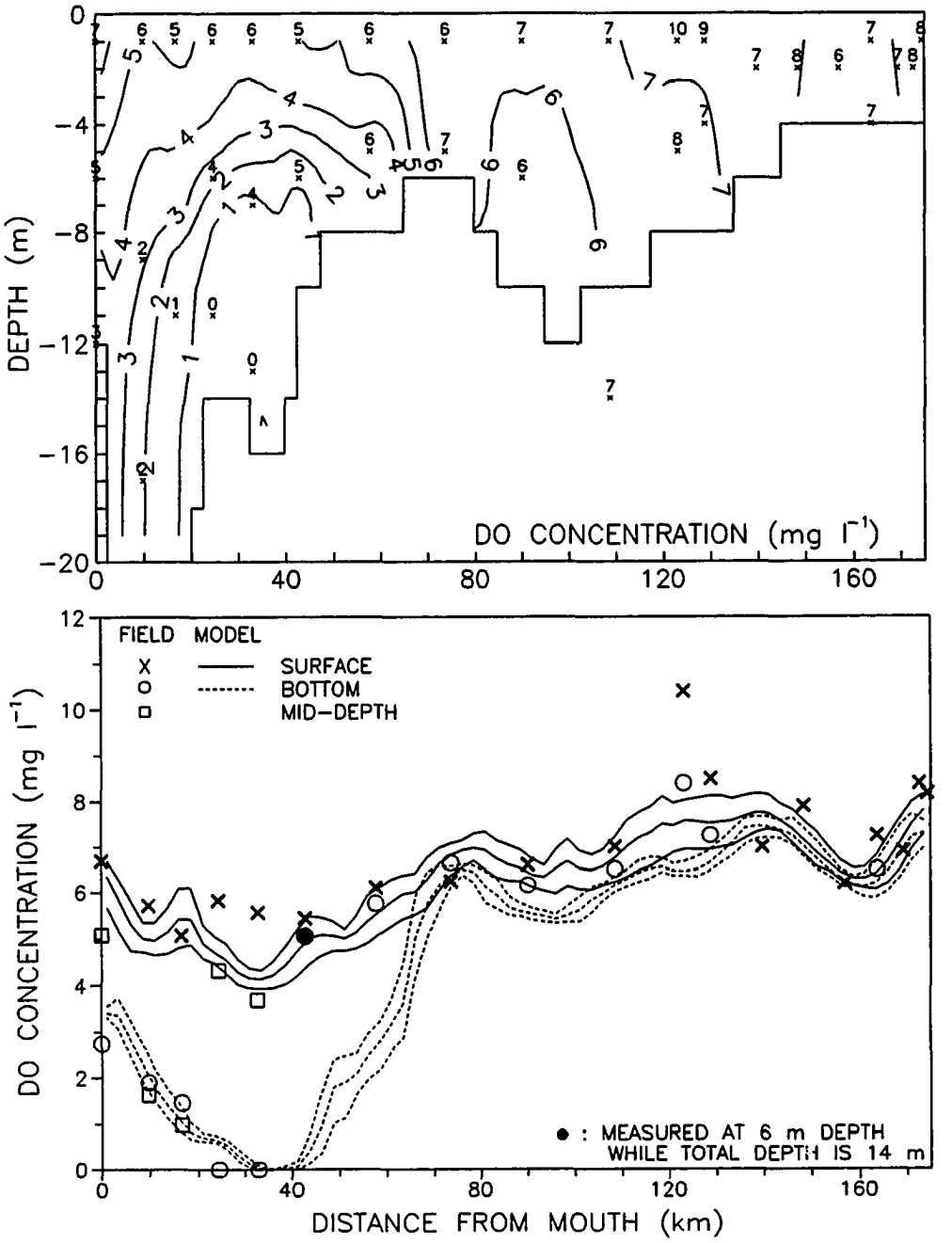

Figure 5-7. Model prediction of DO on 8/07/90 without wind reaeration.

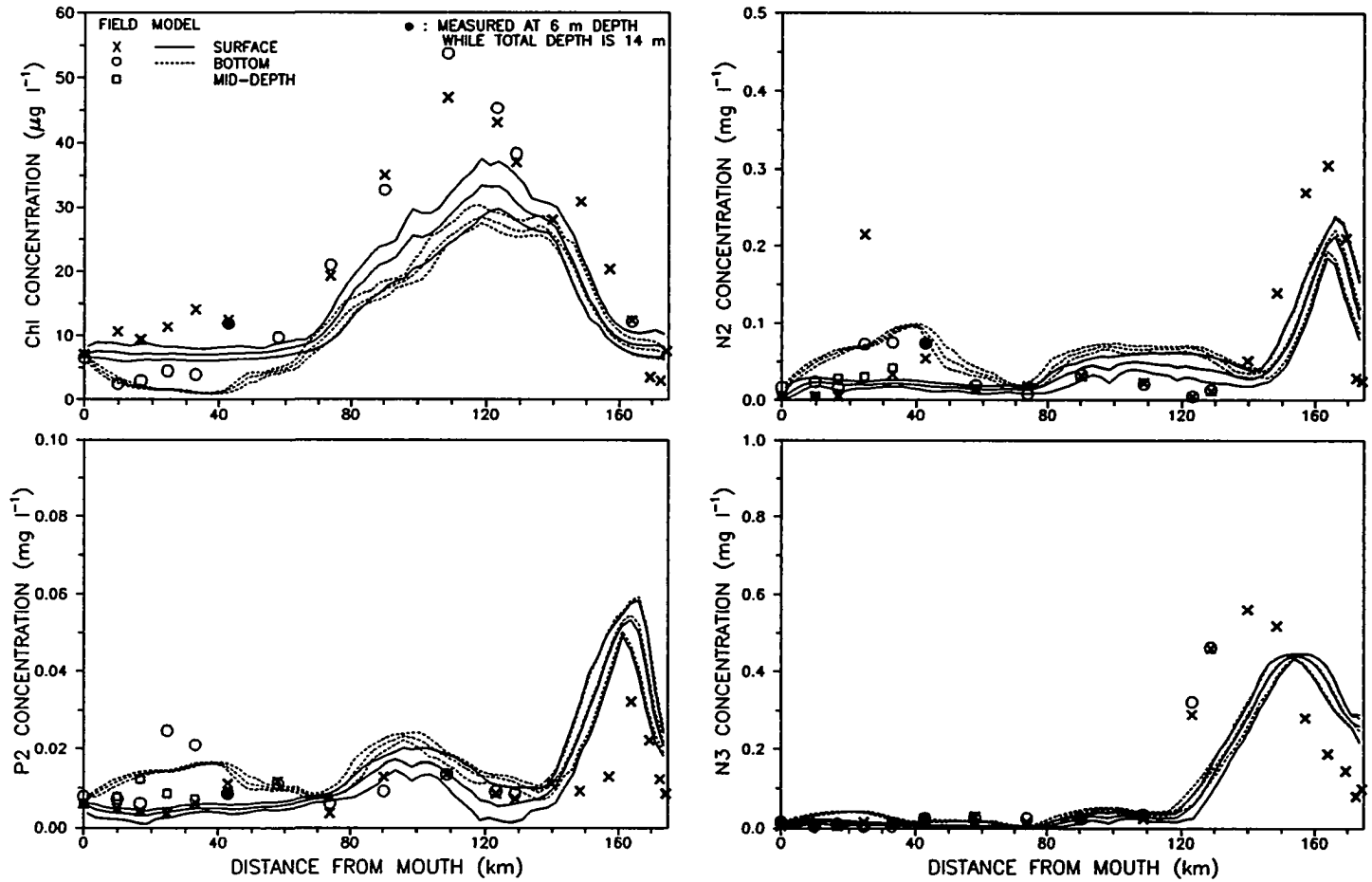

Figure 5-8. Model prediction on 8/07/90 when increasing light availability between km 53-109.

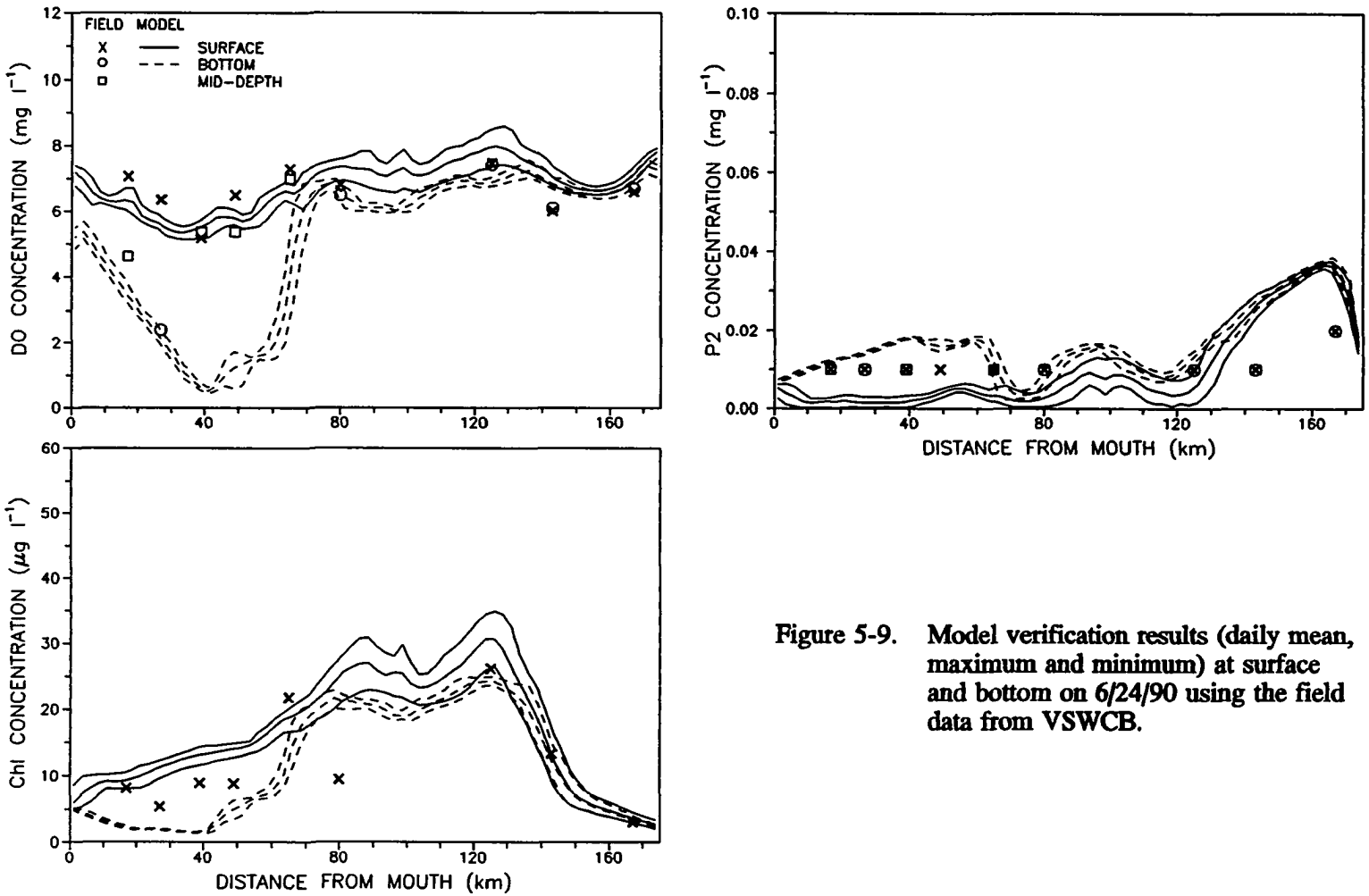

Figure 5-9. **Model verification results (daily mean, maximum and minimum) at surface and bottom on 6/24/90 using the field data from VSWCB.**

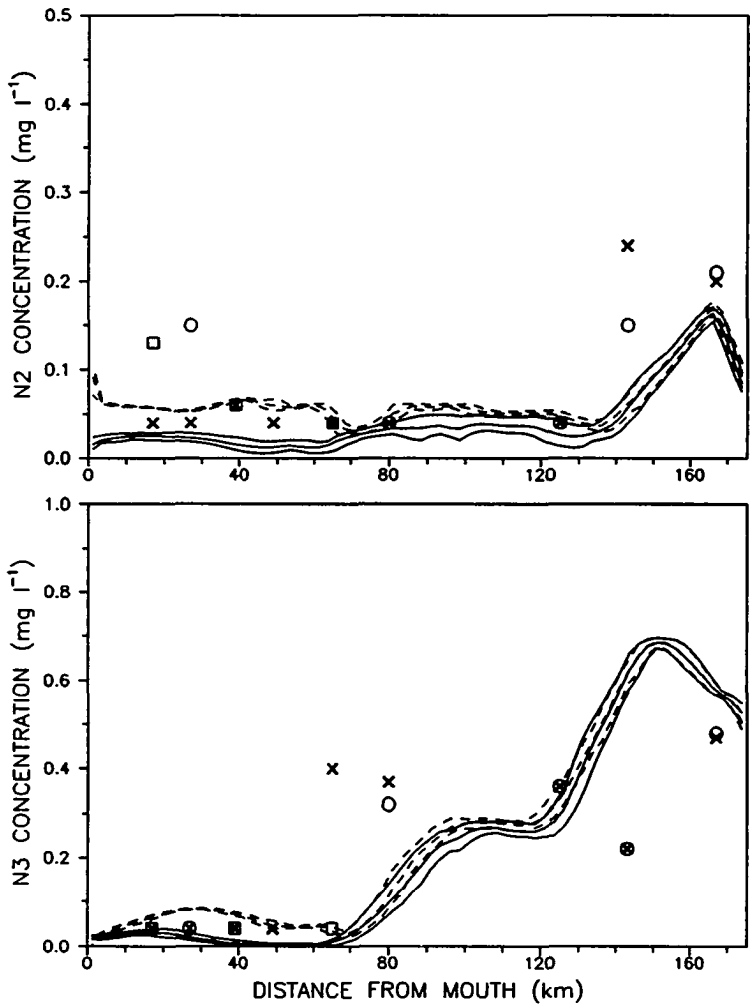

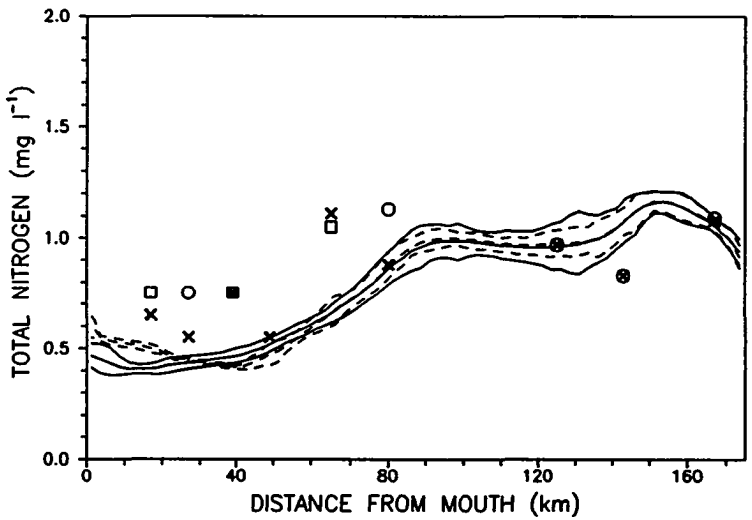

Figure 5-9. (continued).

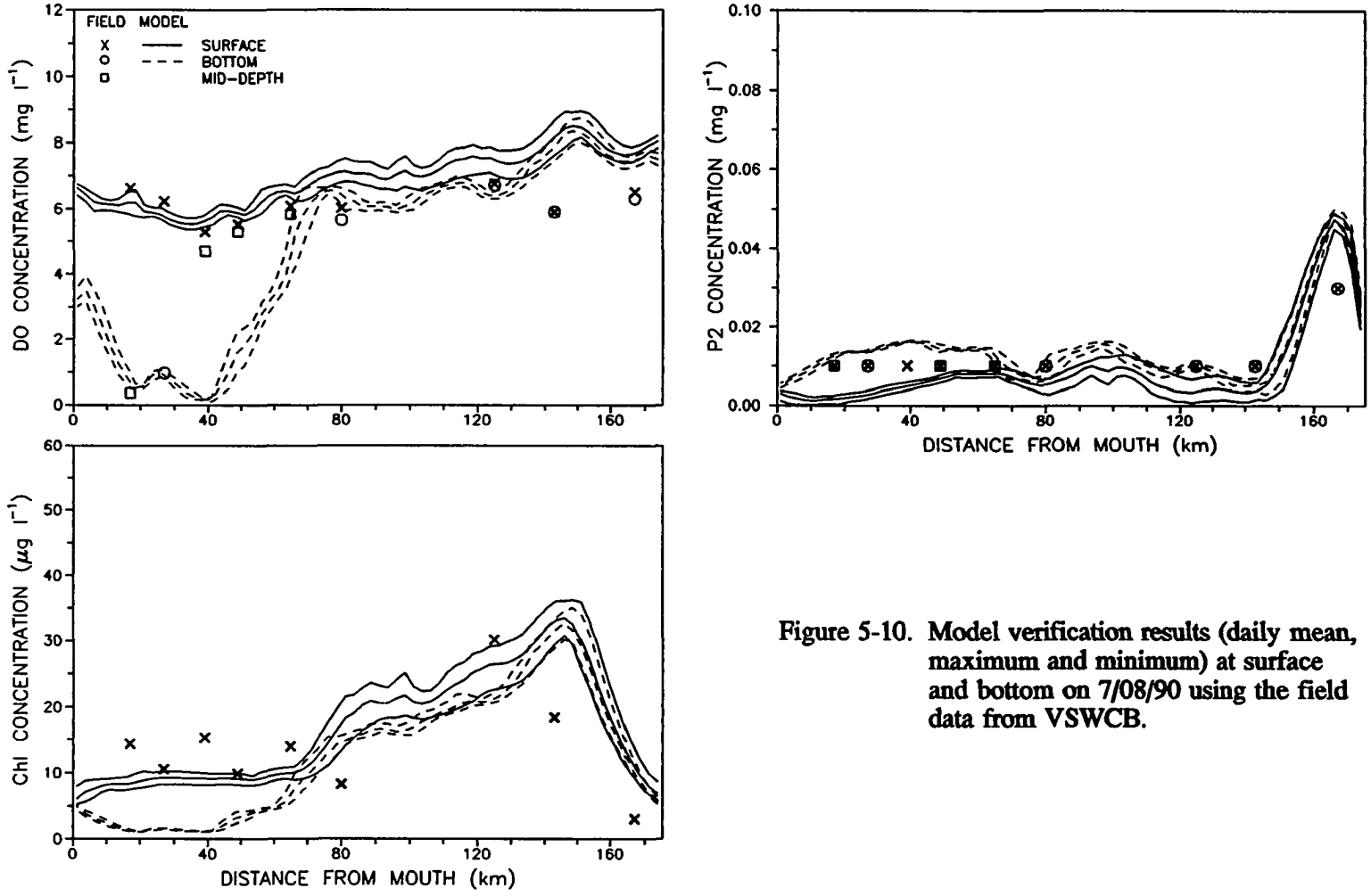

Figure 5-10. Model verification results (daily mean, maximum and minimum) at surface and bottom on 7/08/90 using the field data from VSWCB.

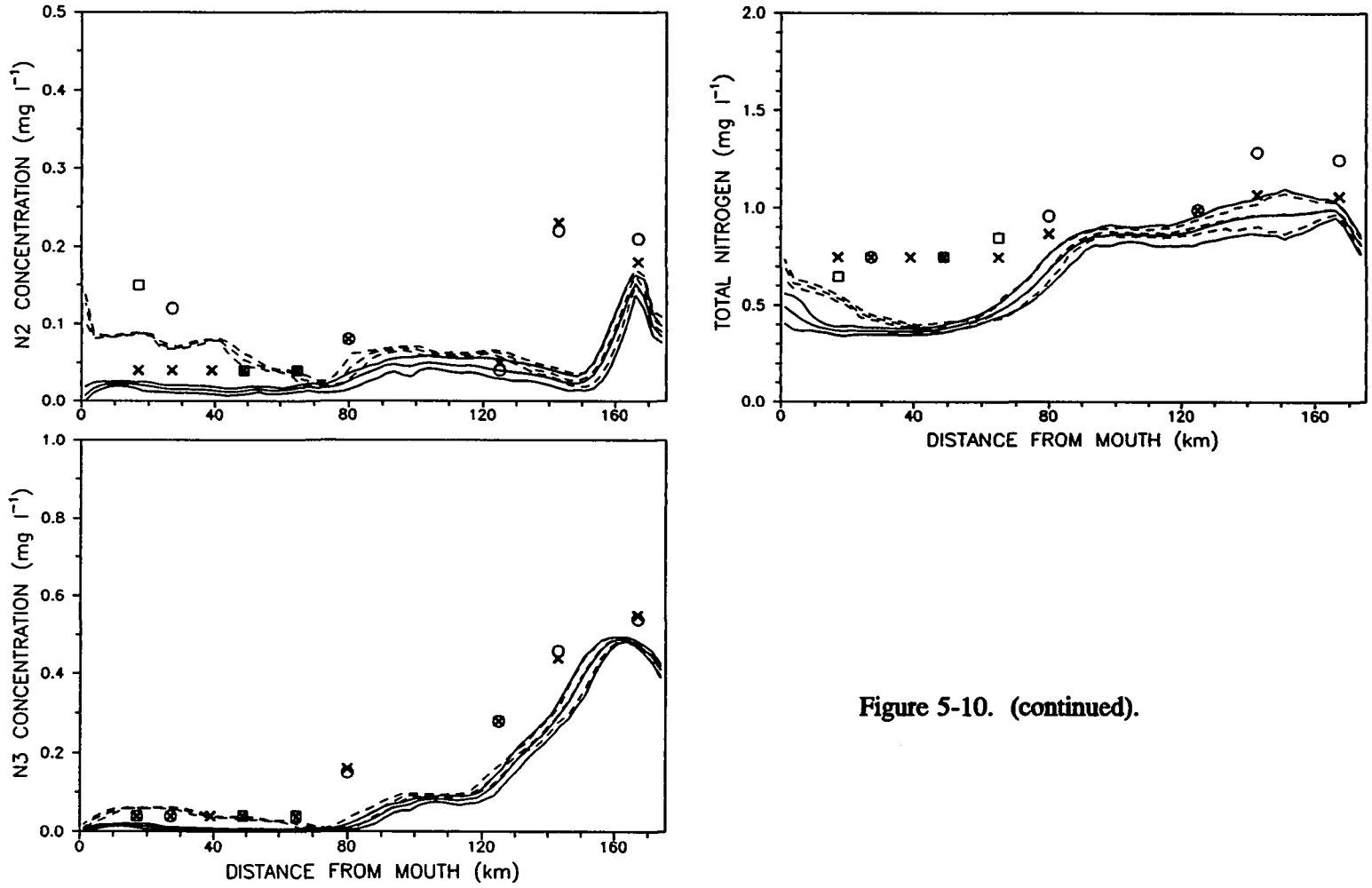

Figure 5-10. (continued).

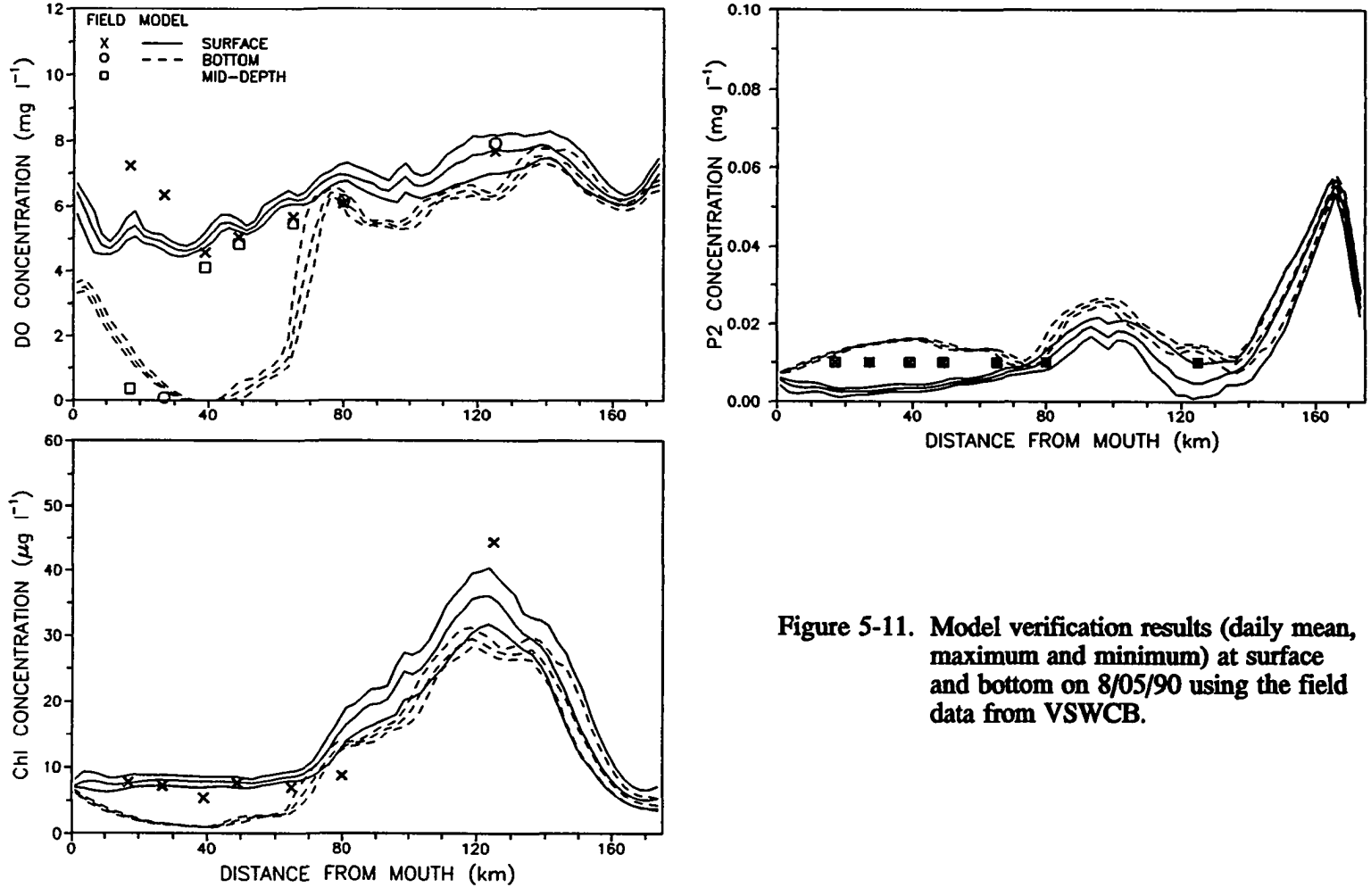

Figure 5-11. Model verification results (daily mean, maximum and minimum) at surface and bottom on 8/05/90 using the field data from VSWCB.

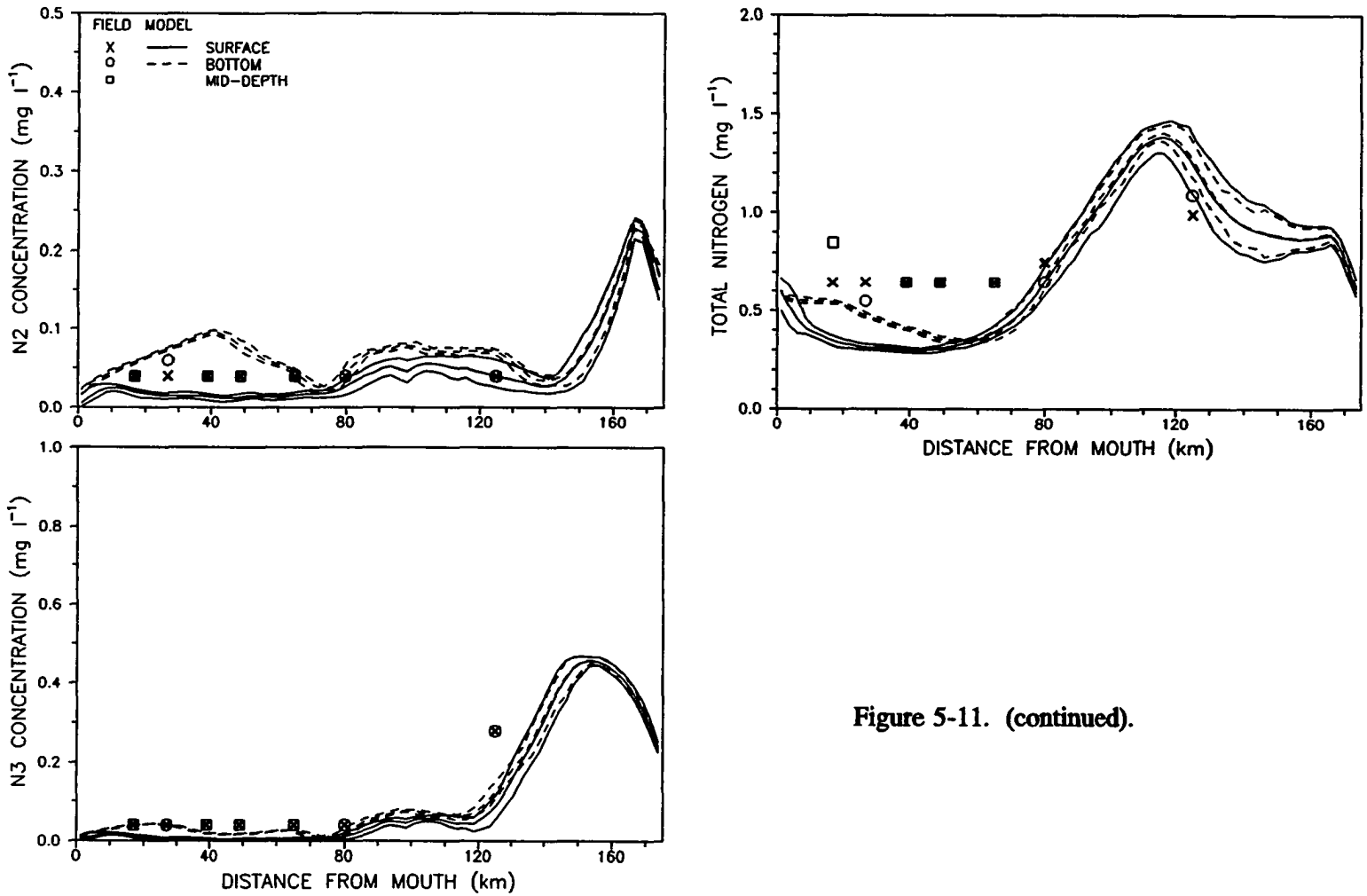

Figure 5-11. (continued).

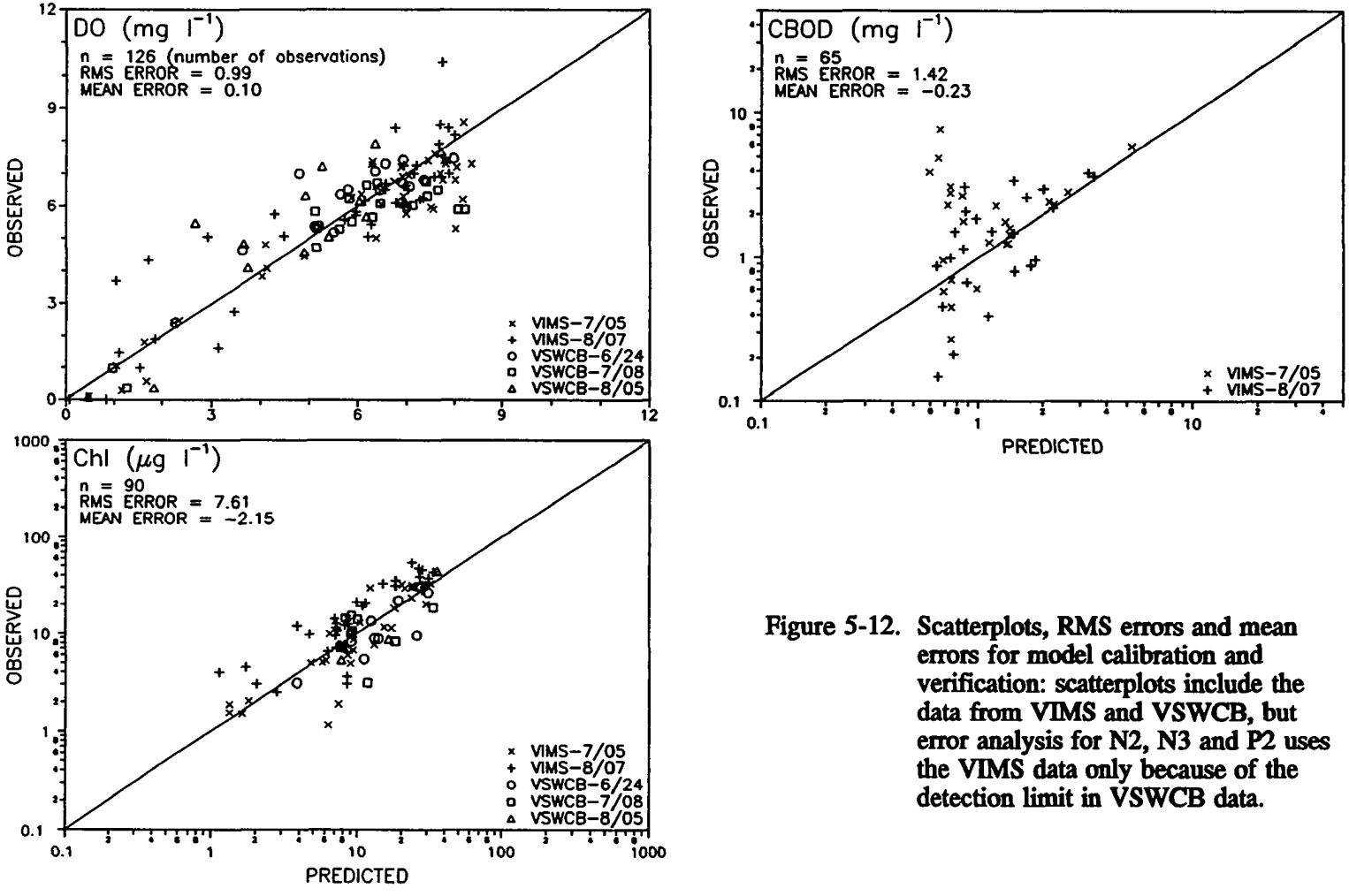

Figure 5-12. Scatterplots, RMS errors and mean errors for model calibration and verification: scatterplots include the data from VIMS and VSWCB, but error analysis for N2, N3 and P2 uses the VIMS data only because of the detection limit in VSWCB data.

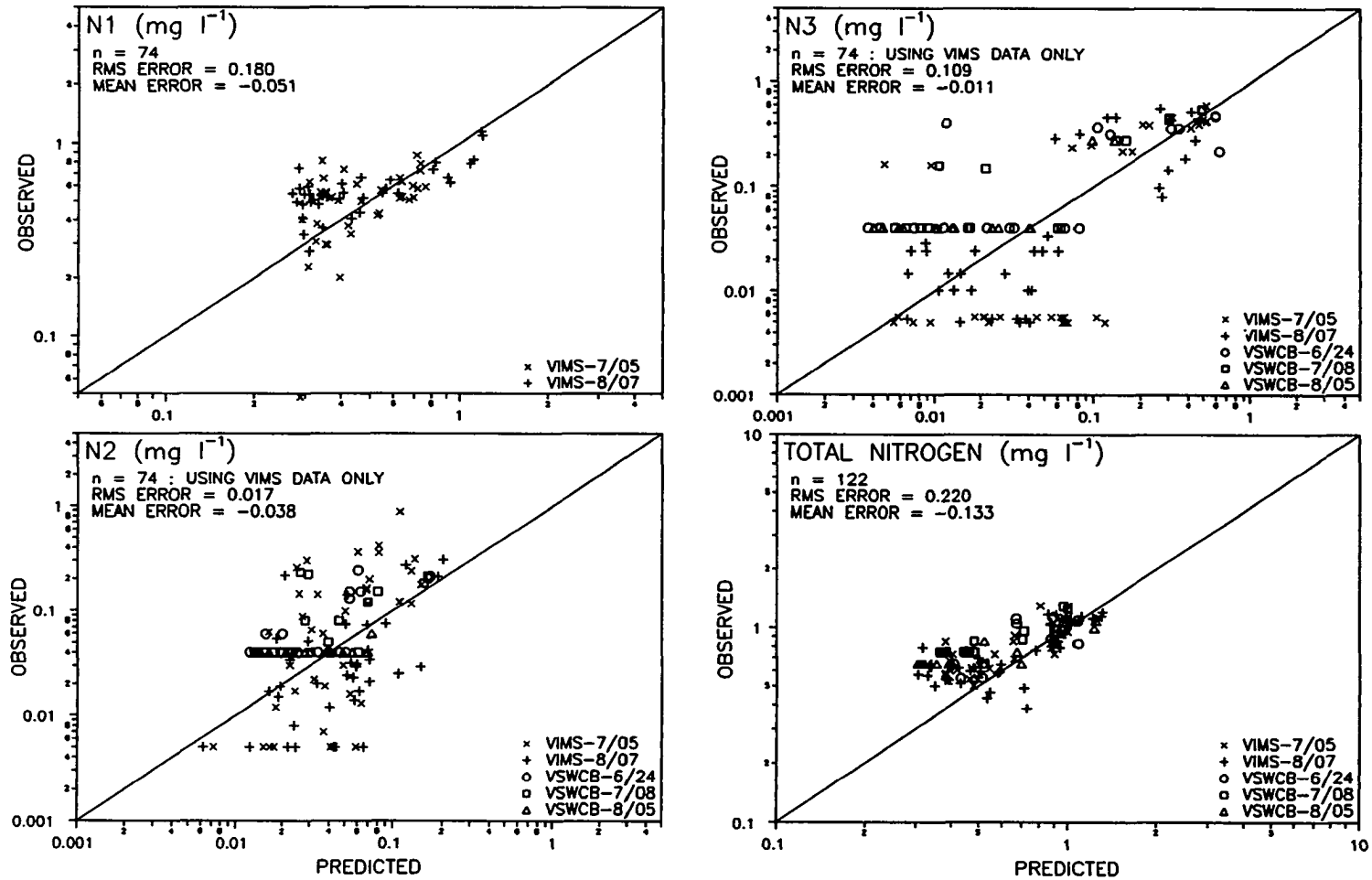

Figure 5-12. (continued).

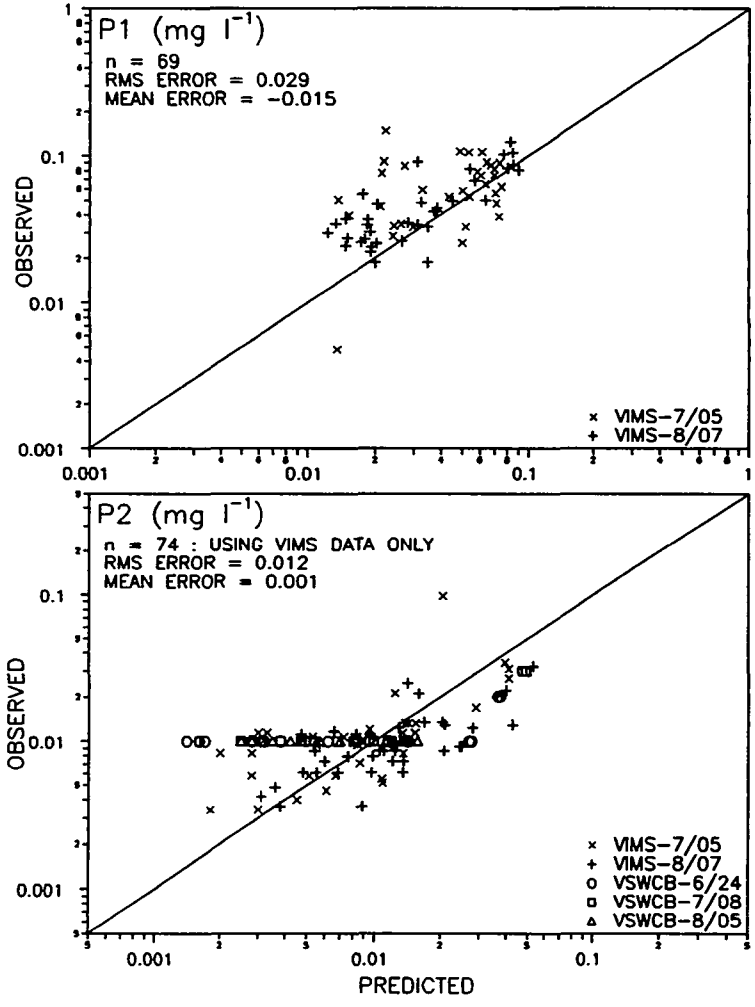

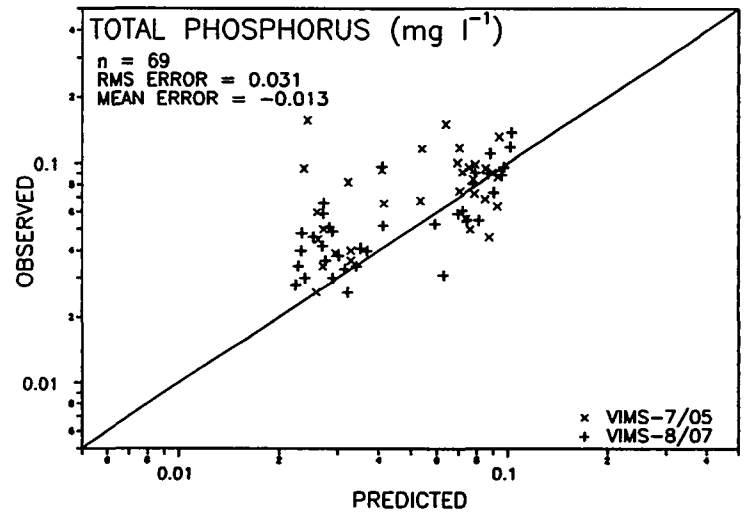

Figure 5-12. (continued).

VI. SENSITIVITY ANALYSIS OF THE WATER QUALITY MODEL

A primary use of the calibrated and verified model is sensitivity analysis to examine the behavior of the prototype in response to any alteration(s) made. In a series of model runs, for example, the effects on the water quality of increasing or decreasing vertical mixing may be examined. Experiments of this nature would be difficult or impossible to conduct on the prototype. Sensitivity analysis is a powerful tool that can be used to improve understanding of the present water quality condition and to explore the factors that are primarily responsible.

From the field observations and model application (calibration and verification), three distinct water quality regimes are noted in the Rappahannock River; the lower reach (between km 0-50), the middle reach (between km 80-145) and the upper reach (between km 155-175). The upper part, immediately downriver of the fall line, receives wastewater discharges from STP's; DO concentrations lower than 5 mg l^{-1} can be found depending upon the quality and quantity of STP discharges. A modeling study (Kuo et al. 1991b) has shown that both point and nonpoint source loadings have significant impacts on water quality with the relative importance depending upon the magnitude of the river discharge.

In the lower portion of the river, hypoxia, or even anoxia, persists during summer in the bottom water, and in the mid-reach of the river, a characteristic Chl maximum has been frequently observed. For these two parts of the river, sensitivity analysis was performed to study the controlling mechanism(s) of the observed phenomena. The sensitivity analysis was conducted by running the model with all

coefficients as in the calibration run except for the one that is being examined. It should be clearly noted that the subsequent sensitivity analysis does not intend to generate precise predictions of prototype behavior under alternative conditions. The variability of natural systems and the effects of random events may act to produce results that would differ from the predictions. The model results should be viewed as best estimates if the conditions remain at their calibrated levels except for the sensitivity parameters.

6-1. Lower Part of the Rappahannock River

In the lower part of the Rappahannock River, hypoxia, or even anoxia, persists during summer in the bottom water. Many studies have been conducted to understand it (Kuo & Neilson 1987; Kuo et al. 1991a; Kuo & Park 1992). Kuo & Neilson (1987) made a qualitative investigation of the bottom DO in the three Virginia estuaries (James, York and Rappahannock estuaries). They reported that hypoxia has been observed most frequently in the deep water of the Rappahannock River, but it occurs rarely in the James River even though it receives the heaviest wastewater loadings among three estuaries. This difference has been attributed in part to the relatively strong gravitational circulation in the James River. Due to these circulation differences, the impact of increased urbanization may be more severe in the Rappahannock River than it has been in the James River.

In the study of the temporal and spatial variability of hypoxia in the lower portion of the Rappahannock River, Kuo et al. (1991a) observed a characteristic longitudinal pattern of bottom water DO in the summer of 1987. The bottom DO concentration decreased upriver from river mouth, reached a minimum at approximately km 42, upriver of the deepest point of the river, then increased as the water became shallower further upriver. The same pattern was observed in the

summer of 1990 and predicted by the model (Figures 5-3 and 5-6). A similar pattern was observed in the Patuxent River, Maryland (Laubach & Summers 1987), another tributary of Chesapeake Bay. Kuo et al. (1991a) also observed a periodic reoxygenation of bottom water that was closely related to spring tide mixing. The destratification-stratification cycle caused by spring-neap tidal cycle has been documented in the Rappahannock River as well as other Virginia estuaries (Haas 1977; D'Elia et al. 1981; Ruzecki & Evans 1986).

A model for the bottom water DO, using a Lagrangian concept, was formulated based on a simple DO budget consisting of only one source (vertical mixing) and one sink (oxygen demand) terms (Kuo et al. 1991a). The predictive application of the model was not always satisfactory due to the lack of complete information for input parameters (vertical mixing and oxygen demand); spatially and temporally varying values for input parameters were called for to improve the predictive capability of the model. The diagnostic study using the simple model, however, enabled them to investigate cause-effect relationships, i.e., effect on bottom DO of residual velocity, vertical mixing, oxygen demand and quality of incoming water from the bay.

Sensitivity analysis using the present model was performed to study the controlling mechanism(s). The primary function of this analysis was to test the theory proposed in Kuo & Neilson (1987) and Kuo et al. (1991a) using detailed hydrodynamics and geometry. The sensitivity of the prototype was examined for the following factors that might be responsible for low DO concentration: quality of the incoming bay water, gravitational circulation, vertical mixing, SOD and water column oxygen demand.

6-1-1. Quality of the incoming bay water

It has been suggested that anoxia in the main channel of Chesapeake Bay might

be a primary contributing factor to hypoxia in the Rappahannock River. The effect of quality of the incoming bay water on the bottom DO inside the river was examined by adjusting the downstream boundary condition for DO and CBOD. In the calibration and verification runs, the time-varying downstream boundary condition was prepared by linear interpolation of the field data at the mouth from 3 slackwater surveys (June 6, July 5 and August 7).

Two new boundary conditions for DO were constructed by linear interpolation of the data after low DO measurements were brought up to 5.5 (or 7.0) mg l^{-1}. The DO boundary conditions in the bottom layer used in two sensitivity runs are presented in Fig. 6-1. Results from two sensitivity runs in Fig. 6-2 indicate that the DO in the incoming bay water can affect the severity of hypoxia but not the shape of bottom DO distribution, particularly the location of minimum bottom DO. Furthermore, the bottom water ends up being hypoxic regardless of the DO concentration in the incoming bay water. This agrees with the conclusions of Kuo et al. (1991a), which were based upon a simple DO budget model for bottom water.

The effect of CBOD in the incoming bay water on hypoxia was examined by decreasing the downstream boundary condition for CBOD. Results from a sensitivity run with a zero-CBOD boundary condition in Fig. 6-3, compared to those in Fig. 6-2, show that the hypoxic condition can be relieved more by eliminating CBOD than by increasing DO in the incoming bay water. Results from a second sensitivity run with the lowest DO boundary condition of 7.0 mg l^{-1} and zero-CBOD boundary condition in Fig. 6-3 indicate that the bottom water ends up being hypoxic regardless of the DO and CBOD concentrations in the incoming bay water.

6-1-2. Gravitational circulation

Differences in the gravitational circulation have been proposed to be responsible

for the systematic variability in the bottom water DO in three Virginia estuaries (Kuo & Neilson 1987; Kuo et al. 1991a). The effect on the DO distribution of residual circulation was examined by changing the constant relating salinity to density (k in Eq. 2-6). Results from an initial sensitivity run (not shown) show that an increase in k, thus strengthening the residual current, lowers the DO concentration slightly over the region where gravitational circulation exists. This is because the enhanced gravitational circulation strengthens the stratification, which in turn reduces the vertical mixing. To alter the strength of the gravitational circulation without affecting the vertical mixing, only the constant involved in calculating the horizontal pressure (density) gradient (Eq. 2-26) was modified. Figure 6-4 shows the results from sensitivity runs with 120% and 130% of the calibration value of k (7.5×10^{-4}).

In Fig. 6-4, two mechanisms are responsible for the increase in bottom water DO with increasing the constant, k; residual circulation and vertical mixing. The lower half of Fig. 6-5 shows the tidal mean velocity vertically averaged over the bottom layer. (Negative velocity indicates that the water flows in the upriver direction). In the base (calibration) run with $k = 7.5 \times 10^{-4}$, the spatial average of tidal mean velocity over the bottom layer is -1.7 cm sec^{-1}. The spatial averages for k $= 9.0 \times 10^{-4}$ (120%) and 9.75×10^{-4} (130%) are, respectively, -2.2 and -3.3 cm sec^{-1}. Therefore, one mechanism to increase the bottom DO in Fig. 6-4 is that faster water movement allows less time for DO to be consumed as a water parcel travels upriver along the bottom, which confirms the argument in Kuo & Neilson (1987) and Kuo et al. (1991a).

The enhanced gravitational circulation increases the velocity shear ($\Delta u/\Delta z$) as well as stratification ($\Delta \rho/\Delta z$). The increase in $\Delta u/\Delta z$ that enhances turbulence is somewhat compensated for by increase in $\Delta \rho/\Delta z$, making the increase in vertical mixing not as large as it can be with the increase in $\Delta u/\Delta z$ only. In the present

sensitivity runs, increasing the constant, k, only in the horizontal density gradient enhanced $\Delta u/\Delta z$ accordingly but not $\Delta\rho/\Delta z$. This made the increase in turbulent mixing due to velocity shear ($\Delta u/\Delta z$) more pronounced than the reduction due to stratification ($\Delta\rho/\Delta z$). The upper half of Fig. 6-5 shows the tidal mean vertical diffusivity (K_z) vertically averaged over total depth. The spatial averages of tidal mean K_z over the estuarine portion are 1.3, 1.8 and 2.8 $cm^2\ sec^{-1}$ for $k = 7.5 \times 10^{-4}$, 9.0×10^{-4} and 9.75×10^{-4}, respectively. Therefore, another contributing factor for the elevated bottom DO in Fig. 6-4 is the increased vertical mixing. With the present model, which contains all terms in the continuity equation and momentum and mass balance equations (Equations 2-1 through 2-5), it was not possible to isolate the part(s) responsible for increasing the gravitational circulation without affecting the vertical mixing.

6-1-3. Vertical mixing

The effect of vertical mixing was examined by varying the constant, α, in the vertical mixing coefficients (Equations 2-16 and 2-17). Figure 6-6 shows the results from sensitivity runs with 120% and 150% of the calibrated α value (1.15×10^{-2}). It shows that increased vertical mixing does relieve the hypoxic condition in the bottom water, which confirms one of the conclusions in Kuo et al. (1991a). The tidal mean velocity and vertical diffusivity, which are comparable to those in Fig. 6-5, are presented in Fig. 6-7. In the upper half of Fig. 6-7, the spatial averages of tidal mean K_z over the estuarine portion are 1.3, 1.6 and 2.7 $cm^2\ sec^{-1}$, respectively, for $\alpha = 1.15 \times 10^{-2}$ (calibration), 1.38×10^{-2} (120%) and 1.725×10^{-2} (150%). Tidal mean velocity in the lower half of Fig. 6-7 shows that the gravitational circulation increases with increasing α between km 0-32. The spatial averages of tidal mean velocity over the bottom layer are -1.7, -1.9 and -2.8 cm sec^{-1}, respectively, for $\alpha =$

1.15×10^{-2}, 1.38×10^{-2} and 1.725×10^{-2}.

This is contrary to the Hansen and Rattray's analytical solution (1965) as well as to the results in Figures 4-17 and 4-18. Hansen and Rattray's solution dictates that the gravitational circulation decreases as the vertical mixing increases, which is represented by weaker residual velocity during spring tide (Fig. 4-17) compared to neap tide (Fig. 4-18). Hansen and Rattray's solution, however, was based upon the assumption of constant longitudinal salinity gradient ($\partial s/\partial x$). It is $\partial s/\partial x$ integrated over the water column that is the driving force for, and thus determines the strength of, gravitational circulation. In Fig. 6-8, the lower half repeats the tidal mean velocity of Fig. 6-7 and the upper half shows $\Sigma(\Delta S_x) = \Sigma(S_i - S_{i-1})$, the longitudinal gradient of tidal mean salinity integrated over total depth (note constant Δx and Δz were used in the present study). It shows that the driving force for gravitational circulation increases as the vertical mixing increases between km 0-32. To show the effect on the salinity field of increased vertical mixing, two contour plots of tidal mean salinity are presented in Fig. 6-9 for $\alpha = 1.15 \times 10^{-2}$ and 1.725×10^{-2}. An increase in vertical mixing results in more homogeneous conditions with less salt being transported upriver. In the lower part of the river between km 0-30, increased vertical mixing affects the salinity field such that more salt is mixed upward (increasing the salinity near the surface) and less salt is transported upriver (decreasing the salinity near bottom). This altered salinity field for large α (1.725×10^{-2}), along with the same salinity boundary condition at the mouth, increases $\partial s/\partial x$, which in turn enhances the gravitational circulation.

The conditions used to generate the residual velocities in Figures 4-17 and 4-18 are described in Section 4-4-1. Using the same conditions, the tidal mean characteristics, salinity, $\Sigma(\Delta S_x)$ and vertically averaged tidal mean velocity over the bottom layer, during spring and neap tides are presented in Fig. 6-10. The salinity

distributions in the lower part of the river, like those in Fig. 6-9, show that the enhanced vertical mixing during spring tide increases (decreases) the salinity near surface (bottom). However, the difference between spring and neap tides is so small that it may not cause significant change in $\partial s/\partial x$. This is evident in the plot of $\Sigma(\Delta S_x)$ in Fig. 6-10. With virtually the same $\partial s/\partial x$ during spring and neap tides, the residual velocities in Figures 4-17 and 4-18 follow Hansen and Rattray's analytical solution. That the spring tide provides more mixing energy and thus has weaker residual circulation is shown in the plot of tidal mean velocity in Fig. 6-10.

As the vertical mixing increases, it has two opposing effects on the residual circulation. One is to weaken the circulation because more mixing enhances vertical momentum exchange, which process is from now on referred to as ME. The other is to strengthen the circulation by increasing $\partial s/\partial x$ and thus the driving force for the gravitational circulation as a result of changes in the salinity field (SG). Whether the residual circulation increases or not as the vertical mixing increases depends upon the relative importance of two processes, ME and SG. When comparing the spring and neap tides (Fig. 6-10), the difference in the vertical mixing and thus that in the salinity field is so small that it cannot cause significant change in $\partial s/\partial x$. Then, the residual circulation weakens during spring tide since ME dominates SG. In Figures 6-6 through 6-9, the increased (50%) vertical mixing changes the salinity field in such a way that the effect of increased $\partial s/\partial x$ (SG) dominates that of ME resulting in the enhanced circulation.

As in Fig. 6-4, therefore, the enhanced DO in Fig. 6-6 is partly due to increased vertical mixing and partly due to faster water movement. Again, the present model, being a complicated model containing all terms in the continuity equation and momentum and mass balance equations (Equations 2-1 through 2-5), cannot separate the effect of the vertical mixing from that of the gravitational

circulation.

6-1-4. Spatial and temporal variations of bottom water DO

A characteristic longitudinal pattern of the bottom DO and its variation caused by spring-neap cycle have been observed in the Rappahannock (Kuo et al. 1991a) and Patuxent (Laubach & Summers 1987) rivers. The temporal variation of the bottom DO in response to spring-neap cycle has also been observed (Kuo et al. 1991a). The destratification-stratification cycle, closely related to the differential mixing over the spring-neap cycle, has been documented in the Rappahannock River as well as other Virginia tributaries of Chesapeake Bay (Haas 1977; D'Elia et al. 1981; Ruzecki & Evans 1986). The model's ability to reproduce these spatial and temporal variations was examined by comparing the DO concentrations during strong spring and neap tides. To eliminate the effect of DO boundary condition, a constant DO downstream boundary condition, that on 7/05/90, was used. Figure 6-11 shows the longitudinal DO distributions during strong spring and neap tides. The more vigorous tidal mixing during strong spring tide than neap tide is well reproduced by the model.

In Fig. 6-11, the location of minimum DO occurs further downriver during strong spring tide compared to neap tide. This again confirms one of the conclusions in Kuo et al. (1991a), which were derived from both field measurements and DO budget. The conditions near the mouth of the Rappahannock River are such that the DO sink terms are greater than the source terms for the bottom water. The DO concentration, therefore, starts to decrease once the bottom water enters the river, and keeps decreasing as it travels upriver into the deep basin. As the bottom water travels beyond the deepest point in the basin into shallower waters, the DO replenishment due to vertical mixing increases. Since water depth generally decreases in the upriver direction, the DO source terms eventually become equal to the sink terms, at which

point the minimum DO occurs. The location of this point depends on the intensity of vertical mixing. Because increase in vertical mixing during strong spring tides increases the DO replenishment rate at a given depth, the balance between the source and sink terms will occur earlier in deeper water. The resulting downriver movement of the minimum DO location was observed periodically around the times of strong spring tides (Kuo et al. 1991a), and is well reproduced by the model (Fig. 6-11).

Another view of the effect on bottom DO of the differential mixing over spring-neap cycle is presented as a time series plot of bottom DO (Fig. 6-12b). The tidal range from the surface elevation measured at the mouth (Fig. 6-12a) represents the intensity of tidal mixing. The temporal variation of the bottom DO in response to the differential tidal mixing is evident in Fig 6-12b; note the sudden decrease in bottom DO in response to that in tidal range around day 31 and increase in bottom DO during and after strong spring tide around day 49. The influence of tidal mixing decreases in the upriver direction with the temporal variation in response to tidal mixing getting smaller in the same direction.

6-1-5. Oxygen demand

The SOD of 2.0 g m^{-2} day^{-1} was obtained from the field measurements and model calibration (Table 5-4). The effect of SOD on hypoxic conditions was assessed in sensitivity runs, in which SOD values of 1.0 and 0.0 g m^{-2} day^{-1} were used. Results in Fig. 6-13 show that a decrease in SOD increases the absolute value of the bottom DO, which again confirms one of the conclusions in Kuo et al. (1991a). In Fig. 6-13, however, the shape of DO distribution changes as SOD is varied, which does not agree with an argument in Kuo et al. (1991a). This difference in sensitivity of DO distribution to SOD change may be attributable to the differences in geometry used. Kuo et al. (1991a) argued, using spatially uniform SOD values and simple

(constant width) geometry, that the relative DO concentration would not be altered by changing the magnitude of SOD. However, Fig. 6-13 shows that when detailed geometry is used, the DO increase is more pronounced around km 40 than around km 20. Oxygen demand in the water column has dimension [M L^{-3} T^{-1}] while SOD has [M L^{-2} T^{-1}], which suggests that the effect of SOD is inversely proportional to a length scale. For the overall effect in a cross-section, the length scale of importance is volume/(bottom area), which is 9.1 m at km 18.6 and 5.3 m at km 38.6 (see Table 4-1). For each particular layer, the DO consumption due to SOD is proportional to the layer bottom area, $(B_k - B_{k+1}) \cdot \Delta x$ and inversely proportional to the layer volume, $B_k \cdot \Delta x \cdot \Delta z$. Since constant layer thickness (Δz = 2 m) and segment length (Δx = 2500 m) are used, the DO consumption due to SOD is proportional to $(B_k - B_{k+1})/B_k$ (see Eq. 2-39b); the vertical mean $(B_k - B_{k+1})/B_k$ is 0.31 at km 18.6 and 0.43 at km 38.6 (see Table 4-1). It is these differences in geometry that make the DO increase due to the SOD reduction more pronounced around km 40 than that around km 20 in Fig. 6-13.

The sensitivity runs for Fig. 6-13 used the same downstream boundary condition and thus the system can have no sensitivity to SOD at the boundary. This suggests that potential sensitivity of DO distribution to any factor may increase with distance from the boundary. However, increase in bottom DO when varying some factors is larger around km 20 than around km 40; see curves (a) and (b) in Fig. 6-15. Therefore, a larger DO increase around km 40, than around km 20, in response to SOD decrease in Fig. 6-13 does not seem to be due to distance from the boundary.

The SOD represents the oxygen demand from the sediment, and three terms, CBOD decay (K_c), nitrification (K_{n23}) and algal respiration (R), represent the oxygen demand in the water column. The calibrated model has the corresponding rate constants at 20°C of 0.1 day^{-1}, 0.3 mg l^{-1} day^{-1} and 0.17 day^{-1} (Tables 5-1, 5-2 and

5-4). The effect of these water column respiration terms was examined in sensitivity runs, in which each and all of three terms were eliminated. Results in Fig. 6-14 show that in the lower part of the river, the CBOD decay consumes the most DO. Field observations, and model calibration and verification (Figures 5-3 and 5-6) show a bimodal distribution of CBOD with one peak in the upper part of the river due to the STP discharges. The other peak in the lower part is due to the downstream boundary condition, and the hypoxic condition can be relieved by eliminating CBOD in the incoming bay water (Fig. 6-3).

To show the relative importance of four oxygen demanding terms, the increase in the bottom DO that is caused by eliminating each term is presented in Fig. 6-15. It indicates that the DO consumption due to the water column respiration including CBOD decay, nitrification and algal respiration is as important as that due to SOD.

6-1-6. Summary

Hypoxia has been frequently observed during summer in the bottom water of the lower part of the Rappahannock River. The sensitivity analysis shows that the bottom water will end up being hypoxic regardless of the DO and CBOD concentrations in the incoming bay water. The hypoxic condition can be relieved more by eliminating CBOD than by increasing DO in the incoming bay water. The sensitivity analysis also reveals that hypoxia is caused by a combination of physical and biochemical processes. Among the physical processes, an increase in either residual velocity or vertical mixing can relieve the hypoxic condition. The present model, being a complicated model, cannot separate the effects of vertical mixing and gravitational circulation.

Oxygen demands in both sediment and water column contribute to the formation of hypoxia in the lower part of the river. Water column respiration, including CBOD

decay, nitrification and algal respiration, is as important as SOD, and the CBOD decay is the most important in the water column.

6-2. Middle Part of the Rappahannock River

The middle part of the Rappahannock River between km 85-145 is bounded by shallow regions at both boundaries (Fig. 3-2). The upper limit of salt intrusion, which moves up and down the river in response to the freshwater discharge, was located around km 85 in the summer of 1990 (Figures 5-3 and 5-6). In this tidal freshwater portion of the river, a characteristic Chl maximum has been frequently observed (Anderson 1986; Kuo et al. 1991b). As possible controlling mechanisms, Anderson (1986) suggested the hydrodynamic trapping of algal biomass in the region of the turbidity maximum, rapid internal cycling of essential nutrients such as silica, and the demise of freshwater algae in the presence of salt.

The high phytoplankton concentration in the tidal freshwater and low salinity regions of estuaries has also been frequently observed in many other estuarine environments (Haertel et al. 1969; Lippson et al. 1979; Cloern et al. 1983; Pennock 1985; Relexans et al. 1988; Schuchardt & Schirmer 1991). Key mechanisms suggested by these investigators are river discharge, water residence time, solar radiation, nutrients, etc. The sensitivity analysis for these suggested mechanisms was performed to study the controlling mechanism(s) for high Chl, and the results from sensitivity runs are shown in Figures 6-16 through 6-20.

6-2-1. Results from sensitivity runs

In model calibration (Section 5-2-5) and verification (Section 5-3-2), the shortcoming of the current model calibration and verification for P2 was acknowledged. Because the quality and quantity of the field data used for the current

calibration and verification are limited, more detailed field data to calibrate the present model are needed before a reliable sensitivity analysis of nutrient limitation can be conducted. The current sensitivity analysis pertaining to nutrients, and results from these analysis should be construed with caution.

In model calibration, an external input of nutrients in the form of benthic flux of P2 and N2 was needed to reproduce the field observation of high Chl concentration in the mid-reach of the river. Results from a sensitivity run without the P2 benthic release are presented in Fig. 6-16, and those without the N2 release in Fig. 6-17. These two sensitivity runs are not intended to assess the limiting nutrient but to assess whether the external input of nutrients (N2 and P2) is needed to maintain the high Chl concentration. Without P2 release from sediment in Fig. 6-16, the model predictions of Chl, P2 and total phosphorus become too low compared to the field data between km 85-140. In Fig. 6-17, the high Chl between km 85-125 cannot be maintained without the N2 benthic flux and the model predictions of total nitrogen between km 80-165 become too low compared to field data. Therefore, both P2 and N2 fluxes from sediment are necessary to maintain the high Chl in the mid-reach and to reproduce the field measurements of total nitrogen and phosphorus.

The shallow embayments, treated as side storage area in the model, may have high primary production owing to the shallow depth along this reach of the river. It, thus was suspected that the contribution from the storage area might be responsible, at least in part, for the high Chl concentration in the main channel. Results from a sensitivity run without the storage area show negative contribution from storage area in the mid-reach of the river (Fig. 6-18), that is, the storage area acts as a sink for Chl. The Chl settling rate of 10 cm day^{-1} was used in both the main channel and the storage area in model calibration. Results from a sensitivity run show that the Chl in the main channel increases with zero settling rate of Chl in the storage area. Because

of the shallower depth in the storage area, the loss of Chl due to settling may be higher in the storage area than in the main channel making the storage area act as a sink for Chl in the main channel.

The effect of light intensity was examined by increasing or decreasing light extinction coefficient (K_e). Results in Fig. 6-19 show that the Chl concentration increases (decreases) significantly as K_e decreases (increases) upriver of km 145. The light availability used in model calibration is necessary to maintain the high Chl concentration between km 85-145. Finally, the results from model simulations with altered freshwater discharge rates are presented in Fig. 6-20. It shows that the effect of freshwater discharge rate over the range used in the sensitivity runs is important only upriver of km 125.

Results in Figures 6-16 through 6-20 indicate that the availability of light and nutrients, phosphate and ammonia, is essential to maintain the high Chl concentration between km 85-125. Anderson (1986) suggested, as one of the possible controlling mechanisms for the high Chl concentration in the mid-reach of the Rappahannock River, the rapid internal cycling of essential nutrients such as silica. The present model, since it does not include the silica cycle, cannot assess the importance of silica. The sensitivity runs, however, do indicate that even with enough silica available in the system, the high Chl concentration during summer cannot be maintained without an external input of phosphate and ammonia.

6-2-2. Hypothesis

If an external input of nutrients is required to maintain the high Chl concentration, an unanswered question is where do the nutrients come from? Another characteristic of high Chl in the mid-reach of the river is the downriver boundary that limits the high Chl upriver of km 85 (Figures 5-3 and 5-6). A hypothesis is proposed

to account for the source of nutrients and the formation of downriver limit.

Four STP's discharge wastewater, which is the primary source of inorganic nutrients, into the upper 10 km reach of the Rappahannock River. It was necessary in model calibration to have a high settling rate of P2 near STP discharges and a loss of phosphate to the sediment has been well established (see Section 5-2-3). The phosphorus-rich sediment particles in the upper part are possible source of P2 in the mid-reach of the river.

Nichols et al. (1981) investigated the sediment response triggered by the high flow event in the Rappahannock River. They suggested from the HIFLO observations in 1978 that transport through freshwater reaches is a stepwise process involving temporary accumulation followed by resuspension and downriver transport. In 1990, the largest freshwater discharge (368 cms) occurred on May 11; a runoff event of this size is about eight times the long-term mean discharge rate (46.8 cms). This "normal" high flow, which has a recurrence interval slightly greater than one year, although not a major flood, is large enough to transport the phosphate-laden sediments to the mid-reach of the river (Nichols et al. 1981). Then, the phosphate release from the accumulated sediments in the mid-reach of the river may be the nutrient source supporting the high Chl concentration.

Since the intensive 1983 algal bloom in the Potomac River, many studies have been conducted on the enhancement of phosphate release from freshwater sediments under high pH, aerobic conditions (Seitzinger 1985, 1986 and 1991; Broderick 1986; Baker & Cerco 1988; Baker 1989). The reported values from these studies using the sediment samples collected from Gunston Cove, a tidal freshwater embayment of the Potomac River are listed in Table 6-1. It shows that the phosphate release rate was less than 0.006 g P m^{-2} day^{-1} at pH = 8 and when pH is higher than 9.5, it increases to higher than 0.02 g P m^{-2} day^{-1}. The Virginia State Water Control Board (VSWCB)

has measured pH and Chl in the Rappahannock River as a part of the Chesapeake Bay Fall Line and Tributary Water Quality Monitoring Program. The seven year (1984-1990) data from VSWCB are plotted for five stations in Fig. 6-21, which shows both pH and Chl were higher in the middle part of the river (TF3.2 at km 125). Even at TF3.2, however, no pH measurement was higher than 9.5 in 1984-1990 and the maximum Chl measurement was approximately 70 $\mu g\ l^{-1}$. The peak Chl observed in the summer of 1990 was 30-50 $\mu g\ l^{-1}$ (Figures 5-3 and 5-6), which is much smaller than those observed in 1983 in the Potomac River (100-300 $\mu g\ l^{-1}$). Therefore, the enhanced phosphate release from sediments with increasing pH does not seem to apply in the mid-reach of the Rappahannock River. The phosphate release rate obtained from the calibration (0.005 g P m^{-2} day^{-1}), compared to those in Table 6-1, does not require high pH either.

The above argument, however, does not exclude the possibility in the Rappahannock River of an intensive algal bloom like that in the Potomac River in 1983. If an intensive bloom like the 1983 bloom in the Potomac River has a recurrence interval greater than seven years (which is quite probable since no major bloom like that in the Potomac River in 1983 has been reported since then), then the pH-Chl data in Fig. 6-21 are not long enough to show the event(s) of high pH. If favorable climatic and hydrologic conditions (continued solar radiation, and below average river flows and wind speed) with adequate nutrients were to occur in the lower portion of tidal freshwater of the Rappahannock River, the Chl concentration might become high enough to increase pH through photosynthesis. Then, the increased pH brings about phosphate release from sediments, which in turn leads to a further increase in photosynthesis and a positive feedback mechanism ensues resulting in an intensive algal bloom.

If sediment transport from the upper part and subsequent nutrient release from

sediment provide nutrients in the mid-reach, another question is why it stops around km 85 to form the downriver limit of high Chl? The mid-reach of the river is shaped like a deep hole with the deepest region occurring around km 100, and is separated from the saline, lower part of the river by a shallow region between km 65-80 (Fig. 3-2). This bottom topography would require a major flood, i.e., freshwater discharge that is much larger than the annual peak discharge, to push the sediment over the shallow region into the lower part of the river. That is, the geometric trapping of the nutrient-laden sediments in the deep hole in the mid-reach of the river may be responsible for the formation of downriver limit of high Chl around km 85.

The turbidity maximum occurring as a result of the gravitational circulation, forms around the null point (Conomos & Peterson 1977; Kuo et al. 1978), which was located around km 85 on 7/5/90. Then, another possibility for the downriver limit of high Chl is the hydrodynamic trapping of the nutrient-laden sediments in the region of the turbidity maximum.

Other possibilities for the downriver limit of high Chl suggested by Anderson (1986) are the hydrodynamic trapping of phytoplankton biomass in the region of the turbidity maximum and demise of freshwater phytoplankton as it reaches the saline part of the river. Without trapping of nutrient-laden sediments in the deep hole over the mid-reach, the sediments would be transported downriver into the lower part and release nutrients into the water column. Figure 6-22 shows the model predictions from a sensitivity run in which both N2 and P2 benthic fluxes were extended to the lower part between km 0-80. The Chl distribution in Fig. 6-22 shows that the hydrodynamic trapping of Chl alone without trapping of sediments cannot limit the Chl maximum upriver of km 85 in the Rappahannock River. Results from another sensitivity run without salt, i.e., assuming homogeneous river (note the gravitational circulation and thus the hydrodynamic trapping of Chl no longer exists), are presented

in Fig. 6-23. The Chl distribution in Fig. 6-23 shows that the trapping of sediments alone without the hydrodynamic trapping of Chl can limit the Chl maximum upriver of km 85.

The upper limit of salt intrusion on July 5, 1990 was located around km 85 (Fig. 5-3), which coincides with the downriver boundary of the deep hole over which high Chl was observed. Since the high Chl occurred in the freshwater part and extended downriver to km 85, death of freshwater phytoplankton in the presence of salt might contribute to the formation of downriver limit of high Chl concentration at the limit of salt intrusion.

6-2-3. Summary

High Chl concentrations in the lower portion of tidal freshwater have been observed frequently in the Rappahannock River and many other estuaries. The sensitivity analysis shows that the high Chl cannot be maintained without an external input of nutrients. A hypothesis is proposed to account for the source of nutrients and the formation of downriver limit of high Chl concentration.

It is likely that the sediments are transported from the upper part of the river during times of high freshwater flow and subsequently nutrients are released from the transported sediments. It seems that the geometric and hydrodynamic trapping of nutrient-laden sediments, and possibly the demise of freshwater phytoplankton in the salt water limit the high Chl concentration to the segment upriver of km 85. To simulate these processes more completely, the water quality model should include a sediment transport model and a sediment diagenesis model. The mechanisms that appear to be of significance include the adsorption of phosphate to sediment particles and subsequent settling, sediment transport in response to high freshwater flow and sediment phosphate release. Differentiation of phytoplankton species is necessary to

assess the effect of the demise of freshwater phytoplankton in the salt water on the formation of the downriver limit of high Chl.

Table 6-1. Average phosphate release rate from sediment as a function of pH in Gunston Cove.

pH	Phosphate Release Rate (g P m^{-2} day^{-1})		
	Seitzinger (1986)	Broderick (1986)	Baker (1989)
8.0	0.004	0.0015	0.006
9.5	0.023		0.1
10.0	0.084	0.032	
10.5	0.071		

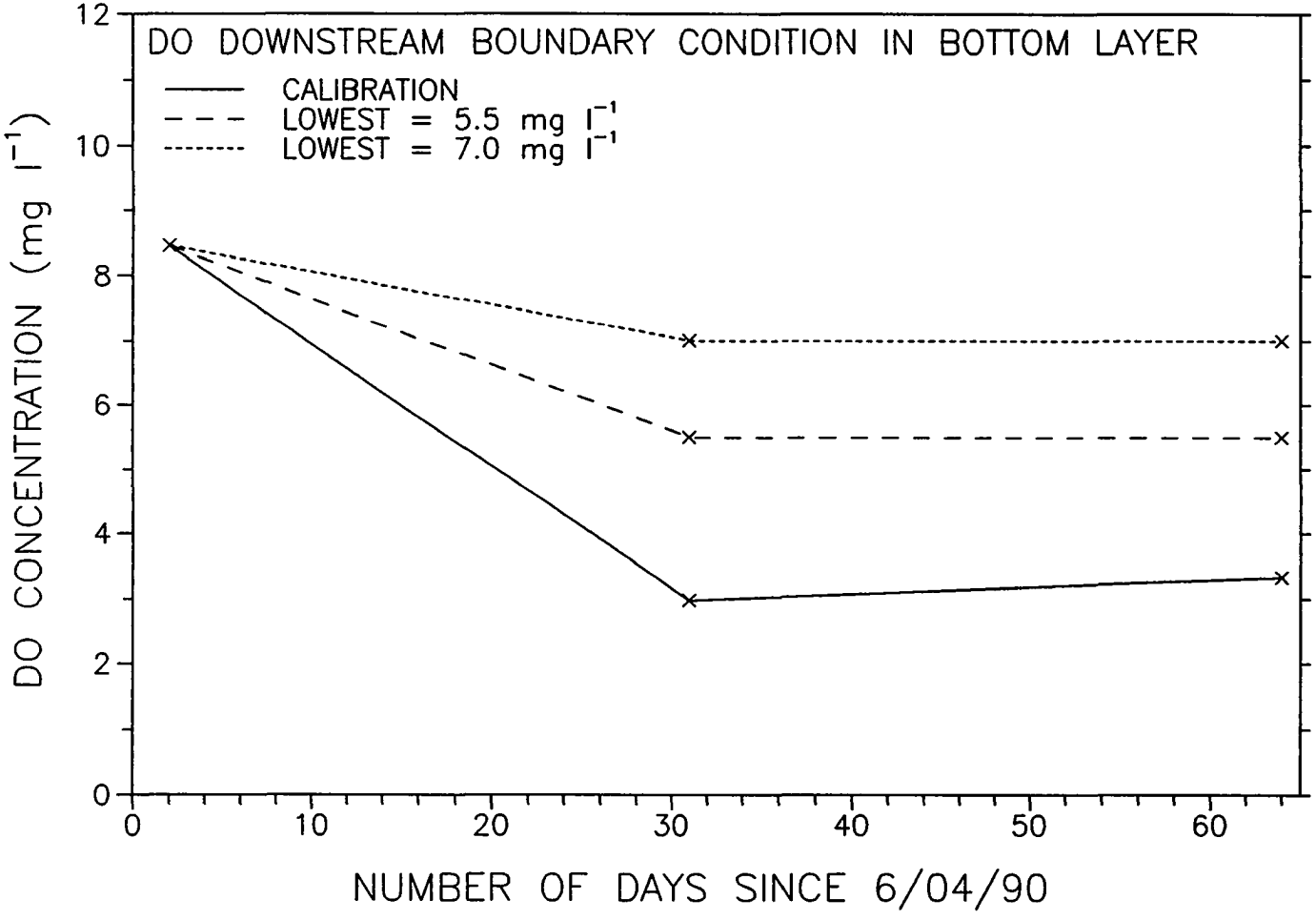

Figure 6-1. DO downstream boundary conditions in the bottom layer used in sensitivity runs.

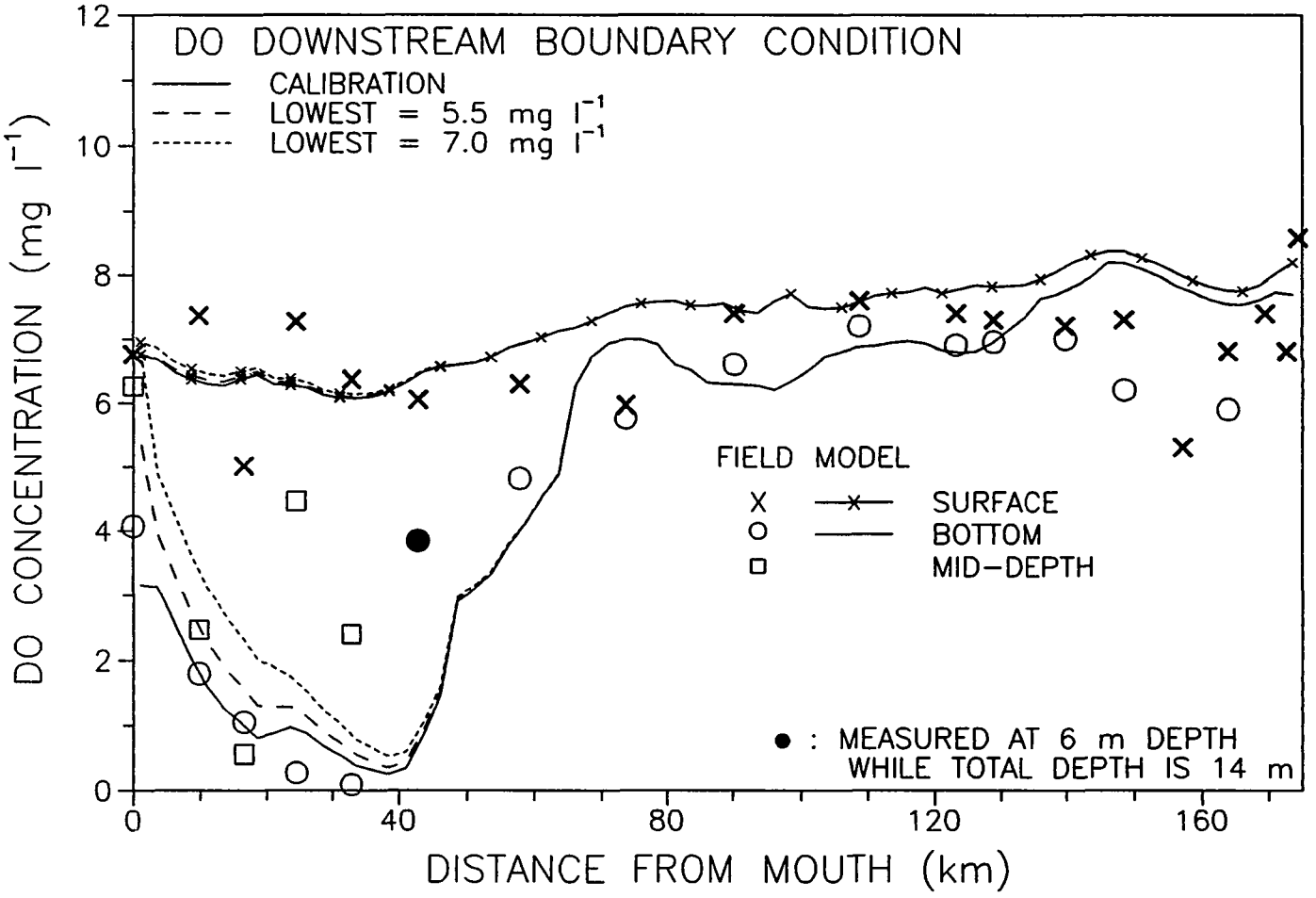

Figure 6-2. Sensitivity to DO downstream boundary condition on 7/05/90.

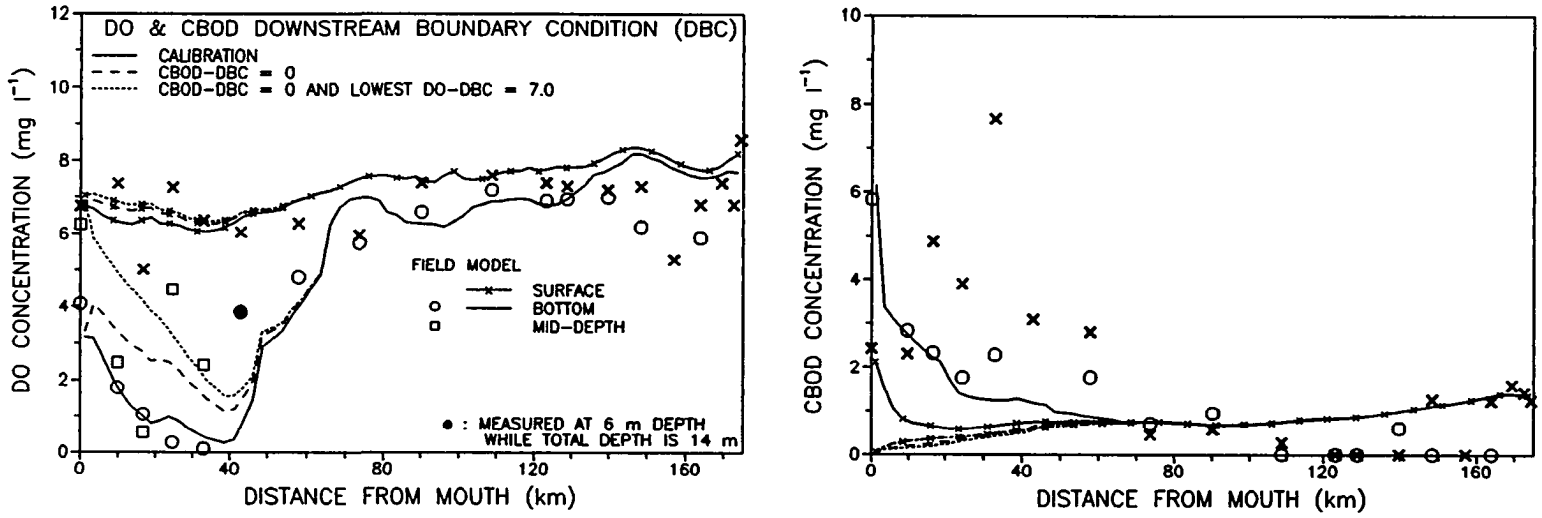

Figure 6-3. Sensitivity to DO and CBOD downstream boundary conditions on 7/05/90.

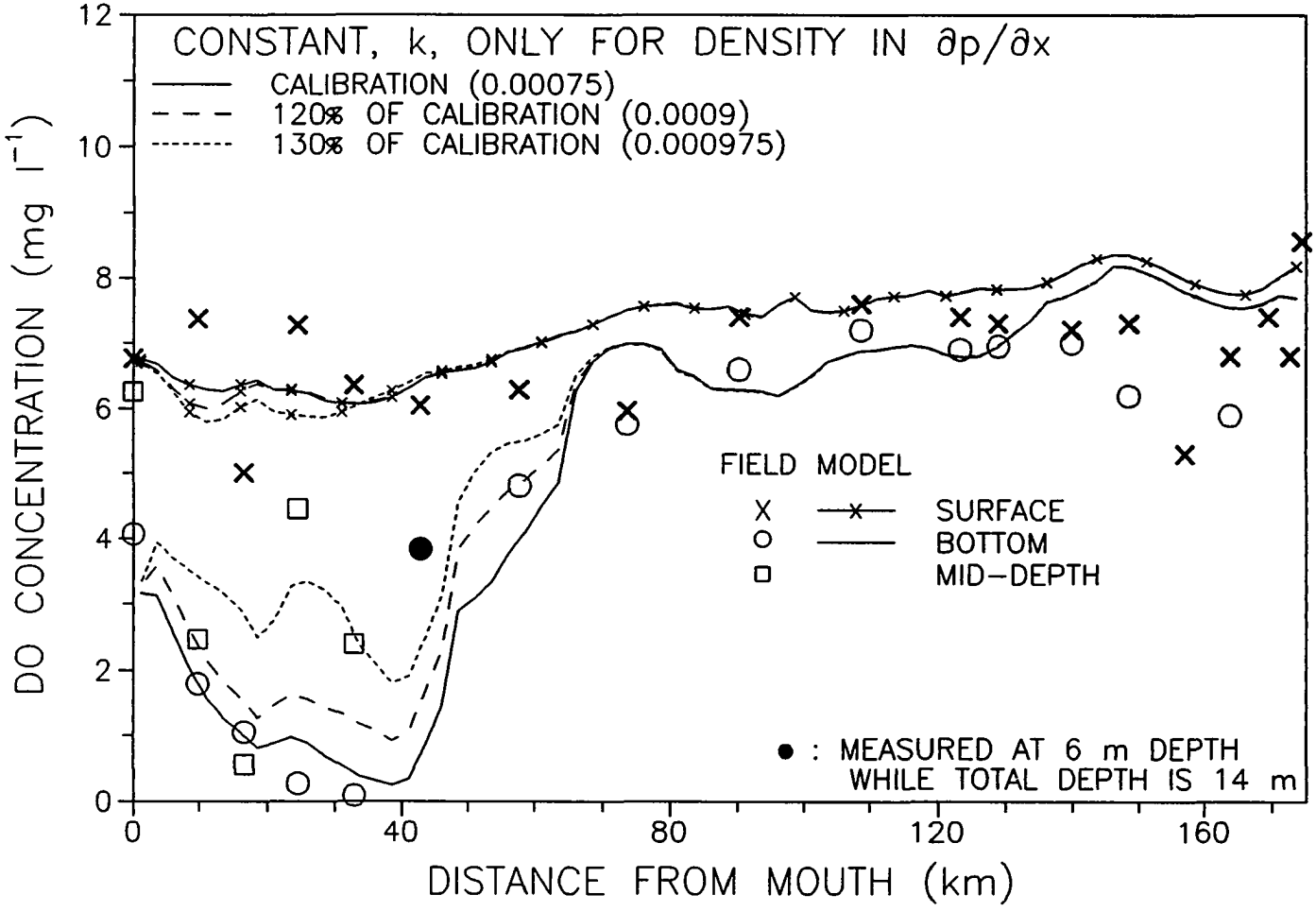

Figure 6-4. Sensitivity to gravitational circulation on 7/05/90.

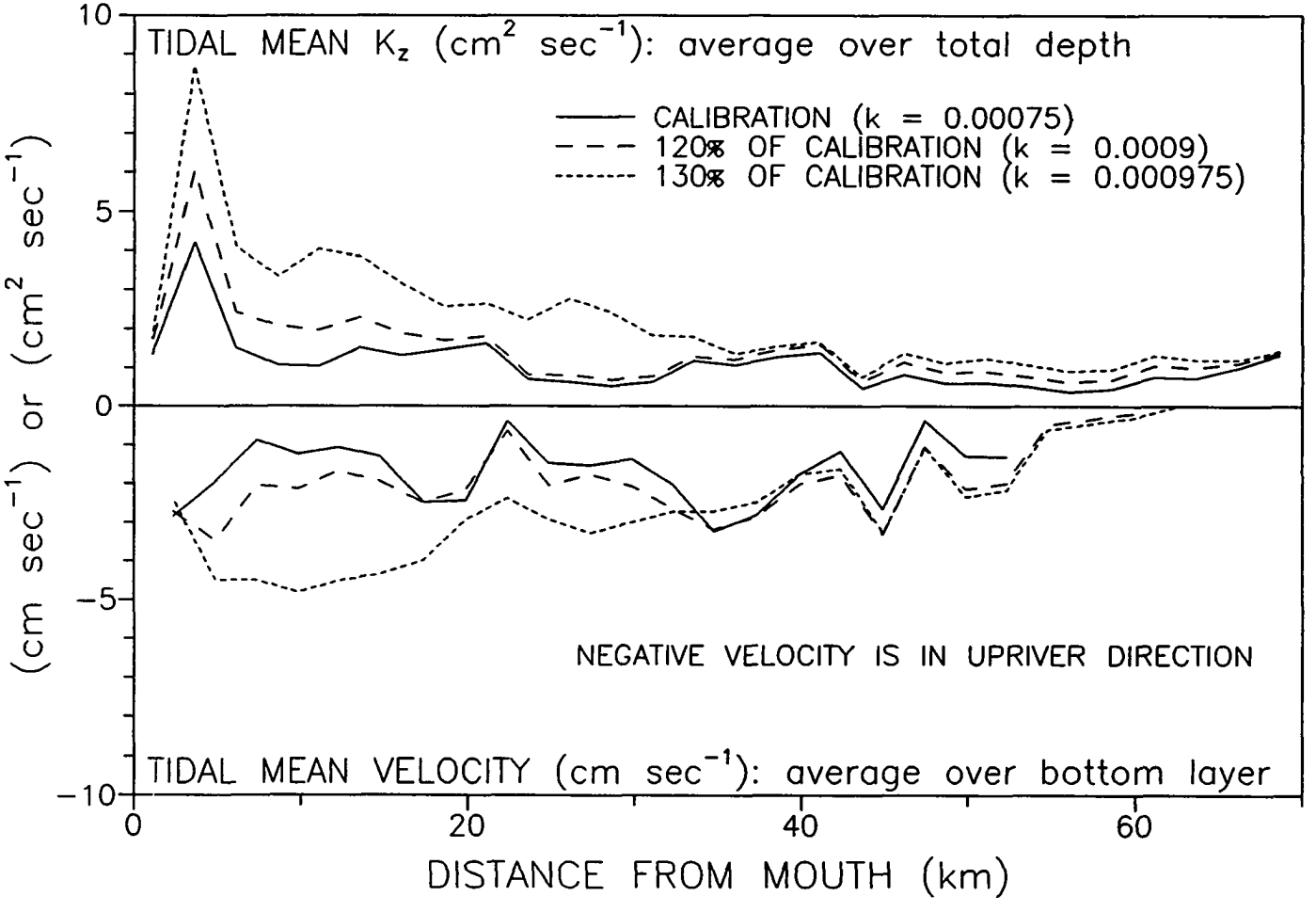

Figure 6-5. Tidal mean vertical diffusivity and velocity on 7/05/90 when varying k.

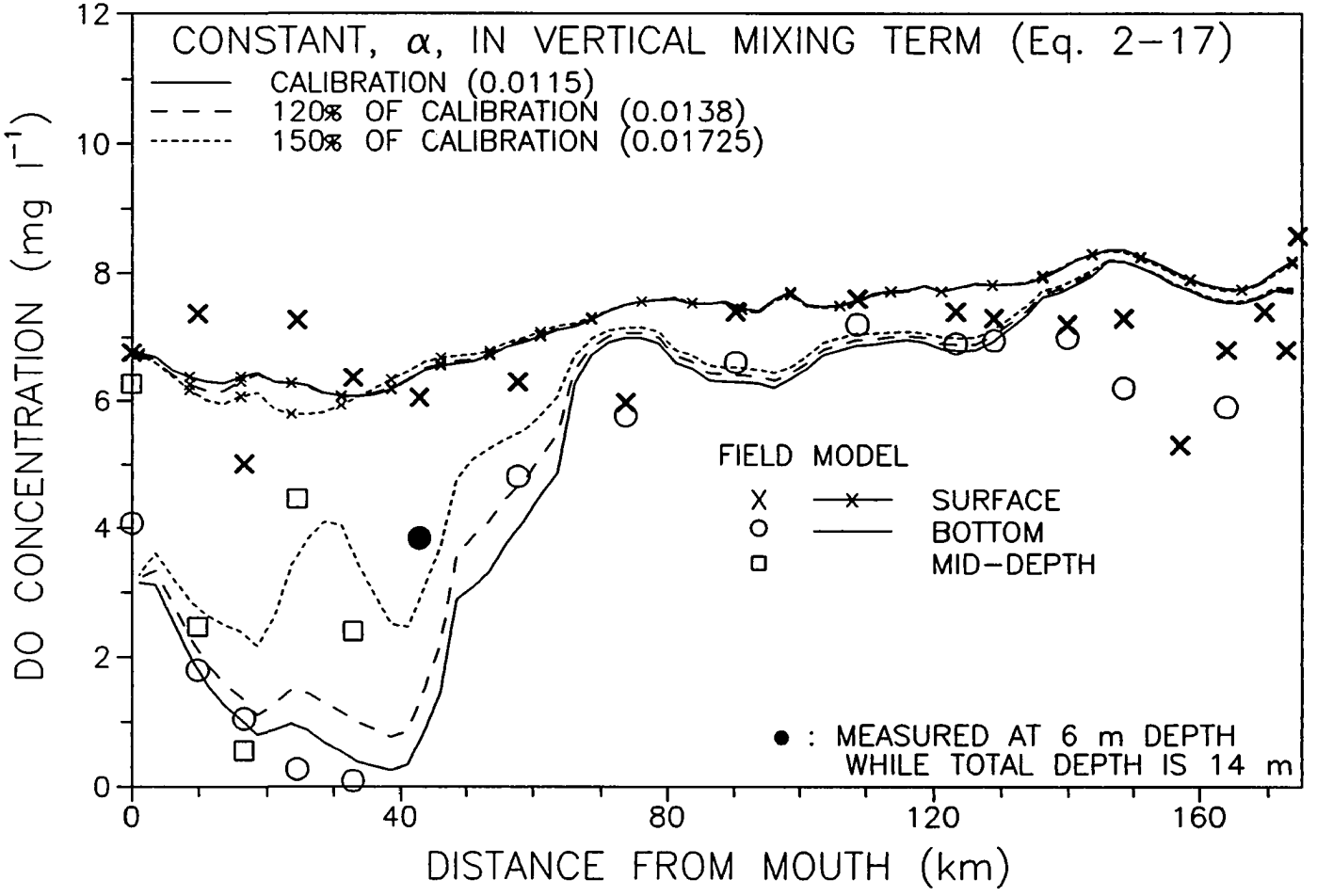

Figure 6-6. Sensitivity to vertical mixing on 7/05/90.

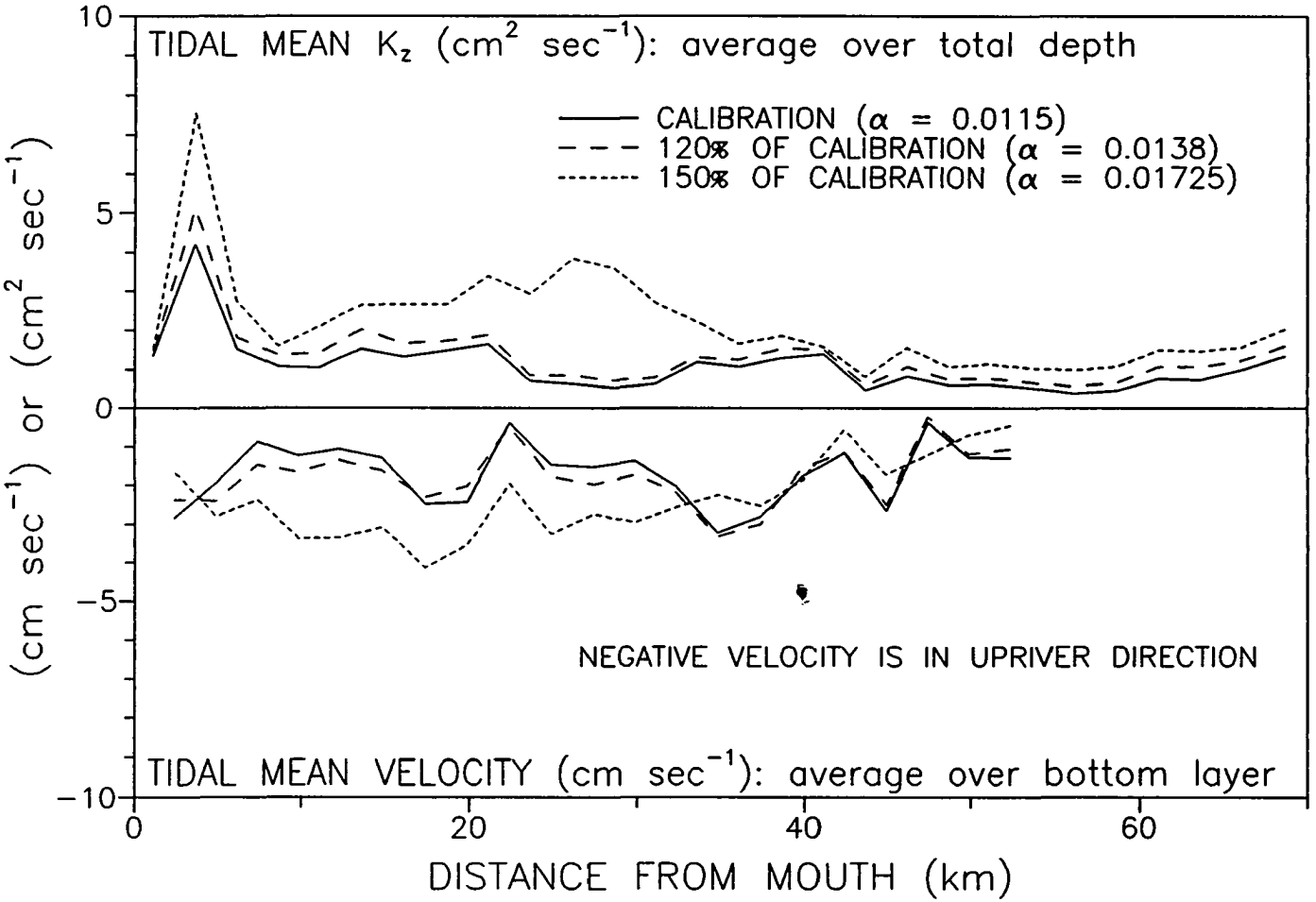

Figure 6-7. Tidal mean vertical diffusivity and velocity on 7/05/90 when varying α.

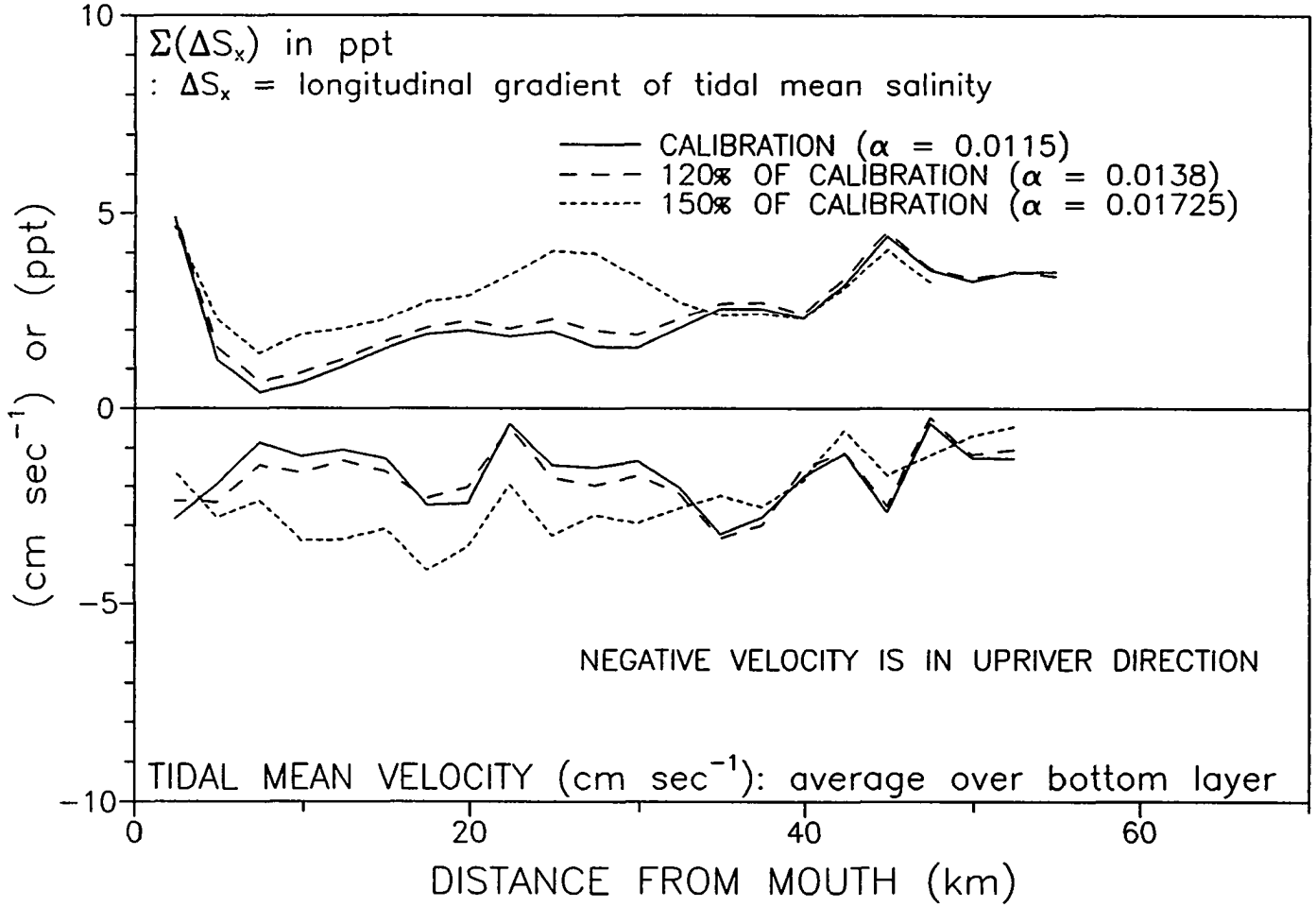

Figure 6-8. Tidal mean longitudinal salinity gradient and velocity on 7/05/90 when varying α.

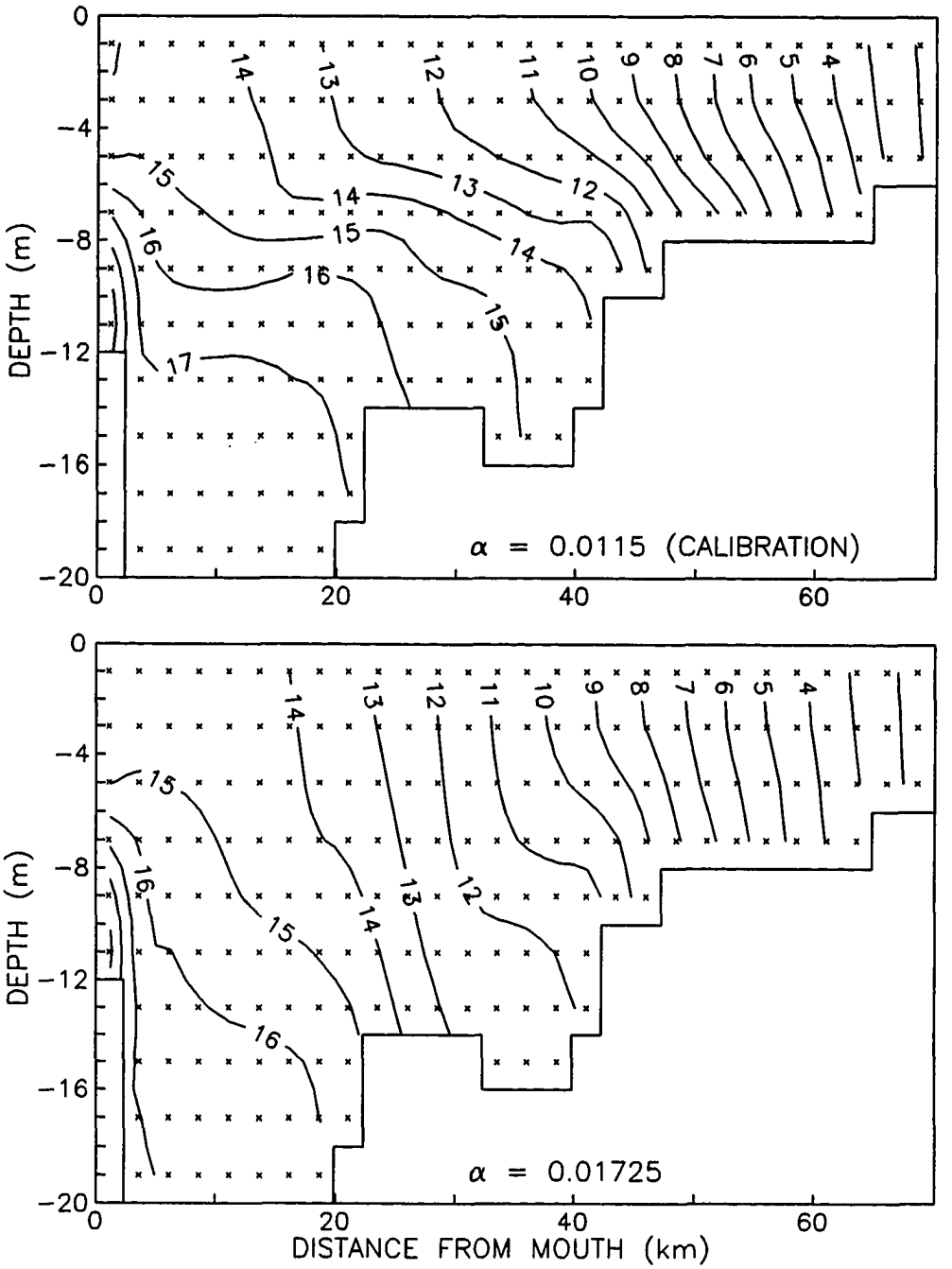

Figure 6-9. Tidal mean salinity distributions on 7/05/90 when varying α.

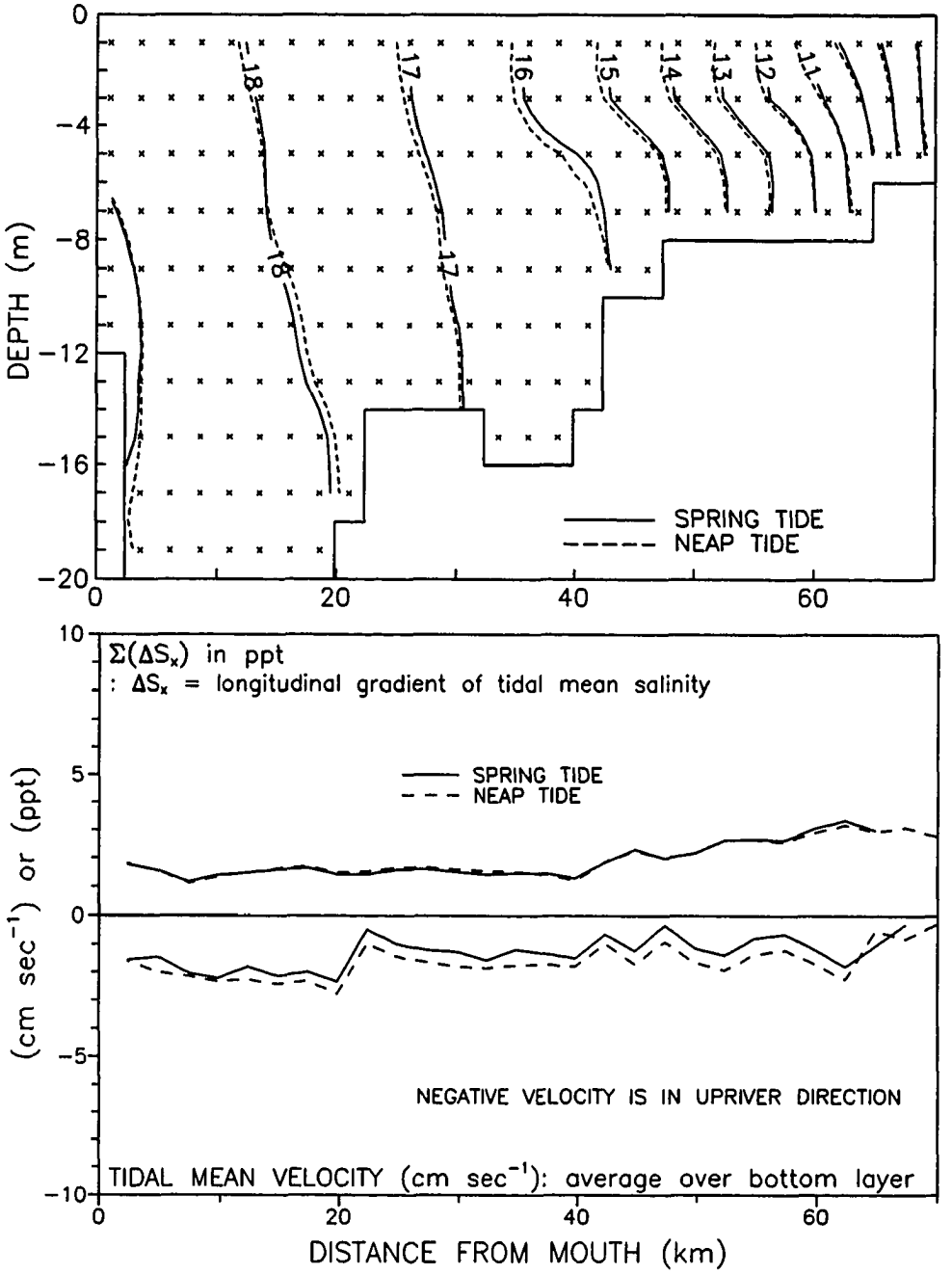

Figure 6-10. Tidal mean salinity, salinity gradient and velocity during spring and neap tides: the conditions used are described in Section 4-4-1.

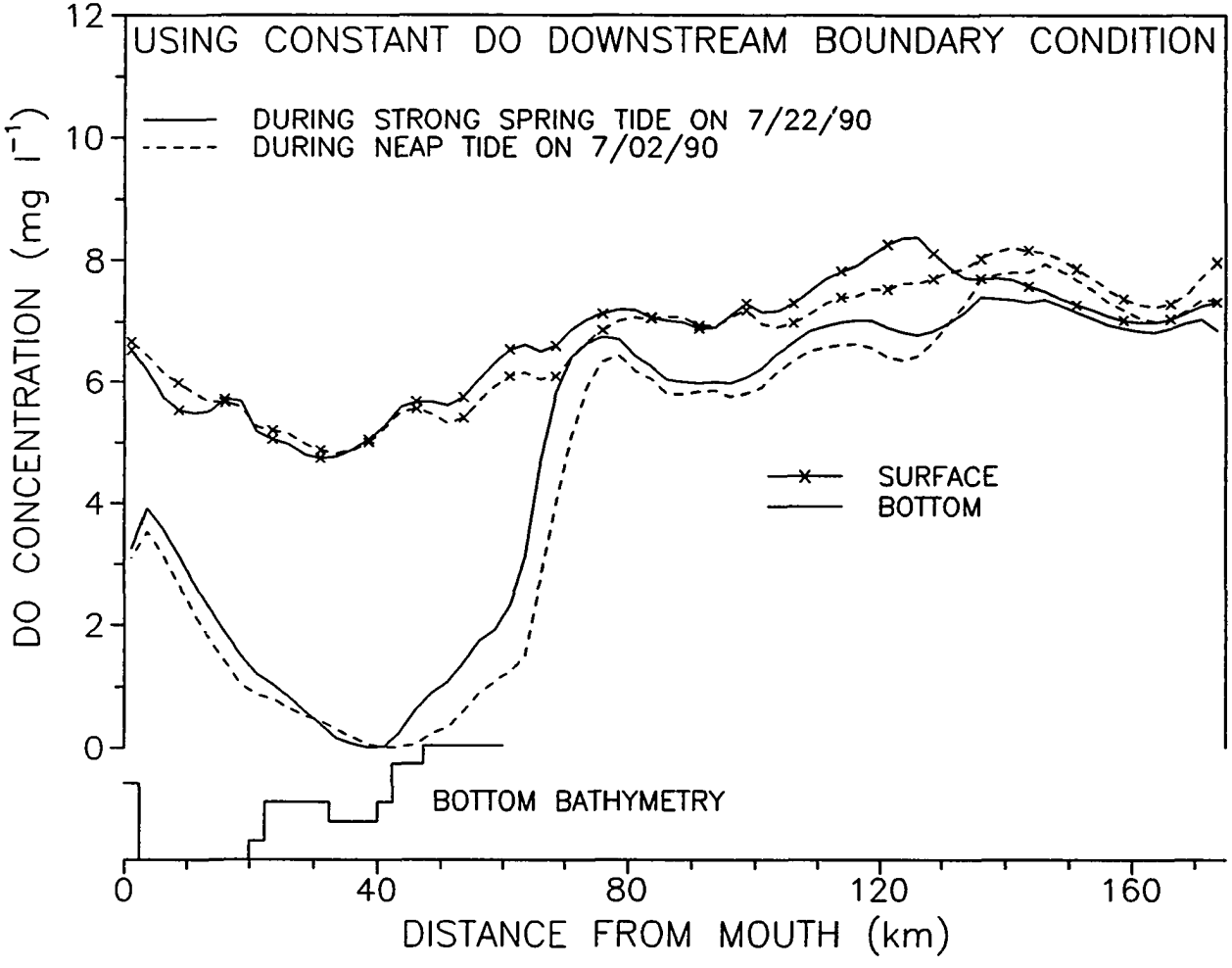

Figure 6-11. DO distributions during strong spring and neap tides using constant boundary conditions.

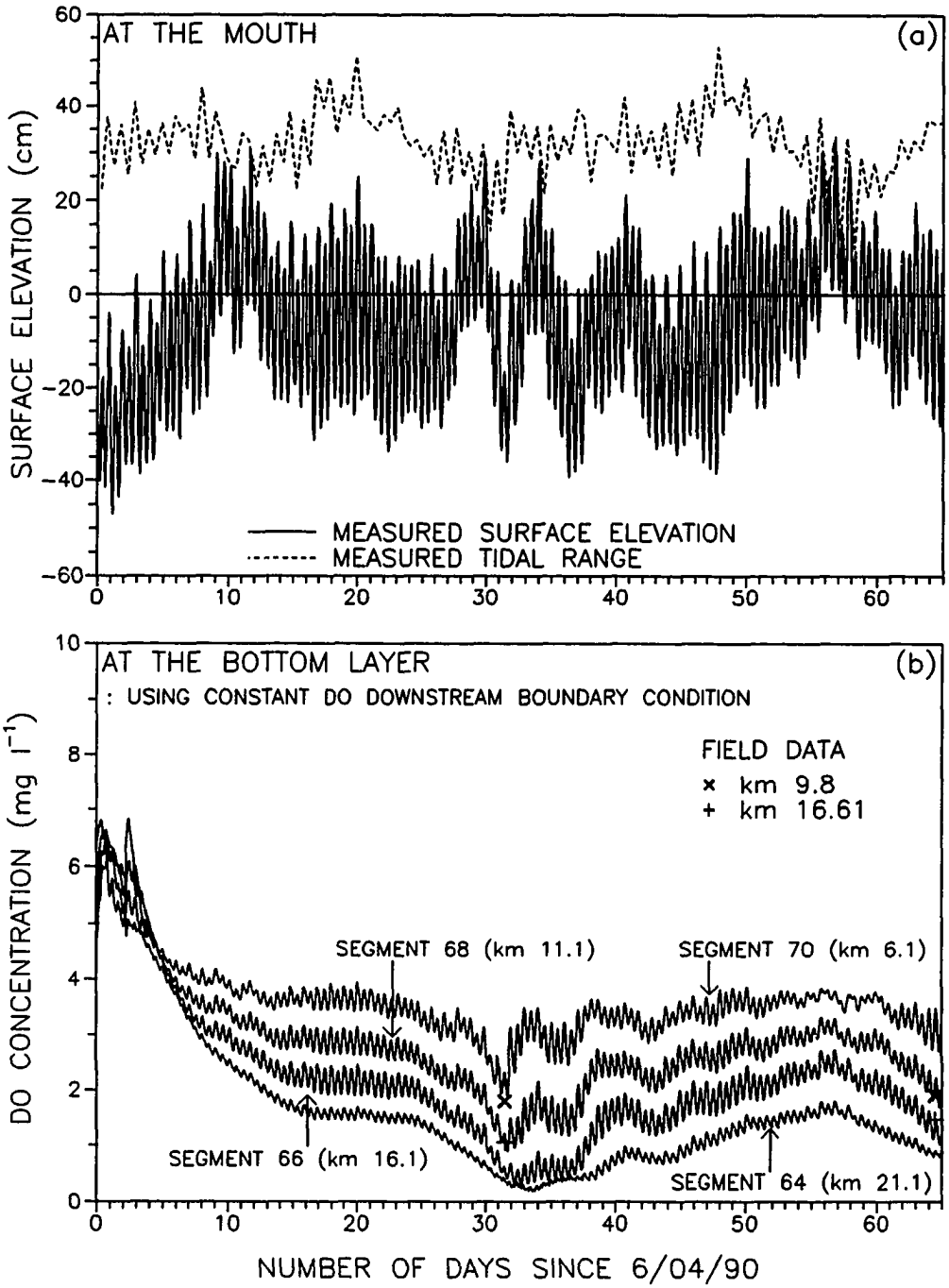

Figure 6-12. Downstream boundary condition for surface elevation (a) and time series of DO at the bottom layer (b).

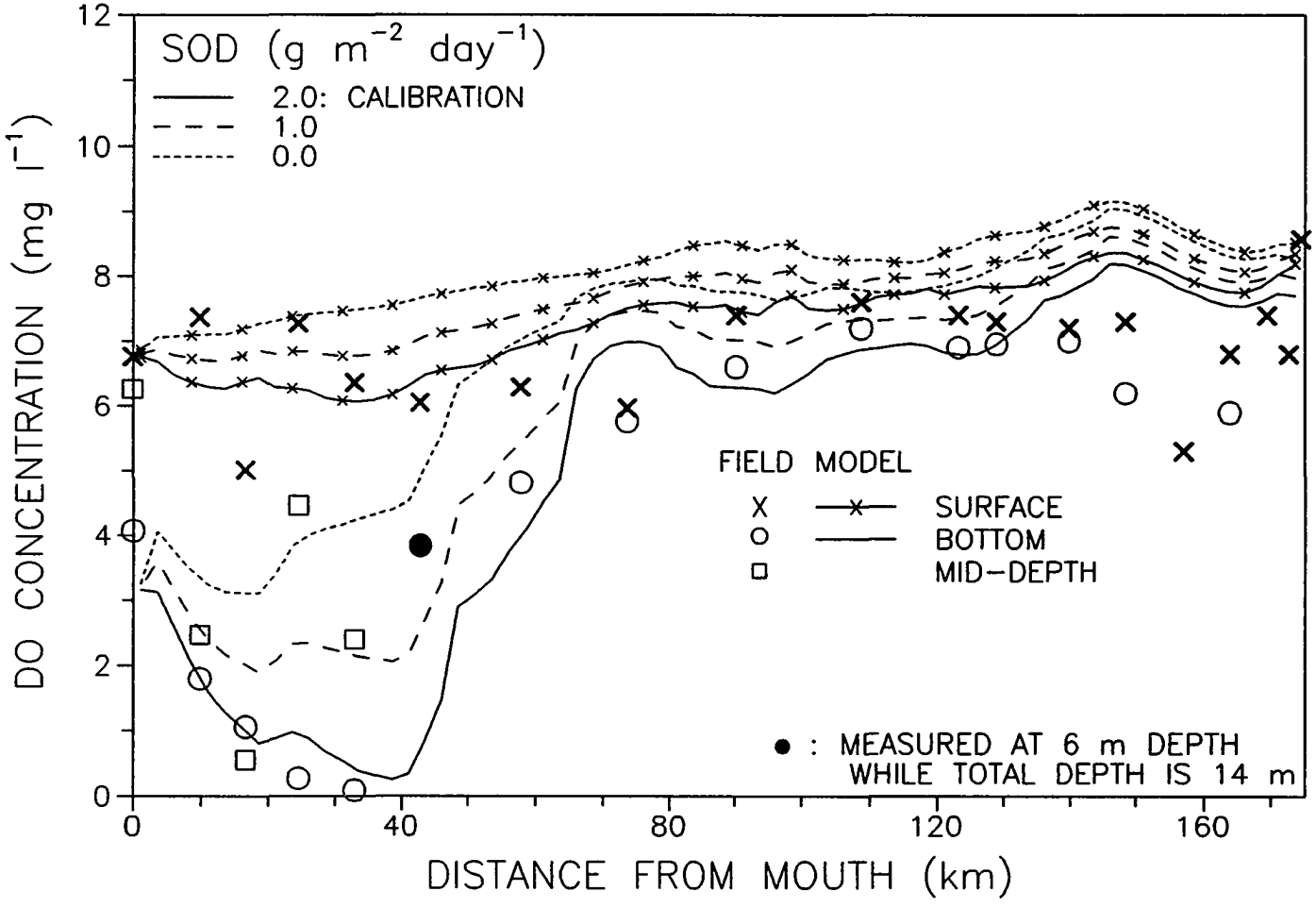

Figure 6-13. Sensitivity to sediment oxygen demand on 7/05/90.

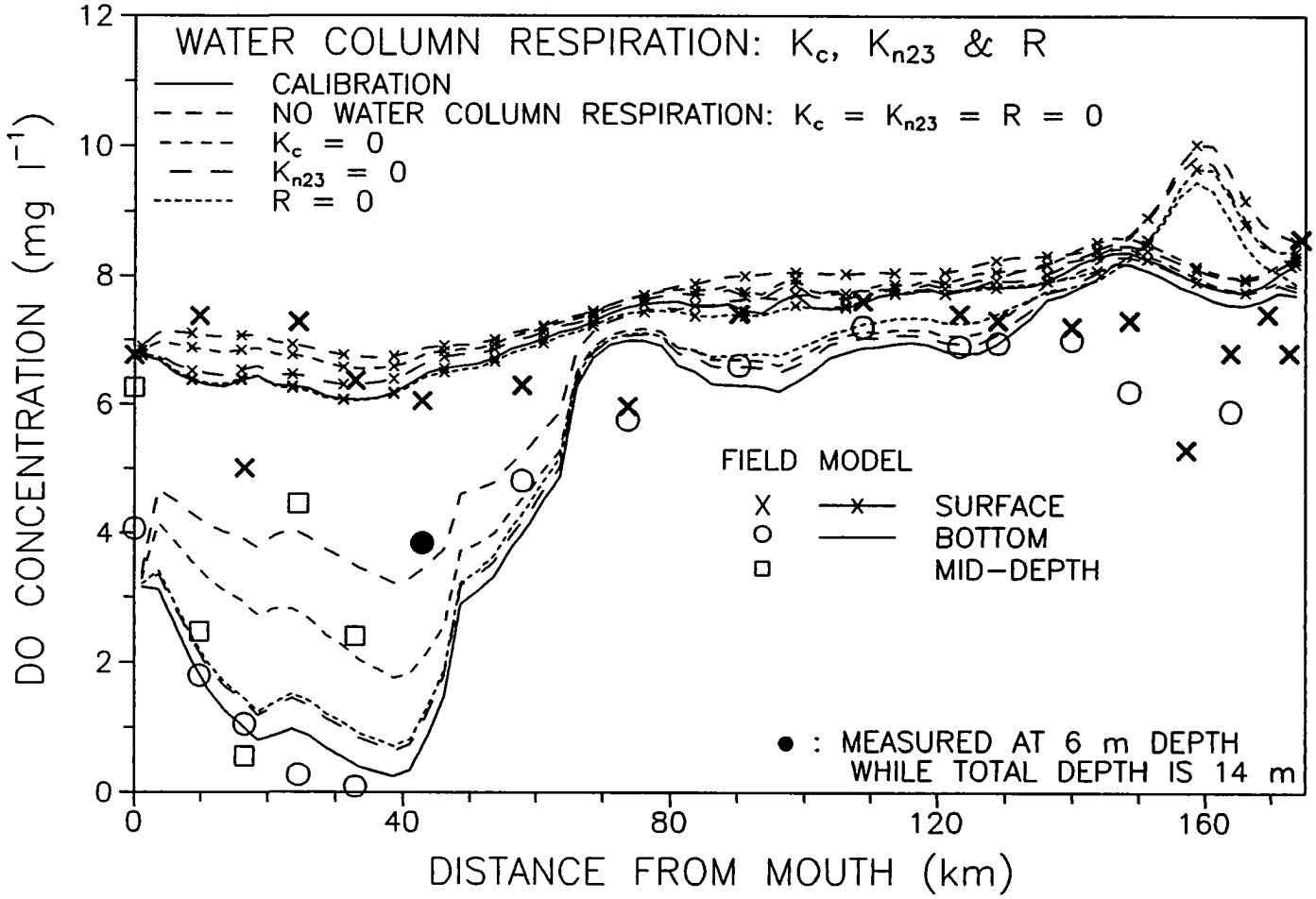

Figure 6-14. Sensitivity to water column oxygen demand on 7/05/90.

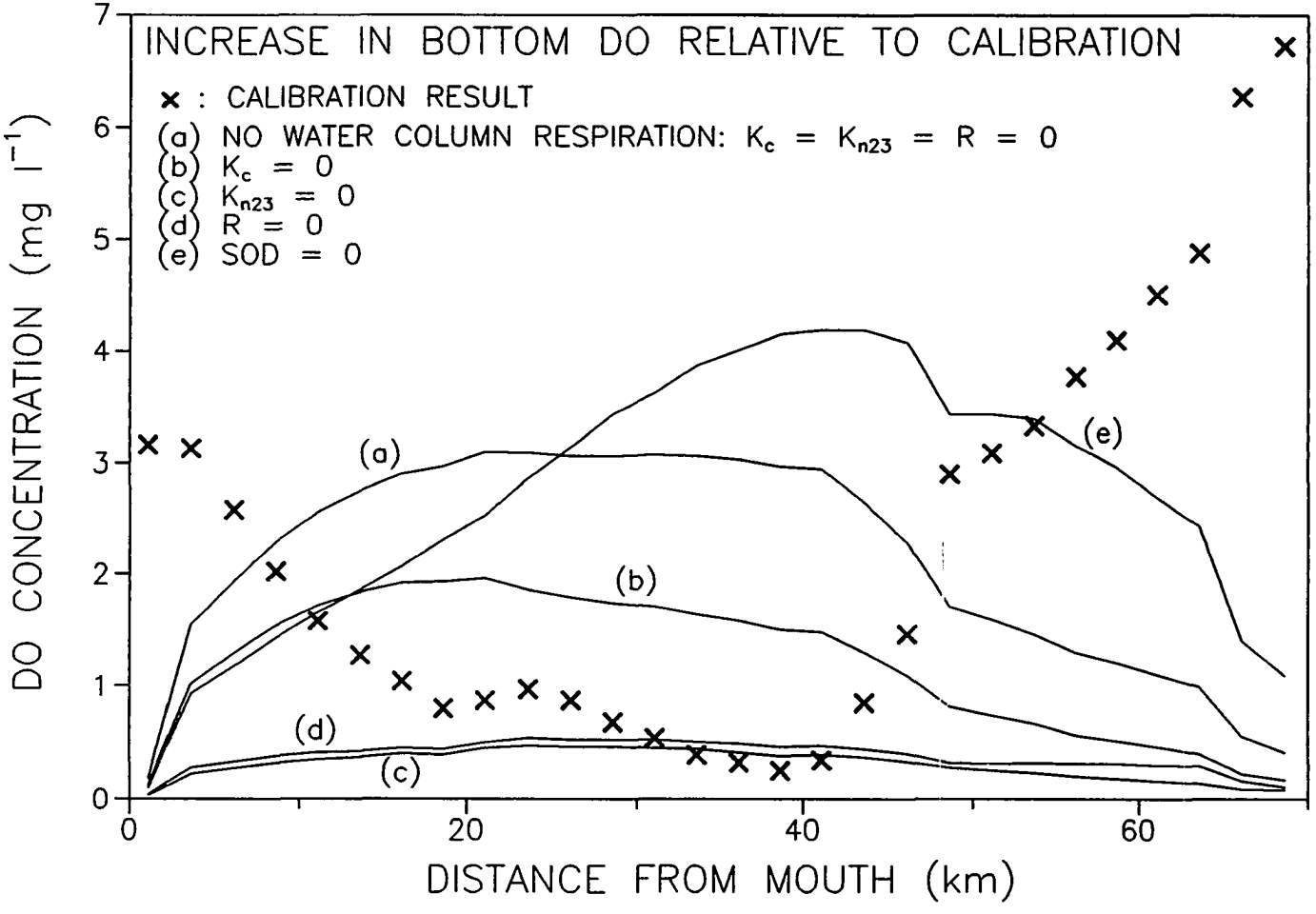

Figure 6-15. Contribution to hypoxia of oxygen demands in water column and sediment on 7/05/90.

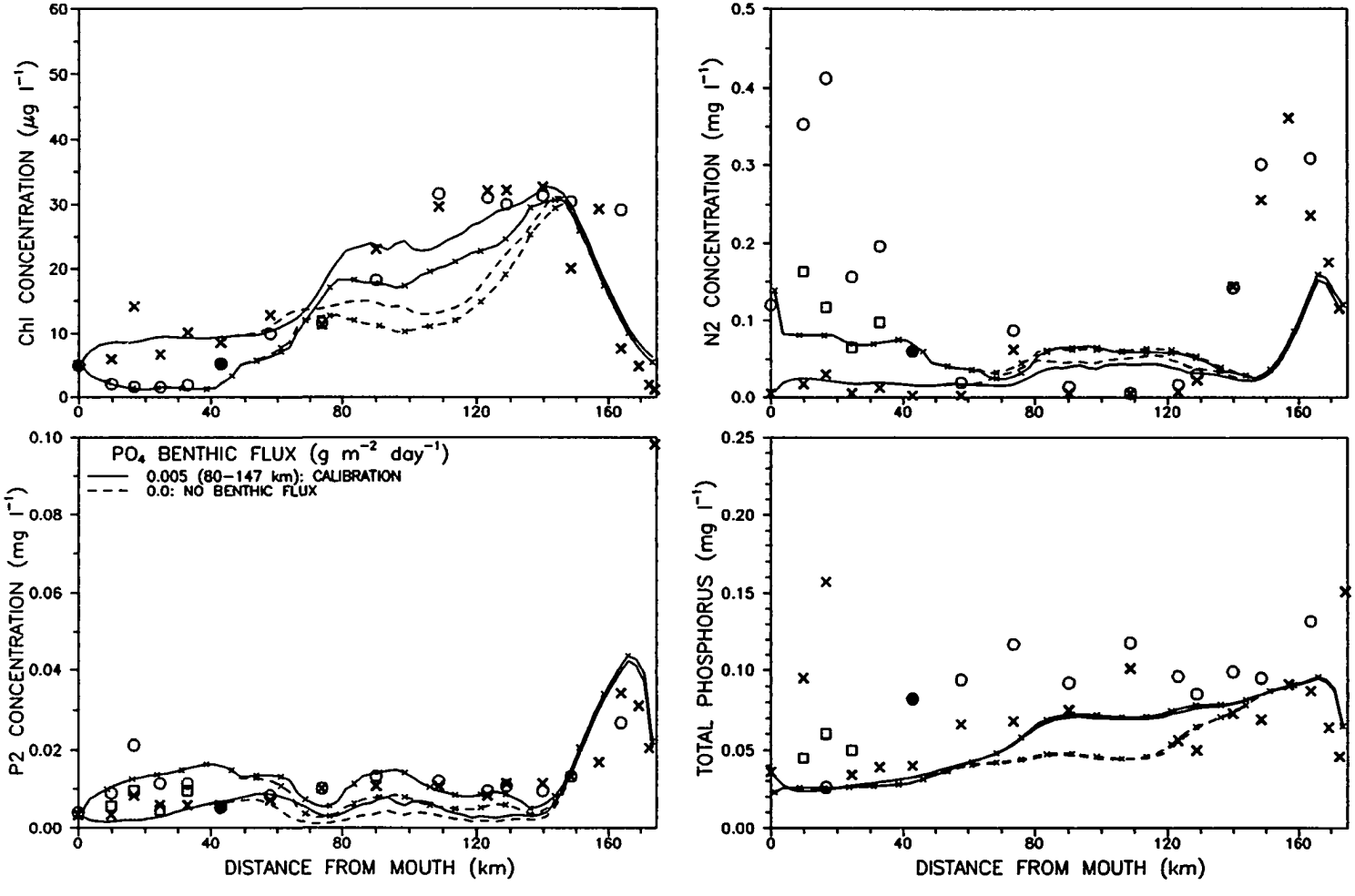

Figure 6-16. Sensitivity to benthic flux of phosphate between km 80-147 on 7/05/90.

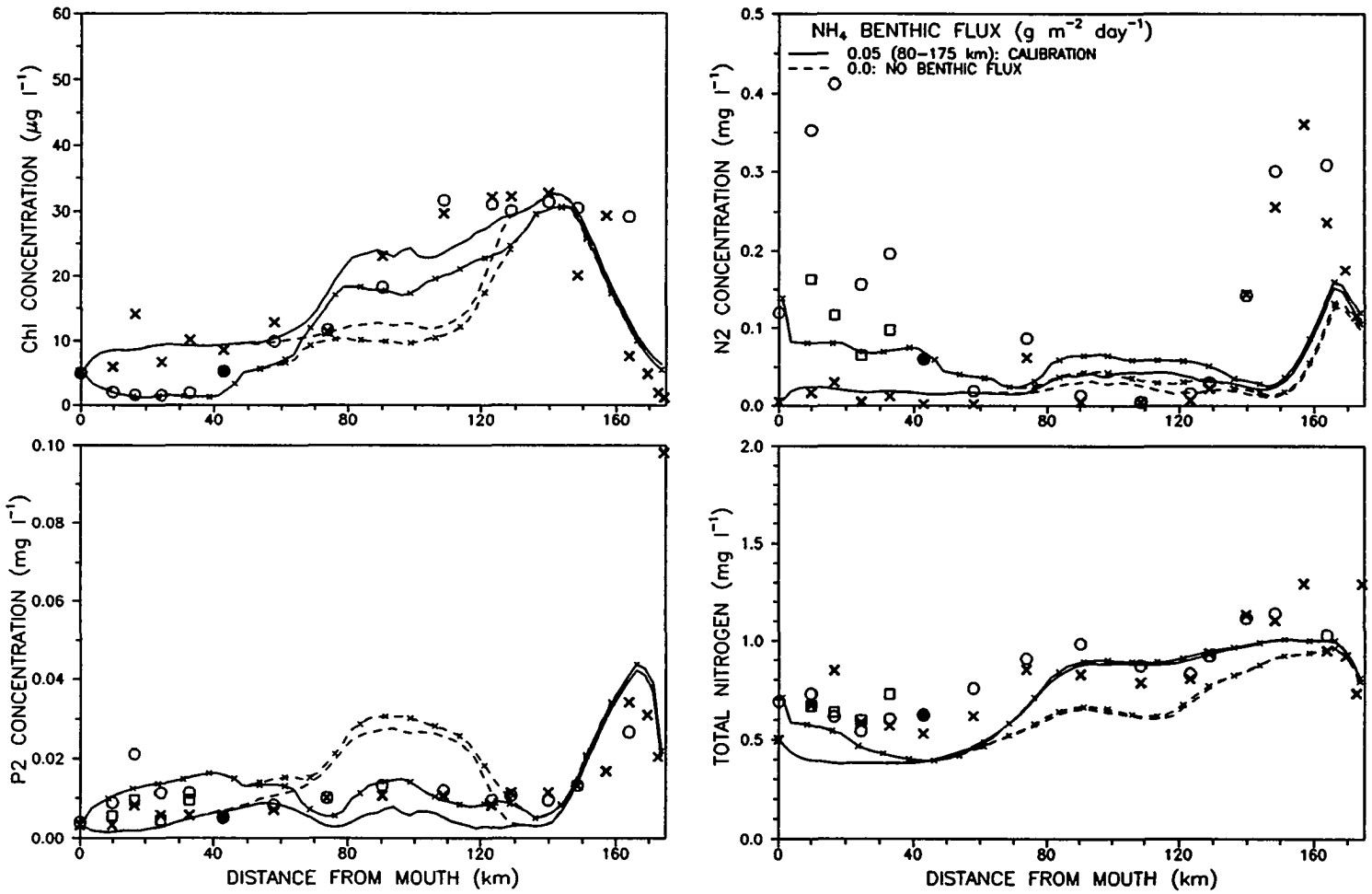

Figure 6-17. Sensitivity to benthic flux of ammonia between km 80-175 on 7/05/90.

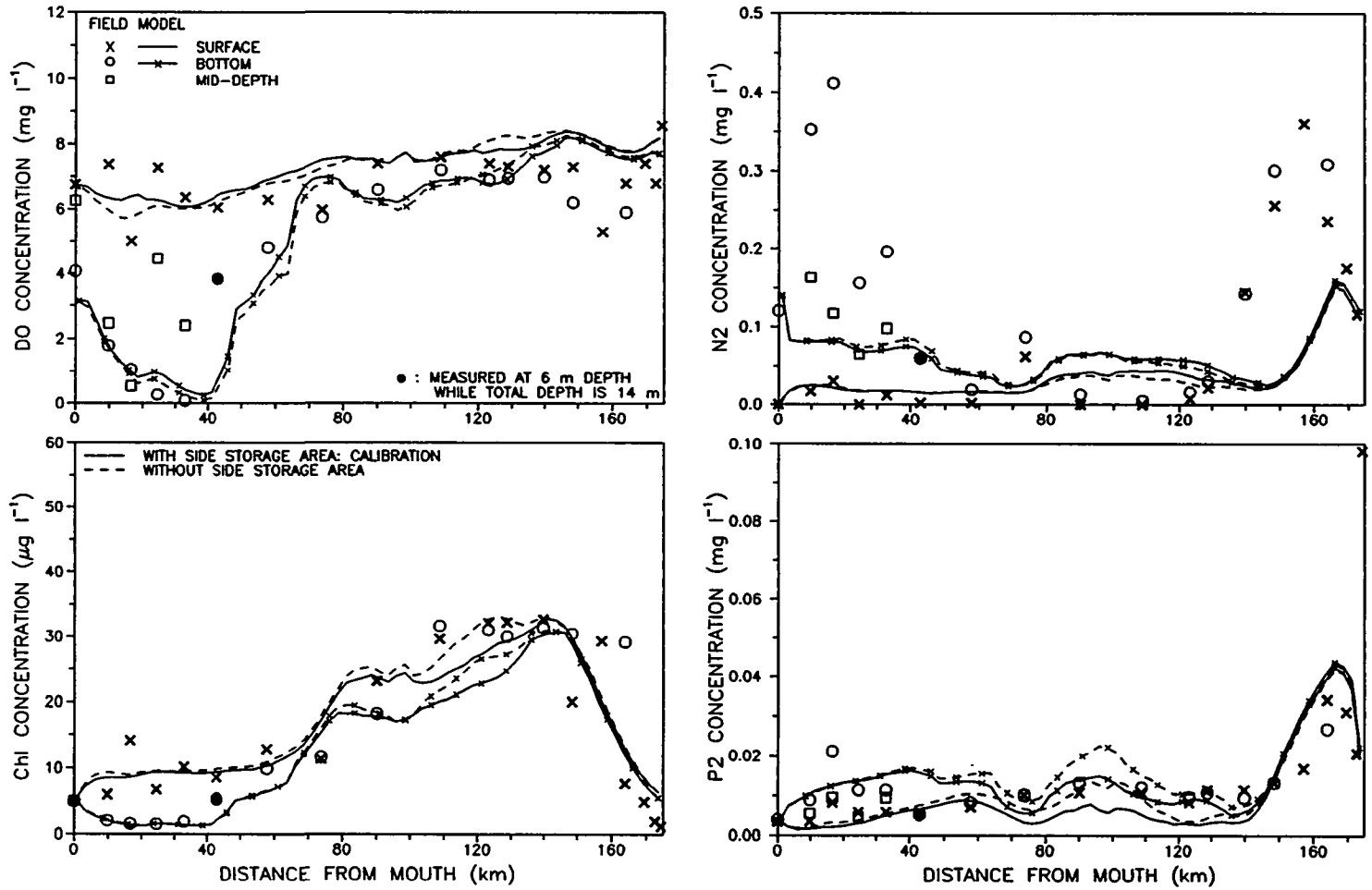

Figure 6-18. Sensitivity to the presence of side storage area on 7/05/90.

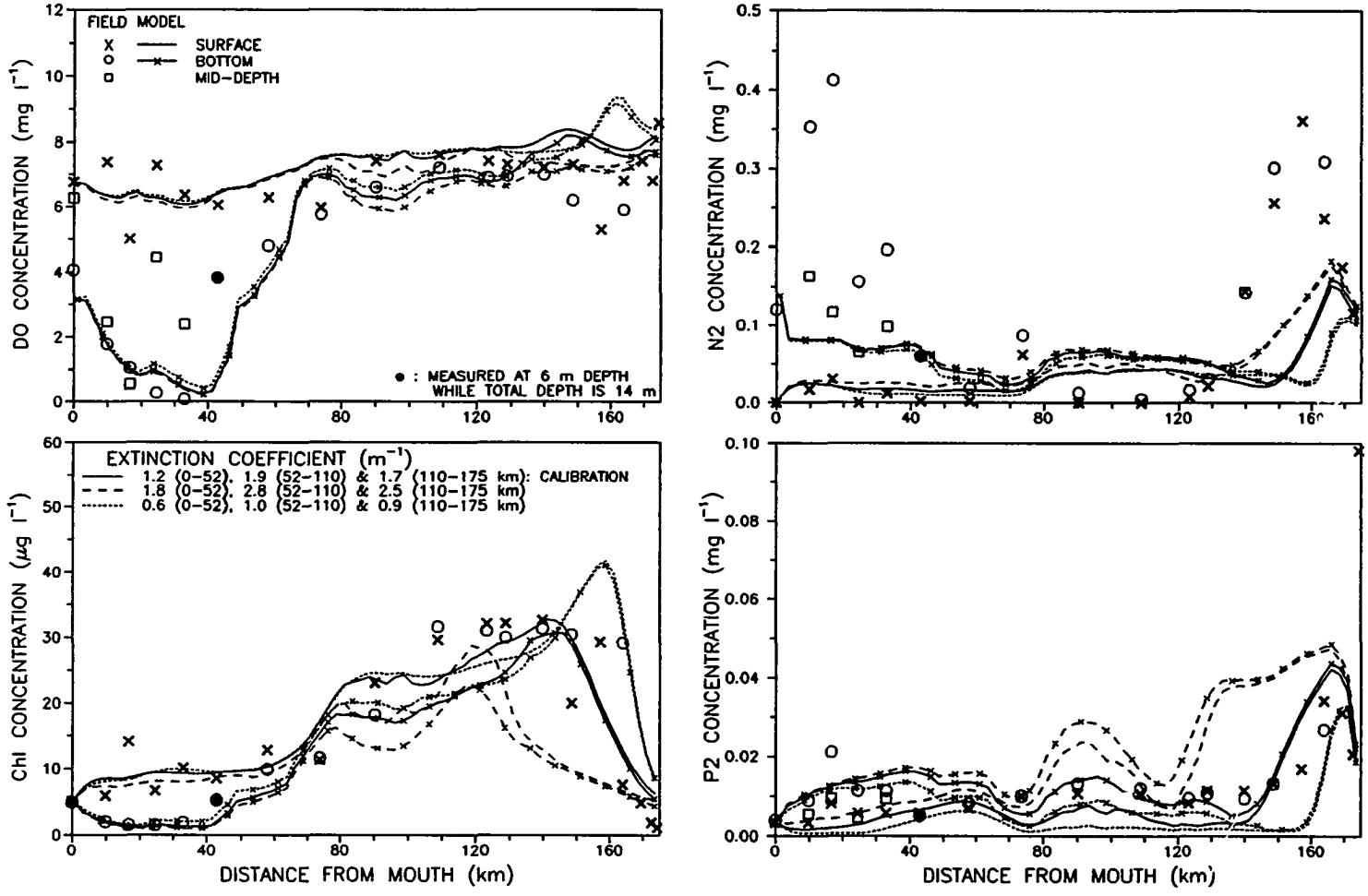

Figure 6-19. Sensitivity to light extinction coefficient on 7/05/90.

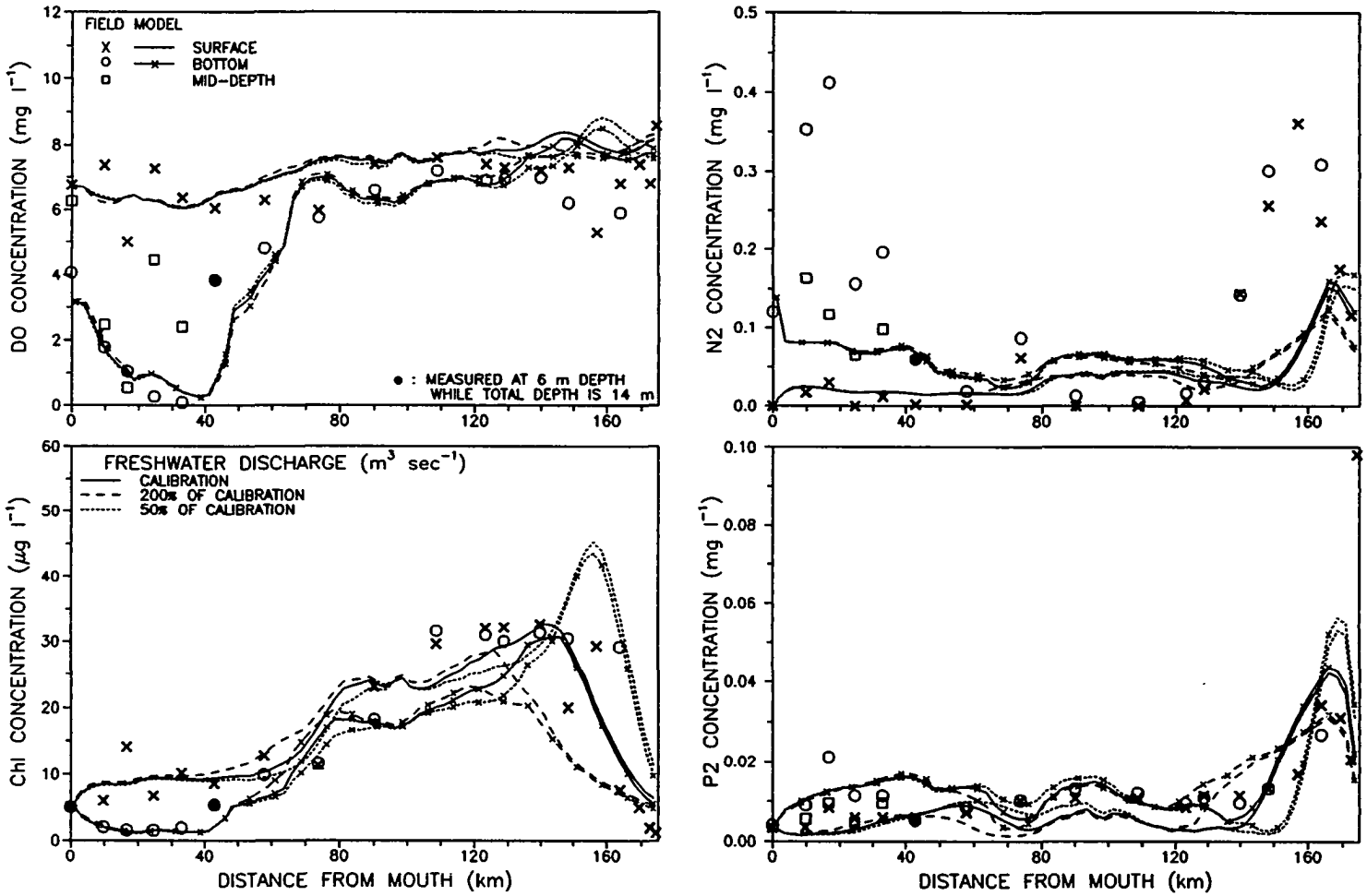

Figure 6-20. Sensitivity to freshwater discharge rate on 7/05/90.

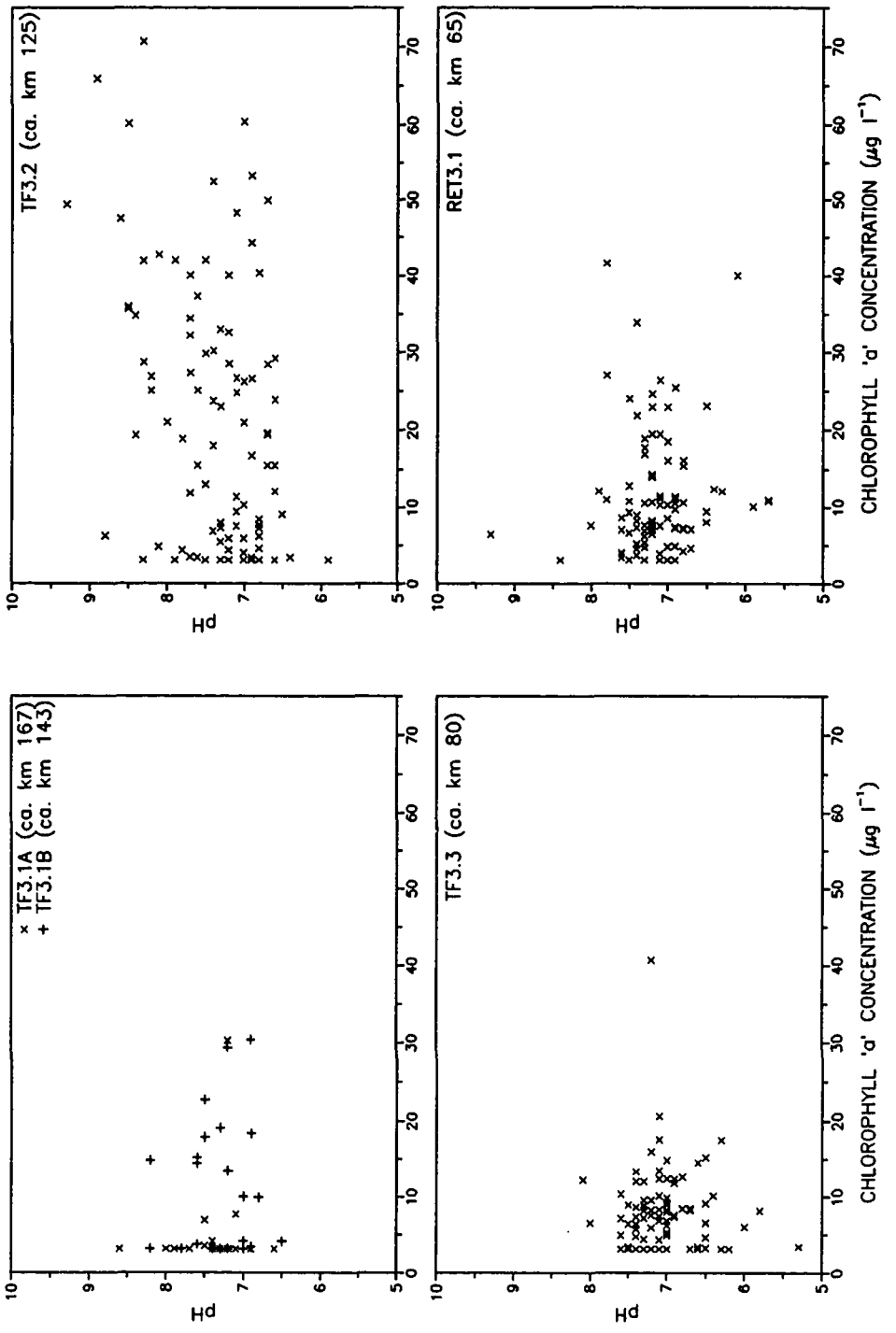

Figure 6-21. pH versus chlorophyll 'a': data from VSWCB.

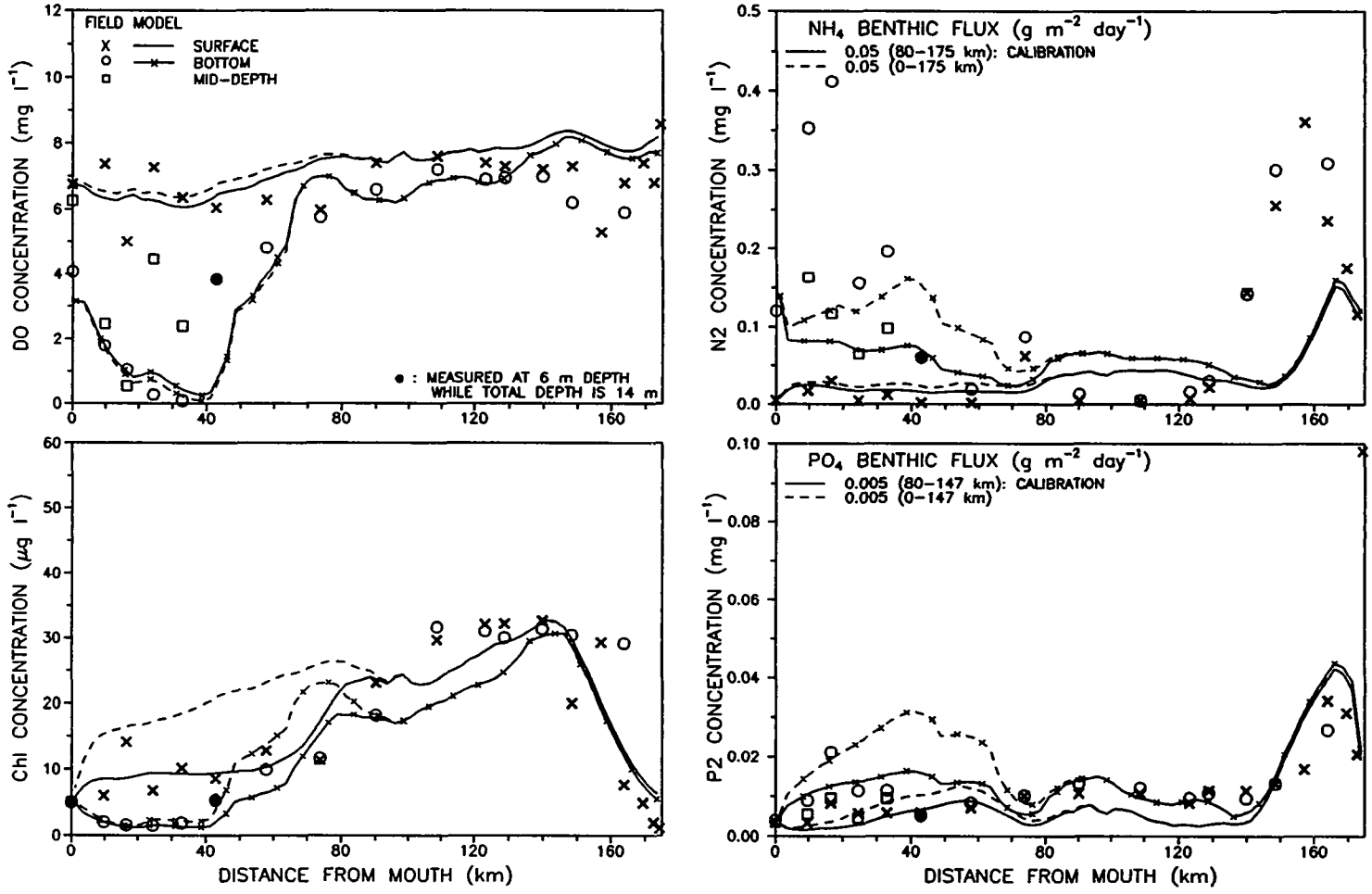

Figure 6-22. Sensitivity to benthic fluxes of ammonia and phosphate between km 0-80 on 7/05/90.

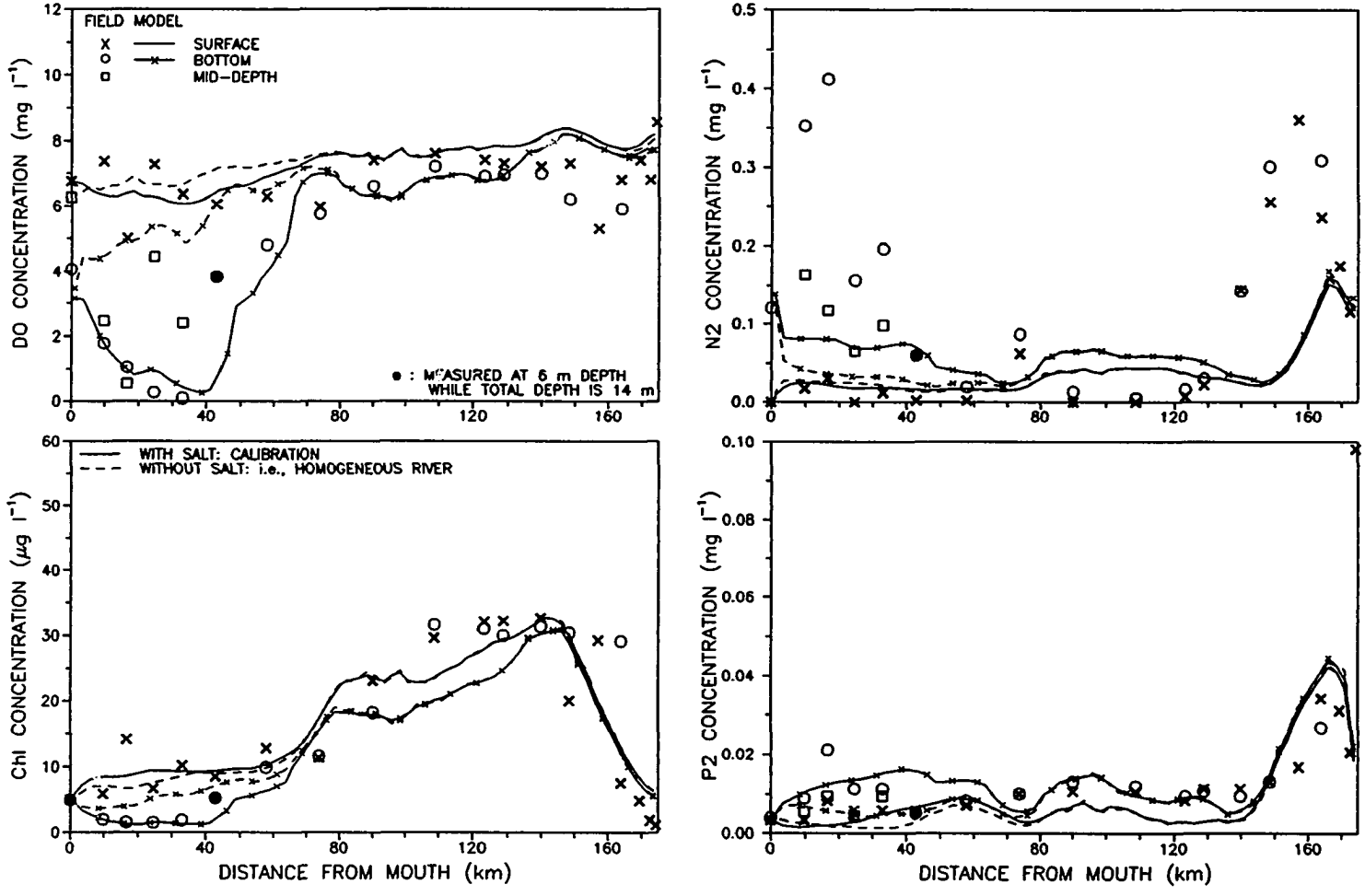

Figure 6-23. Sensitivity to the presence of salt on 7/05/90.

VII. SUMMARY AND RECOMMENDATIONS

7-1. Summary

A mathematical model has been developed to study the hydrodynamic and water quality characteristics of estuaries. The model, consisting of a hydrodynamic model and a water quality model, is a laterally integrated, two-dimensional, real-time model. The hydrodynamic model is based on the principles of conservation of volume, momentum and mass, and the water quality model on the conservation of mass alone. The model was solved using a two time level, finite difference scheme, and was applied to the Rappahannock Estuary, Virginia.

7-1-1. Hydrodynamic model

The hydrodynamic model, which provides real-time predictions of surface elevation, current velocity and transport of a conservative substance (salt), has been calibrated and verified using field data collected in 1987 and 1990. Results from the mean tide calibration show that the model describes very well the tidal characteristics at equilibrium state along the river. The vertical mixing terms were parameterized using the Munk and Anderson-type formulations. Calibration of these terms using the salinity data from 1987 slackwater surveys shows that the model provides very good description of prototype salinity distributions. The model capability of reproducing advective transport was verified by simulating the time series measurements of surface elevation and current velocity in 1987. The subtidal variations in surface elevation and current velocity also were examined. Excellent agreement exists between

predictions and observations for both the semi-diurnal tidal fluctuations and the subtidal (longer-term) variations. The importance of surface wind stress and bay conditions (velocity and salinity) for the residual velocity was discussed. The model capability of reproducing the diffusive transport was verified by the agreement between model predictions and 1990 slackwater survey salinity data.

The hydrodynamic model, once calibrated and verified, was used to study the hydrodynamic features of the Rappahannock River. A reverse longitudinal salinity gradient, an increase in salinity in the upriver direction, has been observed frequently in the Rappahannock River. It was thought that the reverse gradient might be explained by the bottom topography of the river and variations in vertical mixing. The saline bay water, that enters the river through the mouth and moves upriver along the bottom, might be deflected upward in the presence of obstacles such as a sloping bottom, thereby creating the reverse gradient. Sensitivity runs indicated that the reverse gradient could be expected to occur frequently in the Rappahannock River, which has upriver-sloping bottom geometry between km 40-50, but that it might be erased by strong mixing during spring tides and/or by strong winds. This argument was further supported by the salinity data from 1981-1990 slackwater surveys by VIMS.

The model predictions of residual velocity showed the two-layer estuarine circulation present in the lower Rappahannock River, and the magnitude was consistent with the field measurements. The response of residual velocity to the spring-neap cycle indicated stronger residual circulation during neap tide than spring tide. The response to increased freshwater discharge of the downriver movement of the limit of salt intrusion and of the null point, where the level of no-net-motion meets the estuary bottom, was faithfully reproduced by the model.

The distinction between the limit of salt intrusion and the limit of gravitational

circulation in real estuaries with irregular bottom topography was examined. The null point occurs where the longitudinal density gradient integrated over the total depth (baroclinic) balances the mean surface slope due to the freshwater discharge (barotropic). Then, the location of the null point relative to the limit of salt intrusion is a function of longitudinal salinity gradient, total depth and surface slope. If the bottom topography in an estuary is such that an increase in freshwater discharge pushes the limit of salt intrusion downriver into a shallow region (e.g., around km 80 in the Rappahannock River), then, despite the augmented longitudinal salinity gradient, the reduced total depth makes the increase in baroclinic forcing not as large as that in barotropic forcing. The balance between baroclinic and barotropic forcing (i.e., null point) occurs further downriver than the limit of salt intrusion. If the freshwater discharge is large enough to push the limit of salt intrusion downriver of the shallow region into the deep part, the null point occurs closer to the limit of salt intrusion. All these features were well reproduced by the model.

7-1-2. Water quality model

The water quality model, supplied with the information of the physical transport processes from the hydrodynamic model, provides real-time predictions of eight water quality parameters. They are dissolved oxygen, chlorophyll 'a', carbonaceous biochemical oxygen demand, organic nitrogen, ammonia nitrogen, nitrite-nitrate nitrogen, organic phosphorus and inorganic phosphorus.

The water quality model has been calibrated and verified using the field data in the summer of 1990. They include the slackwater survey data by VIMS and the data collected by the Virginia State Water Control Board as a part of the Chesapeake Bay Fall Line and Tributary Water Quality Monitoring Program. Considering the random variability inherent in natural systems and the goal of consistency in calibrated

coefficients, the agreement between model predictions and field observations is more than satisfactory. In general, the agreement between predictions and observations depends upon both the quality and quantity of input data, and the nature and number of observations. The water quality model results are commensurate with the quality and quantity of the data available to this study.

The water quality model, calibrated and verified, was used to study the water quality processes in the Rappahannock River. Hypoxia, even anoxia, has been frequently observed during summer in the bottom water of the lower part of the river. The sensitivity analysis indicated that the bottom water will end up being hypoxic regardless of the DO and CBOD concentrations in the incoming bay water. The hypoxic condition can be relieved more by eliminating CBOD than by increasing DO in the incoming bay water. The sensitivity analysis also revealed that hypoxia is caused by a combination of physical and biochemical processes. Among the physical processes, an increase in either residual circulation or vertical mixing can relieve the hypoxic condition. The present model, being a complicated model, cannot separate the effects of vertical mixing and gravitational circulation though. Oxygen demands in both sediment and water column contribute to the formation of hypoxia. The contribution of water column respiration including CBOD decay, nitrification and algal respiration to hypoxia is as important as that of SOD. In the water column, the CBOD decay is the most important DO consuming process.

High chlorophyll concentrations in the lower portion of tidal freshwater have been observed frequently in the Rappahannock River as well as in many other estuarine environments. Model sensitivity runs showed that the high chlorophyll in the Rappahannock River cannot be maintained without an external input of nutrients. A hypothesis was proposed to account for the source of nutrients and the downriver limit of the high chlorophyll concentrations. It is likely that sediment transport from

the upper part of the river occurs during times of high freshwater flow, and subsequently nutrients are released from the transported sediments. It appears that the geometric and hydrodynamic trapping of nutrient-laden sediments, and possibly the demise of freshwater phytoplankton in the salt water, limit the high chlorophyll concentrations to the segment upriver of km 85.

7-2. Recommendations

During the present study, the following limitations have been noted. These need to be further investigated and to be included in future models to improve the model predictive capability.

1) As almost all other investigators have noticed, it is the turbulence closure model that limits the predictive capability of the hydrodynamic model and thus its applicability to other systems. More understanding and better mathematical representation of the turbulent mixing processes are essential to improve the model capability. We should devote more effort studying the behavior of potentially promising methods, which include the K-ε model, Reynolds stress model, Mellor and Yamada Level 2½ model, etc.

2) Coupling of the water quality model with a sediment transport model and a sediment diagenesis model is important to predict the nutrient movement, particularly for phosphate and sediment-nutrient exchanges. The mechanisms that appear to be of significance include the adsorption of phosphate to sediment particles and subsequent settling, sediment transport in response to high freshwater flow and sediment phosphate release.

3) The demise of freshwater phytoplankton in the presence of salt is thought be a possible mechanism that limits the characteristic high chlorophyll concentration to the tidal freshwater portion of the river, as has been frequently observed in many

estuarine environments including the Rappahannock River. Therefore, differentiation of phytoplankton species in the water quality model is called for to be able to predict the spatial extent, especially downriver limit, of the high chlorophyll concentration.

4) The current calibration and verification of the water quality model has a shortcoming in the prediction of nutrients. It was not because of the model but because of the quality and quantity of the field data used for the current calibration and verification. The present model needs to be calibrated with more detailed field data to perform the sensitivity analysis pertaining to nutrient limitation.

LITERATURE CITED

Ambrose, Jr., R.B., T.A. Wool, J.P. Connolly and R.W. Schanz. 1988. WASP4, a hydrodynamic and water quality model: model theory, user's manual and programmer's guide. EPA/600/3-87/039. Environmental Research Lab. (ERL), Office of Research and Development (ORD), US Environmental Protection Agency (EPA), Athens, GA. 297 pp.

Anderson, G.F. 1986. Silica, diatoms and a freshwater productivity maximum in Atlantic Coastal Plain Estuaries, Chesapeake Bay. Estuarine, Coastal and Shelf Science, 22(2): 183-197.

Asselin, R. 1972. Frequency filters for time integrations. Monthly Weather Review, 100(6): 487-490.

Baker, B.E. and C.F. Cerco. 1988. Sediment nutrient flux data from a seasonal simulation of water chemistry in Gunston Cove, VA. Data Report No. 28. Virginia Institute of Marine Science (VIMS), The College of William and Mary, VA. 33 pp.

Baker, B.E. 1989. Effect of water column pH and NO_3 on ortho-phosphate release rates from freshwater sediments. Master Thesis. VIMS, The College of William and Mary, VA. 59 pp.

Banks, R.B. and F.F. Herrera. 1977. Effect of wind and rain on surface reaeration. J. of the Environmental Engineering Division, American Society for Civil Engineers (ASCE), 103(EE3): 489-504.

Blumberg, A.F. 1975. A numerical investigation into the dynamics of estuarine circulation. Technical Report No. 91. Chesapeake Bay Institute, The Johns Hopkins Univ. 110 pp.

Blumberg, A.F. 1977. Numerical model of estuarine circulation. J. of the Hydraulic Division, ASCE, 103(HY3): 295-310.

Blumberg, A.F. 1986. Turbulent mixing processes in lakes, reservoirs and impoundments, pp. 79-104. In: W.G. Gray (ed.), Physics-based Modeling of Lakes, Reservoirs, and Impoundments, ASCE.

Blumberg, A.F. and G.L. Mellor. 1987. A description of a three-dimensional coastal ocean circulation model, pp. 1-16. In: N.S. Heaps (ed.), Three-dimensional

Coastal Ocean Models, American Geophysical Union.

Bowden, K.F. and P. Hamilton. 1975. Some experiments with a numerical model of circulation and mixing in a tidal estuary. Estuarine and Coastal Marine Science, 3(3): 281-301

Bowden, K.F. 1983. Physical oceanography of coastal waters. Ellis Horwood Ltd. 302 pp.

Bowie, G.L., W.B. Mills, D.B. Porcella, C.L. Campbell, J.R. Pagenkopf, G.L. Rupp, K.M. Johnson, P.W.H. Chan, S.A. Gherini and C.E. Chamberlin. 1985. Rates, constants, and kinetics formulations in surface water quality modeling (second edition). EPA/600/3-85/040. ERL, ORD, US EPA, Athens, GA. 455 pp.

Broderick, T.A. 1986. Phosphorus release from tidal embayment sediments under high pH, aerobic conditions. Master Thesis. Virginia Polytechnic Institute and State Univ. (VPISU), Blacksburg, VA. 78 pp.

Brooks, T.J. 1983. Rappahannock River slack water data report, temperature, salinity and dissolved oxygen 1970-1980. Data Report No. 18. VIMS, The College of William and Mary, VA. 40 pp.

Caponi, E.A. 1977. The simulation of estuarine circulations with a fully three-dimensional numerical model, pp. 332-346. In: M. Wiley (ed.), Estuarine Processes: Vol. II, Circulation, Sediments and Transfer of Material in the Estuary, Academic Press, Inc.

Cerco, C.F. and A.Y. Kuo. 1983. Water quality in a Virginia Potomac embayment: Hunting Creek - Cameron Run. Special Report in Applied Marine Science and Ocean Engineering (SRAMSOE) No. 244. VIMS, The College of William and Mary, VA. 202 pp.

Cerco, C.F. 1985. Sediment-water column exchanges of nutrients and oxygen in the tidal James and Appomattox rivers. VIMS, The College of William and Mary, VA. 110 pp.

Cerco, C.F., A.Y. Kuo and P.V. Hyer. 1987. Model study of eutrophication in Virginia's Potomac embayments, pp. 119-123. In: Proceedings of the Tenth National Conference of the Coastal Society, New Orleans, LA, 1986.

Cerco, C.F. 1989. Measured and modelled effects of temperature, dissolved oxygen and nutrient concentration on sediment-water nutrient exchange. Hydrobiologia, 174: 185-194.

Chesapeake Bay Program. 1992. Chesapeake Bay coordinated split sample program annual report, 1990-1991. Chesapeake Bay Program/Technical Report Series 76/92.

Analytical Methods and Quality Assurance Workgroup of the Chesapeake Bay Program Monitoring Subcommittee, Annapolis, MD. pp 34.

Conomos, T.J. and Peterson D.H. 1977. Suspended-particle transport and circulation in San Francisco Bay: an overview, pp. 82-97. In: M. Wiley (ed.), Estuarine Processes: Vol. II, Circulation, Sediments and Transfer of Material in the Estuary, Academic Press, Inc.

Cloern, J.E., A.E. Alpine, B.E. Cole, R.L.J. Wong, J.F. Arthur and M.D. Ball. 1983. River discharge controls phytoplankton dynamics in the northern San Francisco Bay Estuary. Estuarine, Coastal and Shelf Science, 16(4): 415-429.

D'Elia, C.F., K.L. Webb and R.L. Wetzel. 1981. Time varying hydrodynamics and water quality in an estuary, pp. 597-606. In: B.J. Neilson and L.E. Cronin (eds.), Estuaries and Nutrients, The Humana Press.

Division of Water Resources. 1970. Rappahannock River basin comprehensive water resources plan, Vol. I - Introduction. Planning Bulletin 219. Virginia Dept. of Conservation and Economic Development, Richmond, VA. 122 pp.

Dyer, K.R. 1973. Estuaries: a physical introduction. John Wiley & Sons, Inc., NY. 140 pp.

Edinger, J.E. and E.M. Buchak. 1980. Numerical hydrodynamics of estuaries, pp. 115-146. In: P. Hamilton and K.B. Macdonald (eds.), Estuarine and Wetland Processes with Emphasis on Modeling, Plenum Press.

Edinger, J.E. and E.M. Buchak. 1981. Estuarine laterally averaged numerical dynamics: the development and testing of estuarine boundary conditions in the LARM code. Miscellaneous Paper EL-81-9. Prepared by J.E. Edinger Associates, Inc., for the US Army Engineer Waterways Experiment Station (WES), Corps of Engineers, Vicksburg, MS. 84 pp.

Effler, S.W. 1985. Attenuation versus transparency. J. of Environmental Engineering, ASCE, 111(4): 448-459.

Falkowski, P.G., T.S. Hopkins and J.J. Walsh. 1980. An analysis of factors affecting oxygen depletion in the New York Bight. J. of Marine Research, 38(3): 479-506.

Festa, J.F. and D.V. Hansen. 1976. A two-dimensional numerical model of estuarine circulation: the effects of alternating depth and river discharge. Estuarine and Coastal Marine Science, 4(3): 309-323.

Fischer, H.B. 1967. The mechanics of dispersion in natural streams. J. of the Hydraulic Division, ASCE, 93(HY6): 187-216.

Fischer, H.B., E.J. List, R.C.Y. Koh and J. Imberger. 1979. Mixing in inland and coastal waters. Academic Press, Inc., NY. 483 pp.

Flemer, D.A., G.B. Mackiernan, W. Nehlsen and V.K. Tippie. 1983. Chesapeake Bay: a profile of environmental change. Chesapeake Bay Program, US EPA. 200 pp.

Ford, D.E. 1976. Water temperature dynamics of Dimictic Lakes: analysis and predictions using integral energy concepts. Ph.D. Dissertation. Univ. of Minnesota, Minneapolis, Minn.

Green, E.J. and D.E. Carritt. 1967. New tables for oxygen saturation of seawater. J. of Marine Research, 25(2): 140-147.

Haertel, L., C. Osterberg, H. Curl, Jr. and P.K. Park. 1969. Nutrient and plankton ecology of the Columbia River Estuary. Ecology, 50(6): 962-978.

Hall, R.W. and R.S. Chapman. 1985. Two-dimensional QUICKEST; solution of the depth-averaged transport-dispersion equation. Technical Report EL-85-3. US Army Engineer WES, Corps of Engineers, Vicksburg, MS. 29 pp.

Haltiner, G.J. and R.T. Williams. 1980. Numerical prediction and dynamic meteorology (second edition). John Wiley & Sons, Inc., NY. 477 pp.

Hamilton, P. 1977. On the numerical formulation of a time dependent multi-level model of an estuary, with particular reference to boundary conditions, pp. 347-364. In: M. Wiley (ed.), Estuarine Processes: Vol II, Circulation, Sediments and Transfer of Material in the Estuary, Academic Press, Inc.

Hansen, D.V. and M. Rattray, Jr. 1965. Gravitational circulation in straits and estuaries. J. of Marine Research, 23(2): 104-122.

Haas, L.W. 1977. The effect of the spring-neap tidal cycle on the vertical salinity structure of the James, York and Rappahannock rivers, Virginia, U.S.A. Estuarine and Coastal Marine Science, 5(4): 485-496.

Huang, C. and N.E. Hopson. 1974. Nitrification rate in biological processes. J. of the Environmental Engineering Division, ASCE, 100(EE2): 409-422.

Ichiye, T. 1967. Upper ocean boundary-layer flow determined by dye diffusion. Physics of Fluids Supplement, 10: S270-S277.

Johnson, B.H., K.W. Kim, R.H. Heath, H.L. Butler and B.B. Hsieh. 1991. User's guide for a three-dimensional numerical hydrodynamic, salinity and temperature model of Chesapeake Bay. Technical Report HL-91-20. US Army Engineer WES, Corps of Engineers, Vicksburg, MS. 41 pp.

Kullenberg, G. 1974. Investigations on dispersion in stratified vertical shear flow. Rapp. P.-v. Réun. Cons. int. Explor. Mer., 167: 86-92.

Kundu, P.K. 1990. Fluid mechanics. Academic Press, Inc., NY. 638 pp.

Kuo, A.Y., A. Rosenbaum, P.V. Hyer and C.S. Fang. 1975. Hydrography and hydrodynamics of Virginia estuaries, VI. Mathematical model studies of water quality of the Rappahannock Estuary. SRAMSOE No. 102. VIMS, The College of William and Mary, VA. 107 pp.

Kuo, A.Y., M. Nichols and J. Lewis. 1978. Modelling sediment movement in the turbidity maximum of an estuary. Bulletin 111. Virginia Water Resources Research Center (VWRRC), VPISU, Blacksburg, VA. 76 pp.

Kuo, A.Y. 1985. Water quality in a Virginia Potomac embayment: Aquia Creek. SRAMSOE No. 277. VIMS, The College of William and Mary. 169 pp.

Kuo, A.Y. and B.J. Neilson. 1987. Hypoxia and salinity in Virginia estuaries. Estuaries, 10(4): 277-283.

Kuo, A.Y. and M.Z. Moustafa. 1989. Hypoxia in the lower Rappahannock Estuary. SRAMSOE No. 302. VIMS, The College of William and Mary, VA. 75 pp.

Kuo, A.Y., K.Park and M.Z. Moustafa. 1991a. Spatial and temporal variabilities of hypoxia in the Rappahannock River, Virginia. Estuaries, 14(2): 113-121.

Kuo, A.Y., B.J. Neilson and K. Park. 1991b. A modelling study of the water quality of the upper tidal Rappahannock River. SRAMSOE No. 314. VIMS, The College of William and Mary, VA. 164 pp.

Kuo, A.Y. and K. Park. 1992. Transport of hypoxic waters: an estuary-subestuary exchange, pp. 599-615. In: D. Prandle (ed.), Dynamics and Exchanges in Estuaries and the Coastal Zone. A.G.U. Coastal and Estuarine Sciences, Washington D.C.

Lake, C.A. and W.G. MacIntyre. 1977. Phosphate and tripolyphosphate adsorption by clay minerals and estuarine sediments. Bulletin 109. VWRRC, VPISU, Blacksburg, VA. 58 pp.

Laubach, E.B. and R.M. Summers. 1987. Patuxent estuary water quality survey 1986 data summary. Report No. 67. Modeling and Analysis Division, Water Management Administration, Maryland Dept. of the Environment. 70 pp.

Leonard, B.P., G.J. Vachtsevanos and K.A. Abood. 1978. Unsteady-state, two-dimensional salinity intrusion model for an estuary, pp. 113-123. In: C. Brebbia (ed.), Applied Numerical Modelling, Pen Tech. Press.

Leonard, B.P. 1979. A stable and accurate convective modelling procedure based on quadratic upstream interpolation. Computer Methods in Applied Mechanics and Engineering, 19: 59-98.

Lippson, A.J., M.S. Haire, A.F. Holland, F. Jacobs, J. Jensen, R.L. Moran-Johnson, T.T. Polgar and W.A. Richkus. 1979. Environmental atlas of the Potomac Estuary. Environmental Center, Martin Marietta Corporation. Prepared for Power Plant Siting Program, Maryland Dept. of Natural Resources, Maryland. 279 pp.

Llansó, R.J. 1992. Effects of hypoxia on estuarine benthos: the lower Rappahannock River (Chesapeake Bay), a case study. Estuarine, Coastal and Shelf Science, 35: 491-515.

Marshall, H.G. 1967. Plankton in James River Estuary, Virginia. I. Phytoplankton in Willoughby Bay and Hampton Roads. Chesapeake Science, 8(2): 90-101.

Marshall, H.G. 1980. Seasonal phytoplankton composition in the lower Chesapeake Bay and Old Plantation Creek, Cape Charles, Virginia. Estuaries, 3(3): 207-216.

Marshall, H.G. and R. Lacouture. 1986. Seasonal patterns of growth and composition of phytoplankton in the lower Chesapeake Bay and vicinity. Estuarine, Coastal and Shelf Sciences, 23(1): 115-130.

Mayer, L.M. and S.P. Gloss. 1980. Buffering of silica and phosphate in a turbid river. Limnology and Oceanography, 25(1): 12-22.

Mellor, G.L. and T. Yamada. 1974. A hierarchy of turbulence closure models for planetary boundary layers. J. of Atmospheric Sciences, 31(7): 1791-1806.

Mellor, G.L. and T. Yamada. 1982. Development of a turbulence closure model for geophysical fluid problems. Reviews of Geophysics and Space Science, 20(4): 851-875.

Miles, J. 1961. On the stability of heterogeneous shear flows. J. of Fluid Mechanics, 10: 496-508.

Morse, D.C. 1947. Some observations on seasonal variation in plankton population, Patuxent River, Maryland, 1943-1945. Publication No. 65. Chesapeake Biological Laboratory. 31 pp.

Munk, W.H. and E.R. Anderson. 1948. Notes on a theory of the thermocline. J. of Marine Research, 7(3): 276-295.

National Ocean Survey. 1989. Tide Tables 1990, East coast of North and South America including Greenland. National Oceanic and Atmospheric Administration (NOAA), US Dept. of Commerce. 289 pp.

Newcombe, C.L. and W.A. Horne. 1938. Oxygen poor waters of the Chesapeake Bay. Science, 88: 80-81.

Nichols, M.M., L.E. Cronin, W.B. Cronin, M.G. Gross, B.W. Nelson, J.W. Pierce and R.E. Ulanowicz. 1981. Response to freshwater inflow in the Rappahannock Estuary, Virginia - Operation HIFLO '78. CRC Publication No. 95. Chesapeake Research Consortium, Inc. 46 pp.

O'Connor, D.J. and W.E. Dobbins. 1958. Mechanism of reaeration in natural streams. Transactions of the American Society of Civil Engineers, 123(2934): 641-684.

Odd, N.V.M. and J.G. Rodger. 1978. Vertical mixing in stratified tidal flows. J. of the Hydraulics Division, ASCE, 104(HY3): 337-351.

Oey, L.-Y., G.L. Mellor and R.I. Hires. 1985. A three-dimensional simulation of the Hudson-Raritan estuary, Parts I-III. J. of Physical Oceanography, 15(12): 1676-1720.

Officer, C.B., R.B. Biggs, J.L. Taft, L.E. Cronin, M.A. Tyler and W.R. Boyton. 1984. Chesapeake Bay anoxia: origin, development and significance. Science, 223(4631): 22-27.

Parfitt, R.L., R.J. Atkinson and R.St.C. Smart. 1975. The mechanism of phosphate fixation by iron oxides. Soil Science Society of America, J., 39: 837-841.

Pattern, B.C. 1963. Plankton: optimum diversity structure of a summer community. Science, 140(3569): 894-898.

Pennock, J.R. 1985. Chlorophyll distributions in the Delaware Estuary: regulation by light-limitation. Estuarine, Coastal and Shelf Science, 21(5): 711-725.

Perrells, P.A.J. and M. Karelse. 1981. A two-dimensional laterally averaged model for salt intrusion in estuaries, pp. 483-535. In: H.B. Fischer (ed.), Transport Models for Inland and Coastal Waters, Academic Press, Inc.

Phoel, W., K.L. Webb and C.F. D'Elia. 1981. Inorganic nitrogen regeneration and total oxygen consumption by the sediment at the mouth of the York River, pp. 607-619. In: B.J. Neilson and L.E. Cronin (eds.), Estuaries and Nutrients, The Humana Press.

Pritchard, D.W. 1960. The movement and mixing of contaminants in tidal estuaries, pp. 512-525. In: E.A. Pearson (ed.), Waste Disposal in the Marine Environment, Pergamon Press.

Relexans, J.C., M. Meybeck, G.Billen, M.Brugeaille, H.Etcheber and M. Somville.

1988. Algal and microbial processes involved in particulate organic matter dynamics in the Loire Estuary. Estuarine, Coastal and Shelf Science, 27(6): 625-644.

Roache, P.J. 1972. Computational fluid dynamics. Hermosa Publishers. 434 pp.

Rossby, C.G. and R.B. Montgomery. 1935. The layer of frictional influence in wind and ocean currents. Papers in Physical Oceanography and Meteorology, 3(3): 1-101.

Ruzecki, E.P. and D.A. Evans. 1986. Temporal and spatial sequencing of destratification in a coastal plain estuary, pp. 368-389. In: J. Bowman, M. Yentsch and W.T. Peterson (eds.), Tidal Mixing and Plankton Dynamics, Lecture Notes on Coastal and Estuarine Studies, Vol. 17, Springer-Verlag.

Schuchardt, B. and M. Schirmer. 1991. Phytoplankton maxima in the tidal freshwater reaches of two coastal plain estuaries. Estuarine, Coastal and Shelf Science, 32(2): 187-206.

Seitzinger, S.P. 1985. The effect of oxygen concentration and pH on sediment-water nutrient fluxes in the Potomac River. Report No. 85-2. Division of Environmental Research, The Academy of Natural Sciences of Philadelphia, PA.

Seitzinger, S.P. 1986. The effect of pH on the release of phosphorus from Potomac River sediments. Report No. 86-8F. Division of Environmental Research, The Academy of Natural Sciences of Philadelphia, PA.

Seitzinger, S.P. 1991. The effect of pH on the release of phosphorus from Potomac Estuary sediments: implications for blue-green algal blooms. Estuarine, Coastal and Shelf Sciences, 33(4): 409-418.

Seliger, H.H., J.A. Boggs and J.A. Biggley. 1985. Catastrophic anoxia in the Chesapeake Bay in 1984. Science, 228(4695): 70-73.

Shanahan, P. and D.R.F. Harleman. 1982. Linked hydrodynamic and biochemical models of water quality in shallow lakes. Report No. 268. Ralph M. Parsons Lab., Aquatic Science and Environmental Eng., Dept. of Civil Eng., School of Eng., Massachusetts Institute of Technology (MIT). 279 pp.

Smith, D.E., M. Leffler and G. Mackiernan (editors). 1992. Oxygen dynamics in the Chesapeake Bay: A synthesis of recent research. Maryland and Virginia Sea Grant College Programs. A Maryland Sea Grant Book, College Park, MD. 234 pp.

Steele, J.H. 1965. Notes on some theoretical problems in production ecology, pp. 383-398. In: C.R. Goldman (ed.), Primary Productivity in Aquatic Environments. Mem. Ist. Ital. Idrobiol., Univ. of California Press, Berkeley.

Swanson, R.L. and C.J. Sindermann. 1979. Oxygen depletion and associated benthic mortalities in New York Bight, 1976. Professional Paper 11. NOAA, U.S. Dept. of Commerce. 345 pp.

Talbot, J.W. and G.A. Talbot. 1974. Diffusion in shallow seas and in English coastal and estuarine waters. Rapp. P.-v. Réun. Cons. int. Explor. Mer., 167: 93-110.

Taylor, G.I. 1931. Internal waves and turbulence in a fluid of variable density. Rapports et Procès-Verbaux des Réunions du Conseil Permanent International pour L'Exploration de la Mer, LXXVI, 35-42.

Tennekes, H. and J.L. Lumley. 1972. A first course in turbulence. The MIT Press. 300 pp.

Thatcher, M.L. and D.R.F. Harleman. 1972. A mathematical model for the prediction of unsteady salinity intrusion in estuaries. Report No. 72-7. MIT, MA. 232 pp.

Thomann, R.V. and J.J. Fitzpatrick. 1982. Calibration and verification of a mathematical model of the eutrophication of the Potomac Estuary. HydroQual, Inc. Final Report to Dept. of Environmental Services, Washington, D.C. 500 pp.

Thomann, R.V., N.J. Jaworski, S.W. Nixon, H.W. Paerl and J. Taft. 1985. The 1983 algal bloom in the Potomac Estuary. The Algal Bloom Expert Panel. Prepared for the Potomac Strategy State/EPA Management Committee, US EPA Region III, Philadelphia, PA.

Thomann, R.V. and J.A. Mueller. 1987. Principles of surface water quality modeling and control. Harper & Row, Publishers, NY. 644 pp.

Thompson, R.O.R.Y. 1983. Low-pass filters to suppress inertial and tidal frequencies. J. of Physical Oceanography, 13: 1077-1083.

Tyler, J.E. and R.W. Preisendorfer. 1962. Chapter 8: Light, pp. 397-451. In: M.N. Hill (ed.), The Sea, Ideas and Observations on Progress in the Study of the Sea, Vol. I: Physical Oceanography, Interscience Publishers, John Wiley & Sons, Inc.

U.S. Army Coastal Engineering Research Center. 1973. Shore protection Manual, Vol. I. Corps of Engineers, Dept. of Army.

U.S. Geological Survey (USGS). 1988. Water resources data, Virginia - water year 1987, Vol I. surface water and surface-water-quality records. USGS Water-Data Report VA-87-1. Water Resources Division, USGS, Richmond, VA. 441 pp.

USGS. 1991. Water resources data, Virginia - water year 1990, Vol I. surface water and surface-water-quality records. USGS Water-Data Report VA-90-1. Water Resources Division, USGS, Richmond, VA. 407 pp.

USGS. 1992. Water resources data, Virginia - water year 1991, Vol I. surface water and surface-water-quality records. USGS Water-Data Report VA-91-1. Water Resources Division, USGS, Richmond, VA. 592 pp.

Veith, J.A. and G. Sposito. 1977. Reactions of aluminosilicates, aluminum hydrous oxide, and aluminum oxide with o-phosphate: The formation of X-ray amorphous analogs of variscite and montebrasite. Soil Science Society of America, J., 41: 870-876.

Wang, D. and D.W. Kravitz. 1980. A semi-implicit two-dimensional model of estuarine circulation. J. of Physical Oceanography, 10(3): 441-454.

Wang, J.D., A.F. Blumberg, H.L. Butler and P. Hamilton. 1990. Transport prediction in partially stratified tidal water. J. of Hydraulics Engineering, ASCE, 116(3): 380-396.

Wild, Jr., H.E., C.N. Sawyer and T.C. McMahon. 1971. Factors affecting nitrification kinetics. J. of Water Pollution Control Federation, 43(9): 1845-1854.

Williams, S.A. and A.Y. Kuo. 1984. Water quality studies of Little Hunting Creek. SRAMSOE No. 268. VIMS, The College of William and Mary, VA. 250 pp.

Woods, J.D. and R.L. Wiley. 1972. Billow turbulence and ocean microstructure. Deep-Sea Research, 19(2): 87-121.

APPENDIX A. MELLOR AND YAMADA LEVEL 2 TURBULENCE MODEL

Mellor & Yamada (1974 and 1982) developed a hierarchy of turbulence closure models depending upon the various degrees of approximations and simplifications made. The Levels 4, 3 and 2½ models require the solution of additional partial differential equations, and the simple Level 2 model gives a set of algebraic equations for A_z and K_z that are comparable to Equations 2-16 and 2-17. The present model has the Mellor and Yamada (M&Y) Level 2 turbulence model as a second choice to estimate A_z and K_z, and the behavior of this turbulence model is described in this appendix.

The M&Y Level 2 model, like Equations 2-16 and 2-17, is based upon the local equilibrium, in which the turbulent kinetic energy produced by shear and buoyancy is balanced by the energy dissipation. The stability functions in the M&Y Level 2 model may be expressed as,

$$\phi_M = \left[\frac{(1 - R_{fc}^{-1} R_f)}{(1 - R_f)^{2/3}} \frac{(1 - R_{f1}^{-1} R_f)}{(1 - R_{f2}^{-1} R_f)} \right]^{\frac{3}{2}} \tag{A-1}$$

$$\phi_S = \frac{1}{P_r^N} \left[\frac{(1 - R_{fc}^{-1} R_f)^3}{(1 - R_f)^2} \frac{(1 - R_{f1}^{-1} R_f)}{(1 - R_{f2}^{-1} R_f)} \right]^{\frac{1}{2}} \tag{A-2}$$

where

$$R_{fc} = \frac{B_1 - 6A_1}{B_1 + 12A_1 + 3B_2} = \text{critical flux Richardson number} \tag{A-3}$$

$$R_{fl} = \frac{B_1(1 - 3C_1) - 6A_1}{B_1(1 - 3C_1) + 12A_1 + 9A_2} \tag{A-4}$$

$$R_{f2} = \frac{B_1 - 6A_1}{B_1 + 3A_1 + 3B_2} \tag{A-5}$$

$$R_f = \frac{1}{2}\frac{1}{P_r^N}\frac{R_{fl}}{R_{f2}}\left[R_i + P_r^N R_{f2} - \sqrt{R_i^2 + 2P_r^N\frac{R_{f2}^2}{R_{fl}}(\frac{R_{fl}}{R_{f2}} - 2)R_i + (P_r^N R_{f2})^2}\right] \tag{A-6}$$

Here, the flux Richardson number (R_f) is the ratio of the buoyant production to shear production of turbulent energy, i.e., $R_f = (\phi_S/\phi_M)\, R_i$, and P_r^N is the turbulent Prandtl number at neutral conditions. Using the constants in Mellor & Yamada (1982),

$$(A_1, B_1, A_2, B_2, C_1, P_r^N) = (0.92, 16.6, 0.74, 10.1, 0.08, 0.80) \tag{A-7}$$

the followings are obtained;

$$(R_{fc}, R_{fl}, R_{f2}, R_{ic}) = (0.191, 0.234, 0.223, 0.196) \tag{A-8}$$

$$R_f = 0.656\left(R_i + 0.178 - \sqrt{R_i^2 - 0.323R_i + 0.0318}\right) \tag{A-9}$$

where R_{ic} is the critical Richardson number above which mixing ceases to exist due to the stable stratification. From Equations 2-11 and 2-12, then, the vertical mixing coefficients without including the effect of wind are expressed as,

$$A_z = \alpha' Z^2(1 - \frac{Z}{h})^2 \left|\frac{\partial u}{\partial z}\right| \left[\frac{(1 - 5.24R_f)}{(1 - R_f)^{2/3}}\frac{(1 - 4.27R_f)}{(1 - 4.48R_f)}\right]^{\frac{3}{2}} \tag{A-10}$$

$$K_z = \frac{\alpha'}{0.80} Z^2(1 - \frac{Z}{h})^2 \left|\frac{\partial u}{\partial z}\right| \left[\frac{(1 - 5.24R_f)^3}{(1 - R_f)^2}\frac{(1 - 4.27R_f)}{(1 - 4.48R_f)}\right]^{\frac{1}{2}} \tag{A-11}$$

where α' is determined through model calibration. Equations A-10 and A-11 with R_f estimated from Eq. A-9 are used to calculate A_z and K_z when $-10 < R_i < R_{ic} = 0.196$ (or $-11.8 < R_f < R_{fc} = 0.191$). When R_i is greater than R_{ic}, the background

value of 0.1 cm^2 sec^{-1} is used for A_z and K_z to avoid numerical instability. When R_i < -10, A_z and K_z are calculated with Equations A-10 and A-11 assuming R_i = -10. Note that since the stability functions (Equations A-1 and A-2) are defined and meaningful even for unstable condition, the R_i are allowed to be negative till -10 below which the R_i is assumed to be -10. This is to prevent the calculation of mixing coefficients from overflowing in the source program.

The model simulation of salinity distribution in 1987 was performed to calibrate the constant, α', in Equations A-10 and A-11. The same conditions described in Section 4-3 were used. The model prediction of salinity on August 10 with α' = 0.16, which is the square of the von Karman constant, is presented in Fig. A-1. It shows that the salinity prediction using the M&Y Level 2 model was too stratified compared to both the field observation and the model prediction using Equations 2-16 and 2-17 (Fig. 4-3). Neither the increase of the α' value nor the use of the overall Richardson number ($R_{i,o}$) instead of local R_i (Eq. 2-13) could relieve the stratification. The overall, or bulk, Richardson number ($R_{i,o}$) used is defined as (Bowden 1983),

$$R_{i,o} = -\frac{g}{\rho}\frac{h \cdot \Delta\rho}{\Delta u^2} \qquad \text{(A-12)}$$

in a shear flow extending to a depth h with a total change of $\Delta\rho$ in density and of Δu in velocity over that depth.

Examination of the tidally averaged K_z values in the model result revealed that in the saline part of the river where the stratification suppresses the vertical mixing, 81% of the tidal mean K_z values were the background value used (0.1 cm^2 sec^{-1}). This indicated that in 81% of the saline part, mostly top 10 m of the water column, R_i was always bigger than R_{ic} = 0.196 (or $R_f > R_{fc}$ = 0.191) throughout a tidal cycle, and that Eq. A-11 was used to calculate K_z in only the remaining 19%. There are

two possible explanations for this odd results. One is that the order of magnitude of R_i calculated by the model may be too big resulting in too much suppression of vertical mixing. The other is that the inhibition of vertical mixing with increasing R_i represented by stability functions in Equations A-1 and A-2 may be too severe.

Blumberg (1975) computed R_i's from the instantaneous observed hourly vertical profiles of current and salinity in the Potomac River for a complete tidal cycle. These values show that the local R_i is less than 0.2 only for 21% of 130 computed R_i's. Compiling the data from several experiments, Kullenberg (1974) reported R_i values in which the overall R_i is less than 0.2 only for 14% of 28 computed $R_{i,o}$'s. Compared to the magnitude of these Richardson numbers derived from the field measurements, the magnitude of R_i from the present model seems to be reasonable.

The stability functions, ϕ_M and ϕ_S, account for the inhibition of vertical exchange of momentum and mass by stable density structure, and are usually expressed as a function of R_i. Various formulations of the stability function for mass (ϕ_S) are compared as a function of R_i in Fig. A-2. The M&Y Level 2 model (Eq. A-2) brings about the largest reduction in vertical mixing at a given R_i, and it completely exterminates the vertical mixing when $R_i > R_{ic} \approx 0.2$. The formulations by Pritchard (1960) and Munk & Anderson (1948) were thought to overemphasize the effect of stability at large R_i (Blumberg 1975), although they reduce the vertical mixing not as much as the M&Y Level 2 model does. It is likely that the M&Y Level 2 model reduces the vertical mixing too much for a given R_i when $R_i < R_{ic} \approx 0.2$. The over-stratification in model prediction (Fig. A-1), however, was not caused by this behavior of the M&Y Level 2 model. Because if so, the increase in the constant, α', should have relieved the stratification in model result, but it didn't.

Another characteristic feature in the M&Y Level 2 model is the critical value of $R_i \approx 0.2$ above which the vertical turbulent mixing ceases to exist. As mentioned

above, the Richardson numbers from model were always larger than 0.2 throughout a tidal cycle in approximately 4/5 of the saline part of the river. It, therefore, was the complete elimination of vertical mixing for $R_i > R_{ic} \approx 0.2$ that caused the over-stratification in model prediction in Fig. A-1. The validity of complete elimination of vertical mixing for $R_i > 0.2$ is questionable. Taylor (1931) showed from Jacobsen's data that the vertical mixing still exists at a $R_i \approx 10$, the K_z measurements ranging from 0.05 to 0.6 $cm^2\ sec^{-1}$ when R_i varying from 2.6 to 10. Kullenberg (1974) reported K_z range of 0.02 to 1.5 $cm^2\ sec^{-1}$ when $R_{i,o}$ varying from 0.4 to 20. These measurements do indicate that the vertical mixing is not likely to vanish completely for $R_i > 0.2$. On the other hand, it has been suggested that turbulence cannot be maintained if $R_i > 0.25$ approximately (Miles 1961; Tennekes & Lumley 1972). Although the field measurements in Taylor (1931) and Kullenberg (1974) show that the intensity of vertical mixing generally decreases with increasing R_i, the smaller K_z does not always occur at the larger R_i. All these seem to imply that the turbulent mixing, being a complex phenomenon, cannot be exactly parameterized by one single non-dimensional number like R_i (or R_f), and that the formulations in Fig. A-2 should be understood to give, at best, very general description of turbulent mixing. In a very simplified turbulence parameterization like those in Fig. A-2, therefore, use of critical Richardson number of ~ 0.2 to cut off the turbulent mixing completely seems to be inappropriate until it is further justified with field observation.

It is interesting to note that the magnitude of the Richardson number varies depending upon the scale on which it is measured (Woods & Wiley 1972). Since in calculating R_i, different vertical spacing (Δz) or different time averaging (Δt) in the velocity and density profiles affects the values of R_i, Blumberg (1975) pointed out that the critical R_i must be specified with extreme caution. Therefore, a formulation that includes the critical R_i above which mixing ceases would not be complete without

explicit specification of the computational method of R_i.

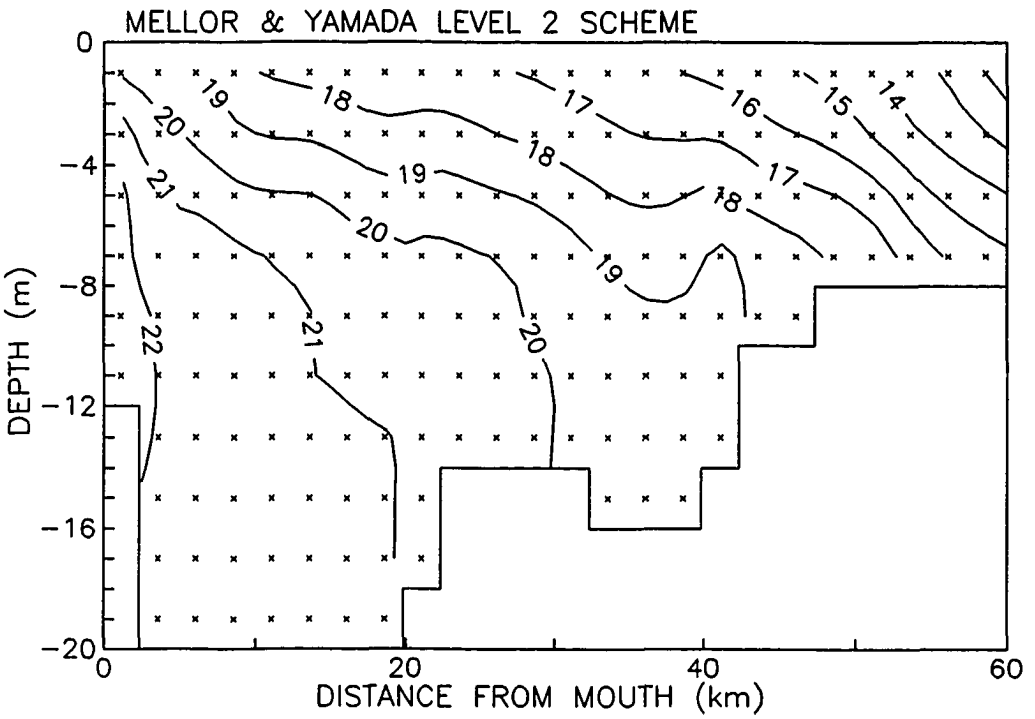

Figure A-1. Model prediction of salinity on 8/10/87 using the Mellor and Yamada Level 2 turbulence model.

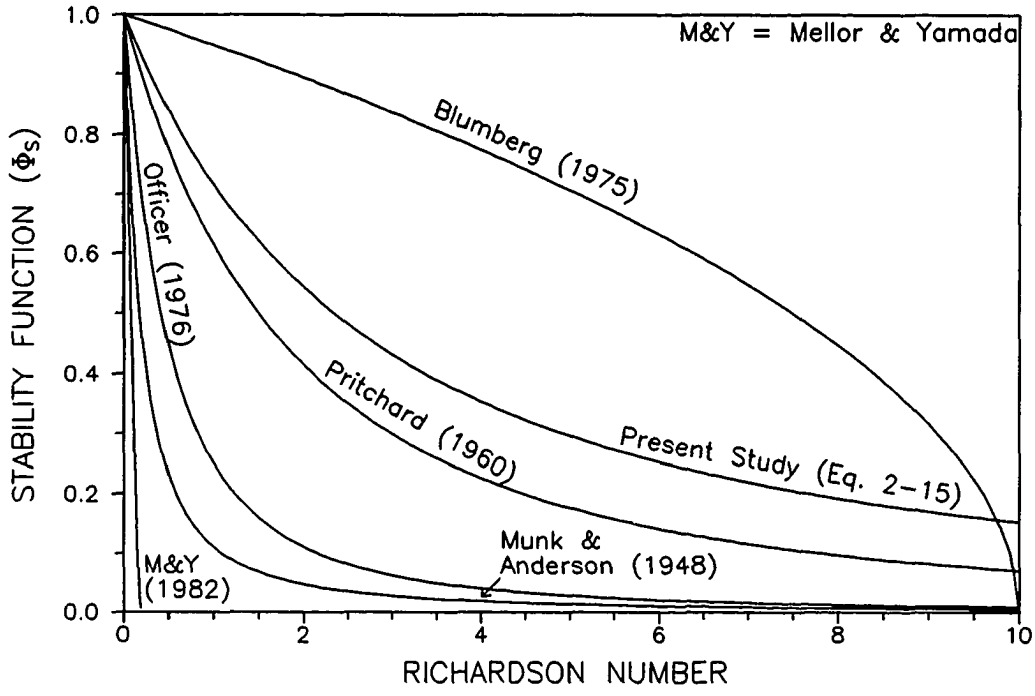

Figure A-2. Comparison of various formulations of the stability function for the vertical mass exchange as a function of Richardson number.

APPENDIX B. FINITE DIFFERENCE EQUATIONS

In this Appendix, the finite difference formulations are given of Equations 2-18 through 2-21. The grid system is shown in Fig. 2-1 using the subscripts, i and k, to represent the number of intervals in the x and z directions, respectively. The subscripts, 1 and 2, denote the time level, old and new, respectively.

B-1. Free Surface Elevation

Equation 2-18 is solved to get η at top layer only, and thus k is always 1 in the following two equations.

$$\eta_{i,2} = \eta_{i,1} + \frac{\Delta t}{B_{i,k}+STB_i}\left[\frac{B_{i,k}+B_{i,k+1}}{2}w_{i,k,1} - \frac{1}{\Delta x}(TMP_{i+1}-TMP_i) + \frac{q_{i,k}}{\Delta x}\right] \quad \text{(B-1)}$$

and

$$TMP_i = \frac{B_{i-1,k}+B_{i,k}}{2}\,\frac{(h_k + \eta_{i-1,1})+(h_k+\eta_{i,1})}{2}\,u_{i,k,1} \quad \text{(B-2)}$$

where

$q_{i,k}$ = lateral volume inflow including the point and distributed nonpoint source discharges,

STB_i = equivalent width of the storage area = $SST_i/\Delta x$.

The inclusion of STB_i in the denominator of Eq. B-1, which accounts for the effect of the side storage area, is explained in Section B-5.

B-2. Conservation of Longitudinal Momentum

The implicit treatment of the vertical viscosity term in Eq. 2-20 results in the equations containing the N×N tri-diagonal matrix where N is the number of layers at each segment. The equations in the vertical direction may be expressed as,

$$[A][u] = [F] \tag{B-3}$$

That is,

$$\begin{bmatrix} D_1 & E_1 & 0 & . & . & . & 0 \\ C_2 & D_2 & E_2 & 0 & . & . & 0 \\ 0 & . & . & . & . & . & 0 \\ 0 & . & C_k & D_k & E_k & . & 0 \\ 0 & . & . & . & . & . & 0 \\ 0 & . & . & . & C_{N-1} & D_{N-1} & E_{N-1} \\ 0 & . & . & . & . & C_N & D_N \end{bmatrix} \begin{bmatrix} u_{i,1,2} \\ u_{i,2,2} \\ . \\ u_{i,k,2} \\ . \\ u_{i,N-1,2} \\ u_{i,N,2} \end{bmatrix} = \begin{bmatrix} F_1 \\ F_2 \\ . \\ F_k \\ . \\ F_{N-1} \\ F_N \end{bmatrix} \tag{B-4}$$

and the non-zero elements, C_k, D_k, E_k and F_k, are given by,

$$E_k = -2\lambda_2 \frac{B_{i-1,k}+B_{i,k}+B_{i-1,k+1}+B_{i,k+1}}{(h_k+\lambda_1\eta_{i-1,2})+(h_k+\lambda_1\eta_{i,2})+2h_{k+1}}(A_{z(i-1,k)}+A_{z(i,k)}) \tag{B-5}$$

$$C_k = (1-\lambda_1)E_{k-1} \tag{B-6}$$

$$D_k = (B_{i-1,k}+B_{i,k})\frac{(h_k+\lambda_1\eta_{i-1,2})+(h_k+\lambda_1\eta_{i,2})}{\Delta t} - C_k - E_k \tag{B-7}$$

$$\begin{aligned} F_k = {} & (B_{i-1,k}+B_{i,k})\frac{(h_k+\lambda_1\eta_{i-1,1})+(h_k+\lambda_1\eta_{i,1})}{\Delta t}u_{i,k,1} - \frac{HAdvM_{i,k}-HAdvM_{i-1,k}}{4\Delta x} \\ & + \frac{\lambda_2}{4}(B_{i-1,k}+B_{i,k}+B_{i-1,k+1}+B_{i,k+1})(w_{i-1,k,1}+w_{i,k,1})(u_{i,k,1}+u_{i,k+1,1}) + 4\lambda_1\frac{B_{i-1,k}+B_{i,k}}{\rho_{i-1,k}+\rho_{i,k}}\tau_w \\ & - \frac{1-\lambda_1}{4}(B_{i-1,k-1}+B_{i,k-1}+B_{i-1,k}+B_{i,k})(w_{i-1,k-1,1}+w_{i,k-1,1})(u_{i,k-1,1}+u_{i,k,1}) \end{aligned} \tag{B-8}$$

$$+ \frac{HDifM_{i,k} - HDifM_{i-1,k}}{2\Delta x^2} - 2\kappa u_{i,k,1} |u_{i,k,1}| (B_{i-1,k} + B_{i,k} - \lambda_2 (B_{i-1,k+1} + B_{i,k+1}))$$

$$- 2(B_{i-1,k} + B_{i,k}) \frac{(h_k + \lambda_1 \eta_{i-1,2}) + (h_k + \lambda_1 \eta_{i,2})}{\rho_{i-1,k} + \rho_{i,k}} \left(\frac{\partial p}{\partial x}\right)_{i,k,2} - \lambda_1 STSink_{i,k}$$

$$\begin{aligned} HAdvM_{i,k} = {} & \{(B_{i-1,k} + B_{i,k})(h_k + \lambda_1 \eta_{i-1,1} + h_k + \lambda_1 \eta_{i,1}) u_{i,k,1} \\ & + (B_{i,k} + B_{i+1,k})(h_k + \lambda_1 \eta_{i,1} + h_k + \lambda_1 \eta_{i+1,1}) u_{i+1,k,1}\} (u_{i,k,1} + u_{i+1,k,1}) \end{aligned} \quad \text{(B-9)}$$

$$\begin{aligned} HDifM_{i,k} = {} & \{(B_{i-1,k} + B_{i,k})(h_k + \lambda_1 \eta_{i-1,1} + h_k + \lambda_1 \eta_{i,1}) A_{x(i,k)} \\ & + (B_{i,k} + B_{i+1,k})(h_k + \lambda_1 \eta_{i,1} + h_k + \lambda_1 \eta_{i+1,1}) A_{x(i+1,k)}\} (u_{i+1,k,1} - u_{i,k,1}) \end{aligned} \quad \text{(B-10)}$$

where

τ_w = wind stress at the water-air interface,

λ_1 = 1 for k = 1 (at top layer), and

0 for $2 \leq k \leq N$,

λ_2 = 1 for $1 \leq k \leq N-1$, and

0 for k = N (at bottom layer).

The term, $STSink_{i,k}$, in Eq. B-8 represents the sink of momentum due to the side storage area, and is explained in Section B-5.

B-3. Conservation of Salt

The implicit treatment of the vertical diffusion term in Eq. 2-21 results in the equations containing the N×N tri-diagonal matrix in the vertical direction. In matrix notation,

$$[AS][s] = [FS] \quad \text{(B-11)}$$

which takes the same form as Eq. B-4, and the non-zero elements, CS_k, DS_k, ES_k and FS_k, are given by,

$$ES_k = -\lambda_2 \frac{B_{i,k}+B_{i,k+1}}{(h_k+\lambda_1\eta_{i,2})+h_{k+1}} K_{z(i,k)} \quad \text{(B-12)}$$

$$CS_k = (1-\lambda_1) ES_{k-1} \quad \text{(B-13)}$$

$$DS_k = B_{i,k} \frac{h_k+\lambda_1\eta_{i,2}}{\Delta t} - CS_k - ES_k \quad \text{(B-14)}$$

$$FS_k = B_{i,k} \frac{h_k+\lambda_1\eta_{i,1}}{\Delta t} s_{i,k,1} - (HAdvS_{i,k} - HAdvS_{i-1,k}) + (HDifS_{i,k} - HDifS_{i-1,k})$$

$$+ \frac{\lambda_2}{4}(B_{i,k}+B_{i,k+1}) w_{i,k,1} (s_{i,k,1}+s_{i,k+1,1}) \quad \text{(B-15)}$$

$$- \frac{1-\lambda_1}{4}(B_{i,k-1}+B_{i,k}) w_{i,k-1,1} (s_{i,k-1,1}+s_{i,k,1}) - \lambda_1 STSinkS_{i,k}$$

$$HAdvS_{i,k} = (B_{i,k}+B_{i+1,k}) \frac{(h_k+\lambda_1\eta_{i,1})+(h_k+\lambda_1\eta_{i+1,1})}{4\Delta x} u_{i+1,k,1} \cdot s^*_{i+1,k} \quad \text{(B-16)}$$

$$HDifS_{i,k} = (B_{i,k}+B_{i+1,k}) \frac{(h_k+\lambda_1\eta_{i,1})+(h_k+\lambda_1\eta_{i+1,1})}{4\Delta x^2} K_{x(i+1,k)} (s_{i+1,k,1}-s_{i,k,1}) \quad \text{(B-17)}$$

where

$s^*_{i+1,k}$ = salinity at the downstream wall face of cell and is given by Eq. 2-22, The term, $STSinkS_{i,k}$, in Eq. B-15 represents the exchange of salt between the conveying main channel and the side storage area, and is explained in Section B-5.

B-4. Conservation of Water Mass

The laterally integrated continuity equation (Eq. 2-19) is solved to get w, and the finite difference formulation is,

$$w_{i,k,2} = \frac{\lambda_2}{B_{i,k}+B_{i,k+1}} [(B_{i,k+1}+B_{i,k+2}) w_{i,k+1,2} + \frac{2}{\Delta x} q_{i,k+1}$$

$$- \frac{h_{k+1}}{\Delta x} \{(B_{i,k+1}+B_{i+1,k+1}) u_{i+1,k+1,2} - (B_{i-1,k+1}+B_{i,k+1}) u_{i,k+1,2}\}] \quad \text{(B-18)}$$

and $B_{i,k+2}$ is assumed to be $B_{i,k+1}$ for k = N-1. Equation B-18 is solved to get $w_{i,k,2}$ for $1 \leq k \leq N-1$, and the vertical velocity is zero at the bottom of the bottom layer, i.e., at k = N.

B-5. Treatment of Embayment as Storage Area

Dispersion produced by tidal trapping may be important for some parts of the estuary with substantial area of side embayments, small branching channels or shallow flanks. A portion of water with its contained substances is stored temporarily in side embayment, while the main flow proceeds along the estuary's major axis on rising tide. If recapture of the stored volume is out of phase with the main flow on falling tide, longitudinal mixing occurs when the tide reverses.

The present model that calculates the longitudinal and vertical variations of the dependent variables along the conveying main channel, cannot calculates the variations in the side embayment area. It however account for the exchange of momentum and mass between the main channel and side embayment by treating the latter as temporary storage area. Since only the time variations of momentum and mass in the storage area affect the main channel conditions, and the total depth in the side embayment is usually shallow, the exchange of momentum and mass may be assumed to happen only at top layer

For the mass exchange of water, since the surface elevation of the storage area rises and falls in accordance with the main channel, it is required to include the equivalent width of the storage area (STB_i) in the denominator of continuity equation (Eq. B-1). When the water enters into storage area (i.e., on rising tide), the storage area in each segment will act as a sink for both momentum and mass, and the mass concentration in the storage area will change because of the mixing between the incoming water and the water in the storage area. When the water leaves the storage

area (i.e., on falling tide), the storage area is assumed to act as a source for the mass only (not momentum), and the mass concentration in the storage area remains the same for conservative substances. For the non-conservative substances, the mass concentration on falling tide will be determined solely by the bio-chemical reactions in the storage area.

For the momentum exchange, therefore, it is needed to include a sink term, $STSink_{i,1}$, in Eq. B-8 only on rising tide, that is,

$$STSink_{i,1} = 2(STB_{i-1} + STB_i)\frac{\Delta\eta}{\Delta t}u_{i,1,1}, \quad if\ \Delta\eta = \eta_{i-1,2} + \eta_{i,2} - \eta_{i-1,1} - \eta_{i,1} > 0 \qquad \text{(B-19)}$$

For the mass exchange of a dissolved substance like salt, a sink (or source) term, $STSinkS_{i,1}$, is needed to be added in Eq. B-15;

$$STSink_{i,1} = STB_i\frac{\eta_{i,2} - \eta_{i,1}}{\Delta t}s_{i,1,1} \qquad if\ \eta_{i,2} - \eta_{i,1} > 0 \qquad \text{(B-20a)}$$

$$STS_i = \frac{STS_i STH_{i,1} + s_{i,1,1}(\eta_{i,2} - \eta_{i,1})}{STH_{i,2}}$$

$$STSink_{i,1} = STB_i\frac{\eta_{i,2} - \eta_{i,1}}{\Delta t}STS_i \qquad if\ \eta_{i,2} - \eta_{i,1} < 0 \qquad \text{(B-20b)}$$

where

STS_i = salinity in the storage area,

$STH_{i,n}$ = depth at the storage area at time step n.

VITA

Kyeong Park

Born in Taegu, Korea on February 11, 1962. Received B.S. from the Department of Petroleum and Mineral Engineering of the Seoul National University, Korea in February, 1985. Received M.S. from the Marine Sciences Research Center, State University of New York at Stony Brook, New York in May, 1987. Entered Ph.D. program in the Virginia Institute of Marine Science / School of Marine Science, College of William and Mary, Virginia in September, 1988.